

THESIS

GEOCHEMISTRY AND CHARACTERISTICS OF BRECCIATION AT THE
LAMPROPHYRE-HOSTED SAPPHIRE DEPOSIT AT YOGO GULCH, MONTANA

Submitted by

Tracey Cotterell

Department of Geosciences

In partial fulfillment of the requirements

For the Degree of Master of Science

Colorado State University

Fort Collins, Colorado

Summer 2022

Master's Committee:

Advisor: John Ridley

John Singleton
Heather Blackburn

Copyright by Tracey Cotterell 2022

All Rights Reserved

ABSTRACT

GEOCHEMISTRY AND CHARACTERISTICS OF BRECCIATION AT THE LAMPROPHYRE-HOSTED SAPPHIRE DEPOSIT AT YOGO GULCH, MONTANA

In 1894 the world class lamprophyre-hosted Yogo Sapphire deposit was discovered on the eastern side of the Little Belt Mountains at Yogo Gulch, located 72 km (45 mi) southwest of Lewistown, Montana. The sapphires are found as small etched wafer-like stones that are cornflower-blue to violet with excellent clarity. The host rock is described as an ultramafic, biotite and clinopyroxene rich, lamprophyre called an ouachitite that has ocelli, which are globular carbonate inclusions. Sapphires in the lamprophyre dike at Yogo are some of the finest in the world and their origin has not been fully constrained. Sporadic breccias associated with the dike that appear to be spatially related to sapphires have been noted, but not evaluated and may play a role in the generation of sapphires.

Field observations and sample collecting suggests that there are two types of breccias in the dike and in the surrounding limestone. The first is a paleokarst breccia in the host Madison Limestone which ranges from yellow to orange and is clast supported with very little matrix. The matrix is composed of a mixture of clays and iron oxides, while the clasts are a combination of coarse sand to boulder sized, yellow to gray limestone with minor coarse sand to pebble sized red siltstone. Paleokarst breccias in the area are found as limestone spires, irregular shaped bodies up to 60 m tall and 15 m wide (200 x 50 ft), and semi- to unconsolidated sediment cones. The second breccia type has been interpreted as paleokarst as well but differs in that it is deep orange to red in color, semi-consolidated to unconsolidated, and is generally matrix supported

with clasts sizes ranging from coarse sand to boulder. These breccias have irregular shaped “blobs” of dike rock incorporated into them and have a higher concentration of red siltstones and shales. The incorporation of magma into the poorly consolidated paleokarst breccias is evidence that magma intruded into the breccia. No textural or mineralogical evidence has been found to suggest hydrothermal brecciation occurred.

It is proposed here that the polymict breccias containing lamprophyre inclusions are a previously undescribed karst peperite. Peperite is a term applied to a rock that has both igneous and sedimentary components. It is interpreted to be the result of magma intruding or extruding over unconsolidated to semi-consolidated wet sediments. They can be described as fluidal, blocky, or ragged and/or there may be a mixture of all three depending on whether the interaction between the magma and sediments was explosive or fluidal. The presence of both fluidal and blocky peperite fabrics suggest it was possible that both interactions occurred at Yogo, although no quenching textures were observed to support the former, both in the field and in thin section.

An important finding from field work is the role karst has on weathering. Secondary permeability of enlarged joints, karst, and karst breccias at Yogo has allowed meteoric water to infiltrate to a depth of at least 94.5 m (310 ft) in the Vortex Mine. Exposure to water allows for advanced weathering of the lamprophyre in subsurface breccias as well as dikes and breccias at depth.

Another conclusion of this study is the recognition that there are two lamprophyre melts at Yogo. The differences can be seen in lamprophyre texture and mineralogy and geochemistry. Lamprophyre 1 samples have a microcrystalline matrix that is composed primarily of carbonate, feldspathoids, and analcime, some of the samples have microphenocrysts of subhedral to

ehedral biotite with minor clinopyroxene. Large phenocrysts of biotite are more abundant than in Lamprophyre 2 samples, and have anhedral, castellated appearance. Ocelli are abundant in Lamprophyre 1 and vary geochemically while Lamprophyre 2 have little to no ocelli. Most of the Lamprophyre 2 samples have a devitrified “glassy” matrix with microphenocrysts of subhedral to anhedral biotite and minor euhedral clinopyroxenes. Phenocrysts of clinopyroxenes are large, euhedral, and range in size from coarse to fine while coarse phenocrysts of anhedral, castellated biotite are rare. Geochemical differences are subtle yet consistent. For instance, when compared to Lamprophyre 2, Lamprophyre 1 is relatively FeO and LREE poor and Al₂O₃ rich. While there is variability which suggests different phases of lamprophyre dike, their overall geochemical similarity suggests they were from the same intrusive event.

The main body of the lamprophyre has abundant xenoliths classified here by hand sample and petrographic descriptions and preliminary geochemical data found by pXRF. They are classified as follows: ultramafic and mafic xenoliths rich in clinopyroxene with elevated concentrations of Cr and Ti suggesting an upper mantle origin; felsic xenoliths from the upper crust found as partially melted granitic clasts with elevated Si and Zr; irregularly shaped quartz xenoliths with thick reaction rims of feldspathoids and altered amphibole interpreted to be quartz veins from an unknown level; metasedimentary xenoliths of recrystallized limestone and bedded ashed crude oil were found as float and are presumed to be from the immediately underlying sedimentary units and were incorporated during the final stages of emplacement; calc-silicate xenoliths of unknown origin are found with no reaction rim suggesting they were in equilibrium with the host at the time of emplacement.

The origin of the sapphires was not a central concern of this work. However, the results allow certain interpretations to be made. No sapphires were seen associated with xenoliths, so it

is unclear if they were picked up from another source. Some of the granitic xenoliths have been partially melted which supports models that there was a more felsic and aluminum rich melt incorporated into the lamprophyre melt that could have allowed for the formation of sapphires. This suggests that the sapphires have a magmatic origin.

ACKNOWLEDGEMENTS

First, I would like to express gratitude for my advisor John Ridley, for his support and guidance as well as his patience, specifically regarding the two surgeries I underwent and through the Covid-19 pandemic as I homeschooled my 8-year-old daughter, Saige. I am also grateful for my committee for their input and patience. My field assistant Brenna Challis and John Childs were invaluable to my field work, without them I would not have been challenged to think outside the box. Secondly, I extend my gratitude to Ron Kunisaki, owner of the American/Kunisaki mine and surrounding property, as well as Don Baide, owner of the Vortex Mine, for allowing us access to their properties and permission to collect samples. A special thanks to local prospector George L. and his wife Beth, who not only acted as tour guides during our research but also treated us to dinner at their home. Don Baide and his wife Oui let us use their facilities and invited us for meals during our stay, as well as regaling us with the history of the Yogo Gulch area. Also, a special thanks goes to the owners of the Blue Nugget Bar for letting us stay in a cabin short notice. Without the research grants provided by both the Society of Economic Geologists and the Colorado Scientific Society, this research would not have been possible, for that I am grateful. Last, but not least, I am grateful to my daughter Saige for her undying enthusiasm and for believing in me throughout my entire education, and my loving, patient partner, Alex, who supported me in more ways than one through this endeavor.

TABLE OF CONTENTS

ABSTRACT.....	ii
ACKNOWLEDGEMENTS.....	vi
CHAPTER I. INTRODUCTION.....	1
History.....	1
Previous Geological Work.....	4
Sapphires in Montana.....	7
This research.....	9
FIGURES: CHAPTER I.....	11
CHAPTER II. GEOLOGIC SETTING.....	12
FIGURES: CHAPTER II.....	17
CHAPTER III. METHODS.....	19
Field methods.....	19
Petrography.....	20
Analytical methods.....	21
Whole rock and trace element geochemistry.....	21
Portable X-Ray Fluorescence (pXRF).....	21
TABLES: CHAPTER III.....	23
CHAPTER IV: FIELD RELATIONSHIPS BETWEEN BRECCIAS AND LAMPROPHYRE.....	26
Regional paleokarst in the Madison Group.....	26
Karst and karst breccias at Yogo.....	27
Breccia and lamprophyre relationships.....	29
Weathering of dike underground.....	31
FIGURES: CHAPTER IV.....	38
CHAPTER V: PETROGRAPHY.....	47
Breccias.....	48
Monomict breccias.....	48
Hand samples.....	48
Petrography.....	48
Polymict breccias.....	49
Hand samples.....	49
Petrography.....	49
Polymict breccias with lamprophyre inclusions.....	49
Hand samples.....	49
Petrography.....	50
Lamprophyres.....	50
Lamprophyre 1.....	50
Hand sample.....	50
Petrography.....	51
Lamprophyre 2.....	53
Hand sample.....	53
Petrography.....	54
Xenoliths.....	56
Ultramafic.....	56
Hand sample.....	56
Petrography.....	57
Mafic.....	57

Hand sample	57
Petrography	58
Felsic	58
Hand sample	58
Petrography	59
Quartz.....	59
Hand sample	59
Petrography	59
Metasedimentary	60
Recrystallized limestone	60
Hand sample	60
Petrography	60
Organic rich metasedimentary	61
Hand sample	61
Petrography	61
Calcsilicate of unknown origin	62
Hand sample	62
Petrography	62
FIGURES: CHAPTER V	69
CHAPTER VI: GEOCHEMISTRY	120
Classification diagrams	120
Total Alkali Silicate (TAS)	120
Discrimination of lamprophyre types with major and trace elements geochemistry	121
Different phases of lamprophyres	122
Fresh lamprophyres.....	122
Weathered lamprophyres	123
Mineralogical controls on geochemical variability	125
Portable X-Ray Fluorescence (pXRF) analysis of dike components	127
Ocelli.....	127
Xenoliths	127
TABLES: CHAPTER VI.....	130
FIGURES: CHAPTER VI	136
CHAPTER VII: DISCUSSION	158
Origin of breccias	158
Paleokarst.....	158
Dike emplacement influenced by paleokarst.....	160
Paleokarst with lamprophyre inclusions	160
Peperite	161
Role of karst on weathering	162
New information on the genesis of the dike	164
Lamprophyres 1 vs 2.....	164
Petrography	164
Geochemistry.....	165
Mineral controls on geochemistry	166
Classifying the Yogo dike	167
Weathering	169
Origin of components of the dike	170
Ocelli.....	171
Xenoliths	171
Implications for the origin of the sapphires	174
FIGURES: CHAPTER VII	175

CHAPTER VIII: CONCLUSIONS	176
Suggested research	176
REFERENCES	178
APPENDICES	182

Chapter I: Introduction

Sapphires have fascinated mankind for centuries and through the ages their use has varied from lavish jewelry to watch bearings, to industrial abrasives. The world class lamprophyre hosted Yogo sapphire deposit, located 45 miles southwest of Lewistown, Montana, has been heralded as one of the only sapphire deposits where the stones do not have to be heat treated to attain the desired clarity sought after by jewelers and laypersons worldwide (Fig. 1.1) (Voynick, 1985). With their unique, natural corn flower blue to violet color combined with their clarity they fetch a high price on the gem market (Fig. 1.2) (Voynick, 1985; Palke et al, 2016). Though the deposit is economic the mining history at Yogo has been turbulent at best.

History

The following history of mining and geological investigation of the Yogo sapphire deposit is summarized from Stephen M. Voynick's book *Yogo the Great American Sapphire* (1985) with additions from Renfro et al (2018).

In 1864 Montana sapphires were first discovered by gold prospectors sluicing sand and gravel from abandoned river channels of the Missouri River. The Montana gold rush did not reach Yogo Creek until 1878, but the venture was abandoned by disappointed prospectors 3 years later. During that time prospectors -only interested in gold- allegedly kept finding blue stones in their gold pans and discarded them.

It was not until 1894 that Jake Hoover, a local mountain man thriving off the harsh landscape, struck gold, rumor has it. Upon prospecting further, he was too, sorely disappointed by the lack of gold in Yogo Creek, but unlike his forbearers he kept the blue stones. The stones

were identified as sapphires and sent to Tiffany & Co in New York city to be appraised by Dr. George Frederick Kunz. This resulted in the discovery of the Yogo Sapphire.

The sapphire-bearing dike itself was discovered by a local sheep herder, Jim Ettien, who noticed a linear progression of gopher diggings that were taking advantage of a zone of softer ground. This zone was marked by a depression in the earth that carried on in a straight line for 3.2 km (2 miles), right to Yogo Creek. He collected dirt from the gopher diggings to wash and found the same type of blue stone that Hoover found. In 1896 sapphire mining at Yogo Creek began with prospectors Hoover, Hobson, and Bouvet as the New Mine Sapphire Syndicate and by 1899 the town of “Sapphire” was founded. Mining operations began with a top-down approach. The strange, sapphire bearing rock was heavily weathered from the surface up to about 15 meters allowing for the easy extraction of sapphires.

By 1902 mining operations were taken over completely by British gem merchants Johnson, Walker, and Tolhurst, Ltd, who began surface workings on the aptly named “English Mine”, seen today as a deep gash in the Earth about half a kilometer long. Mining under the New Mine Sapphire Syndicate was supervised for the next 25 years by Charles T. Gadsden. During this time mining operations extended another ~0.3 km to the west where it is named the Middle Mine.

In 1904 John Burke and Pat Sweeny had developed an underground mining operation on their Fourth of July claim, just west of the English Mine, called the “American Mine” (later the Kunisaki Tunnel) but struggled to make a profit. This property passed to the Yogo American Sapphire Company based in Great Falls, Montana but as with previous developers, the operation resulted in failure and the Yogo American Sapphire Company filed for bankruptcy. By 1914 the

claim was purchased by the New Mine Sapphire Syndicate and Gadsden began underground workings where Burke and Sweeny had abandoned their operation.

Sapphire production remained volatile; dropping to near nothing during World War I and picking up after only to be hindered by drought and the development of synthetic corundum. Gadsden refused to let his mining operation go under, though after a major flood damaged vital infrastructure he had no choice but to shut down sapphire production entirely upon which the New Mine Sapphire Syndicate pulled out of the Yogo area in 1929. The next company to invest in the Yogo sapphire deposit was the American owned Yogo Sapphire Mining Corp. (only to change names once more to the New Mine Sapphire Syndicate), managed by Thomas Sidwell, in 1949. Charles Gadsden remained living and watching over the property, giving tours to visitors like field geologist Stephen Clabaugh, who was surveying Montana's corundum deposits.

Estimated sapphire values at Yogo were based off Geological Survey Bulletin 983, *Corundum deposits of Montana* by Clabaugh, 1952 and gave a simplified interpretation of the deposit. The report was not intended to be the end all be all geological investigations at Yogo and suggested that 100 million carats of sapphires lay waiting in the Yogo dike. All mining was based off this report and contributed to the failure of mining operations. This happened to Yogo Sapphire Mining Corp. in 1956. Ownership of the deposit passed between multiple owners but mining never quite got off the ground. It was not until the late 1970s – 1980s that a more extensive investigation was carried out at Yogo by gemologist and geologic engineer Delmer Brown.

Brown found that the dike was much more complex than Geological Survey Bulletin 983 suggested. He was the first to note the role karst and karst breccia on dike emplacement. Not only this but he noted the presence of xenoliths from the Precambrian basement that suggested

the dike existed at greater depths. By 1980 mining operations were being run by Intergem Ltd. During the first five years of operation, they mined an estimated 750,000 carats of sapphires but as with earlier operations, success rates remained volatile and ended in 1985, where upon Roncor Inc. took it over. 1992 was the last time mining was conducted in the American Mine, now Kunisaki Tunnel, at Yogo.

In 1987 Lanny Perry and Chuck Ridgeway discovered an unmined section of dike west of Yogo Creek adjacent to Kelly Coulee and staked their claim under the name Vortex Mining. Underground operations began with the sinking of a 280 ft shaft following sapphire-bearing rock underground. Mining continued at Vortex until 2004 when it became subeconomic (Renfro, 2018). In 2008 mine ownership passed to Mike Roberts and then to Don Baide in 2017, who is soon to be resuming active underground mining at Vortex.

Previous Geological work

The Yogo Sapphire deposit was first described by Kunz, Prisson, and Pratt in 1897. Kunz's role was describing sapphire distribution in Montana, while Prisson described the lamprophyre dike and related rocks at Yogo Gulch in hand samples and in petrographic thin section. He described the lamprophyre as dark grey biotite, pyroxene rich rock with white and green fragments. The green being altered pyroxene and the white consisting entirely of calcite. He suggested the calcite present in the rock originated as limestone fragments picked up during dike emplacement. In thin section he noted that the lamprophyre consists mainly of anhedral, inclusion filled and altered pyroxene var. diopside and "ragged masses" of biotite. He also describes "clouded, brownish, kaolin-like, aggregate" that he has identified as some sort of feldspathoid. Prisson also suggests that due to the high biotite content the lamprophyre is genetically related to the neighboring minette and Yogo Peak laccolith. The flat wafer-like

sapphires found at Yogo led him to conclude they formed because of the inclusion of aluminum rich shale fragments at depth. Pratt described the overall crystallography in general of Montana sapphires including sapphires at Yogo Gulch. Weed (1899) described the sedimentary sequence of rocks in the Little Belt Mountains and associated igneous rocks, including sapphire deposits at Yogo.

Yogo was not revisited by geologists until Clabaugh in 1952, who briefly described the local geologic setting, the mineralogy in both fresh and weathered dike rock, geochemistry, and petrography. Clabaugh described the deposit itself as “exceedingly simple... A nearly vertical sapphire-bearing igneous dike cuts through gently dipping Limestone.” He suggested that the assimilation of aluminum rich sedimentary or metamorphic rocks resulted in sapphire formation. Most mining decisions made up until the ‘70s were based on his geologic report, which gave an inaccurate representation of the economic viability of the deposit. While still economic it proved to be difficult to mine productively and led to previously outlined complications (Voynick, 1985).

More recently there have been geological studies over the Yogo dike and its sapphires. Brownlow and Komorowski (1988) discussed the geology and origin of the sapphire-bearing Yogo Dike. They described general features of the lamprophyre such as mineralogy and petrography. They determined the lamprophyre varies in composition and contains varying amounts of biotite, olivine (fresh and weathered), diopside, titanite, and hypersthene, as well as xenoliths and ocelli. The variability in lamprophyre composition led them to conclude that the Yogo dike does not quite fit amongst lamprophyre classifications and appears to be a hybrid lamprophyre and classify it as an alkaline lamprophyre with ultrabasic characteristics. Their description of the sapphires note they are etched and coated in spinel suggesting the Yogo dike

has an aluminum rich mantle origin and that the sapphires were out of equilibrium due to addition of other components during its journey to where it is emplaced today.

Meyer and Mitchell's (1988) work focused on mineral geochemistry which was compared to Clabaugh's (1952) single whole rock geochemical data. They conclude that the dike is an ouachitite and based on the etched, pitted, and spinel coated sapphires they suggest the sapphires are xenocrystic.

Dahy (1988) suggests that the dike is multi-phase and classifies it as an ouachitite with pyroxene rich xenoliths, which are the result of pyroxene crystallization at depth prior to dike emplacement. According to his findings, the sapphires are related to xenoliths from the Precambrian basement and did not originate in the parent magma. He describes the breccias as "intrusion breccia" that occurred during dike emplacement which are mostly matrix composed of igneous dike with clasts of the overlying Madison Group, "post-intrusive collapse breccia" composed mainly of limestone, dike, shale, and siltstone as clasts with a matrix of dike, silt, and limestone. Dahy describes other breccias as "limestone solution and collapse breccia" that are entirely formed of limestones from the Madison Group and the overlying Big Snowy Group and finally a "diatreme breccia" containing both dike, clay, and limestone with quartz and pyrite. He also noted the presence of solution and collapse breccias occurring between 36.6 to 48.8 m (120 – 160 ft) below the top of the Madison Group.

Gauthier (1995) presented a K-Ar biotite date of 48.2 ± 1.3 Ma for the Yogo dike. Based on geochemistry, Gauthier (1995) determined that the dike is best characterized as an ultramafic lamprophyre that is not related to the shonkinites and minettes in the area. His geothermobarometric study on a granulite xenolith composed of garnet, clinopyroxene and plagioclase yielded 40 – 70 km depth at 850°C as a depth and temperature of formation. He also

suggests that the Yogo sapphires are related to xenoliths in the dike and that they are xenocrysts themselves. Harlan (1996) used $^{40}\text{Ar}/^{39}\text{Ar}$ dating of phlogopite phenocrysts and yielded a date of 48.66 ± 0.06 Ma which is slightly younger than other rocks of similar composition found in the Little Belt mountains. The ages of other intrusive rocks, such as the shonkinite Yogo stock, in the Little Belt Mountains range from 49.8 to 52.6 Ma (Harlan, 1996).

Mychaluk (1995) revealed that there is a cluster of six subparallel lamprophyre dikes that make up the Yogo Sapphire deposit and that there is a strong control on emplacement by faulting and the presence of karst. He noted that sapphire occurrence is variable between the different dikes and that one dike (~200 m north of the English Mine) is completely barren.

Palke et al (2016) investigated details of sapphire chemistry and the chemistry of melt inclusions in the sapphires and leucocratic ocelli in the lamprophyre. He suggests that the sapphires came from the interaction of lamprophyre magma with an aluminum rich protolith in the mantle such as an anorthosite in the lower crust. Analcime and calcite inclusions found in Yogo sapphires are interpreted to be crystallized melt and have the same mineral composition of ocelli in the lamprophyre. Thus, he suggests the ocelli and sapphires are genetically related (Palke et al, 2016; Palke et al, 2018). Renfro et al (2018) discusses different types of inclusions within the sapphires themselves and suggests that they have an igneous origin. He identified decrepitation haloes and protogenetic inclusions composed of rutile, feldspar, apatite, garnet, metal sulfides, and rare monazite and negative crystals filled with carbonate and analcime.

Sapphires in Montana

Sapphires in Montana are generally found as alluvial deposits and come in an array of pastel colors and varied clarity. They were used historically from the 1920's to 1930's for

industrial purposes and watch bearings, in the 1990's heat treatment was found to vastly improve the color and clarity of sapphires, and this has been since used for jewelry (Palke et al, 2017). The most productive site is the Rock Creek alluvial deposit that has produced over 60 tons of sapphires (Fig. 1.1) (Berg and Dahy, 2002; Palke et al, 2017). The other two alluvial deposits are the Dry Cottonwood Creek and Missouri River bars. Garland (2002) suggests that all the alluvial sapphires came from a metamorphic source from a zone along the outer margin of the Bitterroot core complex. Recent research has suggested that these sapphires were more than likely hosted as xenocrysts and as components of xenoliths in volcanic rocks emplaced at ~50 Ma. The French Bar "dike" is a sapphire-bearing trachybasalt sill located 23 km NE of Helena, MT near the Missouri River bars. Similarity in melt inclusions to the alluvial sapphires at Missouri River suggests they are related though the sill is not large enough to have yielded the number of sapphires along found at the Missouri River (Berg and Dahy, 2002; Palke et al, 2017). Rhyolitic encrustations have been found on sapphires at Rock Creek and are thought to be related to the voluminous rhyolite volcanics in the area (Berger and Berg, 2006; Palke et al, 2017). While there are no sapphire-bearing rocks at Dry Cottonwood Creek they are presumed to have originated in the Lowland Creek Volcanics (Palke et al, 2017). A study of melt inclusions of Montana sapphires by Palke et al (2017) suggests that the sapphires originated from partial melting of an aluminum rich protolith at depth during slab roll back of the Farallon plate which allowed fresh asthenosphere to interact with the base of the continental lithosphere. Alternatively, Berg and Dahy (2002) speculate that sapphires are components of gneissic xenoliths incorporated into the magma during its ascent through the crust.

This research

The Yogo sapphire deposit differs from the other sapphire occurrences in Montana in that it is the only one with a defined bedrock source. The stones have been mined directly from the sapphire-bearing ultramafic lamprophyre dike in Yogo Gulch and are known for their cornflower blue to violet color and excellent clarity (Palke et al, 2016). Knowledge passed from local prospectors and miners through the years has emphasized the importance of weathering in the lamprophyre. Unweathered dike rock extracted by miners over the decades was set out during the winter months to expose it to enough water to weather and extract whole, undamaged sapphires from the rock. Miners have also realized there is a relationship between breccias and sapphire deposition at Yogo, but it is poorly understood as to why.

It has been suggested that there are two phases of lamprophyre present, but no definitive study has been carried out. Different xenoliths and parts of xenoliths found in the Yogo dike have been recognized but have not been study in detail, of which could give clues as to what the possible sources of sapphires are. Sapphires at Yogo have been recognized as xenocrysts or components of xenoliths but melt inclusion chemistry suggest they have an igneous origin (Palke et al, 2016; Palke et al, 2018).

In view of gaps in Yogo work, the objectives of this project are (1) to determine the origin and mode of formation of different types of breccias and their clasts in the Yogo dike and (2) to test the relationships between sapphires, breccia types, different phases of the dike rock, and xenoliths. A combination of field relationships, thin section petrography, whole rock, and trace element geochemistry is used to investigate these relationships.

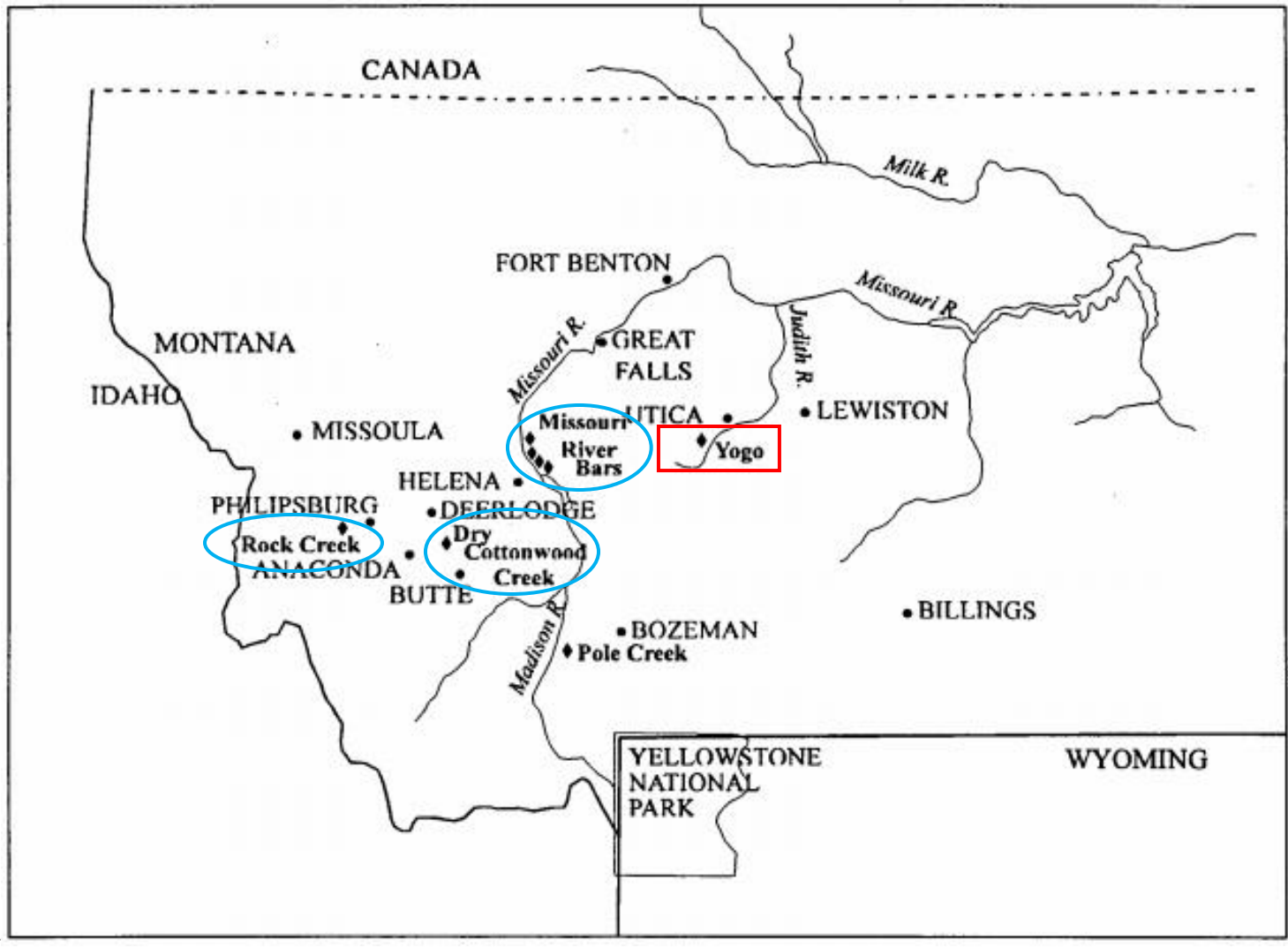


Figure 1.1. Location of the Yogo dike, 72 km (45 miles) southwest of Lewistown, Montana (Modified from Gauthier, 1995). Alluvial sapphire deposits are circled in blue.

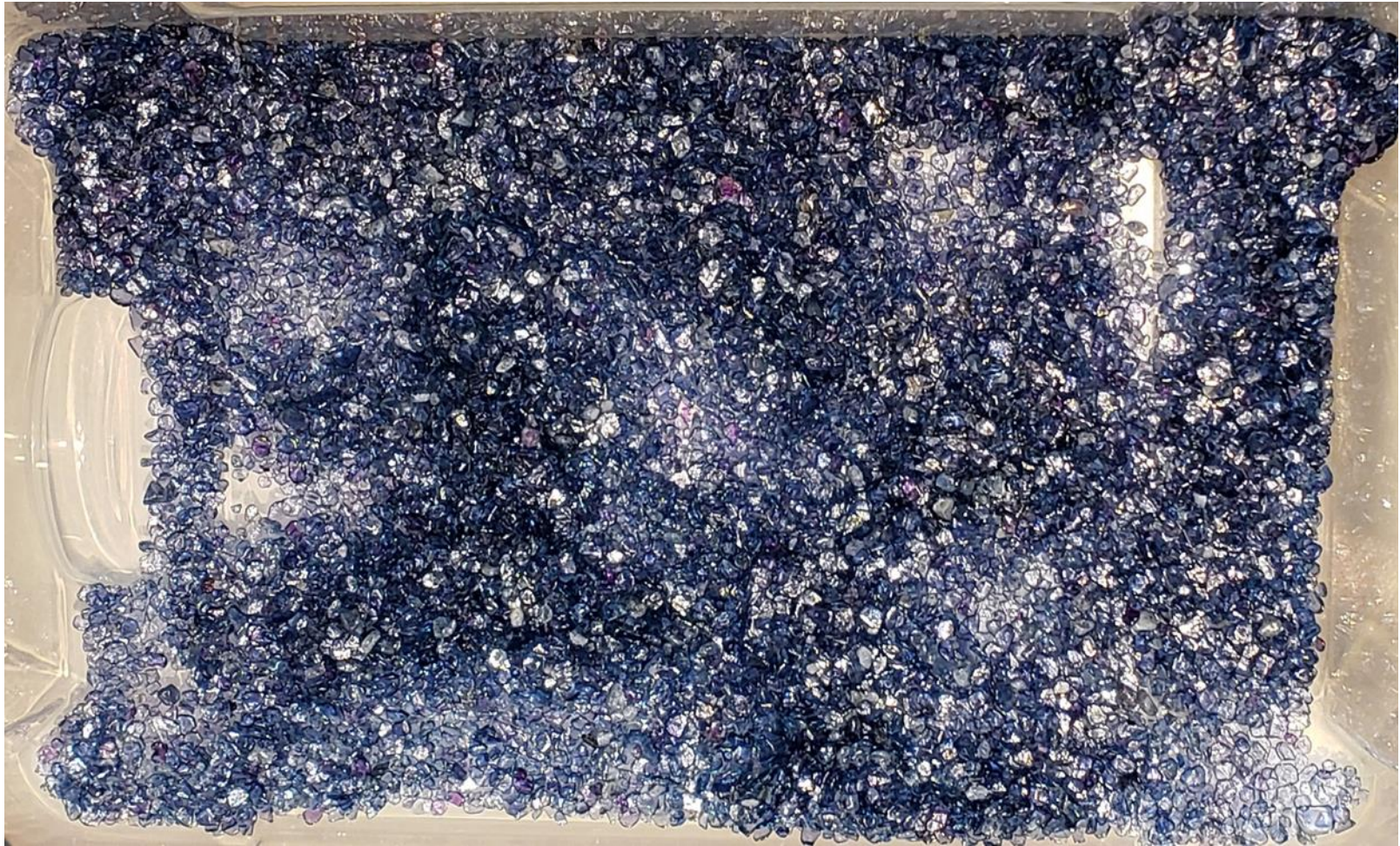


Figure 1.2. A mixture of mainly cornflower blue sapphires from Yogo with a few violet stones.

Chapter II: Geologic Setting

The geologic setting of the study area is outlined based on formations and intrusions in the immediate vicinity of the Yogo dike. The oldest rocks are the Archean basement, unconformably overlain by the Paleoproterozoic Belt Supergroup, the Cambrian Park Shale, Pilgrim Limestone, and Dry Creek Shale. These are then unconformably overlain by the Devonian Jefferson Formation, Maywood Formation, and the Three Forks Shale (Sandberg, 1965; Dahy, 1988). The Mississippian Madison Group, and the overlying Big Snowy Group Formation are the next units and are the primary sedimentary units in the study area (Fig. 2.1). The main tectonic event that affected this area, the Laramide Orogeny, overlapped with the Cretaceous aged Boulder Batholith and other major intrusions that lie in the zone of intense deformation west of the Central Montana Alkalic Province (CMAP) (Sarkar et al, 2009). The Yogo lamprophyre dike emplacement is thought to be related to other alkaline intrusions in the Little Belt Mountains which occurred with the development the Central Montana Alkalic province during the Eocene (Marvin et al, 1973; Harlan, 2006).

About fifteen miles west of Yogo in the Little Belt Mountains Archean basement rocks are exposed as gneisses, amphibolites, schists, granodiorites and metadiorites (Brandt, 2007). The Proterozoic Belt Supergroup strata ~610 m (2000 ft) thick overlie the Archean basement (Dahy, 1988). The Supergroup is dominantly composed of metapelites interbedded with thin laminated to cross bedded quartzites, and micritic limestones (Winston, 1986; Evans, 1986). Division of the units has had a complex history, but the consensus is that there are four main groups: the Lower Belt, Ravalli Group, Middle Belt carbonate, and the Missoula Group (Winston, 1986).

The Proterozoic formations are unconformably overlain by Cambrian aged rocks starting with earliest Flathead Quartzite followed by the Wolsey Shale and Meagher limestone, these are believed to exist at depth beneath the Yogo Dike (Dahy, 1988). Outcropping Cambrian units in the area are the Park Shale, Pilgrim Limestone, and Dry Creek Shale located about 4 km northwest, ~15 km west, and ~8 km southwest of the Yogo dike (Dahy, 1988; Brandt, 2007). The top of the Cambrian is unconformably overlain by Devonian aged marine limestones of the Jefferson and Maywood Formation, followed by the calcareous shales, siltstones, and minor limestones of the Three Forks Shale (Sandberg, 1965; Dahy, 1988). These units are then unconformably overlain by Mississippian aged limestones.

The Mississippian Madison Limestone is the most extensive unit exposed in the study area and is split into two divisions: The lower Lodgepole Formation and the upper Mission Canyon Limestone (Sando and Dutro, 1974). These formations consist of light gray to buff colored, basal limestones, minor evaporite beds and chert nodules, and dense marine limestones and dolostones. In its upper two hundred feet, the top of the Mission Canyon Limestone, there are abundant solution breccias that vary in appearance (Dahy, 1988).

Overlying the Madison Group is the Late Mississippian aged lower Kibbey and middle Otter Formations of the Big Snowy Group (Dahy, 1988; Gauthier, 1995). These units are exposed in the eastern portion of the study area, the best outcroppings found in the Intergem Cut (Gauthier, 1995). The Kibbey Formation is described as red to yellow, calcareous sandstones, siltstones and shales and ranges from 43 – 52 m (140 – 170 ft) thick. This unit is generally slope forming with vegetation (Dahy, 1988). The middle Otter Formation consists of interbedded limestone lenses with green to black calcareous shales. Regionally, the area is assumed to have been covered by Jurassic and Cretaceous strata which has now been eroded from the area.

From Mesozoic to Paleogene the Laramide Orogeny affected the Little Belt mountains as stacked lower “thick-skinned” and upper “thin-skinned” deformation (Parker and Pearson, 2021). Thick-skinned deformation expressed itself as basement uplift as the shallowly subducted Farallon plate scraped against the base of the continental crust (Baker, 1991). The product of this deformation developed the northwest southeast trending anticline that makes up the dome of the Little Belt Mountains. Thin-skinned deformation affected the sedimentary cover and was pressed up against the southwest edge of the anticline (Baker, 1991). Yogo is located on the hinterland of the Laramide deformation front where the most intense deformation occurred from the southwest to the northeast about ~44 km to the southwest of the study area.

Intense alkaline magmatism further to the northeast followed the Laramide Orogeny, coinciding with delamination of the Farallon plate. This event is thought to have resulted in fresh asthenosphere upwelling beneath the crust, creating regional uplift, and interacting with the delaminated slab (Dahy, 1991; Dudas, 1991). The resulting alkaline magmatism is known as the Central Montana Alkalic Province that lasted from ~54 to 48 Ma with minor episodic magmatic pulses occurring until ~45 Ma (Fig. 2.2) (Baker, 1991; Harlan, 1996).

The Yogo lamprophyre dike intrudes on existing joint structures in the exposed Mission Canyon Limestone of the Madison Group (Fig. 2.3) (Dahy, 1988). It is dated at ~48.2 – 48.66 Ma and is related to the cluster of alkalic rocks in the Little Belt Mountains that are ~54 to ~48 Ma (with minor magmatism at 45 Ma) (Marvin et al, 1977; Gauthier, 1995; Harlan, 1996). Igneous intrusions in the Little Belt Mountains are seen as numerous felsic batholiths composed of quartz latite, the closest being the Yogo stock roughly 22 km northwest of the study area. This intrusion is composed of shonkinites, monzonites and syenites (Woodward, 1991). Radiating felsic to mafic dikes and sills identified as minettes, kersantites, and spessarites are observed

over a radius of 16 to 19 km around the Yogo stock and are thought to be related (Woodward, 1991; Gauthier, 1995). A minette sill located ~1 km southwest of Sapphire village at the junction of South Fork and Yogo Creek Roads is exposed in the Otter Formation. While the sapphire-bearing lamprophyre dike is similar in age to the nearby intrusions, Yogo dike emplacement occurred at the end of the period of magmatism (Harlan, 1996).

SYSTEM	GROUP	UNIT	
CRETA- CEOUS		DAKOTA 1st Cat Creek	
		KOOTENAI 2nd Cat Creek 3rd Cat Creek	
JURASSIC	ELLIS	MORRISON	
		SWIFT	
		RIERDON	
		PIPER	
TRIASSIC			
PERMIAN			
PENNSYL- VANIAN	AMSDEN	TENSLEEP	
		ALASKA BENCH	
		TYLER	
MISSISSIPPIAN	BIG SNOWY	HEATH	
		OTTER	
		KIBBEY	
	MADISON		CHARLES
			MISSION CANYON
			LODGEPOLE
			BAKKEN

Figure 2.1. Generalized stratigraphic column of the sedimentary sequence at Yogo, the Madison Group and Kibbey Formation are circled. Modified from Obermajer et al, 2002.

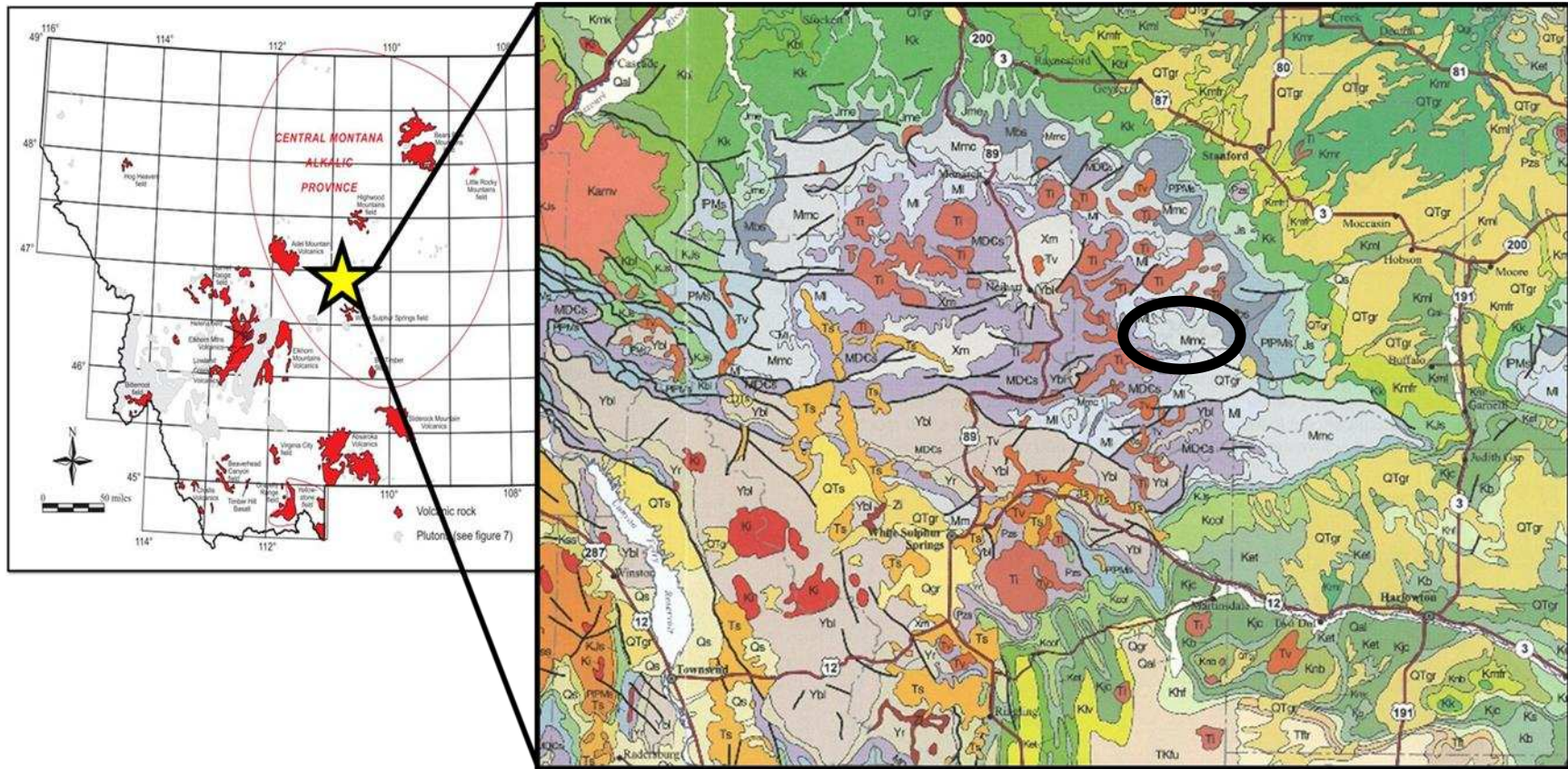


Figure 2.2. Left: location of the Yogo dike within the Central Montana Alkalic Province. Right: Expanded location of the Yogo dike within the Mississippian aged Madison Group (modified from Vuke et al, 2007)

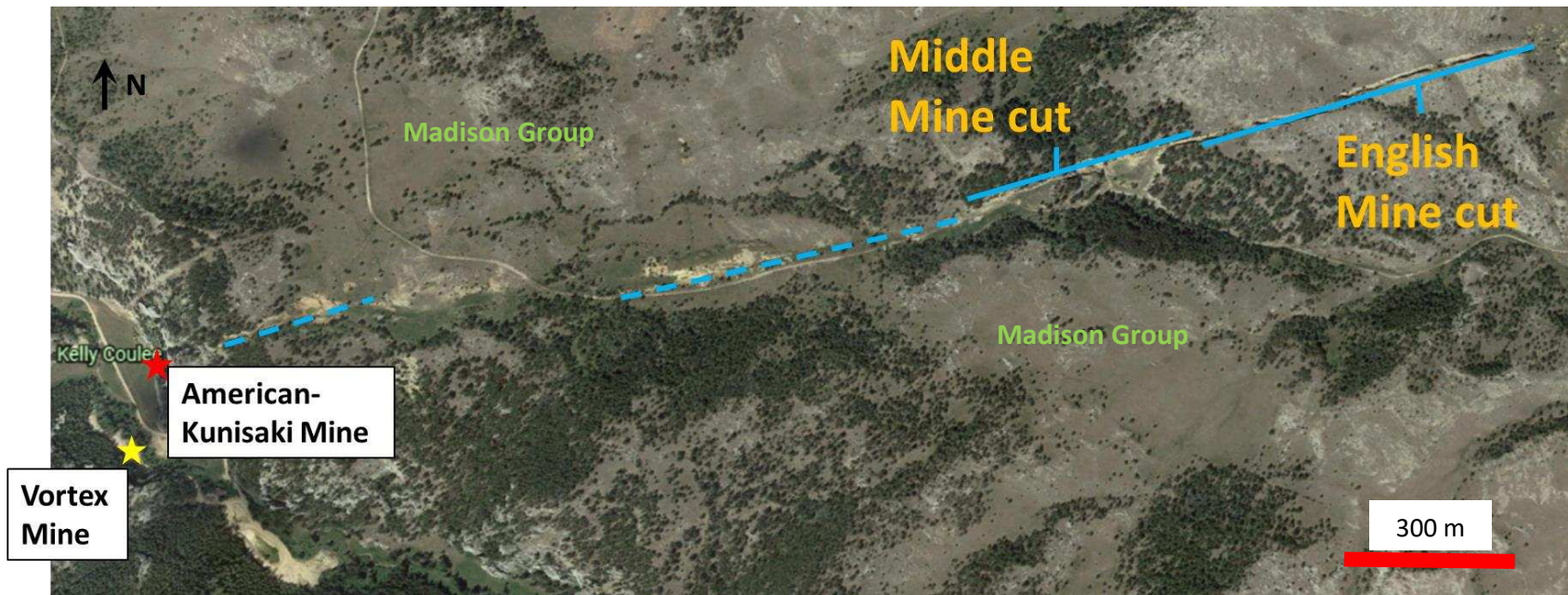


Figure 2.3. Aerial photograph from Google Earth™ showing the location of the old English and Middle mine cuts. The deep gash cutting through the Madison Group limestone is the only evidence that the lamprophyre dike existed. Dashed lines represent inferred dike beneath the surface that has not been mined. The location of underground workings at the American-Kunisaki tunnel and Vortex mine are across from and adjacent to Kelly Coulee.

Chapter III: Methods

Field methods

During the first two weeks of June 2019, we conducted a field study of the Yogo Dike and related breccias and structures. Utilizing maps from Dahy (1988) and aerial photography, we investigated portions of the dike both above and below ground over a strike length of ~10 km (6 miles). Field documentation of available exposures of different phases of the dike rock and breccias, on the surface and underground tell us about relative timing, nature, and controls of brecciation. This information is compared with the local knowledge of the known distribution of sapphires provided by personal communication from Intergem cut diggers, Don Baide -owner of Vortex mine- and mine workers George Linde and Butch of the Kunisaki mine, to investigate spatial relationships between breccias and sapphire occurrence. While in the field we sampled different phases of the dike rock, breccia types, and clast types. During the first three days we were accompanied by Dr. John Ridley and the last four days we were accompanied by Dr. John Childs with Childs Geoscience, Inc. Two local prospectors George Linde and Butch assisted us with access to property surrounding the main part of the dike. All samples, and their use are listed in table 3.1.

Lamprophyre samples were chosen based on xenolith abundance and mineralogy, and on the presence of sapphires. All the remaining surface outcrops that were not mined have been weathered out, so most of these samples were taken from mine dumps adjacent to the English Mine cut or from the tailing piles at the mouth of the American Tunnel and the tailings pile just below the Vortex mine entrance. In-situ samples of weathered, and irregularly spaced dike were collected above the American Tunnel, along strike of the English Mine and Middle Mine cuts.

These dike samples were hosted in an unconsolidated to semi-consolidated breccia meaning that these samples are contaminated by the breccia components. The only fresh in-situ samples were collected in the underground dike exposures of the Vortex mine. Various weathered samples were also collected underground in the Vortex Mine but without contamination of breccia.

Breccia samples were collected within the mined portion of, and adjacent to, the strike of the dike. Sampling was based on color, matrix to clast distribution, clast type, and whether there was lamprophyre present in the sample. Two breccia types were identified in the field using these parameters, a monomict breccia and a polymict breccia. The size of breccia bodies was measured by tape where possible and estimated elsewhere.

Petrography

Thirty-five lamprophyre samples were chosen for petrography based mainly on xenolith content and type, followed by mineralogy, and then ocelli abundance. The representative samples were classified using grain size, texture, mineralogy, and xenolith composition. Two lamprophyre types were identified using these parameters and have been named Lamprophyre 1 and Lamprophyre 2.

Five breccia samples were selected for petrographic analyses based on matrix to clast ratio, matrix color, clast type and presence of lamprophyre inclusions. Two minette samples were selected based on mineralogy and xenolith content. One recrystallized/bleached limestone and one ashed crude oil sample were also selected for petrography.

All thin sections were scanned using Meyer Instruments' PathScan Enabler under plane and cross polarized light prior to petrographic analyses. Petrography was done using a Leica DM2500P polarization microscope with a Clemex Camera for image capture.

Analytical methods

Whole rock and trace element geochemistry

Eight representative samples of both lamprophyre types were sent out for geochemical analyses: five samples from Lamprophyre 1 and three samples from Lamprophyre 2. These samples were chosen based upon their lack of xenoliths. Eight weathered samples, chosen by their color (grey, red, yellow) were sent out as well as two minette samples. Geochemistry was performed by ACTlabs out of Ancaster, Ontario, Canada under code 4E-Expl see table 6.1a and 6.1b for sample list, analysis method, and geochemistry.

- Fusion Inductively Coupled Plasma Mass Spectrometry (FUS-ICP) was used to determine major elements as well as Ba, Be, Sr, V, Y, and Zr concentrations.
- Instrumental Neutron Activation Analysis (INAA) was used to analyze a various REEs, Trace elements, and transition elements.
- Near-Total Digestion Inductively Couple Mass Spectrometry (TD-ICP) was used to analyze Ag, Bi, Cd, Cu, Mo, Ni, Pb, and Zn.

Some of the elements have been analyzed by a combination of these analyses.

pXRF

One-minute (two 30 second beam) analyses were done using the Geochem mode on the Olympus Delta Premium portable X-Ray Fluorescence device with collimator enabled at a spot size of 1x3 mm or collimator disabled at a spot size of 3x8 mm. The collimator enables the laser beam to be more focused allowing us to sample smaller spots and when disabled the beam is dispersed allowing for a larger spot to be analyzed. Data retrieved from the pXRF is semi-quantitative as no standard has been analyzed to compare the data to. The data provided by

pXRF testing does give relative abundances of major and trace elements which can aid in supporting classification of xenoliths, mineralogy, and ocelli found in the lamprophyre. It is important to note that lighter elements, such as sodium, are not analyzed by pXRF. The element magnesium is the lightest of the elements measured and as such it is considered to be the most subject to error; results may be unreliable, so it is best to refer to whole rock geochemistry for magnesium concentrations.

Samples chosen for analysis by pXRF were based on their ocelli and xenolith content and type. Parameters used to determine which xenoliths to test were mineralogy, size (greater than 1x3 mm), and color. Ocelli were chosen based on size (>1x3 mm) and zonation was considered as well. A table has been provided to show which samples were used, spots tested, and beam sized used (table 3.2).

Table 3.1. All samples used in petrography, geochemistry, pXRF				
Type	Sample #	Petrography	Whole rock geochemistry	pXRF
Breccia (B)				
Monomict	B25	x		
Monomict	B26	x		
Monomict	B29	x		x
Monomict + red cement	B28			x
Polymict impregnated	B3	x		
Breccia + English mine lamprophyre	EM45	x		
Breccia + English mine lamprophyre	EM46	x		
Vortex mine breccia (VMB)	VMB2	x		
Lamprophyre				
English mine (EM)	EM3			x
	EM4			x
	EM10a	x		x
	EM10b	x		x
	EM12a	x		
	EM12b	x		
	EM14a	x		
	EM14b	x		
	EM15a	x		x
	EM15b	x		x
	EM15c	x		x
	EM26a	x	x	x
	EM26b	x	x	x
	EM26c	x	x	x
	EM26d	x	x	x
	EM31/26a	x	x	
	EM31/26c	x	x	
	EM3a	x		
	EM3b	x		
	EM47a	x		x
	EM47b	x		x
	EM7	x		x
	EM7a	x		
	EM7b	x		
	EM7c	x		
	EMOCTa			x
	EMOCTb	x	x	x

Table 3.1 continued. All samples used in petrography, geochemistry, pXRF				
Type	Sample #	Petrography	Whole rock geochemistry	pXRF
Kelly Coulee (KC)	KC1	x	x	x
English mine October sample	EMOCTc	x	x	x
Minette (M)	M1a	x	x	x
	M1b			
	M2b	x		
Vortex mine (VM)	VM10	x	x	
	VM15	x		
	VM5			x
	VM6	x		
	VM6a	x		
	VM6b	x		
	VM7a	x	x	x
	VM7b	x	x	x
	VM9	x	x	x
Weathered Lamprophyre				
	EM42		x	
	EM44		x	
Vortex mine weathered dike (VMWD)	VMWD1		x	
	VMWD2		x	
	VMWD4		x	
	VMWD5		x	
	VMWD6		x	
	Intergem weathered dike (IGWD)	IGWD1		x
Miscellaneous				
Ashed crude oil	?1			x
Ashed crude oil	?2	x		
Recrystallized/bleached limestone	?3a	x		
Recrystallized/bleached limestone	?4b	x		x
Recrystallized/bleached limestone	?4c	x		x

Table 3.2. Samples used in pXRF as well as the number of spots and the type of spots analyzed (e.g. xenoliths, ocelli, matrix, or clast).

Sample #	Number of Spots	Xeno	Ocelli	Matrix	Clast	Other
EM10	10	x				
EMOct	5	x		x		
?4	2			x		
B28	2			x	x	
M1a	5	x				
M1b	6	x				
?Bb	3			x		
VM5	3	x				
EMOcta	5	x				
EMOctc	1	x				
EM15	8	x				
EM47	6	x	x			
EM7	11	x	x			
VM9	1		x			
EM3	3	x				
EM26	15	x	x			x
EM4	4	x				

Chapter IV: Field relationships between breccias and lamprophyre

A major topic of this research is the nature of breccias in and around the Yogo dike, hence I will first summarize the paleokarst breccias known in the Madison Group and then describe breccias at Yogo. Different breccia types are distinguished in karst and are recognized at Yogo. Crackle breccias are breccias that have had little clast displacement and retain a clast orientation close to that of unbrecciated rock, whereas rubble breccias are those that have had significant clast displacement (Fig. 4.1) (Morrow, 1982). Crackle breccias generally occur at the top and along margins of the collapsed cavern while rubble breccias occupy the center of the body (Fig. 4.2) (Sangster, 1988).

Regional paleokarst in the Madison Group

Karst and paleokarst has been described throughout the Madison Group across Montana, Wyoming and into South Dakota. The consensus is that there was karst formation and subsequent collapse during deposition of the Madison Group and Big Snowy Group from the Late Mississippian to Early Pennsylvanian (Sando, 1974; Sando, 1988). Post Madison deposition there was a period of karst formation, before the deposition of red siltstones, sandstones and shales of the overlying Kibbey Formation (lower Big Snowy Group) that filled enlarged joints and sinkholes in the upper 60 m (200 ft) of the Mission Canyon Limestone (Bull Ridge) member of the Madison Group (Sando, 1974; Demiralin, 1993; Luebking et al, 2001). These enlarged joints and sinkholes later collapsed due to dissolution and the overlying weight of the Big Snowy group. This created irregular shaped bodies of polymict breccias dominated by the red siltstones, sandstones, and shales of the Kibbey Formation (Sando, 1974). Further collapse of caves occurred in areas of uplift during the Laramide (Sando, 1974; Sando, 1988).

Modern caves have developed up to 122 m (400 ft) from the surface in the Madison Group along joints and bedding planes from the mid to late Pleistocene to the present (Sando, 1974; Greene and Rahn, 1995; Paces et al, 2020). Underground investigations have shown that these modern caves developed preferentially within older cave collapse (Fig. 4.3). Some sinkholes have been filled by the overlying Kibbey unit of the Big Snowy group as seen in Horsethief cave of northcentral Wyoming and southcentral Montana (Sando, 1974; Sando, 1988). The sinkhole fill, referred to as sediment cones, is composed of semi-consolidated to unconsolidated red siltstones, tan silty limestone clasts in a matrix of loose red clays, sands, and evaporites. They are found capped partially or completely by drip stone (Fig. 4.4).

Two main types of karst breccias have been described in the Madison Group. One has been described as containing mostly clasts of the host Madison from a mixture of facies within the unit. The clasts have been described as dark grey to tan, silty or sandy limestones, oolitic limestone, fossiliferous limestones, and brecciated limestone that have a characteristic yellow to ochre weathering product (Middleton, 1961; Sando, 1988; Demiralin, 1993). These breccias vary in matrix to clast ratio, some are entirely clast supported and some mainly matrix supported composed of carbonate and clays, in some of the literature these breccias have been divided into separate groups based on this ratio (Demiralin, 1993). The second breccia type has been described as polymict, containing mixture of fragments including red siltstones and sandstones, tan limestone clasts, and yellow limey mudstones, with a red matrix dominated by silt and carbonate (Middleton, 1961; Sando, 1974; Sando, 1988; Demiralin, 1993).

Karst and karst breccias at Yogo

Classic karst topography is visible in aerial photography as infilled sinkholes, also known as dolines, north and south of the English Mine cut (Fig. 4.5). There are limestone columns and

towers found along the Yogo Creek Valley as well as partially collapsed openings in the limestone cliffs. Field observations have shown that these are the result of cave development within older paleokarst breccias (Fig. 4.6).

The most abundant karst breccias found in the study area are found as limestone spires and irregular shaped bodies up to 60 m tall and 15 m wide (200 x 50 ft), displaying rubble and crackle breccias (Fig. 4.7 and 4.8). No spires in the study area are unbrecciated, but unbrecciated areas in the Madison Group can be seen in the limestone walls along the road along Yogo Creek Valley. These breccias vary slightly in matrix to clast ratio and concentrations of disseminated hematite. The first type, ranges from yellow to ochre in color and is clast supported, cemented by a limey clay matrix that has varying concentrations of disseminated hematite, the coloration is presumed to be a weathering product. Some matrix in these samples may have minor coarse sand to pebble sized red limey siltstones. The clasts themselves are coarse sand to boulder-sized (up to ~0.5 m (2ft)), yellow to grey Madison Group limestones. These breccias will be referred to as “monomict breccia” due to the single origin of their clasts.

One monomict breccia body 400 m (1/4 mile) northwest from the American Mine tunnel ranges from deep orange to red in color as a result of high concentrations of disseminated hematite in the silicate rich matrix which may show bedding. These breccias are also composed entirely of Madison Group limestones, some fossiliferous, and have the same to greater amounts of matrix than breccias described elsewhere in the group. For further hand sample descriptions refer to the petrography chapter.

The second karst breccia type is the one that is reported -according to local prospectors- to contain sapphires in the Intergem cut. This semi- to unconsolidated, rubble breccia is deep orange to red in color and is matrix supported with clasts sizes ranging from coarse sand to

boulder. It is composed mainly of red limey siltstones and shales with minor, yellow limestone clasts. See the petrography section for a more in-depth description of this breccia. Due to this breccias mixed clast composition it will be further referred to as “polymict breccia”. Field observations determined that it is generally along and above strike of the dike and may be capped by limestone blocks that have not been excavated or weathered away (Fig. 4.11). The limestone blocks are coherent or display crackle breccia. Dimensions of the bodies are undecipherable due to burial but appear to range from 1.5 m (5 ft) to at least 30 m (100 ft) in length and 3.6 m (12 ft) in height. Importantly, irregular shaped “blebs” of dike rock may be found within some of these breccias.

Breccia and lamprophyre relationships

Lamprophyre inclusions in the polymict breccia range dramatically in size and morphology. In the hand dug prospecting pits at the Intergem cut there are inclusions of weathered lamprophyre within the polymict breccia that are found as angular blocks and fragments, bulbous, lensoidal, lobate, and as irregular blebs that range from 7.6 – 12.2 cm (.25” – 40”) in dimension and small veinlets that are around 3.8 – 7.6 cm (.125” – .25”) in width (Fig. 4.9). These inclusions are seen between and surrounding breccia clasts and as a component of the matrix. The lamprophyre itself is soft and friable, easily dug into, and is dark to light green in color with lime green flecks and lose biotite. A more comprehensive description of the weathered lamprophyre in polymict breccia is provided in the petrography chapter.

Inclusions of lamprophyre in the polymict breccia are also found at the west end of the Middle Mine cut and in prospect pits along strike of the dike (Fig. 4.10). At the eastern end of the western most Middle Mine cut there is a monomict brecciated wall ~10 m long and 2.5 m high (30 x 10 ft) facing south that ranges from a crackle breccia on its eastern end to rubble

breccia on its western end. The lower contact of this wall rests on a unit of similar sized semi- to unconsolidated polymict breccia that is soft and easily into with a rock pick, in which are small lamprophyre inclusions (Fig. 4.11). At the west end of the final Middle Mine cut there is a 2.5 to 5 cm (1 to 2 in) vein-like inclusion of lamprophyre between an upper large limestone block and a lower semi consolidated polymict breccia (Fig. 4.12). Above the Kunisaki/American tunnel there is a dig site that has a large, monomict breccia wall 14 m (45 ft) long and 4 m (12 ft) high that is dips $\sim 85^\circ$ to the southeast. At the base of this wall there are lamprophyre inclusions in the semi consolidated polymict breccia (Fig. 4.13).

Brecciated (monomict and polymict) and unbrecciated areas of the Madison Group both were observed underground in both the Kunisaki-American mine and the Vortex Mine. Easier access to the Vortex mine afforded better images and sampling. In the Kunisaki-American mine damp ochre-colored, polymict breccias have no evidence of lamprophyre inclusions (Fig. 4.14a).

Underground in the Vortex Mine there is a room referred to as the electrical bay located 30.5 m (100 ft) below the surface with estimated dimensions of 11 x 9 m (35 x 30 ft) with a 4 m (12 foot) tall ceiling. The walls of this room are entirely polymict breccias, the mixture of clast types, ranging from around 2.5 to 61 cm (1 to 24 in) in size. One eighth to 0.3 m (0.5 to 1 ft) wide blocks of limestone have been stained black, but the red shales and siltstones have retained their color, as well as the smaller yellow altered limestone clasts (Fig. 4.14b). The matrix of these breccias is red to orange in color in color and is composed of carbonate mud. There is one section seen on the southeast end that has lamprophyre in the matrix that has been weathered to an orange, grey-green color (Fig. 4.14c).

Weathering of dike underground

Lamprophyre dikes are partially to completely weathered where exposed at significant depths in the Vortex Mine in areas both with and without breccias. At 40 m (130 feet) below the surface there is a breccia exposed in a natural karst room (estimated dimensions are 19.5 x 20 m (64 x 65 ft) with a 6 m (20 ft) tall ceiling), but no lamprophyre was detected as clasts or matrix. On the ceiling of the same room there is a discontinuous narrow section of the dike, ranging from 5 to 20 cm (2 - 8 in) across, that has weathered completely to a maroon-ish red and a yellow clay rich rock (Fig. 4.15c). At 94.5 m (310 ft) wider sections of the lamprophyre dike are viewed ranging from 20 to 30 cm (8 - 12 in) in width. These sections of dike have fresh lamprophyre with weathered lamprophyre on the contact between the Madison Limestone host and the dike, there is also some weathering present along fractures in the lamprophyre (Fig. 4.15a/b). It is important to note that there appears to be different weathering profiles at different depths. Weathering is intense and occurs in a large volume at shallower depths and with the same intensity at greater depths but with smaller volumes.

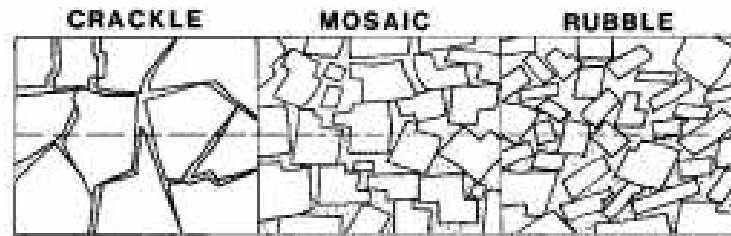


Figure 4.1. Schematic diagram showing breccia fabrics from Morrow, 1982.

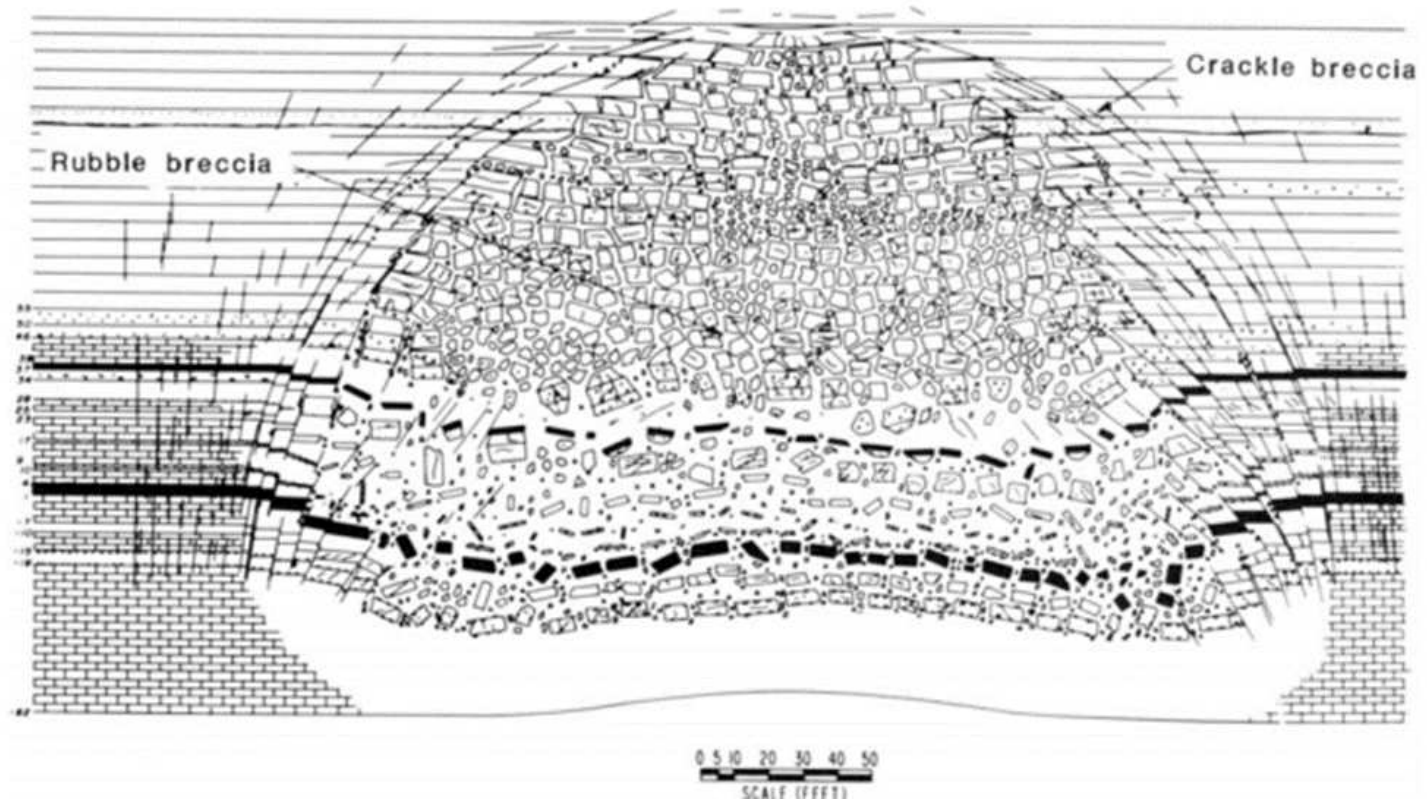


Figure 4.2. Schematic drawing showing the possible distribution of crackle and rubble breccias found in karst collapse from Sando, 1988.



Figure 4.3. Karst breccia inside Horsethief cave located in the Bighorn Basin of northcentral Wyoming and southcentral Montana. The photo on the left is an example of karst development within a brecciated zone in the Madison Group. The red silt and clay dominated zone with tan limestone clasts is interpreted to be a collapsed infilled sinkhole that received its material from the overlying depositional sequence that is now eroded at the surface. There is a zone directly under the collapsed sinkhole that is composed entirely of Madison Group limestones. The photo on the top right is a close-up of the red breccia, it is soft and easily dug into.

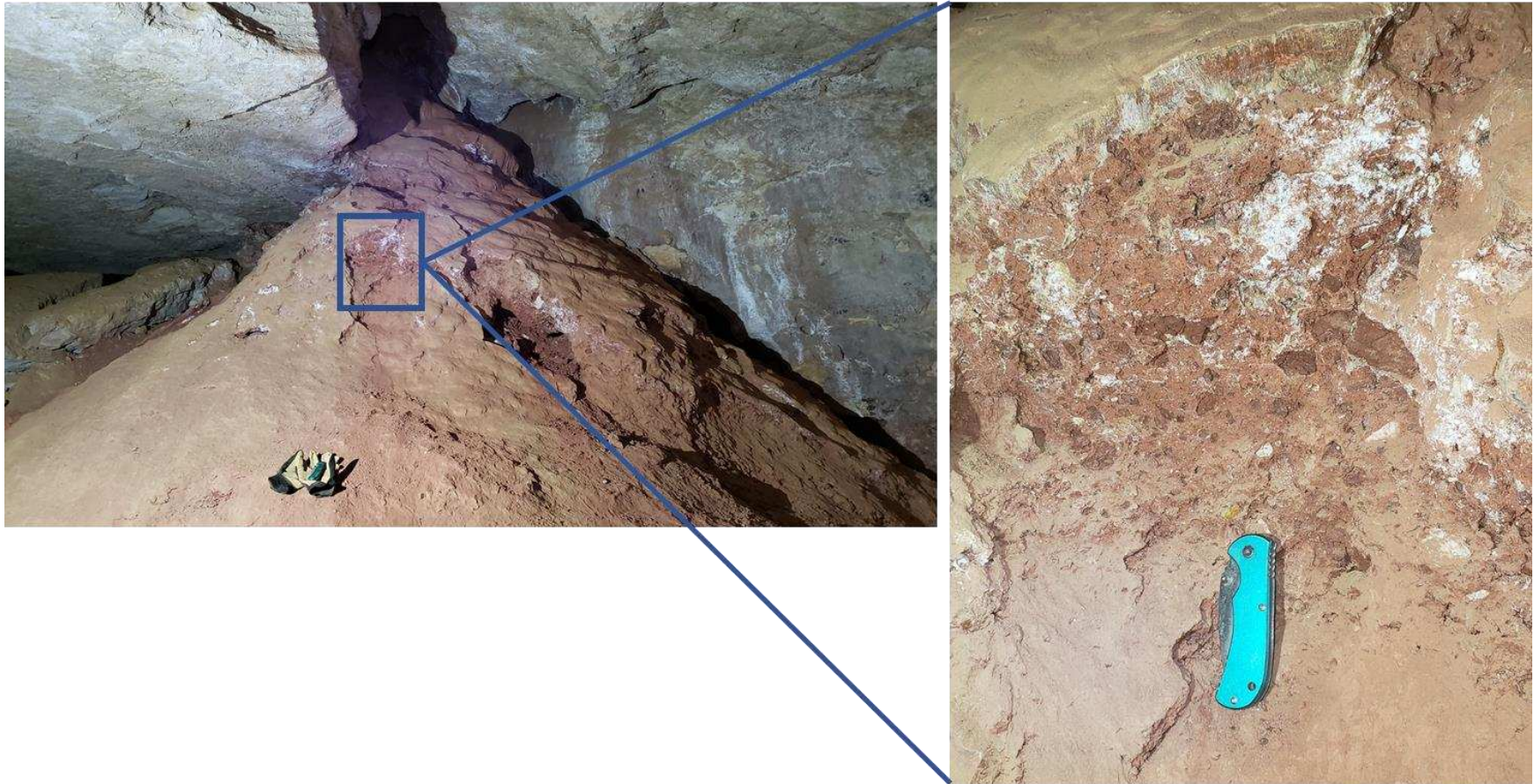


Figure 4.4. The left-hand photo is of a sediment cone capped by drip stone in Horsethief cave. It is an example of a doline that has been preserved. The right-hand photo shows an exposed area of unconsolidated to semi consolidated sediment that shows red siltstone, clay stones with small yellow limestone clasts.

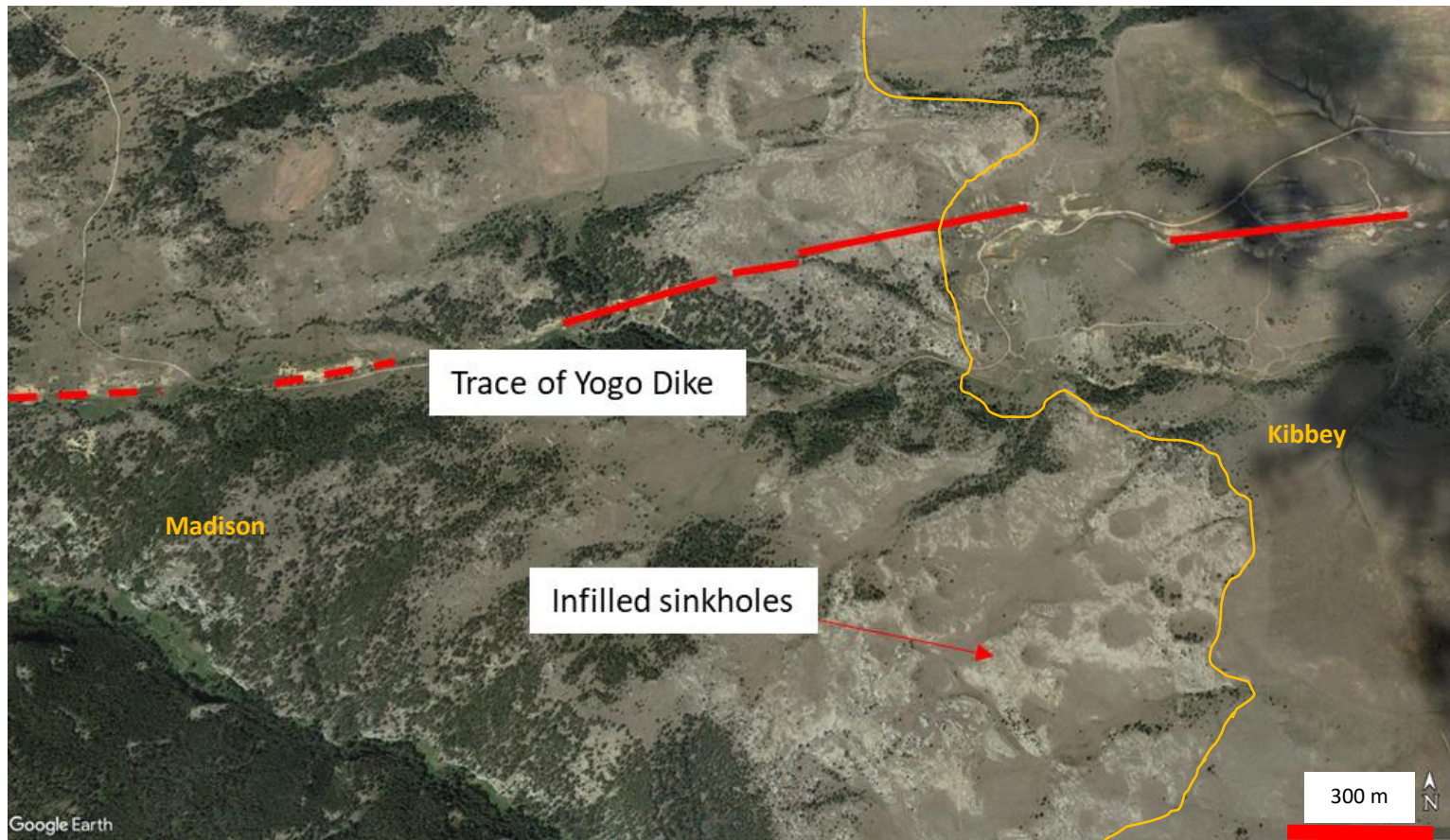


Figure 4.5. Aerial photograph from Google Earth™ that shows classic karst topography north and south of the Yogo dike in the upper unit of the Madison Group. The “swiss-cheese” topography is the result of infilled sinkholes also known as dolines. These occur in the upper most Mission Canyon Limestone of the Madison Group, below the Kibbey formation the contact of which is seen in the eastern most part of the study area.



Figure 4.6. Top photo view from above the Kunisaki-American mine tunnel looking west across Yogo Creek Valley towards the Vortex mine shaft. The central spire is composed entirely of monomict breccia and is estimated to be ~70 m (200 ft) tall. The bottom left photo is of a passage through a collapsed breccia that is about 2 m (6 ft) tall. Both images show dissolution post collapse.

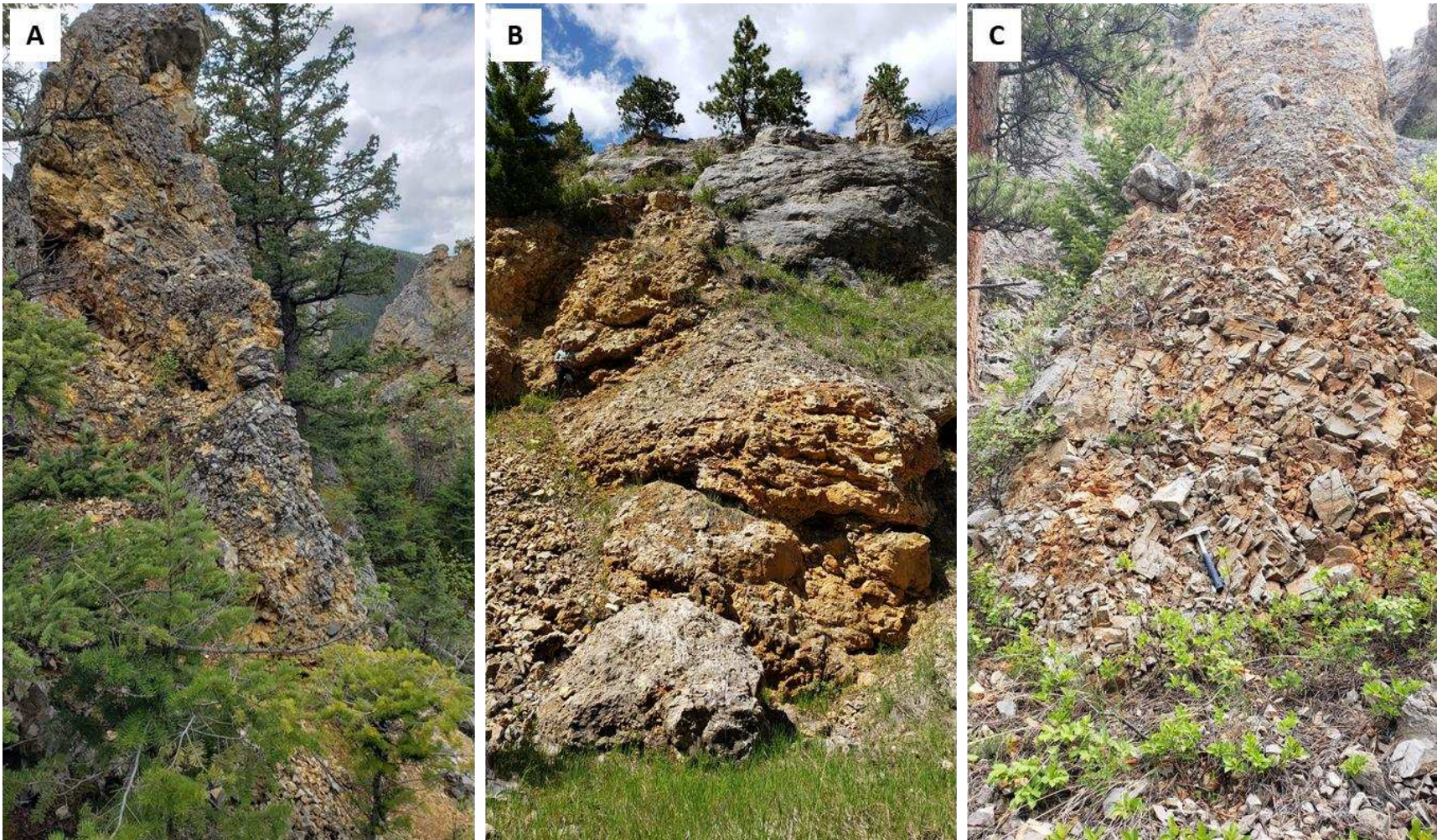


Figure 4.7. A. photo of a monomict rubble breccia spire estimated to be 4 m (13 ft) tall above the Kunisaki- American Mine tunnel. B. A large bulbous shaped monomict rubble breccia in Kelly Coulee, field partner for scale. C. A small monomict rubble breccia 0.4 km (0.25 mi) northwest of the Kunisaki-American Mine along the Yogo Creek Valley.

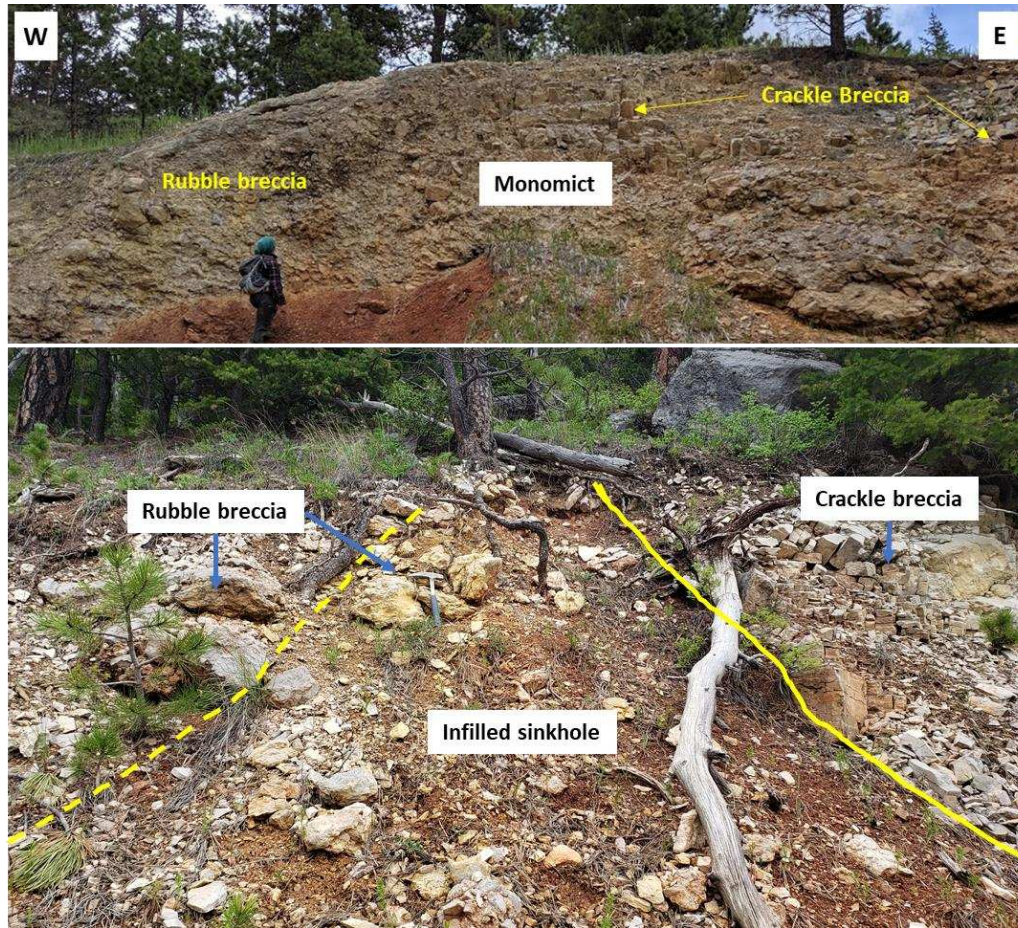


Figure. 4.8. The upper photo at the eastern end of the western most cut of the Middle Mine (Fig. 4.10, location 4.11 + 4.8) It shows an upper unit of tan monomict breccia (Madison Group limestone) that grades from a rubble breccia on the western side of the outcrop to a more coherent crackle breccia on the eastern side. The lower photo is above the Kunisaki-American Mine tunnel and shows the relationship between the surface with an infilled sinkhole of unconsolidated polymict breccia with monomict rubble and crackle breccias bordering it (the contact between the two breccias is dashed where estimated). Note there is a tree growing out of the doline, owing to the unconsolidated nature of the polymict breccia.

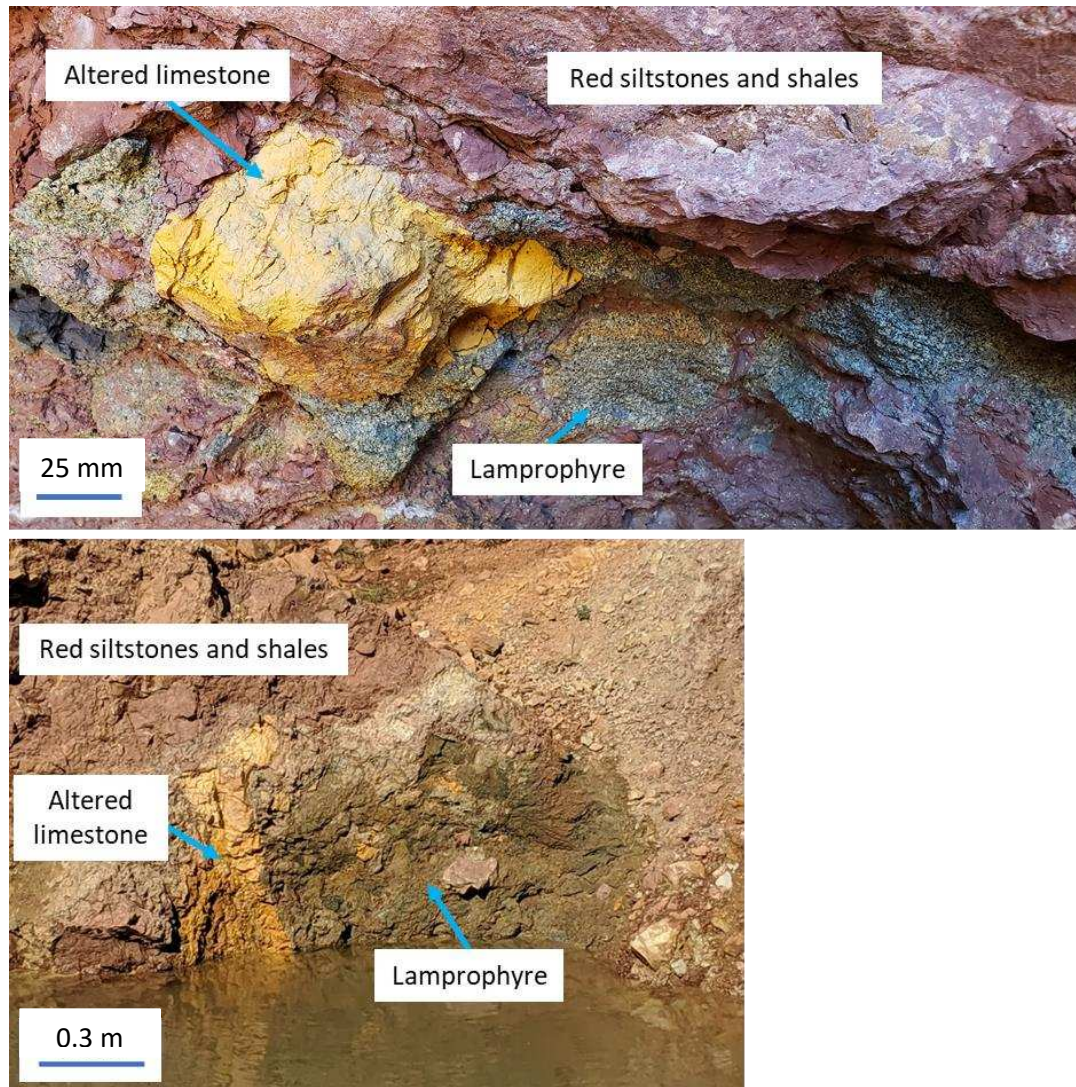


Figure 4.9. Top image shows small blebs of lamprophyre with various shapes. There is a round inclusion as well as irregular and angular shaped inclusions around a weathered limestone and between the siltstones and shales. Left image shows a large bleb of lamprophyre encapsulating a large, altered limestone clast with smaller limestones as well as a clast of red shale.

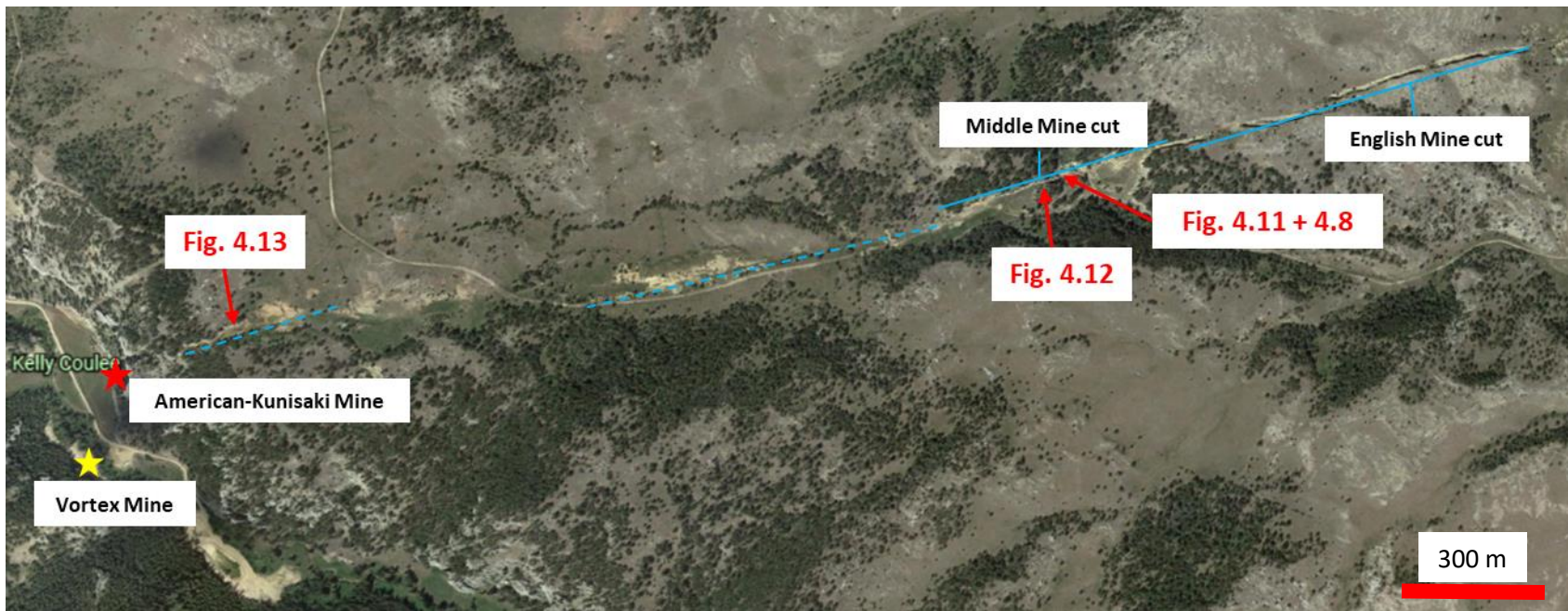


Figure 4.10. Map created using Google Earth Pro showing part of the Yogo dike, mines, and figure localities that show the relationship between breccias and lamprophyres. Location Fig. 4.12 coincides with metasedimentary xenoliths found as float on the surface as well, see chapter 5 Xenoliths, subheading Metasedimentary for further descriptions. Figures 4.11 + 4.8, 4.12 and 4.13 show the relationship between monomict breccias and polymict with lamprophyre inclusion breccias.

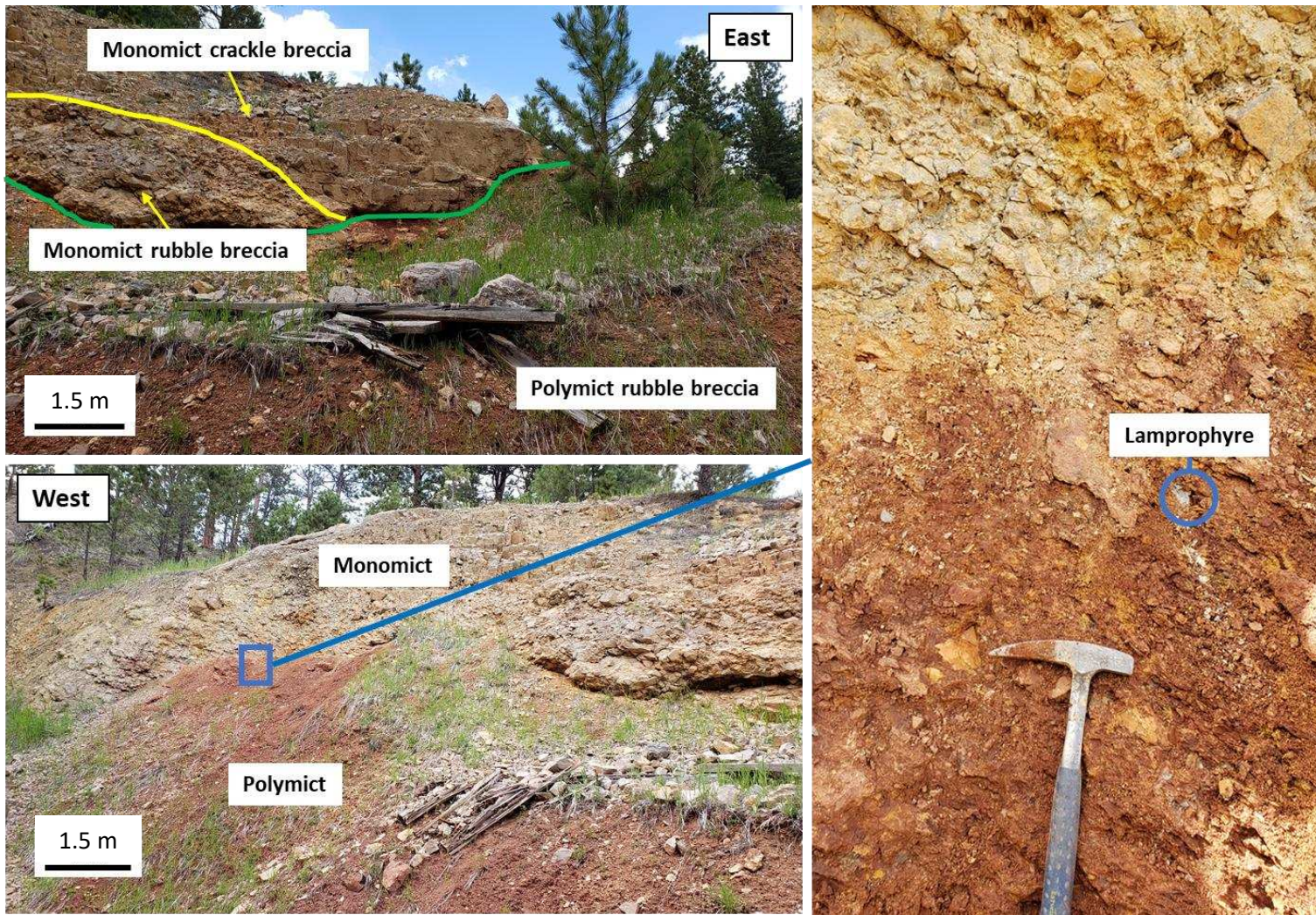


Figure 4.11. Top left, photo the eastern end of an outcrop in the Middle Mine cut showing the fabric of a monomict breccia atop an unconsolidated, slope forming polymict rubble breccia. Yellow line, contact between monomict crackle breccia and monomict rubble breccia. Green line, contact between monomict breccia and polymict breccia. Bottom left, photo of the western end of the same outcrop showing an upper monomict breccia atop an unconsolidated polymict breccia. Right, photo of the contact between the monomict and polymict breccias. Small lamprophyre inclusions are found here.

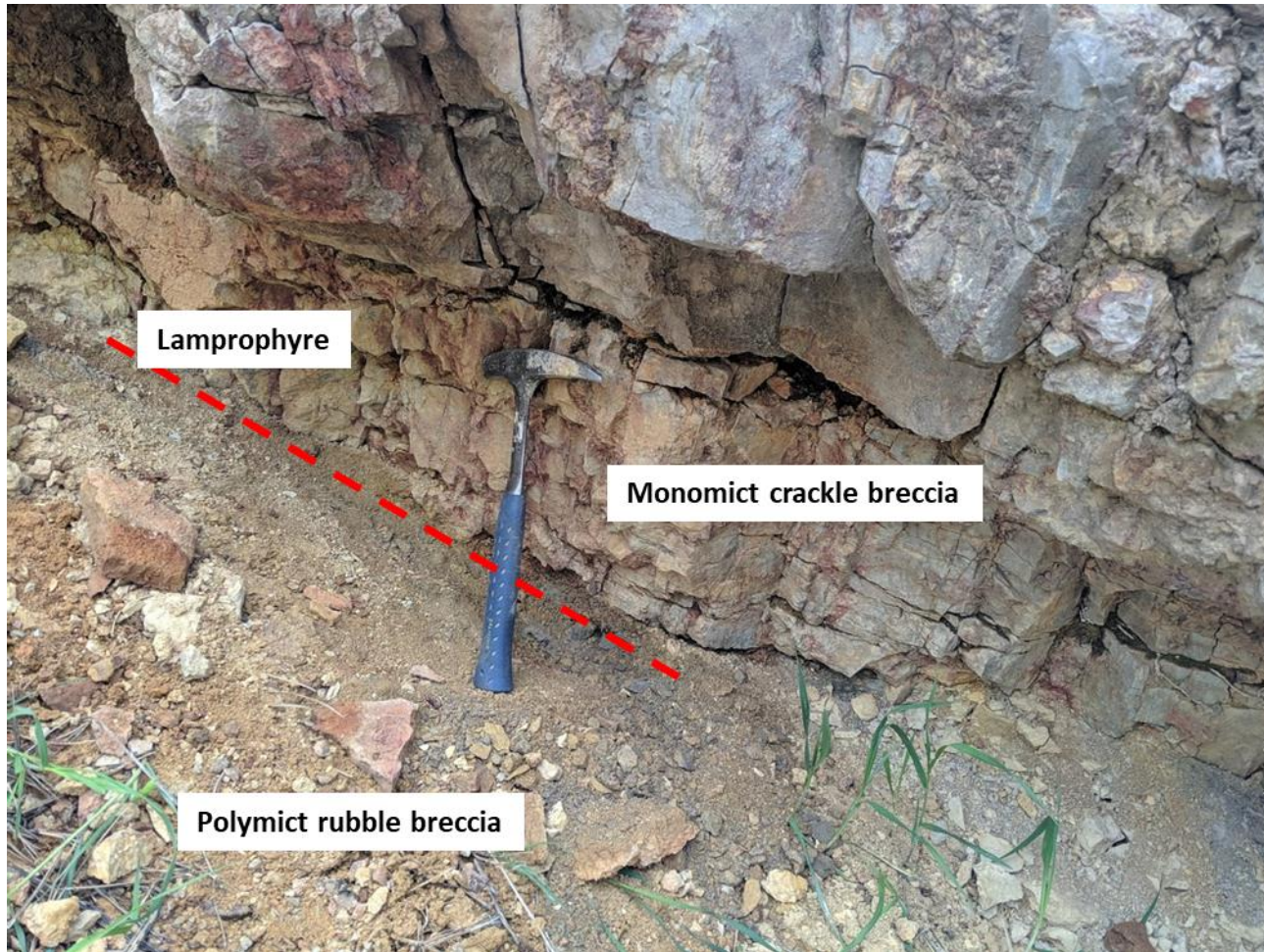


Figure 4.12. Grey monomict crackle breccia atop a polymict rubble breccia. There is a discontinuous seam of lamprophyre inclusions at the contact between the two.

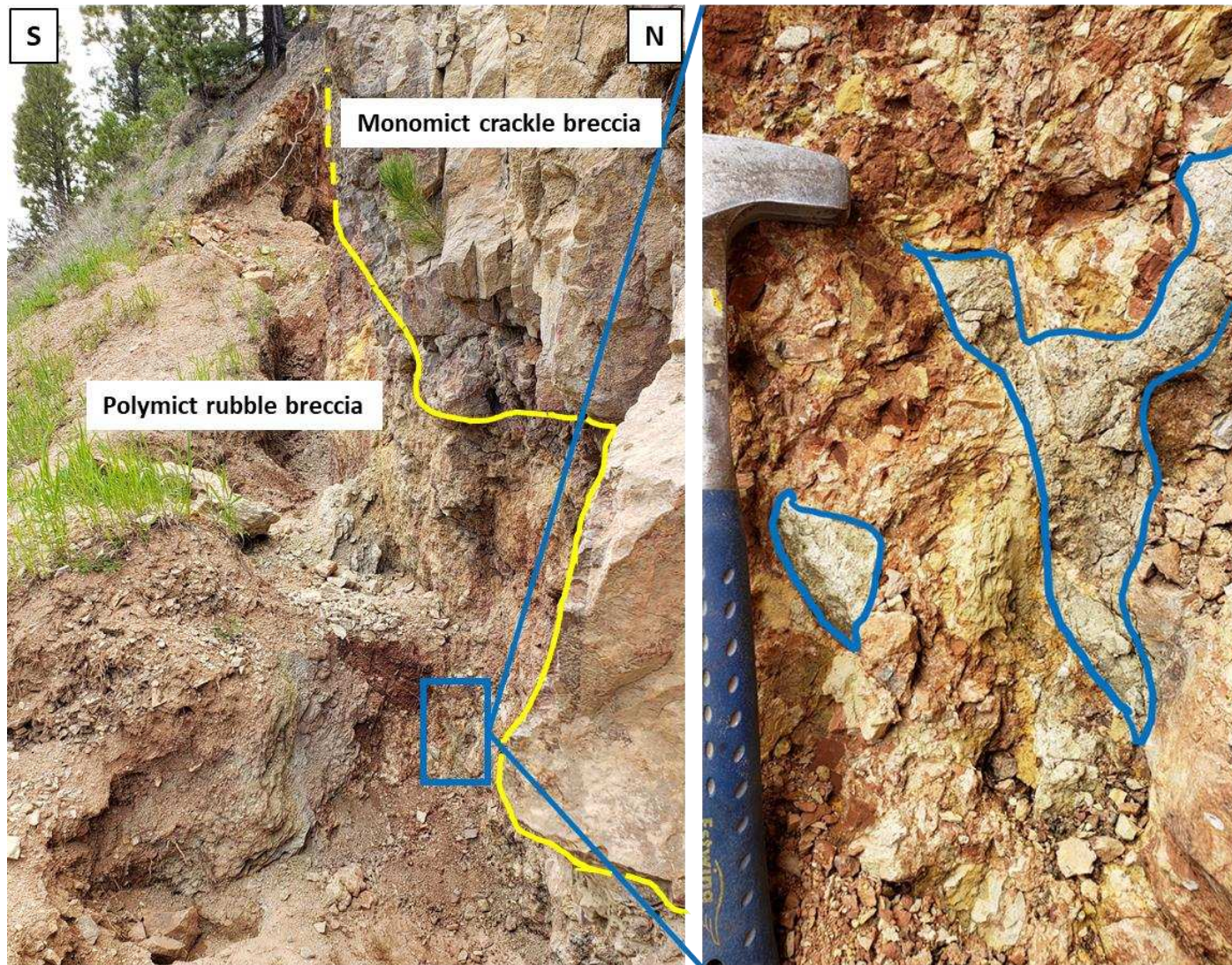


Figure 4.13. Looking westward above the Kunisaki-American Mine tunnel (Fig. 4.10). On the north side of the left-hand photo there is a wall of Monomict crackle breccia resting atop and polymict breccia. This area is soft and has been partially mined out by hand. The right-hand photo is a zoomed in view of an irregular shaped inclusion of lamprophyre in a polymict matrix.

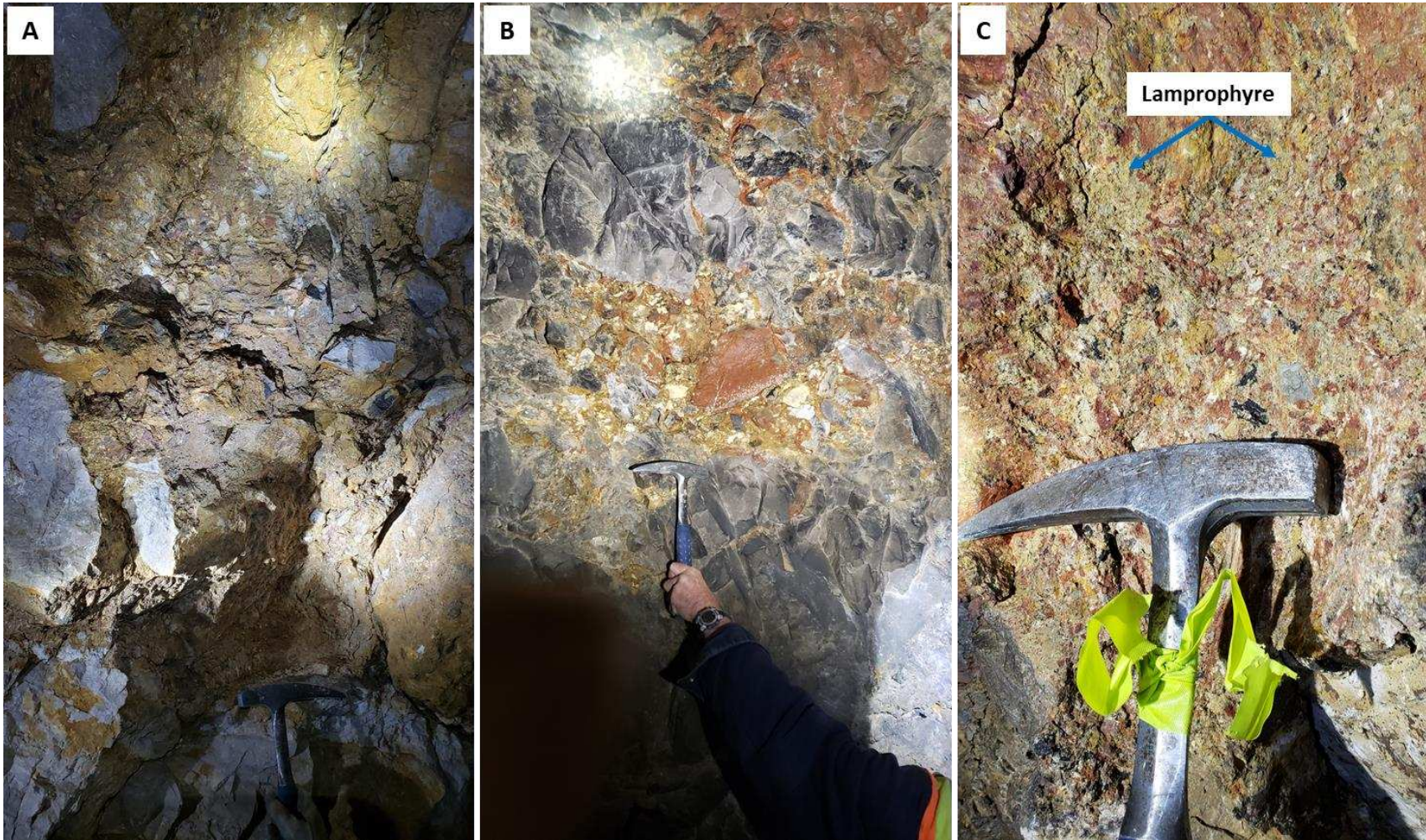


Figure 4.14. A. Ochre colored monomict rubble breccia found in the Kunisaki-American Mine, no lamprophyre clasts or matrix was observed. B. Photo taken in Vortex Mine at the Electrical Bay 30 m (100') depth. Monomict breccia with large blackened (presumably by diesel exhaust) limestone clasts with a red siltstones and shales of varying sizes as well as tan to yellow altered limestone clasts, no lamprophyre was observed as matrix or clasts. C. This image was in the Vortex Mine at the electrical bay location. This polymict breccia is fine grained and has lamprophyre as matrix. The lamprophyre is orange to grey green in color.

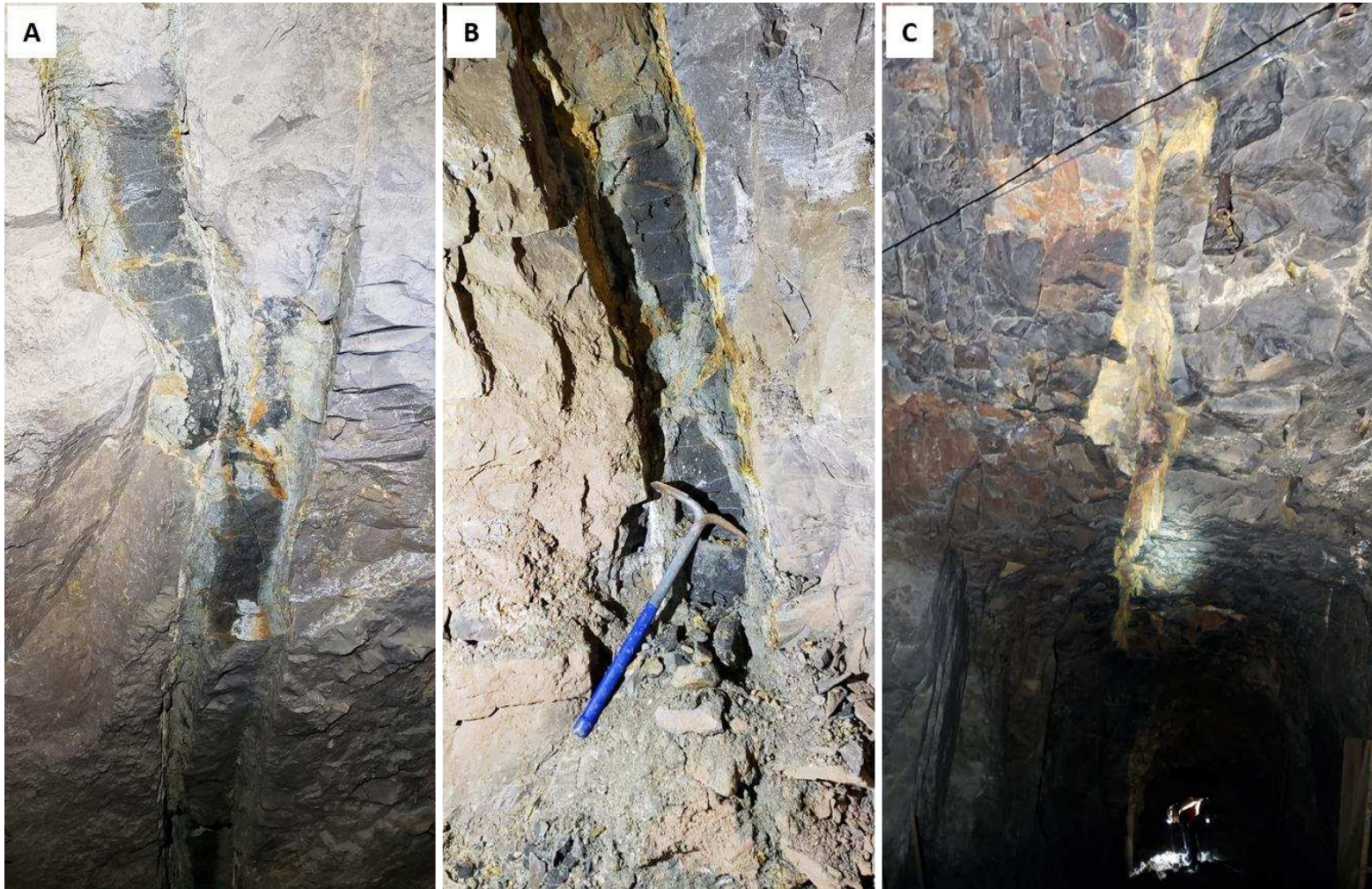


Figure 4.15. A. Dike exposed on the ceiling of the Vortex mine at 94.5 m (310') below the surface. This section of dike is ~0.2 m (8") wide and shows green alteration of the lamprophyre along the contact with the host Madison Group. B. Photo of a portion of the dike exposed on a wall at the 94.5 m (310') level. There is a maroon weathering facies seen in the upper section of this photo that grades into green against fresh rock. Alteration along fractures in the lamprophyre itself and along the contact between the dike and Madison is present. C. Photo of a completely weathered section of the dike exposed on the ceiling at the 80 m (260 ft) depth. The section of this dike grades from maroon-ish red to yellow.

Chapter V. Petrography

Forty-three breccia samples and fifty-two lamprophyres were analyzed via hand sample description prior to petrographic analyses. Petrographic thin sections are described as follows: breccias (5 total), breccia with lamprophyre inclusions (2), lamprophyre (47), of which include all include xenoliths. Breccias have been divided into three types, monomict breccia, polymict breccia, and polymict breccia with lamprophyre inclusions. Lamprophyres are split into two types based mainly on texture; Lamprophyre One primarily found in the tailings of the English/American mine and Lamprophyre Two primarily found in the underground workings of the Vortex mine. Xenolith types are described in order of abundance from most to least starting with mafic/ultramafic, calc-silicate, felsic/granitic, and finally metasedimentary/sedimentary.

An important result of the study is the recognition that there are two lamprophyre melts at Yogo. Texturally they are different, but they are similar in mineralogy (Fig. 5.1). Lamprophyre One samples have a microcrystalline matrix that is composed primarily of carbonate, feldspathoids, and analcime, some of the samples have microphenocrysts of subhedral to euhedral biotite with minor clinopyroxene (Figs. 5.2a/b and 5.3a/b). Large phenocrysts of biotite are more abundant than Lamprophyre Two samples, and have anhedral, castellated appearance (Fig. 5.17). Clinopyroxenes are in equal abundance, 15 – 45%, but generally finer than biotite (Figs. 5.2a and 5.2b). Most of the Lamprophyre Two samples have a devitrified “glassy” matrix with microphenocrysts of subhedral to anhedral biotite and minor euhedral clinopyroxenes (Figs 5.2c/d and 5.3c/d). Phenocrysts of clinopyroxenes are large, euhedral, and range in size from 0.125 – 3.25 mm (Fig. 5.1c/d) while coarse phenocrysts of anhedral, castellated biotite are rare.

Breccias

Monomict breccias

Hand samples

These breccias are composed entirely of Madison Group micritic limestone clasts that range from coarse sand to boulder in size. For the most part they are clast supported with minor silty calcareous matrix that is yellow to orange in color (Fig. 5.4). Most of the hand samples have a yellow weathered surface, but the fresh interior shows a combination of dark grey to light greyish tan clasts.

Breccias in the cliff outcrops 0.4 m (0.27 mi) northwest of the American Tunnel vary in appearance. These samples range from red to orange in appearance due to high concentrations of hematite-rich matrix. Some areas are matrix supported while others are clast supported. There are brecciated corals and other fossils preserved in these samples and the fine silt matrix is composed of mainly hematite and silica and shows weak laminar bedding between clasts (Fig. 5.5).

Petrography

These sections have a fine-grained carbonate to quartz rich mud matrix with clasts of carbonate siltstone and various types of limestone fragments. The fragments range from micritic to fossiliferous to oolitic with varying concentrations of fine disseminated organic material (Fig. 5.6). Figure 5.6b is an example of fossiliferous oolitic limestone with a laminated hematite rich zone with ooids and fossil fragments. Lenses of the matrix show soft sediment deformation and have, in part, been replaced diagenetically by quartz.

Polymict breccias

Hand samples

These semi to unconsolidated breccias are deep orange to red in color and matrix supported. The matrix is a combination of yellow orange to red calcareous mud to silt with minor limestone grains as coarse sand. The clasts are angular and primarily composed red calcareous silt to mudstones that may show weak laminar bedding, brown to tan crystalline limestone, grey micritic limestone, and yellow lime mudstone (Fig. 5.7). Importantly these breccias are easily broken apart by hand and when exposed to water they disintegrate into mud.

Petrography

The polymict breccias samples have a carbonate rich mud matrix with varying concentrations of clays and disseminated hematite which give the sections a red-orange color. Clasts in these samples are composed of carbonate cemented quartz siltstone with varying concentrations of disseminated hematite as well as silty limestone fragments.

Polymict breccias with lamprophyre inclusions

Hand samples

The previously described polymict breccias in some locations host veinlets and irregular shaped “blebs” of lamprophyre (see chapter 4 on field relationships for further field descriptions). Inclusions of the lamprophyre range greatly in size from gravel to boulder size that are bulbous to irregular in shape. Importantly, there is no obvious thermal interaction between the lamprophyre and breccia components. There is evidence neither of quenching of the lamprophyre nor of baking or recrystallization of adjacent limestone (Fig. 5.8).

Petrography

As with the hand sample, the overall petrographic description of the brecciated sedimentary part of these sections is the same as the polymict breccias. Interaction between the lamprophyre and the breccia is subtle (Figs. 5.9 and 5.10). There is minor fracturing of some clasts that have been filled with recrystallized calcite and minor zeolites, the fracturing maybe due to heat and subsequent cooling which resulted in shrinkage leaving void space to be filled by calcite (Fig. 5.9a). Some margins of the clasts are lined by recrystallized calcite with an inconsistent thickness ranging from .1 to .75 mm. These may, again, be due to shrinkage rather than significant recrystallization contact between the lamprophyre intrusion and breccia clasts. There is evidence that the lamprophyre pushed or infilled space between clasts -which could cause some fracturing- as weak alignment of biotite parallel to the margins of the lamprophyre suggests (Figs. 5.9b and 5.10b). The lamprophyre itself shows no quenching at the margins and is texturally and mineralogically like the Lamprophyre 1 samples, which are discussed in the coming paragraphs.

Lamprophyres

Lamprophyre 1

Hand samples

These samples are found as rounded cobbles and boulders in mine dumps around the main dike cut. The samples are grey green with some orange staining on the weathered surface and have grey to grey-green fresh surfaces (Fig. 5.11). The ground mass is fine grained to aphanitic carbonate mixed with other minerals, probably feldspathoids. They are composed of 30 – 48% matrix, 25 – 38% phenocrysts, 1 – 10% xenoliths of varying type and 1 – 4% ocelli.

Twenty-five – 50% of the phenocrysts are clinopyroxene that are green to grey green in color, are euhedral and are approximately .125 mm but can be up to 2.5 mm in size. Biotite ranges from 25 – 50% and is found as rounded grains .25 mm to 4 mm in size and fine plates that are subhedral to anhedral. Sapphire is trace and range from 1 – 2 mm thick and 2 – 5 mm long. The ocelli are compositionally zoned with mainly calcite and possible analcime, they are circular to elliptical in shape with some irregularities and range in size from .75 mm to 10 mm in diameter. No evidence of olivine is visible in hand samples. There are also trace amounts of an unidentified red, hexagonal, euhedral mineral that has a completely altered core composed of calcite. Palke (2018) discusses coloration of sapphires at Yogo and describes them as ranging from cornflower blue to violet and rarely red enough to be considered ruby. These range in size from 7 – 9 mm wide and 8 – 10 mm long. Palke (2018) describes rare reddish violet sapphires to rubies found at Yogo, but their description does not coincide with the red hexagonal mineral described here, so they are likely not rubies. Weathered samples retain their biotite but the remainder of the rock weathers to a grey green clay rich friable rock (Fig. 5.12).

Petrography

The matrix makes up 30 – 48% of the rock and is microcrystalline composed of carbonate, feldspathoids, and analcime ± microphenocrysts of subhedral to euhedral of biotite (Fig. 5.13). One – 10% xenoliths varying in composition from felsic to mafic to a calcsilicate xenolith of unknown origin. Twenty-five – 38% phenocrysts with 1 – 4% ocelli make up the rest of the rock.

Fifteen – 45% of phenocrysts are clinopyroxene that are euhedral and are generally .125 - 3.25 mm in size, with a few 4 mm phenocrysts throughout (Fig. 5.14). Zonation in the clinopyroxenes is relatively subtle from the core to a single rim on the outside of the

phenocrysts. The zonation is not distinctive in that it goes both up and down in birefringence color. Over 75% have some sort of alteration to a combination of mainly calcite with some sericite. Alteration appears within most of the clinopyroxene as spongy texture with circular to amoeboid pits that range from 7 – 20 μm in size with occasional pits up to 117 μm . The pits often contain fine grained mixtures of minerals including calcite which is interpreted to be recrystallized melt inclusions (Ma et al, 2015). Some have pitted cores with crisp margins while others have zones of pitting with clean cores and margins. There are few that are completely pitted and are nearly completely overprinted by alteration.

25 – 50% of phenocrysts are biotite variety phlogopite that are generally anhedral and castellated. In thin section phlogopite appears to dominate because of its coarser grained appearance (Fig. 5.15). They range from .125 - 2 mm in size. Zonation is present from the core of the phenocryst to the outside margin. It appears as a single outer zone of darker pleochroism. There is also intergrowth of analcime and carbonate in some of the phenocrysts with possible apatite.

1 – 4% of phenocrysts are analcime. Some appear as interstitial “dusty grey” anhedral grains while others are euhedral hexagonal phenocrysts (Fig. 5.16). They are fine grained (0.1 – 0.5 mm) and sometimes intergrown with biotite. All of them have been partially altered to presumably calcite and feldspathoids and look like dusty dark grey grains. They retain enough of their original crystal shape and are identified by their isotropic nature. Importantly most of the analcime in these samples is tied up in the matrix.

Less than or equal to 1% of phenocrysts are olivine. If olivine is present in the samples, it is completely altered to iddingsite, carbonate and sericite. They are generally .128 - 2 mm in size and are euhedral (Fig. 5.17).

Apatite is ubiquitous through sample and hosted as microscopic grains in the pleochroic rims of biotite. They are distributed randomly through with no specific crystallographic orientation (Fig. 5.18).

Less than 1 – 4% of ocelli make up the lamprophyre. Ocelli vary in size and abundance. They range from circular to ameboid in shape and range dramatically in size, from 1 x 1 mm up to 8 x 13 mm (Figs. 5.19 and 5.21). The ocelli are zoned to varying degrees with diffuse margins. The outer zonation is dominated by feldspathoids and amphibole that has been largely replaced by calcite and range from .125 – 5.5 mm in thickness (Fig. 5.20). The next zone is dominated by coarse euhedral calcite, some of which have internal growth zonation. This zone may have minor analcime and feldspathoids (Fig. 5.22). The inner zone may be dominated by very fine calcite which may grade into a core of fibrous, locally radial, zeolites (Fig. 5.23). Ocelli without zeolites have euhedral calcite cores (Figs. 5.19 and 5.21).

One – 10% of lamprophyre components are xenoliths of varying composition, refer to section below for more information.

Lamprophyre 2

Hand sample

These samples were mainly collected from underground in the Vortex mine although there were some collected in the tailings pile near the mine entrance. They are blockier and more angular than the other lamprophyre phase and have a dark grey to grey-green weathered surfaces. The fresh interior of these samples is dark grey to nearly black with an aphanitic groundmass dominated by calcite (Fig. 5.24). They have an approximate modal composition as follows: 30 - 50% matrix, 20 - 45% phenocrysts, 1 - 5% xenoliths with few ocelli (<1%). Twenty – 80 % of

the phenocrysts are clinopyroxene that range in size from 0.125 – 3.25 mm, they are euhedral and appear free of alteration. 10 - 19% of the phenocrysts are 0.25 – 2 mm euhedral olivine which have been replaced by iddingsite, calcite, and serpentine with little remaining of the original olivine. There are 1% biotite as rounded phenocrysts that are around 1 mm in size. Trace sapphire is present. Two facies of clay-rich weathered samples of Lamprophyre 2 were collected underground in the Vortex mine the first is red in color and the second is yellow to peach. There are samples that have coloration that lies in between these two (Fig. 5.25). Sapphires were collected in the yellow to peach colored facies of the weathered lamprophyre, which aided in identifying the intensely weathered rock. The fresh lamprophyre is denser than both the red and yellow facies, with yellow being the least dense, which suggests intense leaching. This was detected by hefting samples of similar size and comparing them to each other.

Petrography

These samples are composed of 20 – 45% phenocrysts and 1 – 5% xenoliths of varying types, no ocelli were found in these samples. The of 30 – 50% matrix is dark grey to brown in color and has microphenocrysts of biotite, and minor clinopyroxene. The dark, isotropic, and dusty nature of the matrix suggests that it is glass, devitrified glass, with opaques as microphenocrysts. There are patches of microcrystalline calcite, feldspathoids, and analcime in the matrix as well (Fig. 5.26).

20 – 80% of the phenocrysts are clinopyroxene that are euhedral and .125 – 3.25 mm in size. They have sharp crystal margins with varying degrees of alteration. Some appear fresh while others have pitted cores, a single zone of pits within the phenocryst or are completely pitted, which again may melt inclusions that have been devitrified or crystallized to an intergrowth of multiple minerals including calcite and possible sericite (Fig. 5.27). There are

phenocrysts that are compositionally zoned from the core to the margin, but it is found as a weak change in birefringence on the rim of the phenocryst (Fig. 5.28). The zonation goes both up and down in birefringence, so it is not distinctive. Alteration also appears along cleavage planes. As previously stated, there are some microphenocrysts of clinopyroxene of similar birefringence in the matrix. Clinopyroxene in Lamprophyre 2 is essentially indistinguishable from clinopyroxene in Lamprophyre 1.

10 - 19% of the phenocrysts are euhedral olivine .5 - 2mm in size. Most of the olivine has been replaced by calcite, iron oxides, and serpentine with very little of the original mineral remaining (Fig. 5.29). The pseudomorphs have retained their classic hexagonal and elongated hexagonal shapes and some conchoidal fracture surfaces within the remaining crystal help to identify them.

1% biotite var. phlogopite is rarely found as coarse phenocrysts but where they are, they have a rounded castellated appearance that may be zoned from the core to the outside as rims of darker pleochroism (Figs. 5.30e/f and 5.28). Otherwise, biotite is found as subhedral to euhedral microphenocrysts (Figs. 5.27, 5.29 a/b and c/d, 5.30, 5.31 c/d and e/f).

1 - 2% xenoliths of varying composition make up the lamprophyre. Further description of xenoliths are described in the coming paragraphs.

Apatite is ubiquitous throughout the samples, but it hosted in microphenocrysts of biotite and are thus challenging to identify. They are not oriented along any preferred crystallographic axis (Fig. 5.30).

Trace sapphire is present in VM6 with a thin layer of fine-grained opaque minerals surrounding it and fractures through the elongate section. (Fig. 5.31)

Xenoliths

Xenoliths are found in both lamprophyres and are identified mineralogically and texturally. In Lamprophyre 1 the xenoliths appear to be more abundant and diverse than Lamprophyre 2. The most common xenoliths are mafic/ultramafic, characterized by clinopyroxene ± biotite, but there are also xenoliths of granitic, quartz, metasedimentary/sedimentary and calcsilicate of undetermined origin. Ultramafic xenoliths and one quartz xenolith were found in Lamprophyre 2. Most of xenolith in both lamprophyres are found as rounded clasts with varying sizes and amounts of alteration. Hand sample and petrographic descriptions are in the following paragraphs.

Ultramafic

Hand sample

Ultramafic xenoliths are the most abundant and are found as rounded circular to elongate clasts that range in size from 1 mm at their smallest and 35 mm at their largest. Some have weathered out leaving behind vestiges of their mineralogy in spherical to elliptical vugs of similar size (Fig. 5.32). Others have crisp apple green margins surrounding an altered core composed of fine carbonate (Fig. 5.33). They are composed of euhedral .125 – 7 mm, sea green to apple green clinopyroxene with 1 – 10% biotite that is subhedral to anhedral in appearance and ranges from 1 – 4 mm in size. These xenoliths have subtle to no reaction rim in hand sample. Although these xenoliths contain calcite as an alteration product, their abundance of clinopyroxene suggests they are ultramafic in origin.

Petrography

In thin section there are two distinct types of ultramafic xenoliths. The first is a clinopyroxenite, composed entirely of clinopyroxene that range from <.125 – 7 mm in size and are euhedral with little to no zonation (Fig. 5.34). The second type of ultramafic xenolith, biotite clinopyroxenite, have up to 10 - 98% euhedral clinopyroxene and 3 – 90% biotite that is subhedral to anhedral with minor chloritization, and 1-2% pseudomorphed garnet (Figs. 5.35 and 5.36). Spinel may be present with biotite in these xenoliths as blue to green, euhedral, phenocrysts that are 10 – 80 μm in size (Fig. 5.37). Some xenoliths have been completely altered to calcite and sericite, leaving only a rim of clinopyroxene \pm biotite (Fig. 5.38)

Mafic

Hand sample

Mafic xenoliths are found as rounded clots that contain 50 – 70% euhedral muscovite that range from 0.25 – 2 mm in size, 3 – 40% subhedral to euhedral clinopyroxene < 0.5 - 1 mm, 1 – 10% euhedral potassium feldspar that are 0.25 – 4 mm in size (Fig. 5.39). These are interpreted as mafic xenoliths that have been altered by addition of potassium from the lamprophyre, replacing plagioclase feldspar with potassium feldspar, which in turn altered to muscovite. Sample EM14b has a xenolith that is dominated by aligned muscovite with minor potassium feldspar and has a margin of blue muscovite that is 0.5 – 2 mm wide (Figs. 42b). There is also a reaction rim composed of a fine intergrowth of calcite and other light-colored minerals around the xenolith in EM14b that is ≤ 0.25 mm.

Petrography

In thin section, mafic xenoliths have 50 – 70% subhedral to euhedral muscovites that are 0.1 – 2 mm in size, 2 – 40% subhedral to euhedral clinopyroxene 0.5 – 1 mm, 1 – 10% subhedral potassium feldspar 0.25 – 4 mm (Fig. 5.40). In addition to these minerals there may be up to 3% anhedral tremolitic amphibole, 1% microscopic ($\leq .05$ mm) euhedral garnet, and 1% microscopic euhedral spinel 0.05 – 0.1 mm in size. Some mafic xenoliths may be zoned (Fig. 5.40). The combination of aluminous and mafic minerals suggests that, though altered, these xenoliths are of magmatic origin.

Sample EM14b has the previously mentioned accessory minerals. Garnet crystals are associated with clinopyroxene while the spinel is hosted within the reaction rim of the xenolith (Fig. 5.40). Importantly, it is apparent that the muscovite has replaced much of the potassium feldspar and that blue muscovite and possibly chlorite has started to replace the muscovite on the margin of the xenolith. Sample EM47b also has muscovite replacing potassium feldspar but in this sample, microcrystalline calcite, and nepheline series feldspathoids are intergrown with isotropic material occurring along grain boundaries within the xenolith and is interpreted to be partial recrystallization of glass after melt (Fig. 5.41).

Felsic (granitic)

Hand sample

Felsic xenoliths contain equal amounts of quartz and plagioclase \pm potassium feldspar with interstitial zones of patchy, irregularly shaped aphanitic grey noncrystalline material \pm muscovite (Fig. 5.42). Some samples are dominated by quartz and have very little plagioclase. In

sample EMOctc aligned quartz and potassium feldspar define a weak fabric, supported by a swath of grey aphanitic material of similar orientation.

Petrography

In thin section felsic xenoliths exhibit thick irregular shaped reaction rims from 2 – 5 mm (Fig. 5.43) composed of feldspathoids from the nepheline series (75%), altered amphibole (25%), and minor (<1%) euhedral clinopyroxene (Fig. 5.44). The xenoliths are composed of 63 – 74% irregular wormy to ameboid shaped quartz that range in dimension (1 – 2 mm), 1 – 7% irregularly shaped plagioclase up to 1 mm in size, while the remaining 24 – 30% of the xenolith is dominated by brown to black, isotropic, dusty material found along grain boundary that is presumably glass after melt (Fig. 5.45).

Quartz

Hand sample

Quartz xenoliths are sub-angular to rounded and are 6 – 23 mm in diameter (Fig. 5.46). They have reaction rims of fine calcite intergrown with other minerals that are .25 – 1 mm thick. The samples are composed of large interlocking crystals, which suggests that they may have originated from quartz veins.

Petrography

Quartz xenoliths found in thin section are irregularly shaped with thick reaction rims (.5 – 1mm) composed mainly of feldspathoids (74%), replaced needles and rosettes of amphibole (25%), and 1% opaques. Calcite is the replacement mineral. The xenoliths themselves are made of massive quartz grains that minor fractures filled with fine calcite (Figs. 5.47 and 5.48).

Metasedimentary

Two metasedimentary xenolith types were found as loose blocks on the surface at the western end of the Middle Mine cut on strike of the dike (Fig. 4.11). There was no exposed contact between the dike and these samples, but the evidence of metamorphic recrystallization suggests they were eroded out of the dike.

Recrystallized limestone

Hand sample

This rock type is found as float in the western end of the Middle Mine cut. It is exposed as patchy white, tan, and grey, irregular block with cross-cutting veinlike seams of reddish-brown hematite rich carbonate (Fig. 5.49). The interior of the rock displays stylolite-like seams and patches of fine gray carbonate that appear to be following bedding planes. The grey material grades to the reddish-brown carbonate from the interior to the exterior of the sample. Between the fine-grained stylolite-like seams there is uniform granoblastic white to tan crystalline calcite with coarser grained areas that may or may not grade into vuggy open space (Fig 5.50).

Petrography

The samples show a very uniform, granoblastic texture. Fine to medium crystalline calcite makes up 99% of the rock with around 1% quartz grains. There is local brown to orange-ish colored areas composed of silt sized carbonate. Areas of coarser crystalline limestone exist within the mostly uniform recrystallized limestone that rim small vugs 0.25 - 0.5 cm in dimension or have completely crystallized into the earlier open spaces.

Organic rich metasedimentary

Hand sample

In the field these samples are found as float near the center of the west end of the Middle Mine cut and there is no outcrop found. The exterior of the rock is black and leaves a black residue on your skin when handled. This is probably carbonaceous matter. The interior of the rock displays alternating bands of black carbonate rich mudstones that range from 1 - 10 mm in width and grey moderately to poorly sorted bands of calcite (20 - 50%), organic material and opaques (30 - 50%), rock fragments (5%) and minor quartz (1%) that are 1.5 - 13 mm thick (Fig. 5.51). Calcite is present as cement and as very fine to medium sand that is subangular to rounded. The organic material is fine to medium grained and is subangular to subrounded. Rock fragments are a combination of yellow, angular, upper medium to upper very coarse sandy limestone and red, angular, lower medium to medium pebbles of red silty limestone (Fig. 5.52).

Petrography

In thin section the bedding in these samples is marked by variations of abundance of carbonate, opaque minerals, and rock fragments with minor quartz in the same abundances outlined in the hand sample description. The mixture of fine-grained organic material and what appears to be an oxide, such as hematite or ilmenite, throughout the sample suggests contact metamorphism where oxides were crystallized out of heated metals contained in organic material and primary clays (Fig. 5.53).

Calc-silicate of unknown origin

Hand sample

The second most prominent xenolith is found as pink-, black- and buff-colored rounded blebs to irregular shaped clots that vary dramatically in width (2 – 10 mm) and length (2 – 100 mm) throughout the samples (Fig. 5.54). They are composed of 0.125 – 2 mm long black, amphibole needles with interstitial calcite and have an orange to peach colored unidentified mineral presumably an altered feldspathoid (Fig. 5.55). The overall mineralogy of these xenoliths suggests they are calc-silicates.

Petrography

In thin section, the xenoliths are rounded to irregular ameboid shaped with thin or no reaction rim which suggests that the entire xenolith has reacted and equilibrated with host lamprophyre (Fig. 5.56). These xenoliths contain 15 – 30% hornblende as euhedral blades and rosettes .125 - .55 mm long with occasional crystals that are 2 mm long. Fifteen – 30 % of the xenolith is composed of a mineral with a hexagonal outline that has been largely replaced by fine carbonate and may be a feldspathoid, although their near isotropic character suggests it could be analcime. The matrix of these xenoliths is composed of microscopic feldspathoids, crystalline calcite, devitrified glass and patchy areas of red opaques which are more than likely a replacement product (Fig 5.57). Interestingly, some of ocelli have margins of the same mineralogy as these unknown xenoliths (Fig. 5.22).

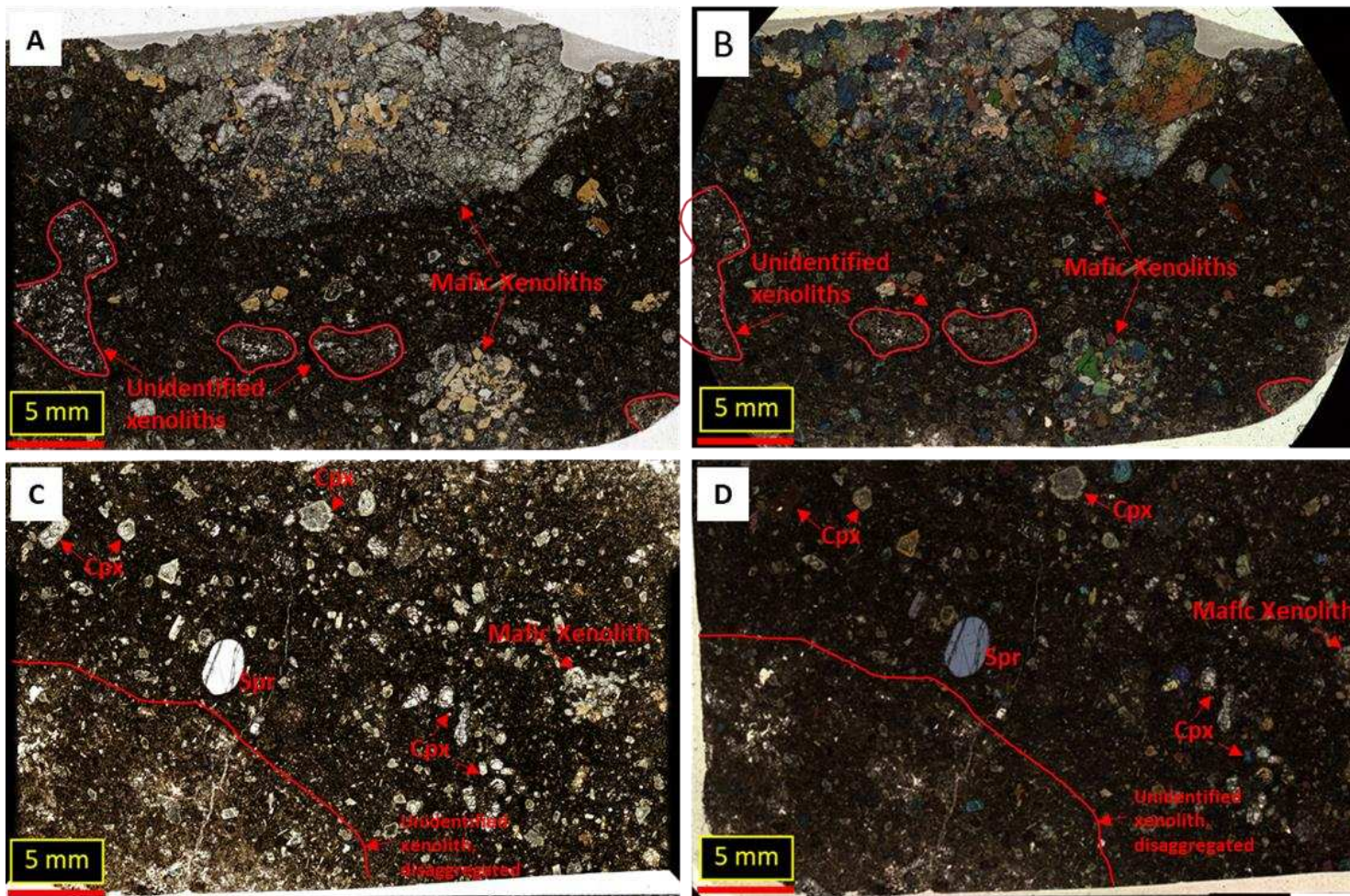


Figure 5.1. Scanned petrographic thin sections of representative examples showing textural differences between lamprophyre 1, EM31.26c (A and B) and lamprophyre 2, VM6 (C and D). Lamprophyre 1 (A and B) has phenocrysts of medium to fine biotite visible in the matrix of the sample with few visible clinopyroxene phenocrysts. This sample also shows a denser concentration of xenoliths (mafic and unidentified). Lamprophyre 2 (C and D) show large phenocrysts of variously altered clinopyroxene, some are fresh whereas others have altered cores, there is no visible biotite in this sample. This section hosts a sapphire (Spr), one mafic xenolith and what appears to be a disaggregated calcite rich xenolith. The following figures show zoomed in difference between these samples. Note: the sapphire will be discussed in further detail in the section of lamprophyre 2 petrography.

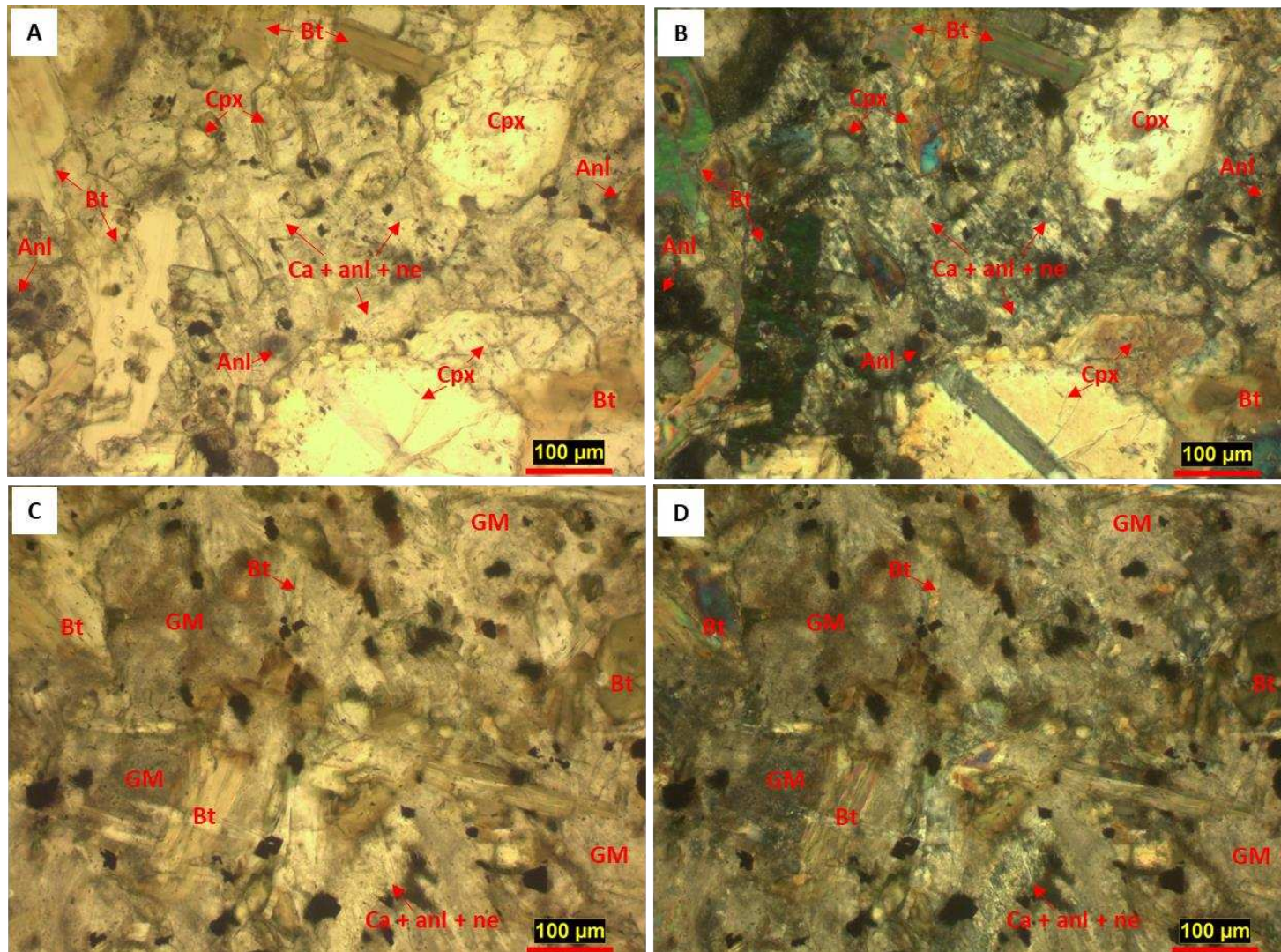


Figure 5.2. Photomicrographs of slides in figure 1 of samples EM31.26c (A and B) and VM6 (C and D). Lamprophyre 1 (A and B) shows microphenocrysts of biotite (Bt) and clinopyroxene (Cpx) in a matrix of microcrystalline calcite (Ca), analcime (An) and nepheline (Ne). Lamprophyre 2 (C and D) shows microphenocrysts of biotite with a patchy matrix of isotropic ground mass (GM) with minor patches of microcrystalline calcite, analcime and nepheline.

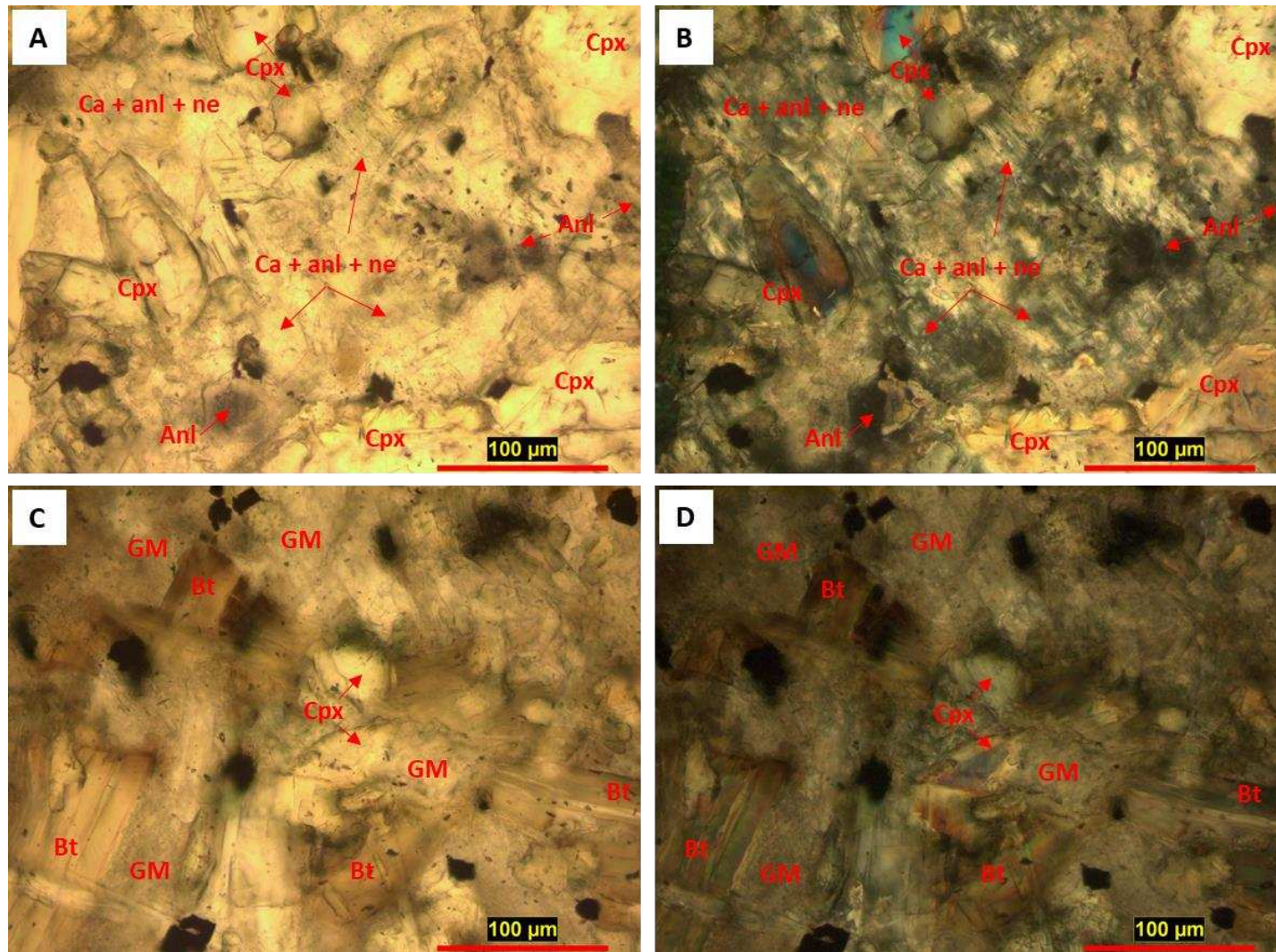


Figure 5.3. Magnified images of the same slides as figures 1 and 2 of samples EM31.26c (A and B) and VM6 (C and D). Lamprophyre 1 (A and B) has a microcrystalline ground mass (GM) composed of calcite, analcime, and nepheline series feldspathoids with microphenocrysts of clinopyroxene and dusty analcime and minor opaques. Note that the ground mass in lamprophyre one appears felted. Lamprophyre 2 shows a dusty, isotropic ground mass with microphenocrysts of biotite and clinopyroxene and opaques.

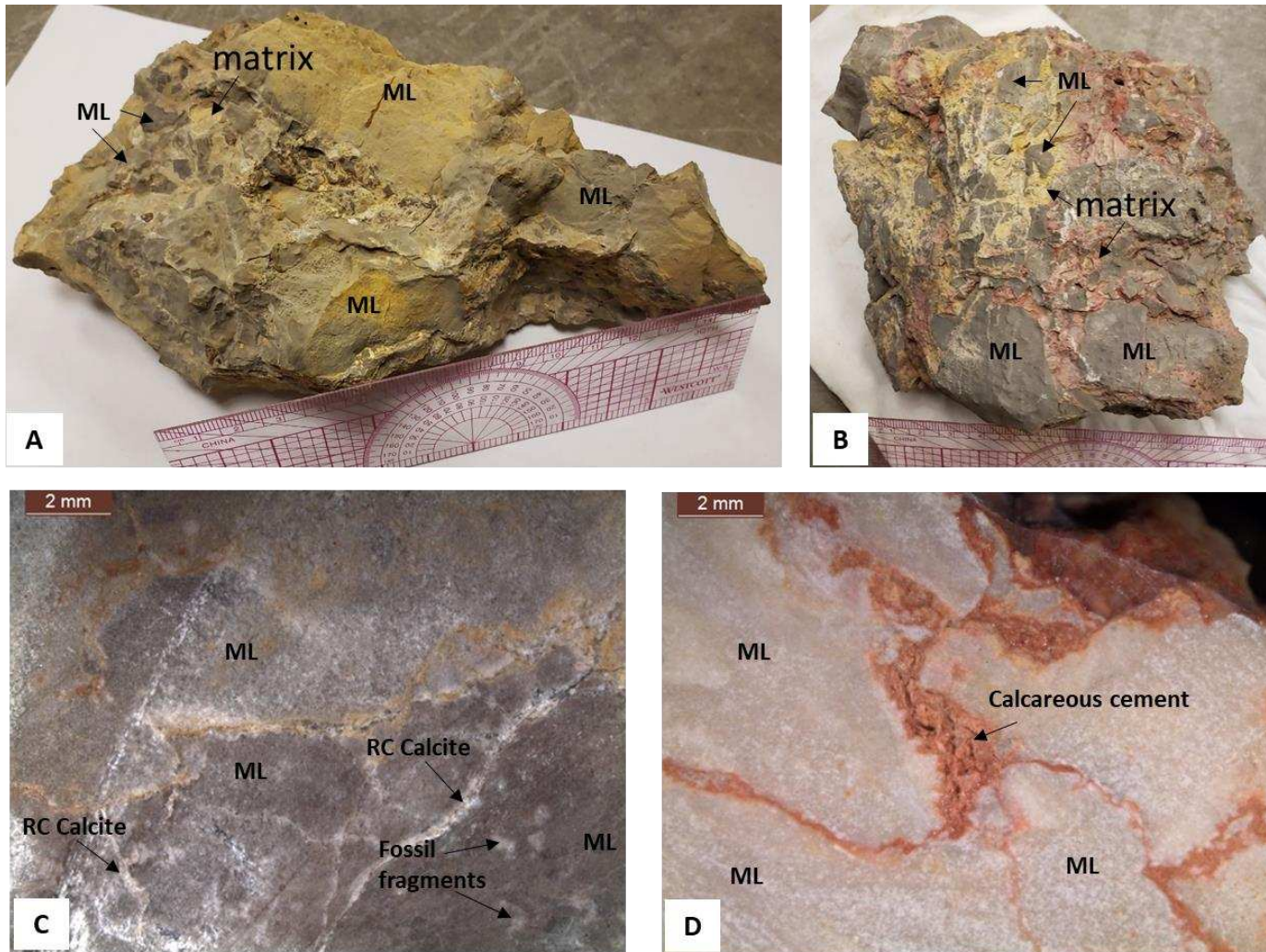


Figure 5.4. Representative hand samples and cut slabs of the monomict breccia found at Yogo. A: B10, yellow breccia clast to matrix supported with grey Madison Limestone (ML) clasts. B: B19, red to yellow carbonate matrix supported breccia with Madison Limestone clasts. C: B29, cut slab of a Madison Limestone showing clasts supported early breccia with recrystallized (RC) calcite in older fractures. D: B25, (cut surface) buff clasts of Madison Limestone considered to be clast supported with little to no matrix that is carbonate rich with disseminated hematite. See figure 6 for microphotographs of samples C and D.

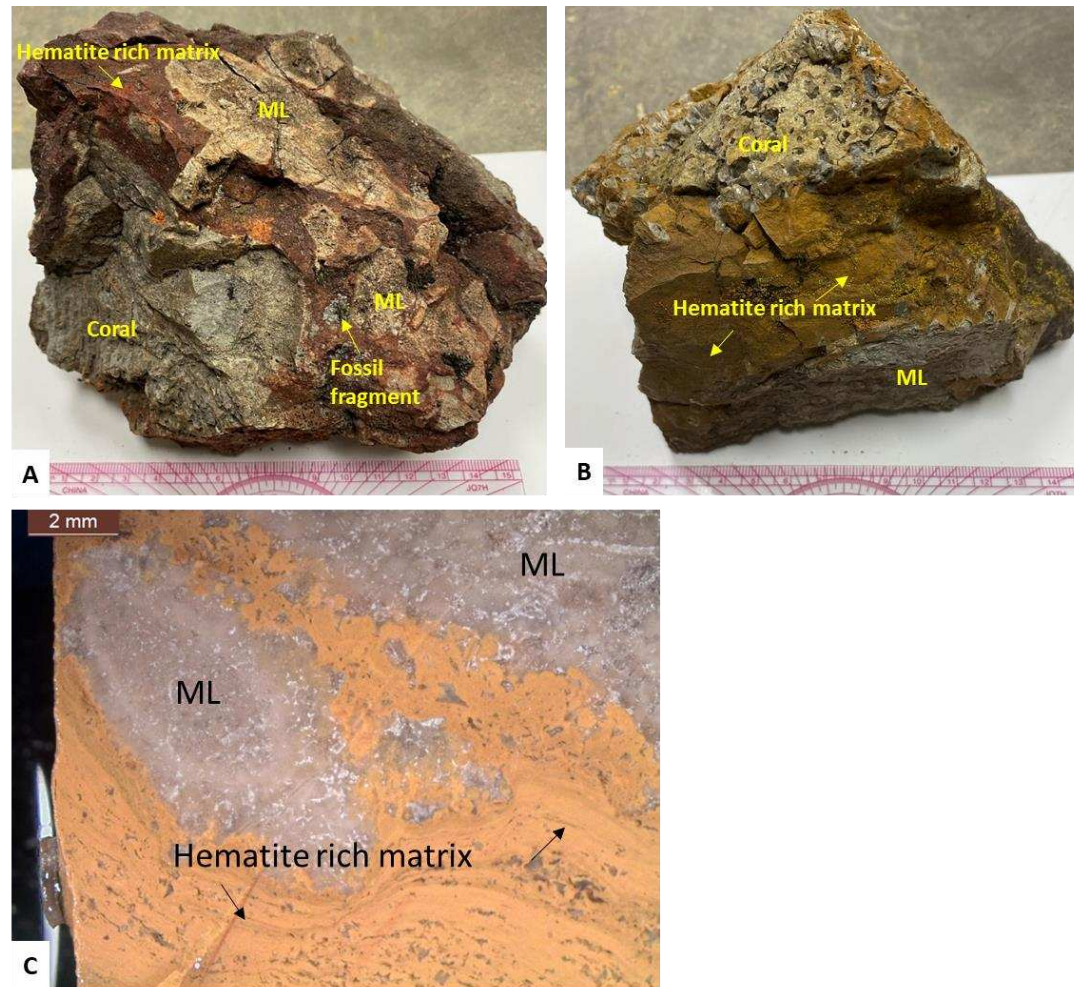


Figure 5.5. Representative hand samples and polished slabs of the monomict breccia with a siliceous, hematite rich matrix ranging from red to orange and orange yellow. A: sample B33, red matrix supported with Madison Limestone (ML) clasts and coral as well as other small fossil fragments. B: sample B32, orange yellow matrix supported with Madison Limestone clasts as well as brecciated corals. C: Sample B26, oolitic Madison Limestone with orange laminated hematite, see figure 5.6 for photomicrographs of this sample

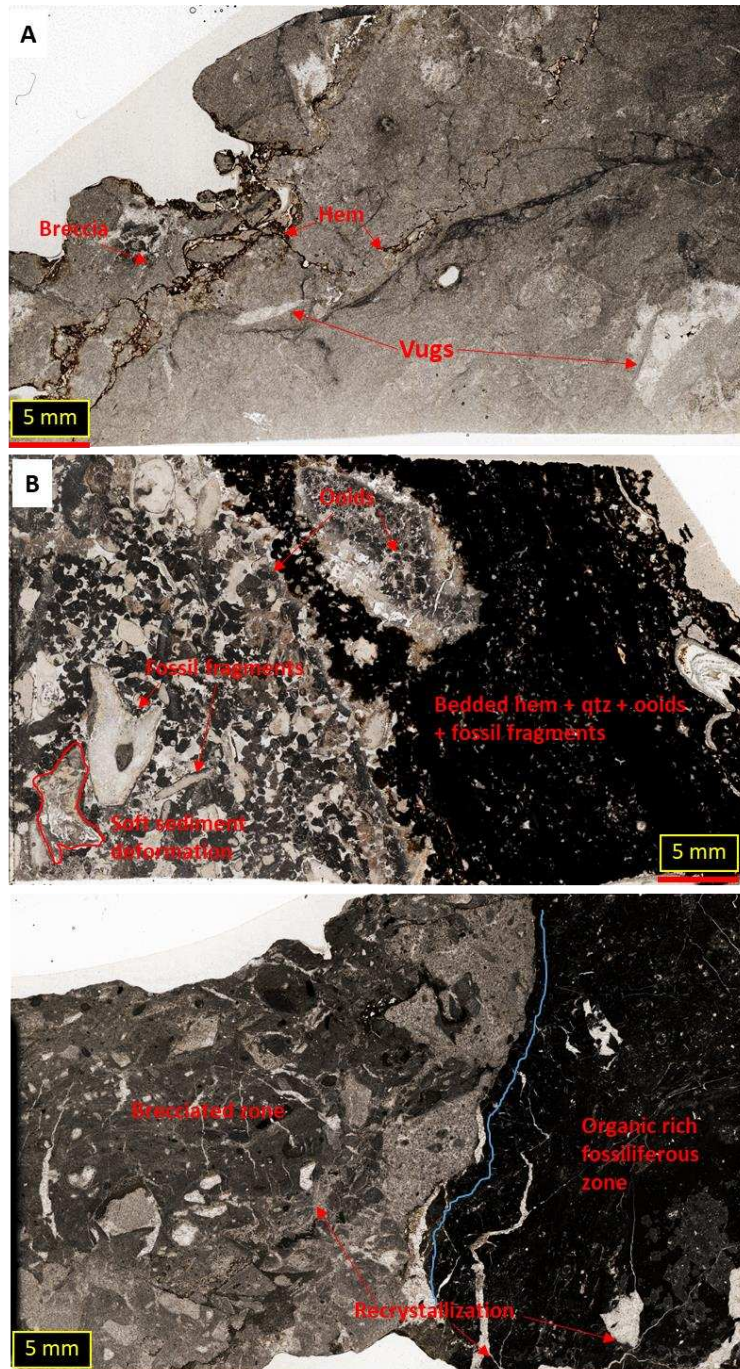


Figure 5.6. Scanned petrographic thin section of the Monomict breccia; samples B25 (A), B26 (B), and B29 (C) under plane polarized light. A shows a breccia of fine-grained carbonate with hematite rich matrix. There is recrystallized open space (vugs), the top right side of the thin section has a higher concentration of organic material. B is an example of a fossiliferous oolitic limestone that has a lens with soft sediment deformation and thick bedded zone of hematite rich sediment with fossil fragments and ooids. Quartz is not seen in thin section and presumed to be present and cryptocrystalline. C shows multiple episodes of brecciation adjacent to a zone of fossiliferous limestone with a dense concentration of fine organic material. There are areas of calcite recrystallization in former fractures of this sample as well small lenses of recrystallized calcite that could have been voids or fossil fragments.



Figure 5.7. Polymict breccia sample B3 showing the variety of calcareous clasts found in these samples. They are fragile rocks that are semi consolidated to unconsolidated by nature and are difficult to sample. This sample shows the common component of red siltstones (SS), yellow limey-mudstones (MS), and tan limestone (LS) clasts in an orange to yellow mud matrix. This sample also hosts a small floating bleb of lamprophyre.

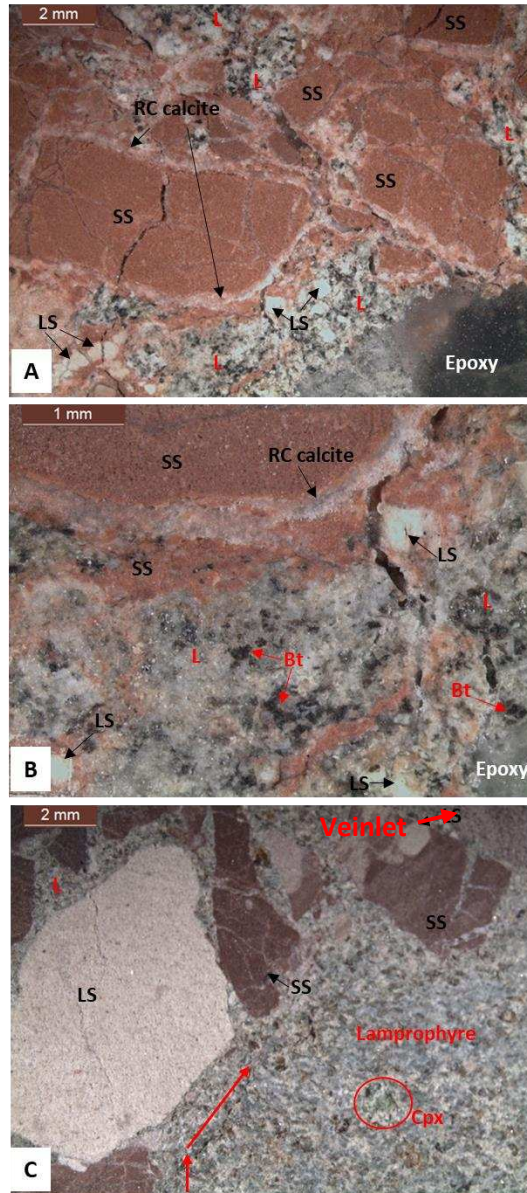


Figure 5.8. Impregnated and cut slabs of Representative Polymict Breccia with lamprophyre. A and B: Sample EM45, showing dominantly red calcareous with minor quartz siltstones (SS) and minor limestone (LS) clasts with blebs and veinlets of altered lamprophyre (L). The sedimentary clasts are fractured with recrystallized calcite. Most of these clasts are lined by recrystallized calcite where lamprophyre interacted with the siltstones and limestones. The lamprophyre shows subhedral biotite in a grey green aphanitic matrix owing to the breakdown of clinopyroxene, calcite, and feldspathoids. C: Sample EM46 is a sample dominated by lamprophyre with tan silty limestone clasts showing weak bedding and minor quartz as well as red calcareous siltstones that show minor fracturing and leaching of hematite, as their patchy appearance suggests. Black to brown phenocrysts in the sample are biotite and one altered apple green pyroxene remains intact, otherwise the lamprophyre is completely altered. On the left-hand side of this sample there is a weak fabric (shown with arrows) along the margin of brecciated clasts suggesting flow. In the upper right-hand corner of the section there is an arrow pointing to a small injection veinlet in a red siltstone clast.

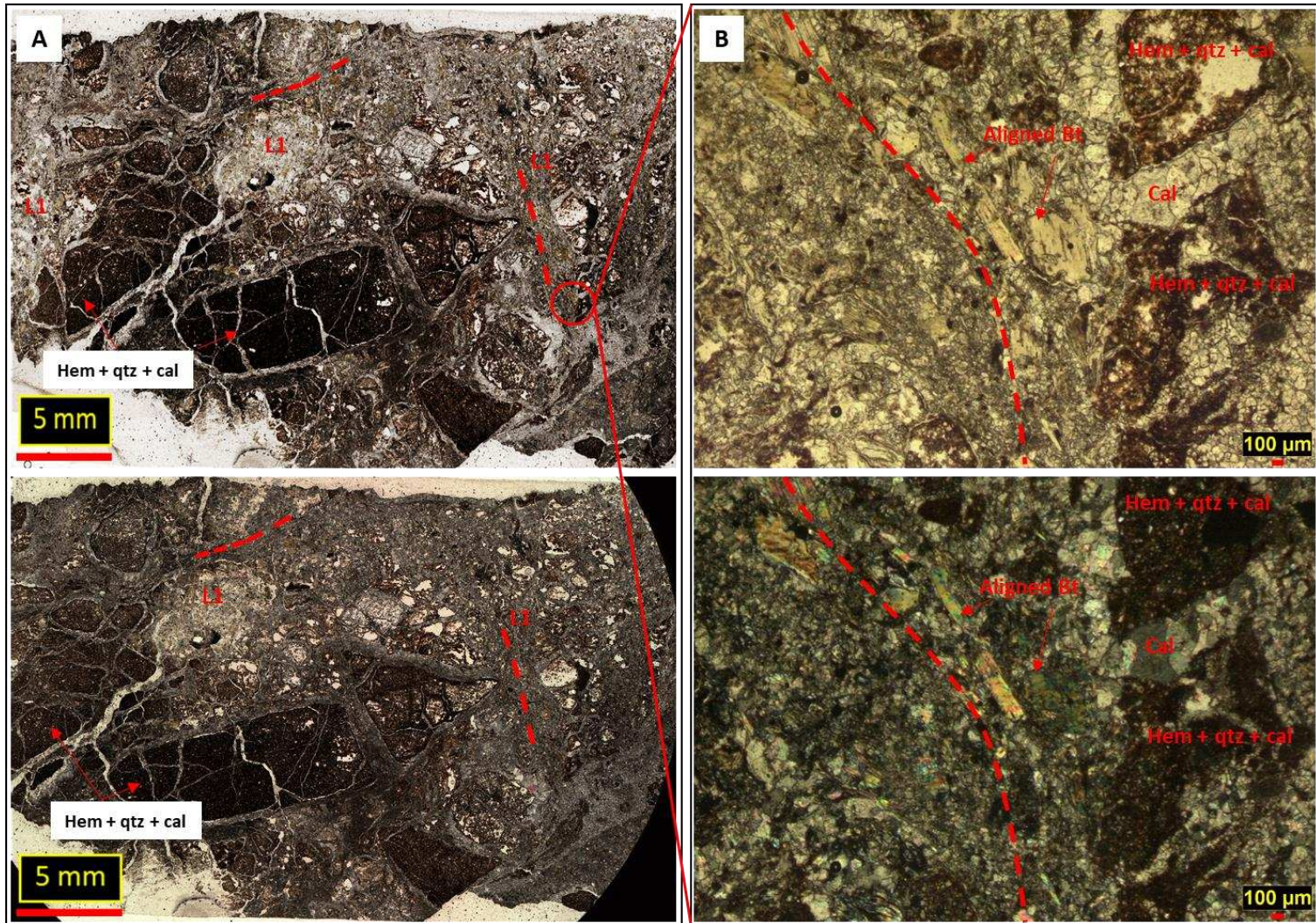


Figure 5.9. Polymict breccia sample EM45. A. plane polarized and cross polarized images of scanned petrographic thin section showing subtle fabric of lamprophyre 1 around fractured carbonate cemented quartz siltstone with disseminated hematite. Calcite veins fill fractures and lines sedimentary clasts. B, plane polarized and cross polarized photos of aligned biotite in altered lamprophyre 1 near the margins of and between breccia clasts.

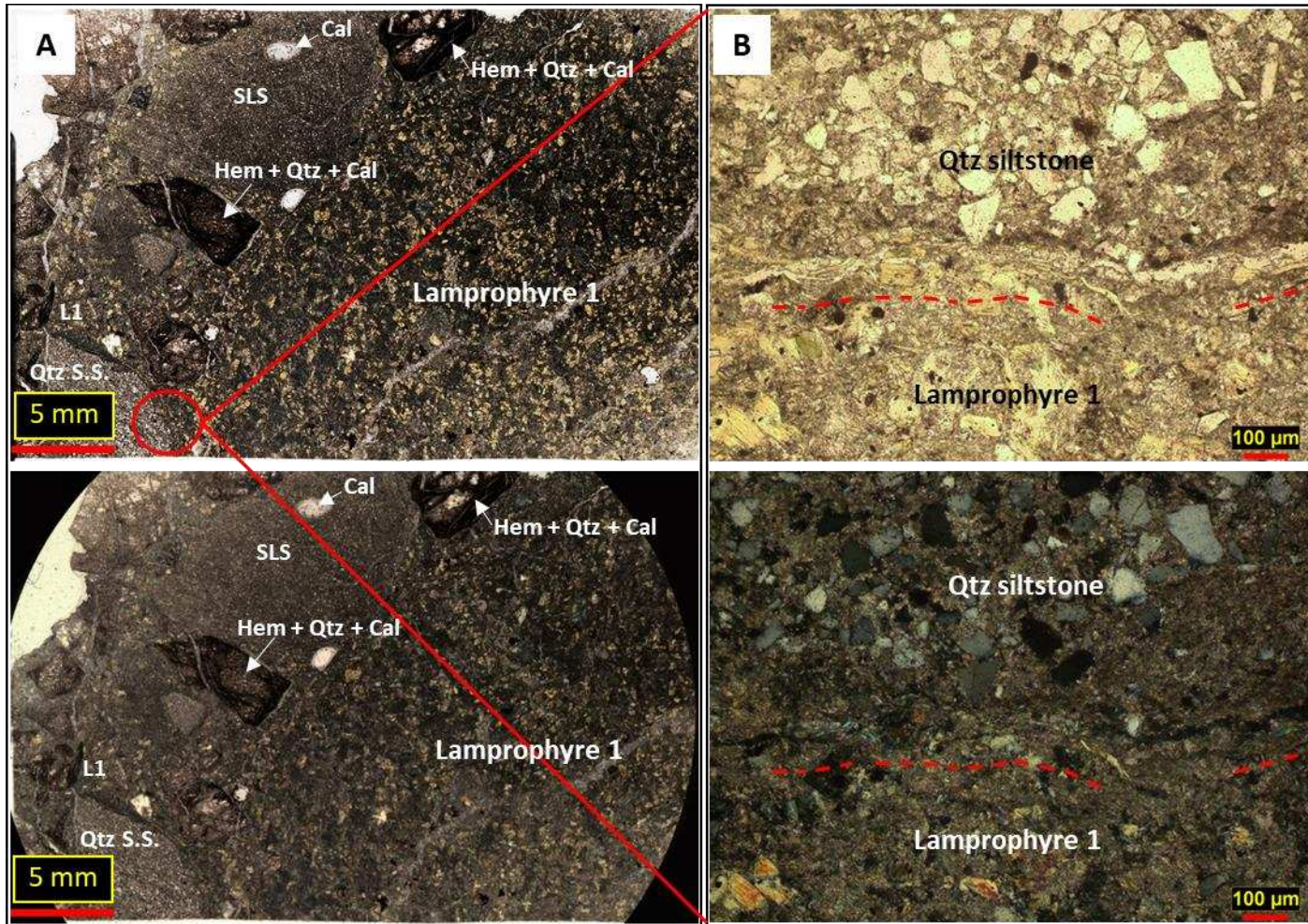


Figure 5.10. Polymict breccia sample EM46. Images in A are plane polarized, and cross polarized scans of the slide showing the variety of carbonate rich clasts found in the polymict breccias with lamprophyre (type 1) interaction. SLS, silty limestone clasts; Hem + Qtz + Cal, carbonate cemented quartz siltstone with disseminated hematite; Qtz S.S., quartz siltstone with carbonate cement. B photos are plane polarized and cross-polarized photomicrographs of the zone where there is a subtle fabric of aligned biotite suggesting flow.

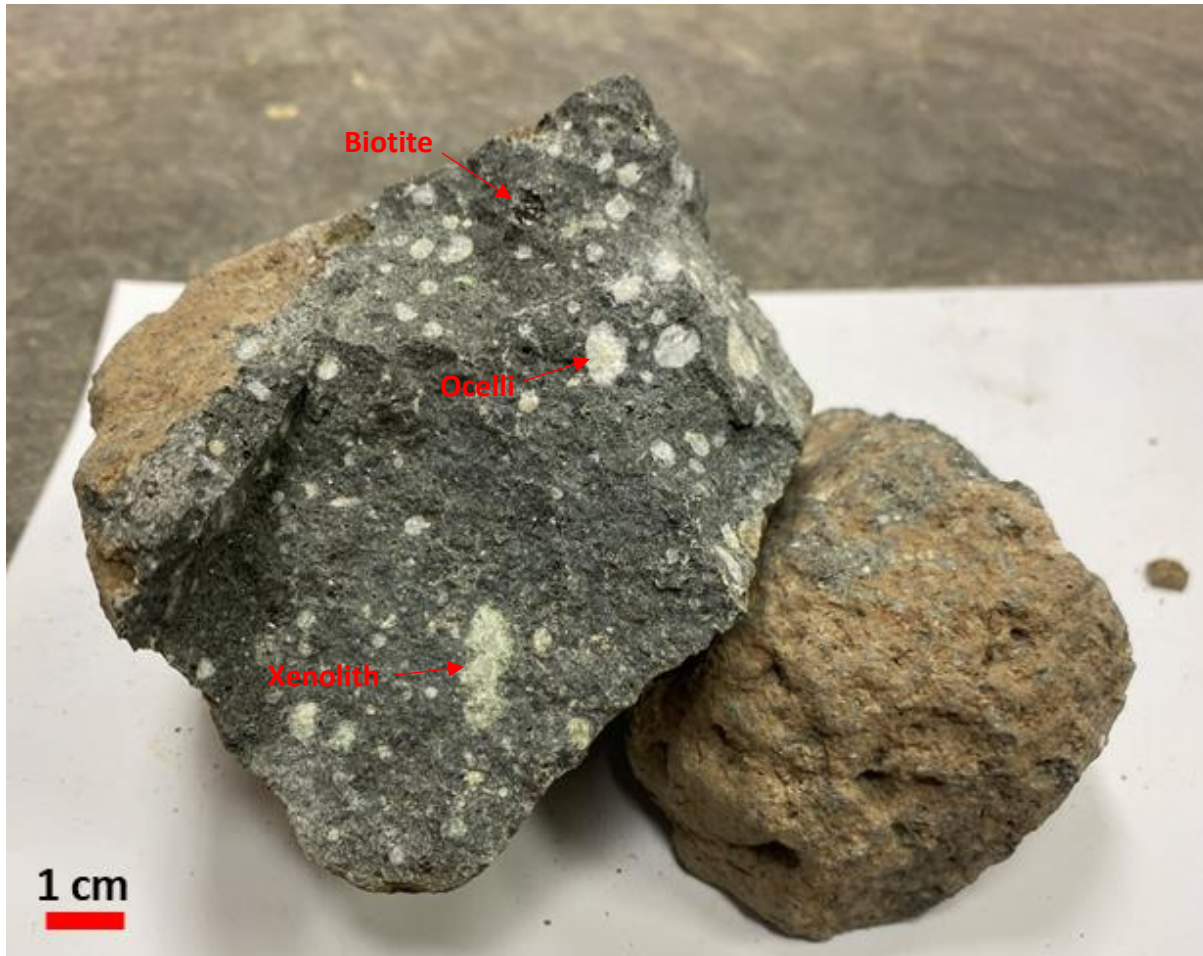


Figure 5.11. Representative hand sample of Lamprophyre 1 number EM 24. The weathered surface has an orange tint while the fresh interior of the sample is grey green with abundant ocelli, coarse anhedral biotite with altered xenoliths.

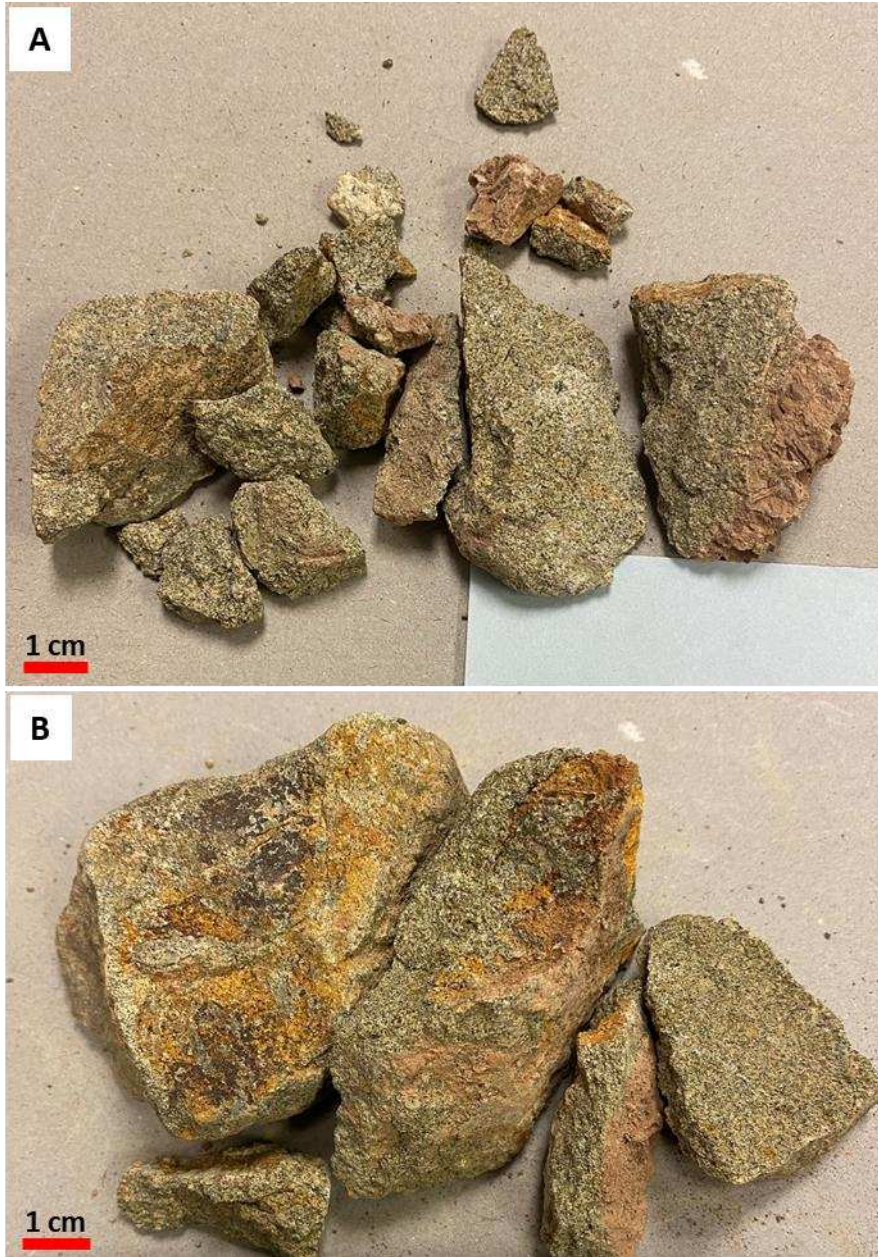


Figure 5.12. Mottled grey to green to orange hand samples of weathered Lamprophyre 1. Both images show red clasts similar to the polymict breccia clasts seen in figure 10. A. Sample EM44 illustrates the friable nature of the weathered rock. It breaks apart easily by hand. B. Sample EM42, a larger hand sample with orange weathering.

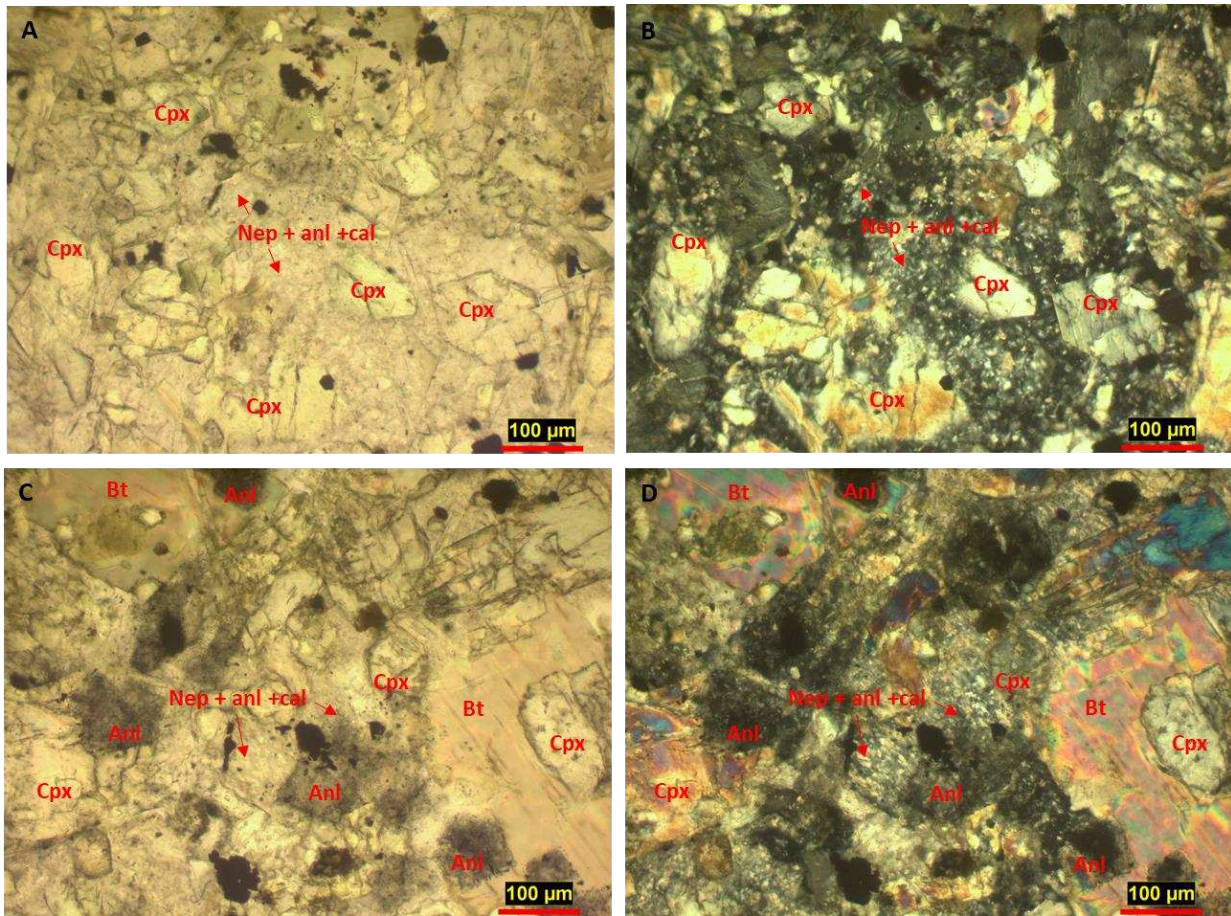


Figure 5.13. Examples of matrix of Lamprophyre 1 samples. Photos A and B are from sample EM10 and show microphenocrysts of clinopyroxene and opaque iron oxides in a nepheline analcime and calcite matrix. Photos C and D are from sample EM31.26a and show analcime and opaque iron oxides in a nepheline, analcime, and calcite matrix.

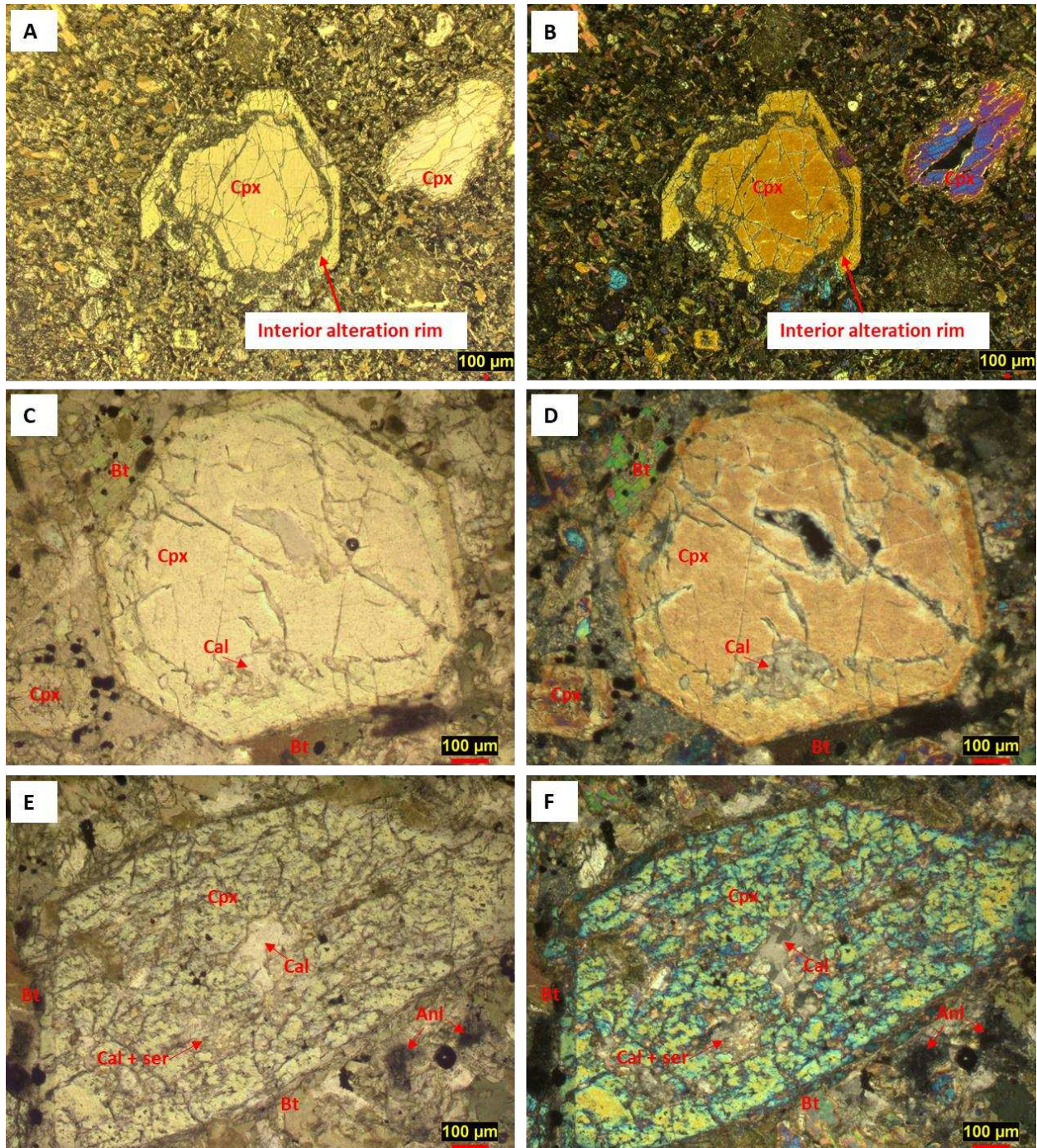


Figure 5.14. Examples of clinopyroxenes in Lamprophyre 1. A and B are from sample EM7a1 and show a euheedral clinopyroxene that has an interior zone of alteration. C and D are from sample EM26b is an example of a generally fresh clinopyroxene with minor calcic alteration and a clean outer zone. E and F are from sample EM26d and have an example of a pitted and altered clinopyroxene. There are areas in this phenocryst that have been replaced by calcite and other areas that have been replaced by calcite and sericite. Note that pitting and replacement occurs along cleavage and as irregular shaped blebs.

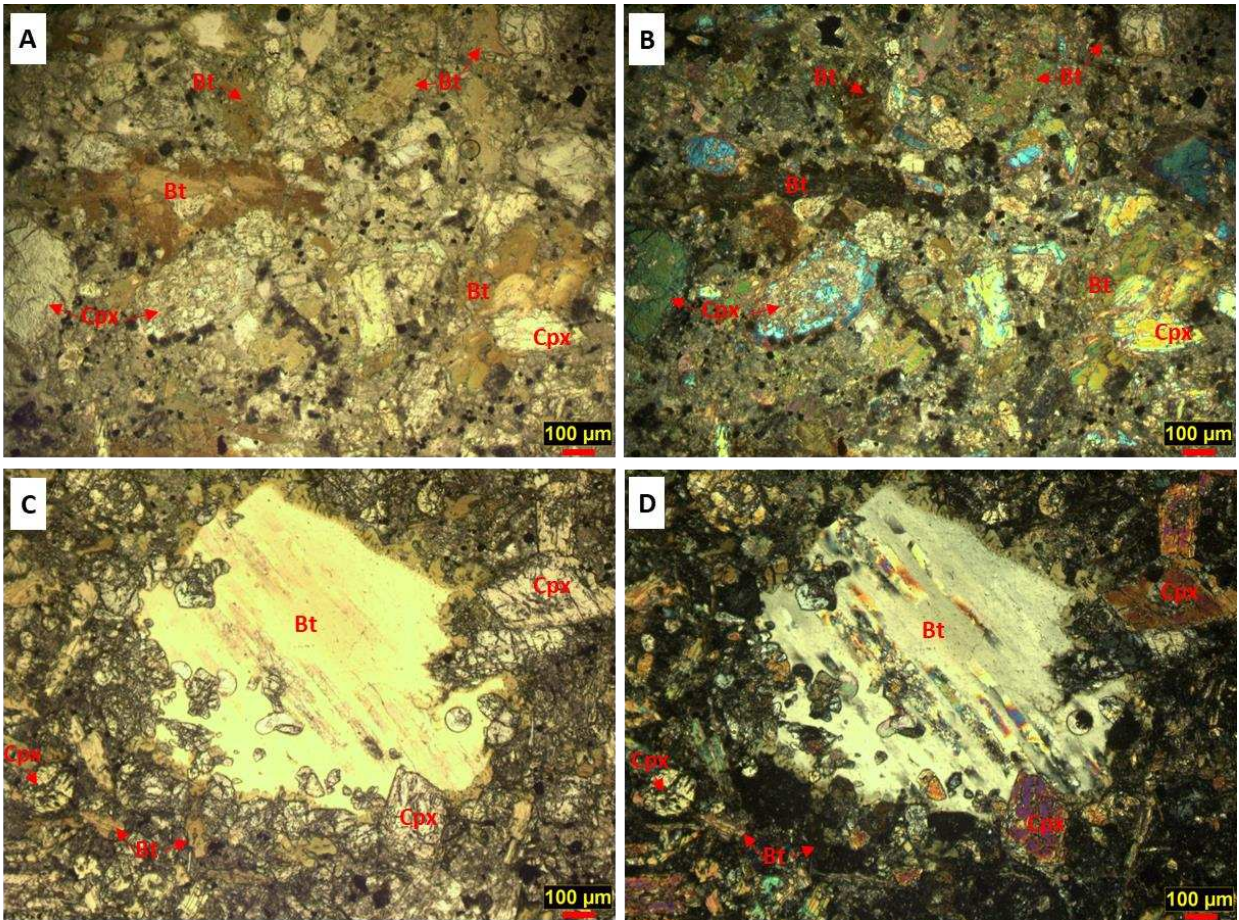


Figure 5.15. Examples of biotite in Lamprophyre 1. Photos A and B are from sample EM7b. This section shows anhedral, castellated biotite with zonation shown as dark brown pleochroic rims. There is also a fresh clinopyroxene adjacent to a nearly replaced clinopyroxene with only the rim of the crystal intact. Images C and D are from sample EM10b and show a large biotite phenocryst that is also castellated and has a very narrow dark pleochroic rim zone.

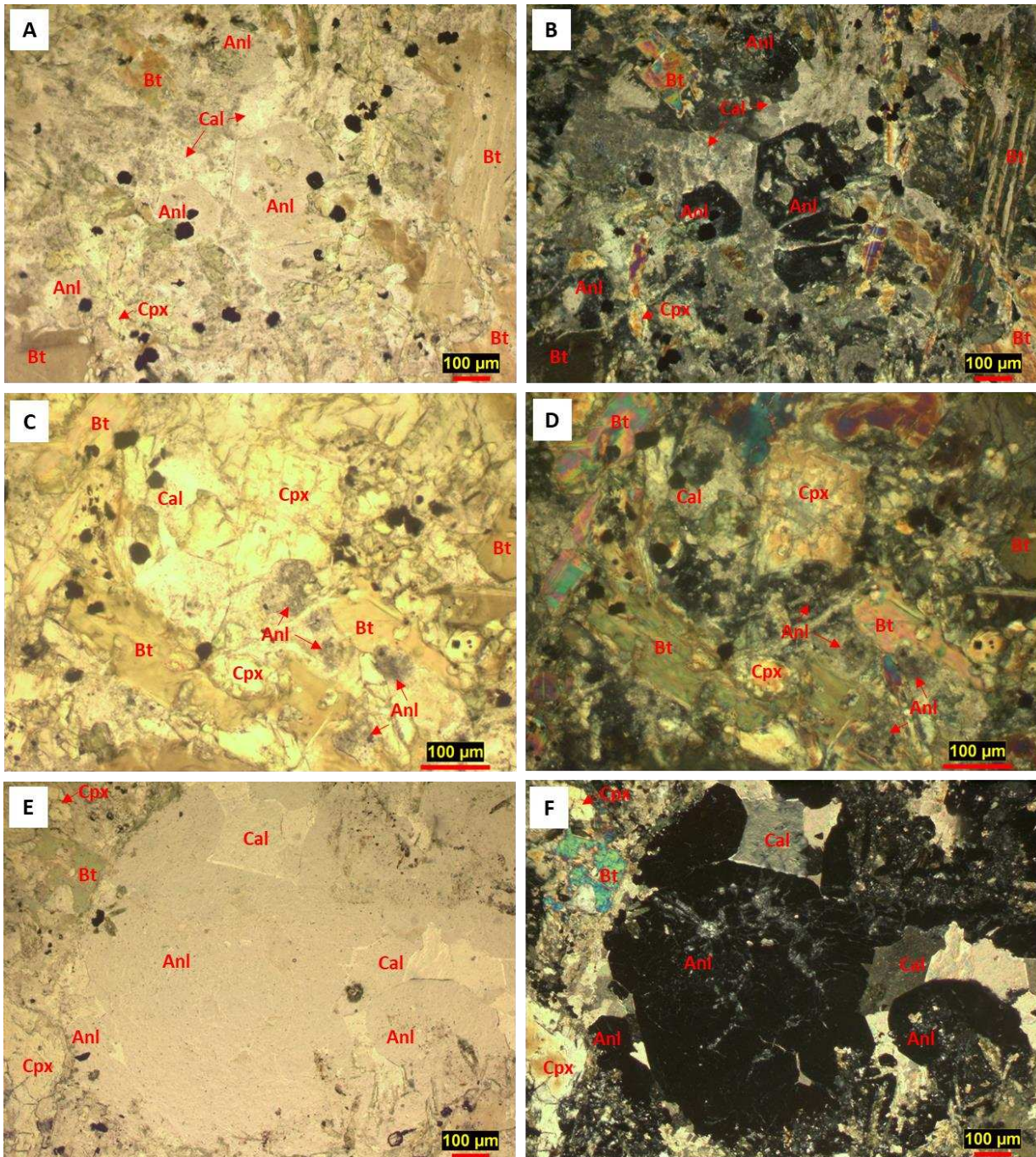


Figure 5.16. Various examples of analcime in Lamprophyre 1, some appear nearly fresh, while others are dusty and partially replaced. A and B are from sample EM3a and show euhedral analcimes with minor calcite replacement and calcite matrix surround them. C and D are from sample EM10a and show dusty euhedral, hexagonal microphenocrysts in a matrix that retain some of the isotropism seen in analcime. E and F are from sample EM12a and show large, euhedral, unaltered analcime with euhedral calcite surrounding it.

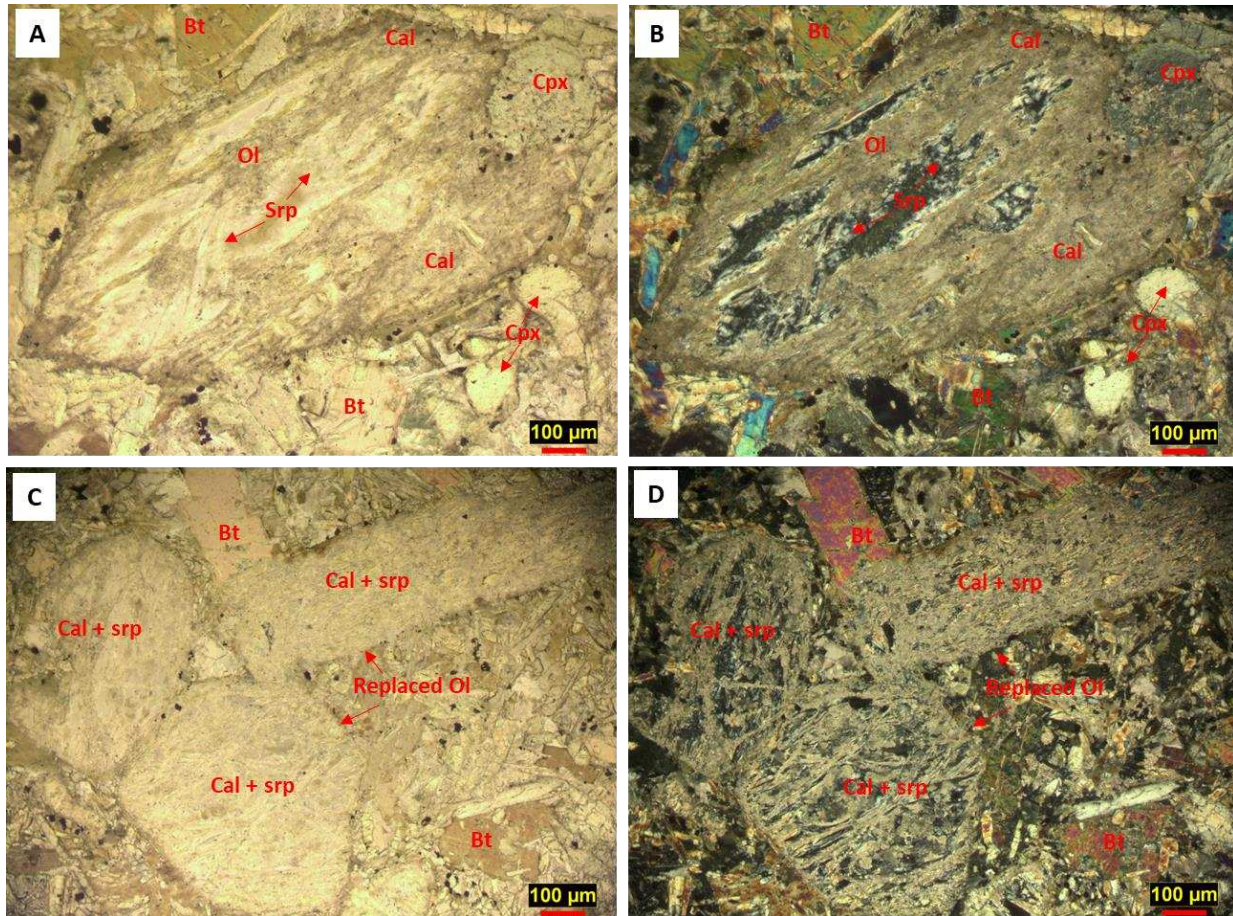


Figure 5.17. Examples of completely altered olivine in Lamprophyre 1. A and B were taken from EM3a and show an elongated hexagonal olivine with a weakly altered clinopyroxene partially included. The olivine has been completely replaced by a mixture of serpentinite and calcite with opaques (presumably magnetite) lining the rim of altered phenocryst. C and D were taken from EM3b at 100x and show a cluster of replaced olivine that has also been replaced by serpentinite (srp), calcite and opaques.

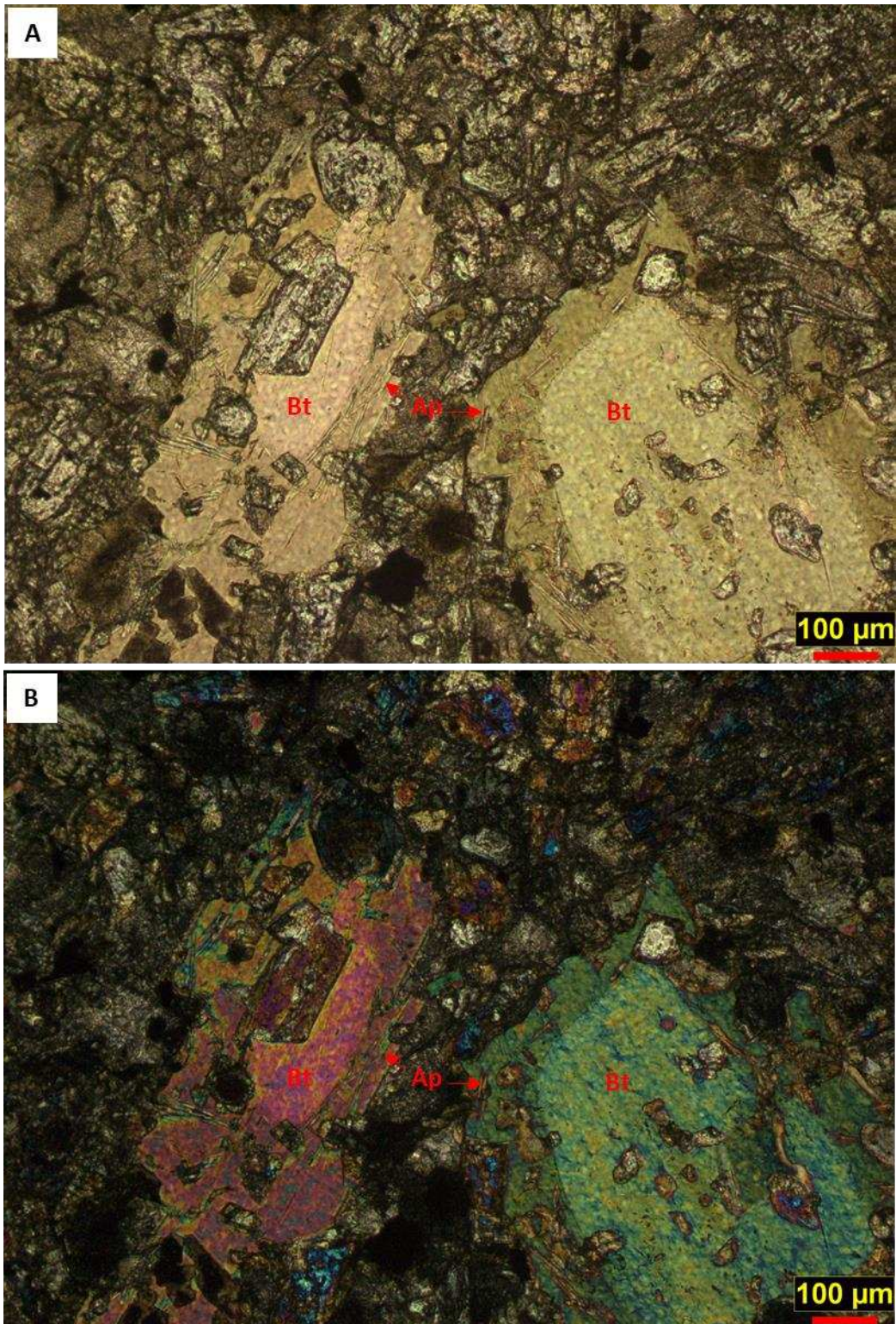


Figure 5.18. Representative micrograph of apatite (ap) found in pleochroic rims of biotite from sample EM26b.

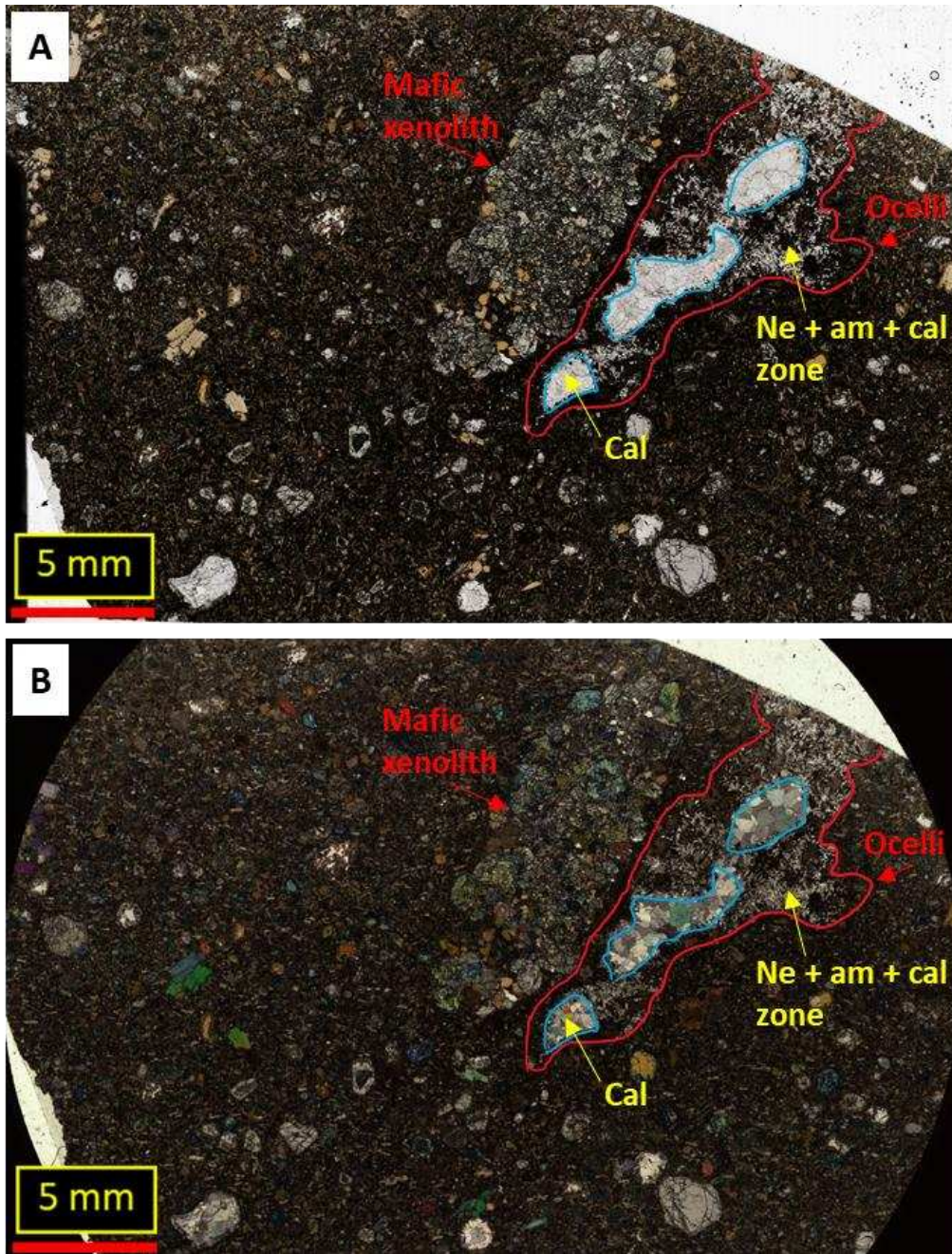


Figure 5.19. Scanned petrographic thin sections of sample EM47 showing an ameboid shaped ocelli with an inconsistently thick alteration rim of nepheline series feldspathoid with needles of amphibole and calcite. The core of this ocelli is largely euhedral calcite with minor analcime (Fig. 5.20).

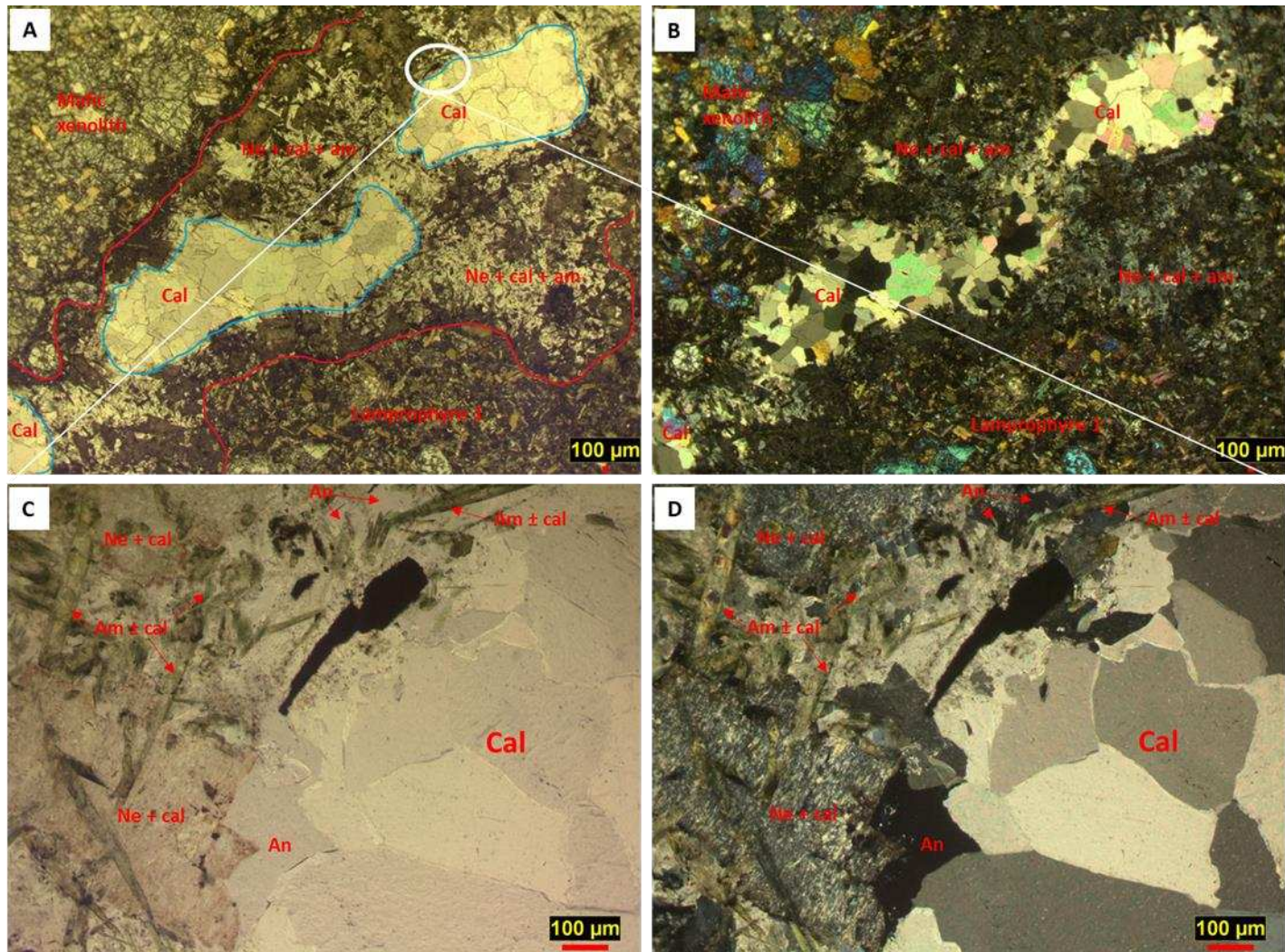


Figure 5.20. Photomicrographs of sample EM47a ocelli. A and B are a closeup photos of the distribution of the exterior diffuse rim of nepheline series feldspathoid (ne), amphibole (am) and calcite. C and D show the contact between the outer ne + cal + am rim and the central core of euhedral calcite with minor analcime. The amphibole has been largely replaced by calcite.

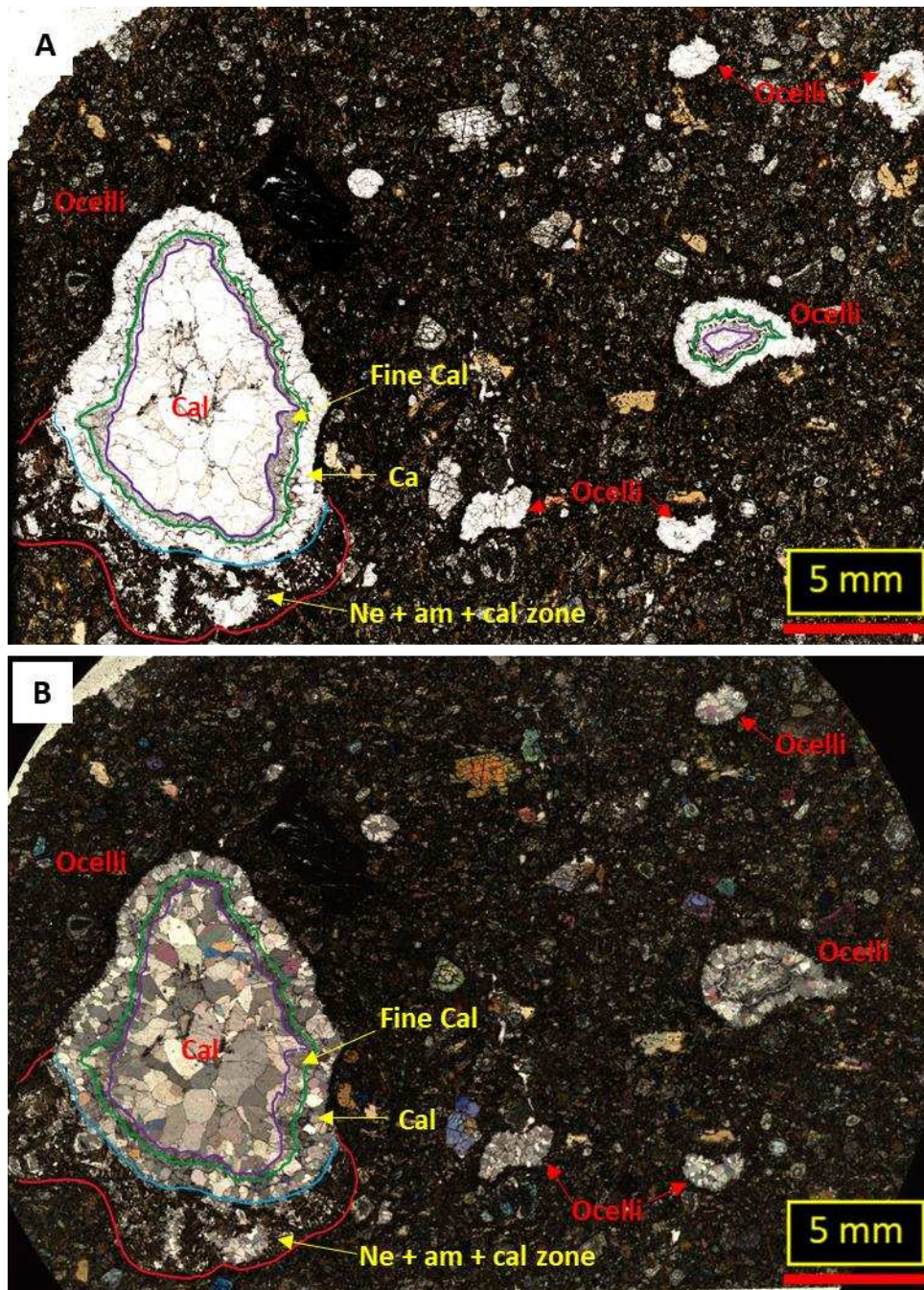


Figure 5.21. Scanned petrographic thin sections of sample EM7a. This sample shows a variety of ocelli shape and size ranging from small and rounded to large and irregular shaped. The large ocellus on the left-hand side has an outer rim of nepheline series feldspathoids, amphibole and calcite restricted to the bottom of the ocelli. This is followed inwards by euhedral calcite then fine calcite and changes back into a euhedral calcite core. Close up photos explore this ocelli (Fig. 25).

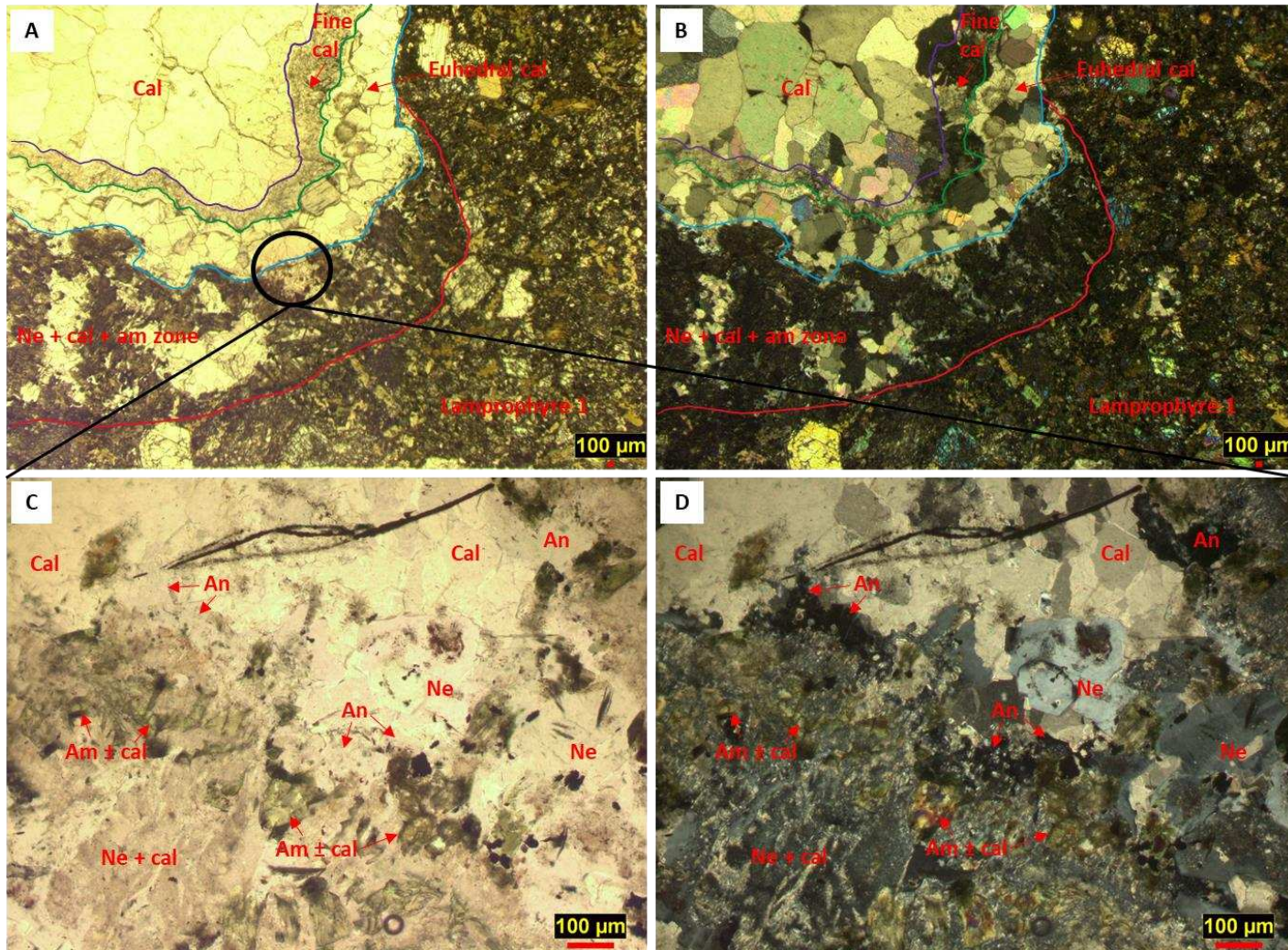


Figure 5.22. Close up images of ocelli in sample EM7a. A and B show the overall distribution of the different zones and their distributions. The outer rim is of a semi consistent thickness restricted to one segment at the bottom of the ocelli, while the inner zones have a constant thickness but are irregular in shape. Sparry calcite dominates the center of this ocelli. C and D are images of the margin between the first and second zones. The outer zone is dominated by fine nepheline series feldspathoids with amphibole needles partially replaced by calcite. On the righthand side of the image there is euhedral nepheline. The euhedral calcite zone has minor analcime.

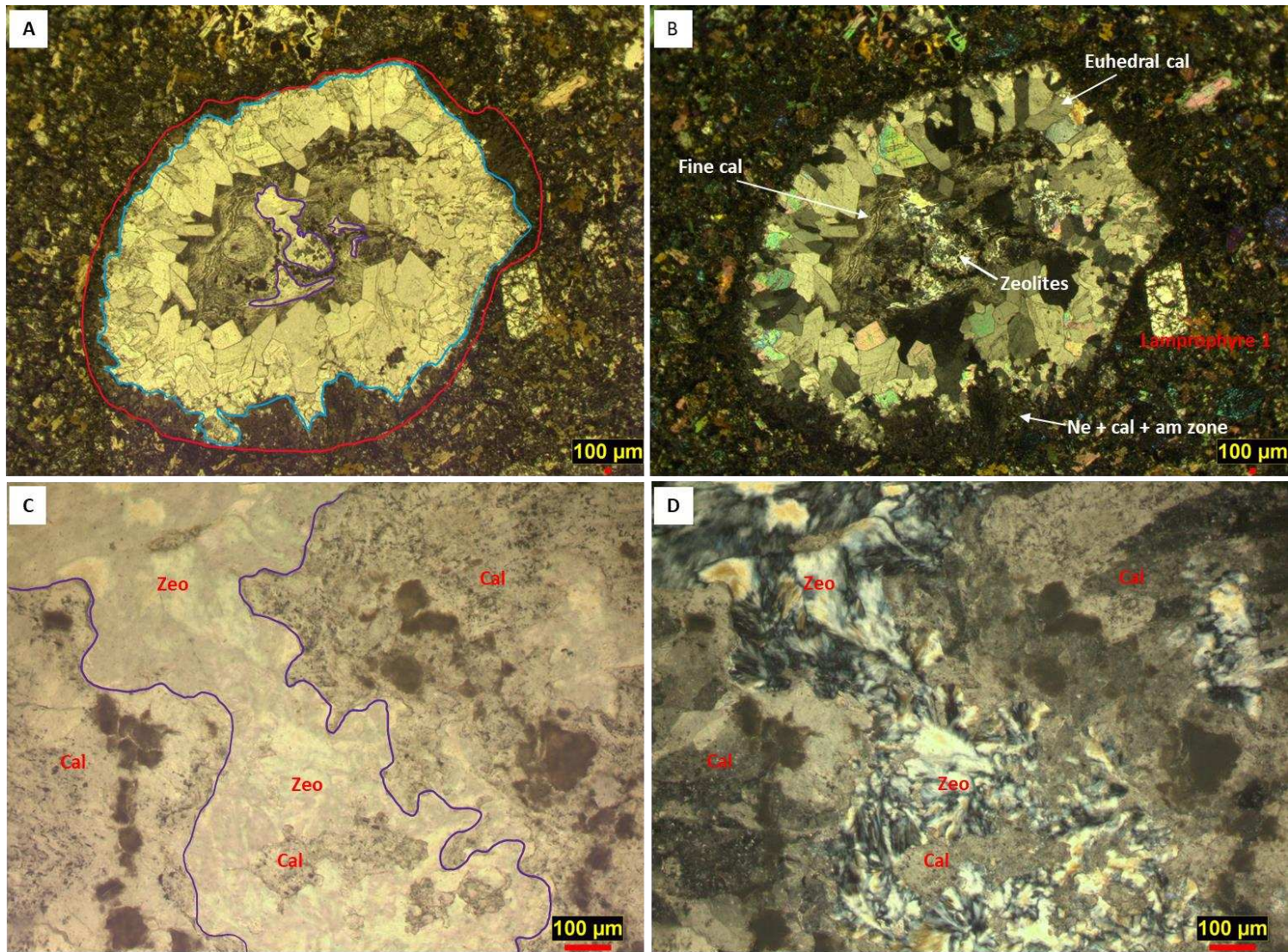


Figure 5.23. Photomicrographs of an ocelli from EM26a. A and B shows a thin zone of inconsistent thickness of nepheline series feldspaths, calcite, and amphibole followed by a thick comb calcite zone with euhedral terminations, and then fine calcite which grades into zeolites. C and D are closeup photos of fine calcite which grades into a fibrous zeolite zone.



Figure 5.24. Photo of representative sample VM6 of Lamprophyre 2. The outer surface of the rock is dark grey to green with minor yellow-orange staining. The fresh interior is black and aphanitic with small orange phenocrysts of presumably altered olivine and calcite veins.

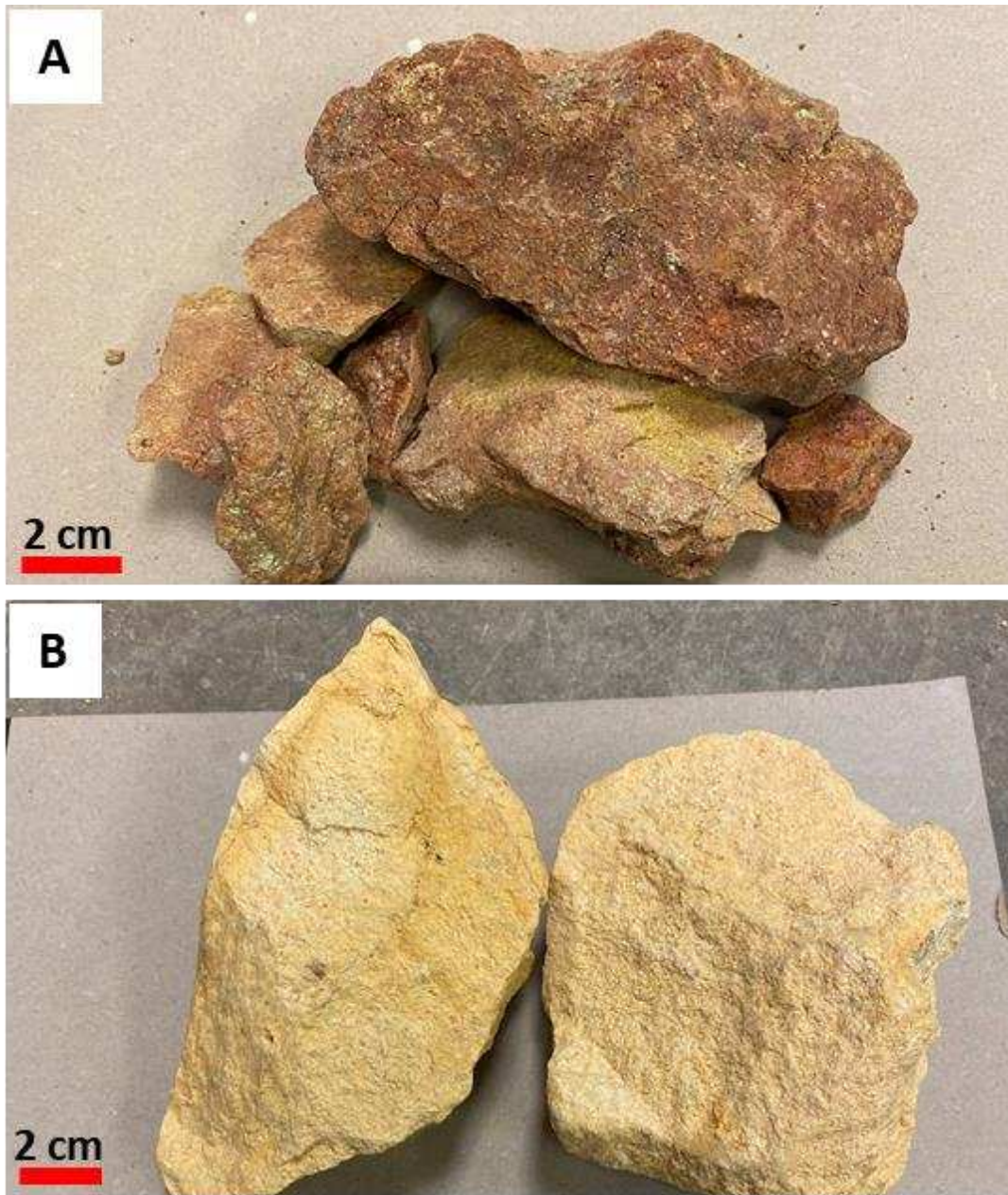


Figure 5.25. A, sample VMDW5 collected underground in the Vortex mine and represents one of two the clay-rich weathering facies found in Lamprophyre 2. It is red to orange in color, with fine sea-green flecks of presumably altered clinopyroxene. B, sample VMDW4 is representative of the second weathering facies found underground in the Vortex mine. This sample is yellow to peach in color and may have remaining evidence of weathered clinopyroxene as well, sapphires were found in this area.

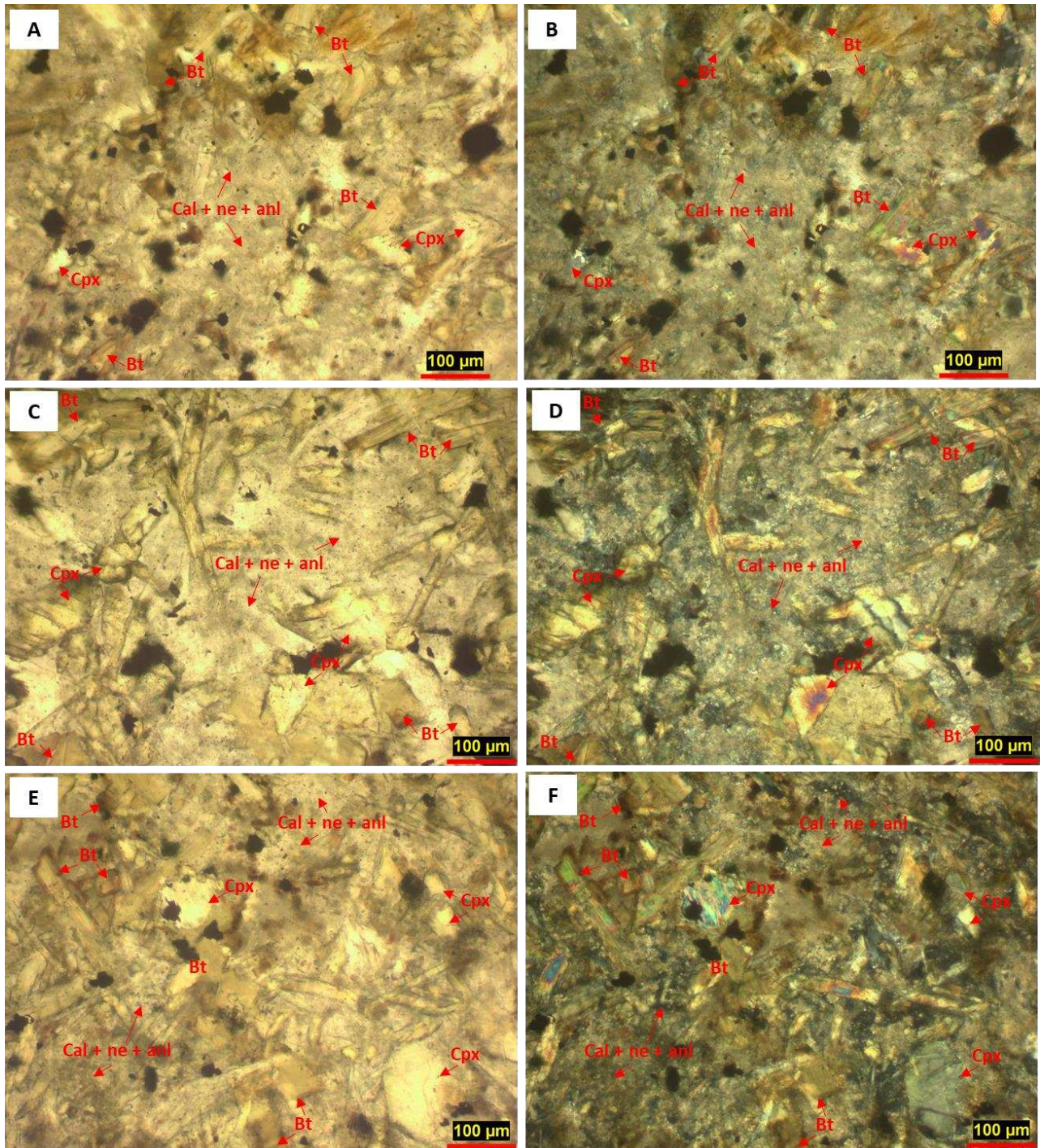


Figure 5.26. Representative photomicrographs of matrix in Lamprophyre 2 samples. The matrix is dusty and mostly isotropic with microphenocrysts of opaques, biotite and minor clinopyroxene. There are some areas in the matrix that have patches of microcrystalline calcite, nepheline series feldspathoids, and analcime. A and B: Sample VM6. C and D: Sample VM6b. E and F: VM7b

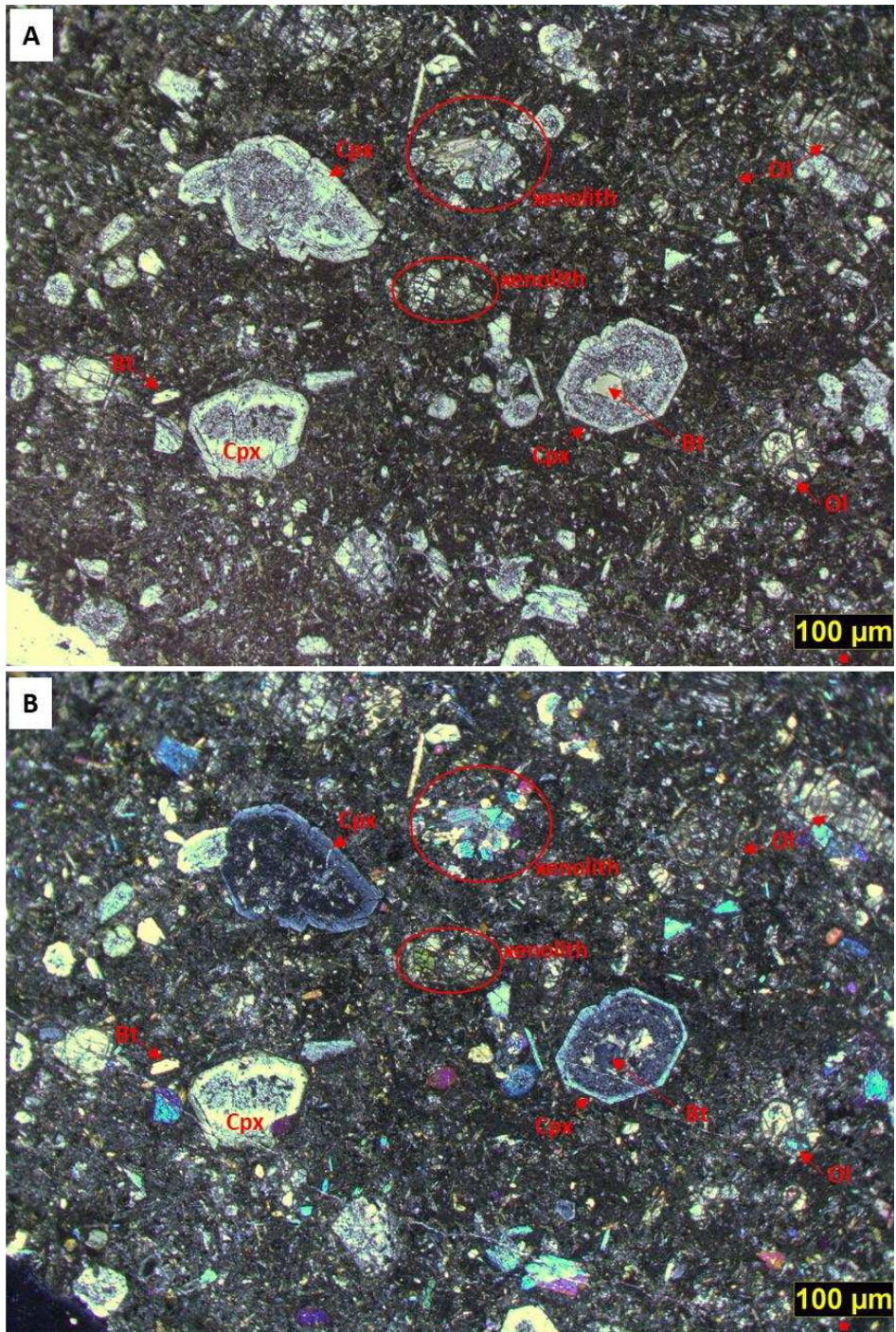


Figure 5.27. Plane polarized (A) and cross polarized (B) Images from sample VM7b showing zonation in clinopyroxenes as a moderate to weak change in birefringence from the core the margin of the phenocrysts. Clinopyroxenes are also pitted to varying degrees. There is one subhedral biotite phenocryst in these images and a biotite is included within an altered clinopyroxene. Olivine (Ol) as well as ultramafic xenoliths are present.

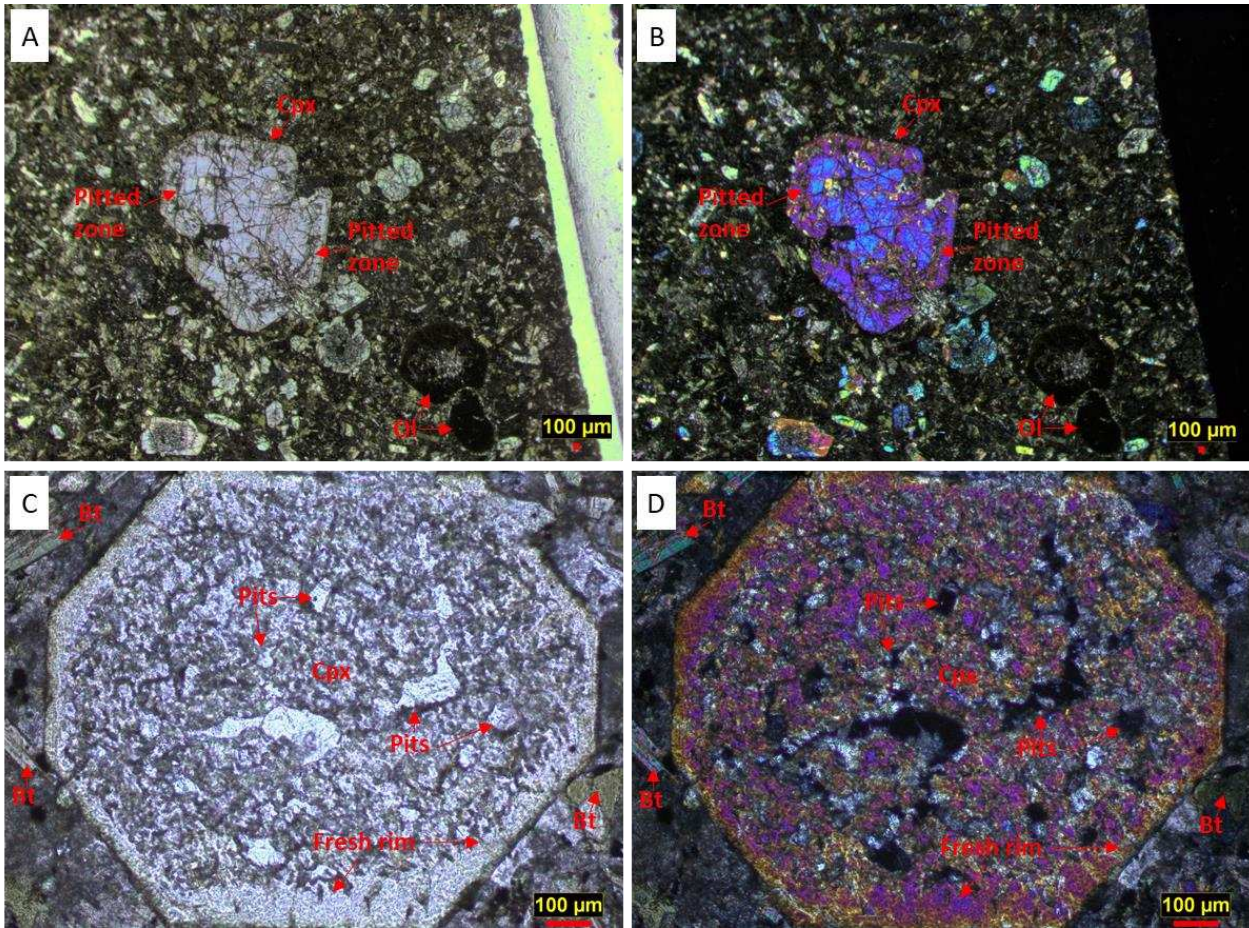


Figure 5.28. Images of the variation in distribution of alteration as pits in clinopyroxene found in Lamprophyre 2. A and B were taken from sample VM6a and show a relatively fresh clinopyroxene with a single zone of pits. C and D are representative images of clinopyroxenes that have pitted cores and were taken from sample VM6b. This image shows the variation in size and shape of pits found throughout a single phenocryst. The isotropic nature of parts of some of the pits suggests that they may have been melt inclusions that have been partially quenched to glass. Anisotropic pits are a combination of carbonate and sericite. There are microphenocrysts of euhedral biotite in the matrix of this image.

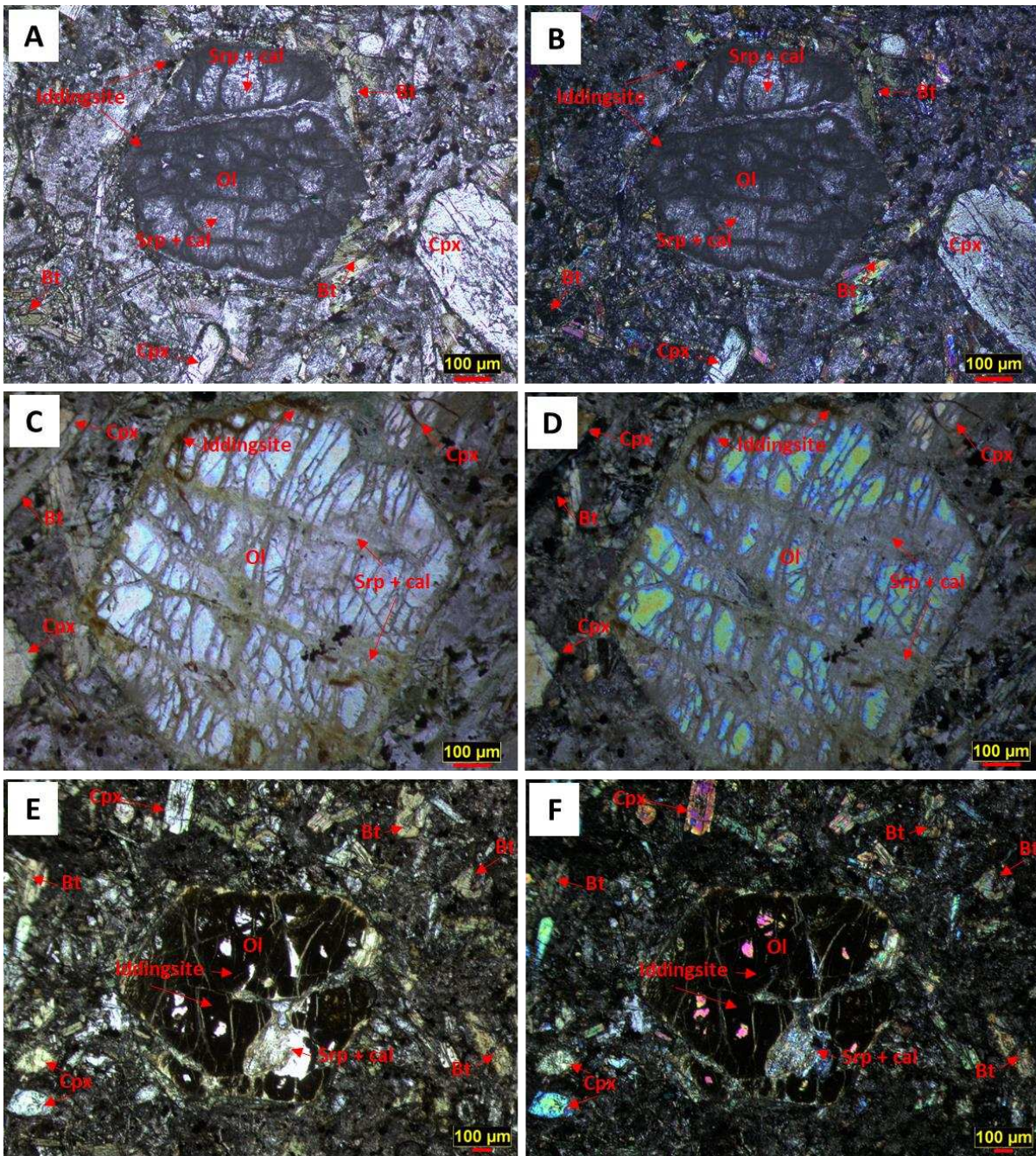


Figure 5.29. These images are representative of olivine found in Lamprophyre 2. They show variations in alteration degree, type, and appearance. A and B were taken from sample VM7a and show a completely altered olivine that has a dusting of opaques, presumably iron oxides, around the margin and along fracture planes of the phenocryst, there they are probably intergrown with calcite and serpentine. Between the fracture planes the phenocrysts has been completely altered to microcrystalline serpentine and calcite. C and D were taken from VM6 and are an example of a partially altered olivine. Iddingsite has replaced parts of the rim of this phenocryst, while calcite and serpentine alteration follows fracture planes. E and F are images of sample VM6a of an olivine that has been nearly completely replaced by mostly iddingsite with a small amount of serpentine and calcite. Very little of the original olivine remains. Euhedral plates of microcrystalline biotite are shown in all six images.

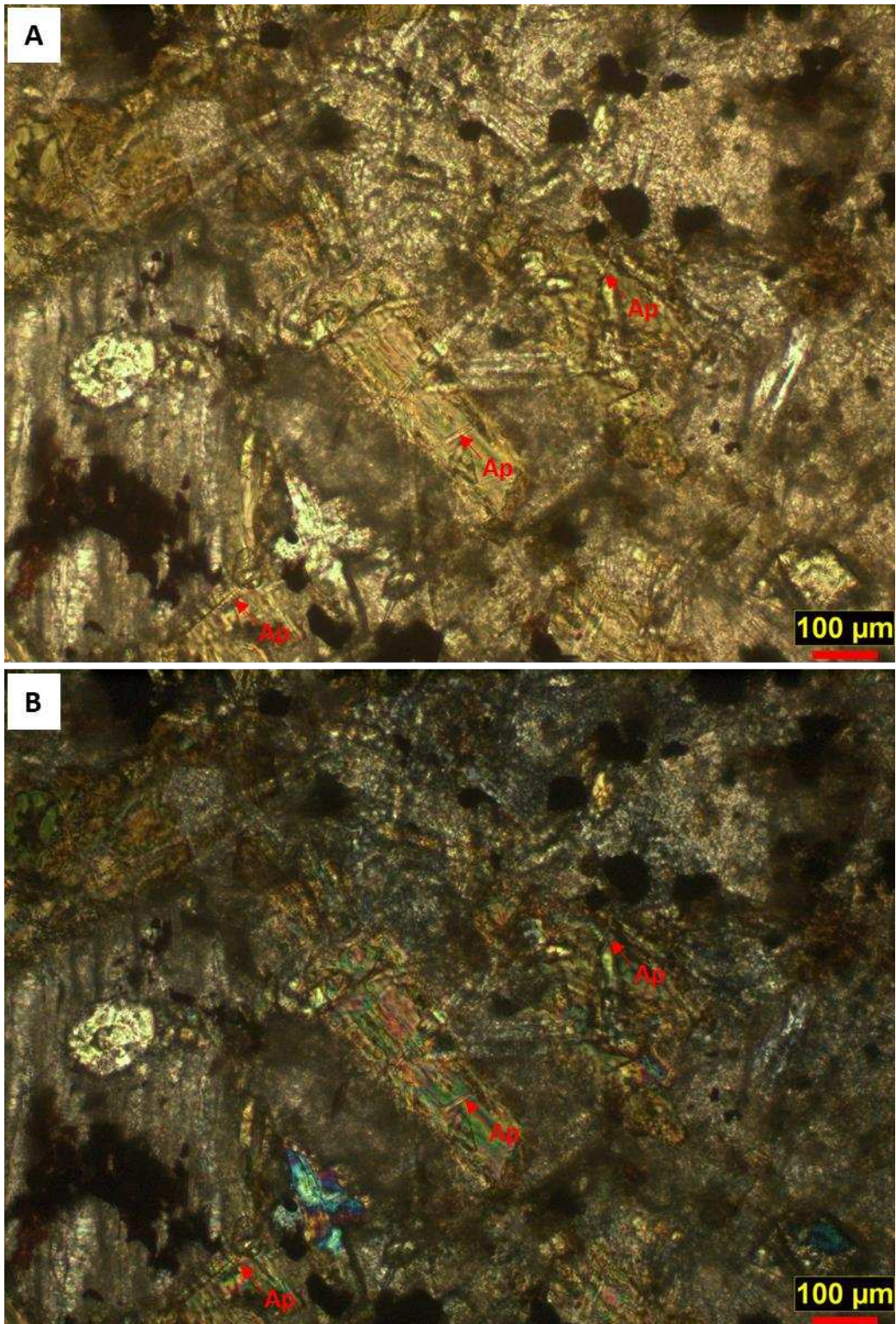


Figure 5.30. Images A and B are representative of apatite needles found in microphenocrysts of biotite in Lamprophyre 2. As with apatite in Lamprophyre 1, they are randomly oriented.

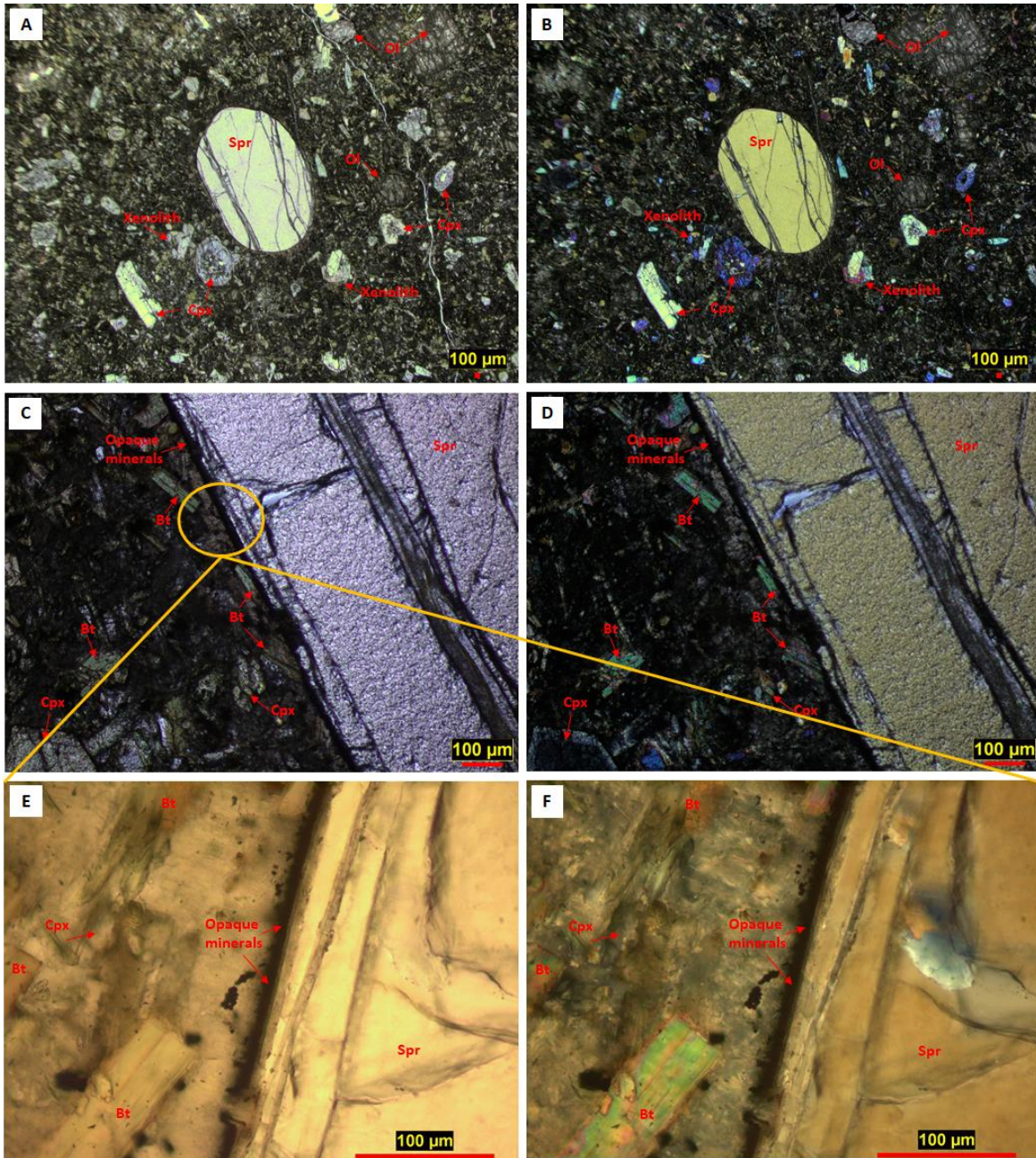


Figure 5.31. Photos of the single sapphire found in thin section across the entire suite of samples. These images came from sample VM6. A and B, show the sapphire in a dark aphanitic ground mass with small ultramafic xenoliths, clinopyroxene and altered olivine. C and D are representative of the microphenocrysts of biotite in the matrix surrounding the sapphire as well as the opaque rim surrounding the sapphire itself. E and F is a closeup of microcrystalline opaque minerals (possibly chromite) lining the sapphire with micro-biotite and micro-clinopyroxene visible in matrix.

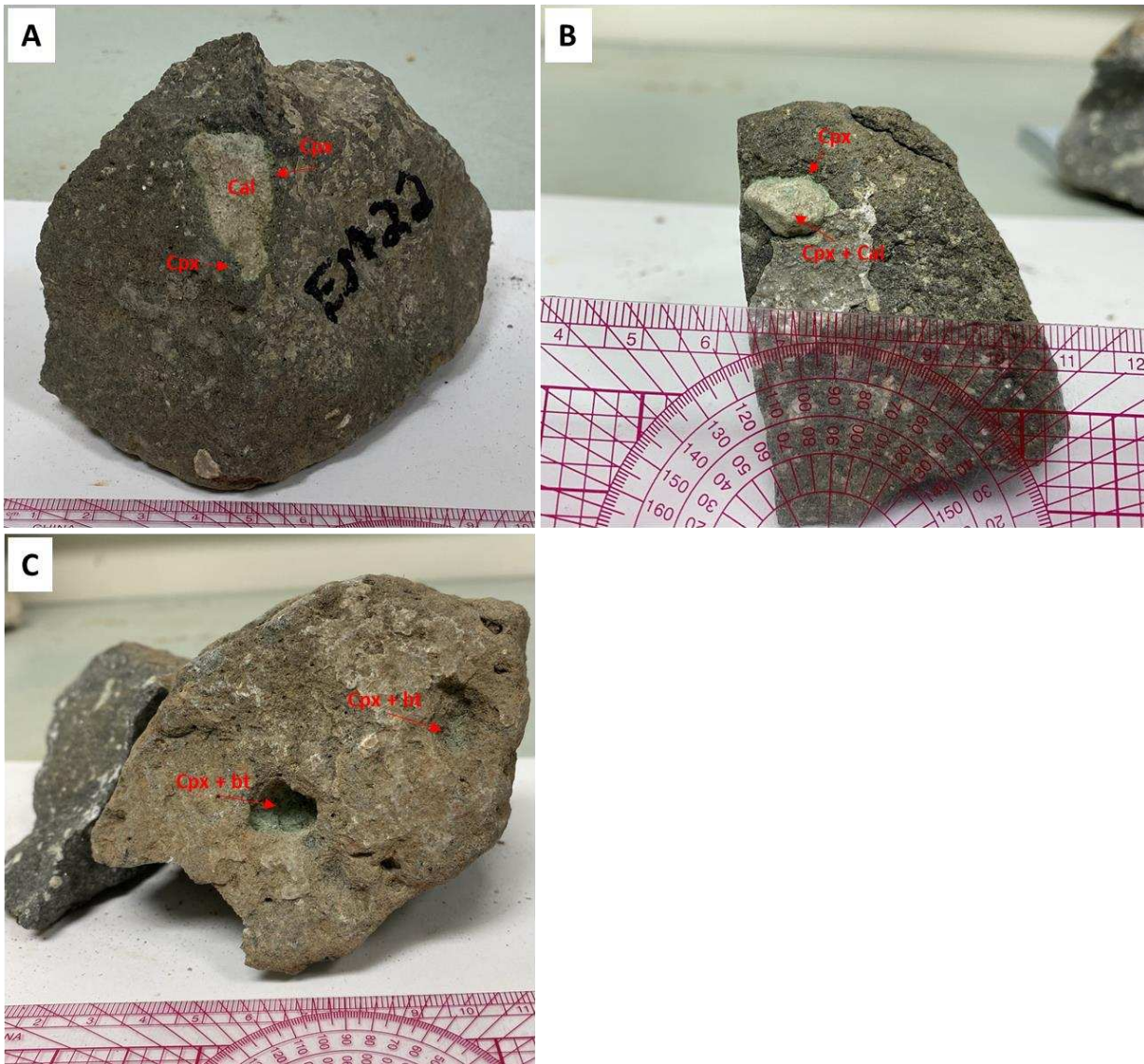


Figure 5.32. Lamprophyre hand samples containing ultramafic xenoliths.

- A. Sample EM22 shows a large ultramafic xenolith with an altered calcite core and clinopyroxenite rim.
- B. Sample EM14 is representative of an altered ultramafic xenolith protruding from the lamprophyre. The outer margin is clinopyroxene and the altered core is clinopyroxenite and calcite.
- C. Sample EM24 is representative of vugs left behind from ultramafic xenoliths weathering out of the host rock. In both vugs there are vestiges of clinopyroxenite and biotite.

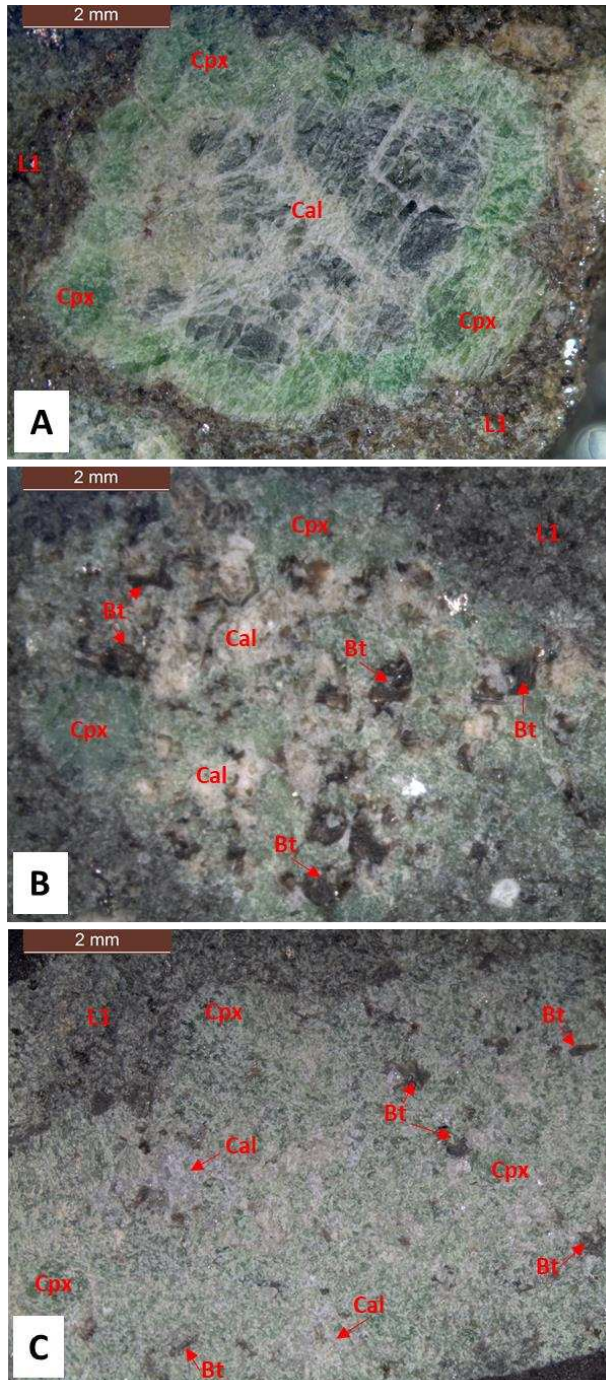


Figure 5.33. Representative cut slabs of lamprophyre samples containing ultramafic xenoliths. All samples are from lamprophyre 1 suite.

- A. Sample EM14 showing a clinopyroxenite xenolith with an altered core of calcite after clinopyroxene.
- B. Sample EM12. A biotite clinopyroxenite with coarse biotite and clinopyroxenite. Calcite has replaced some of the interior of this xenolith.
- C. Sample EM47. A fine-grained biotite clinopyroxenite with minor calcite alteration.

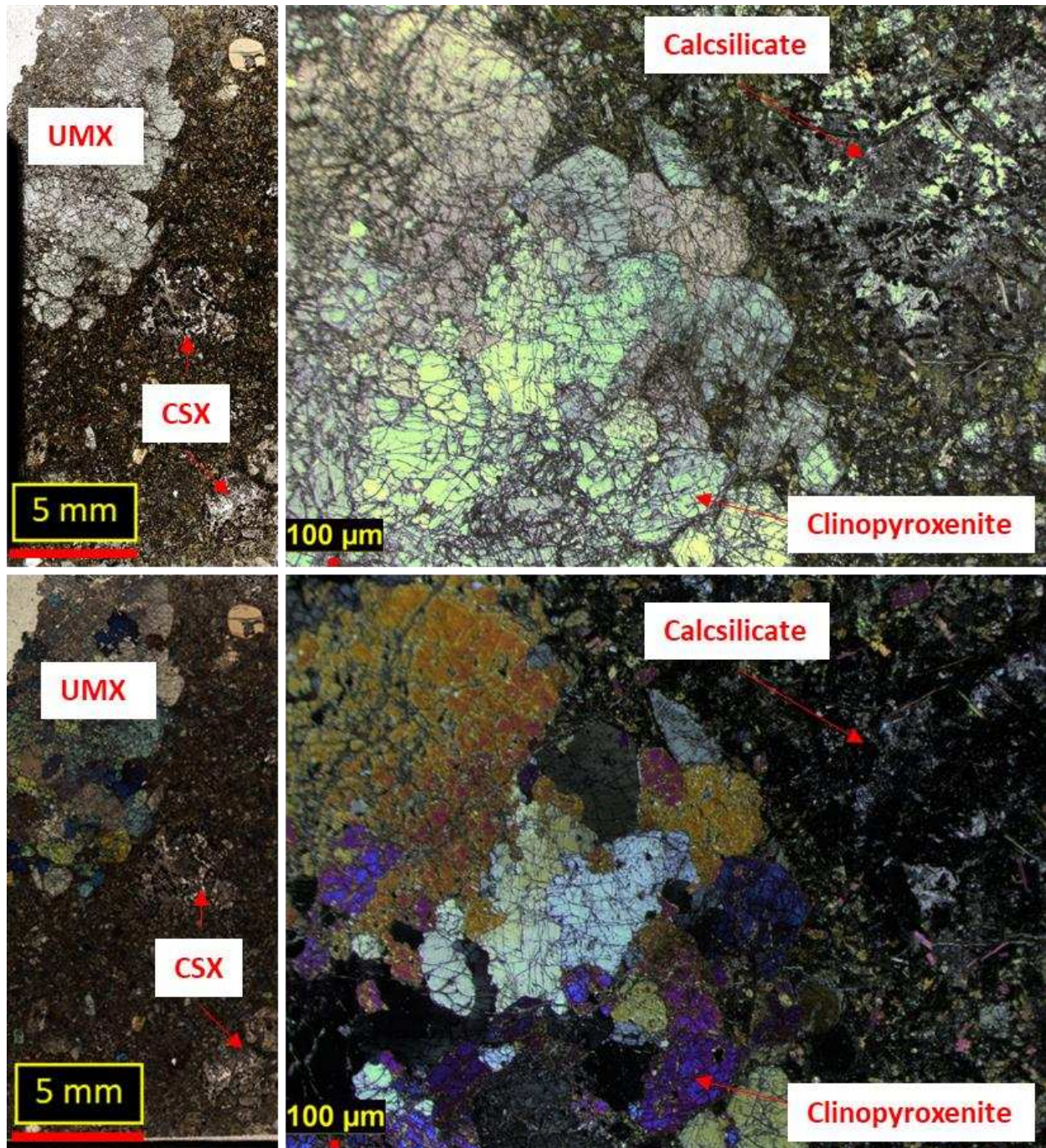


Figure 5.34. Images of representative clinopyroxenite in sample EM10b. The top and bottom left-hand images are scans of the petrographic thin section showing an ultramafic xenolith (UMX) and calcsilicate xenoliths (CSX). The top and bottom right-hand images show a clinopyroxenite as well as a calcsilicate of unknown origin composed of calcite, analcime, amphibole and feldspathoids.

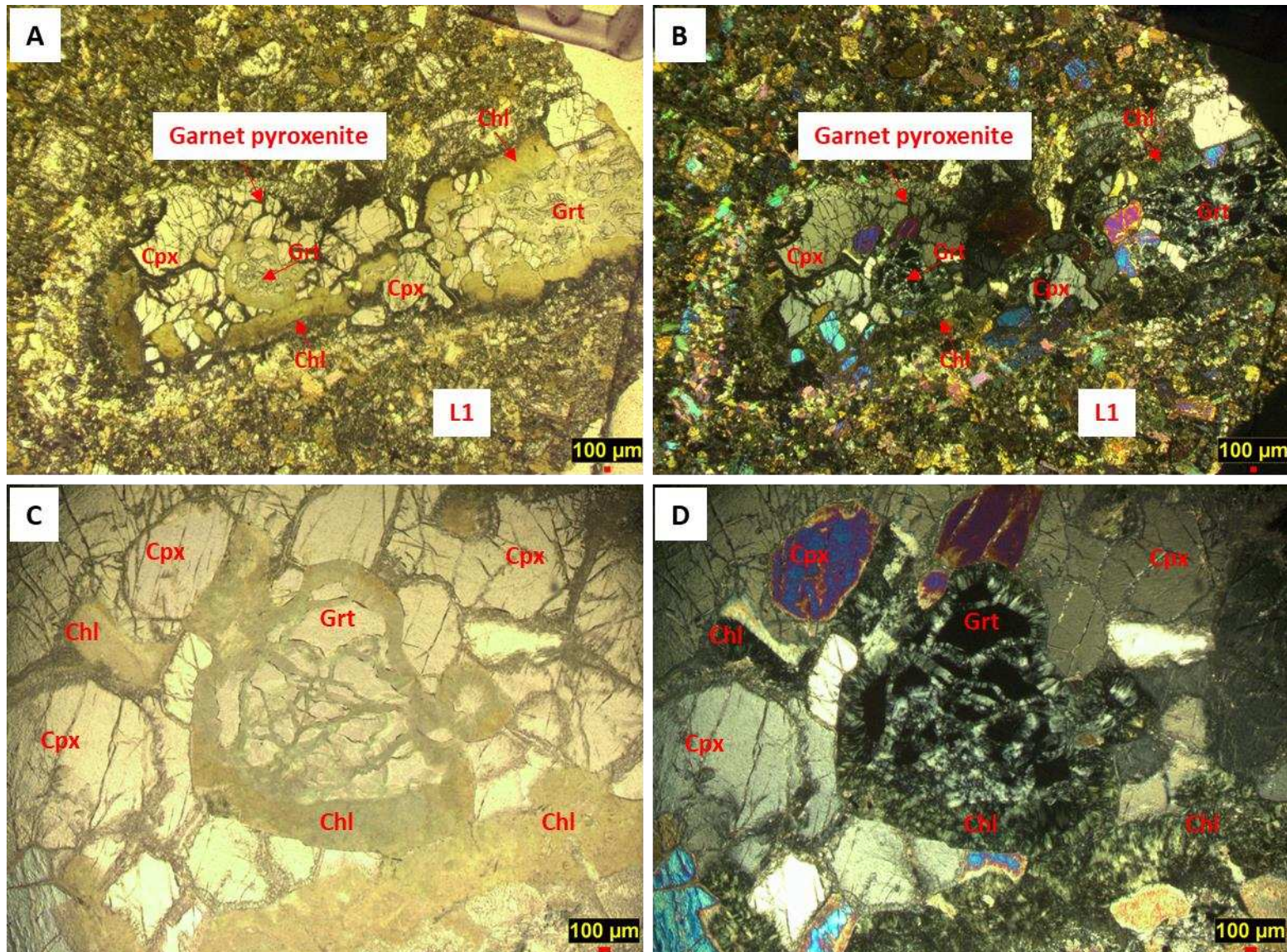


Figure 5.35. Photomicrograph of sample EM26b showing a garnet pyroxenite in thin sections. This sample is composed of clinopyroxene with minor garnet that has been largely replaced by chlorite. Lamprophyre 1 (L1) hosts this xenolith.

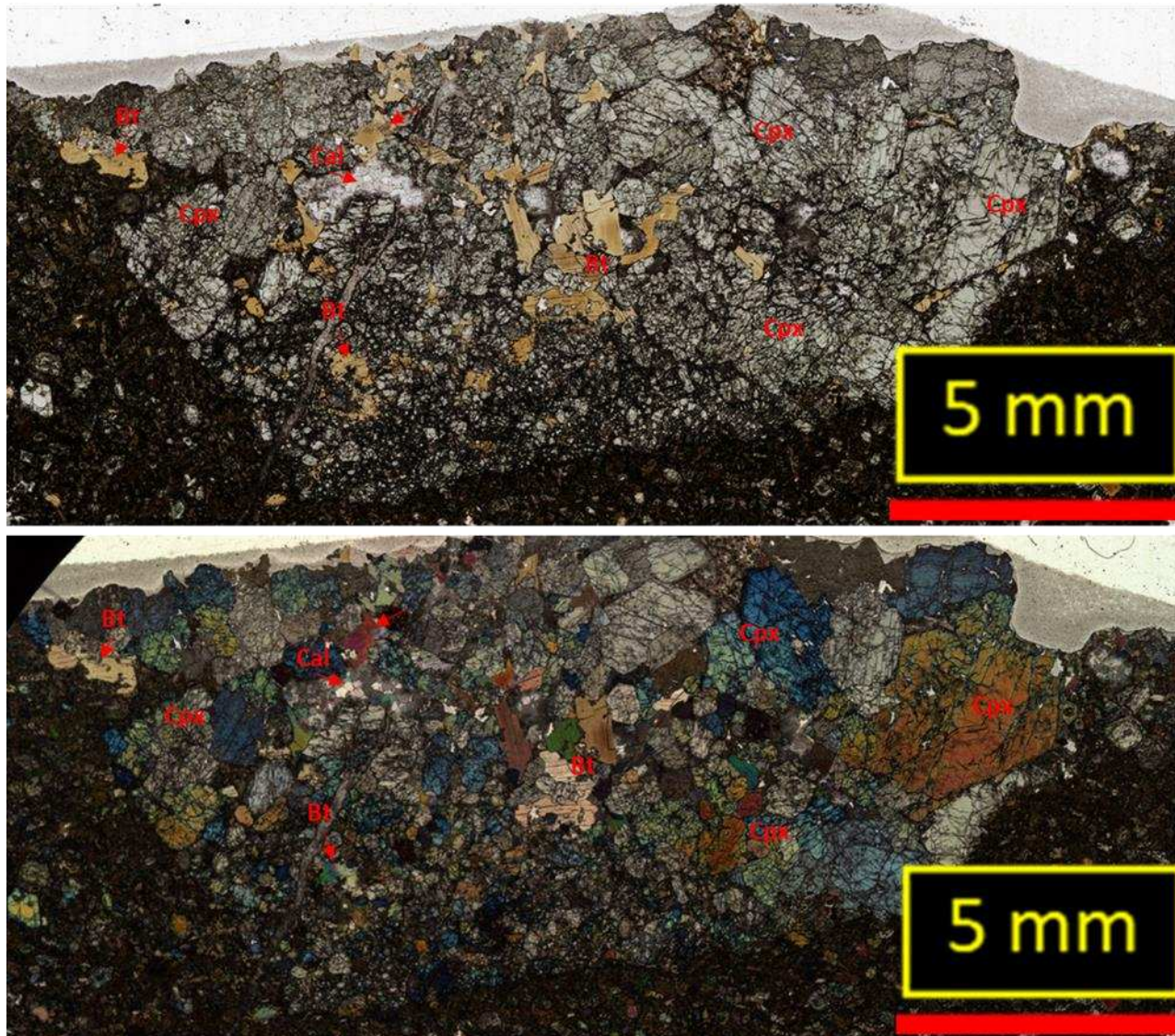


Figure 5.36. Scanned thin section EM31.26c showing a large biotite pyroxenite. Clinopyroxene is medium to coarse grained and euhedral while biotite anhedral and fine to medium grained. Some minor calcite alteration has occurred in the left-hand side of the xenolith.

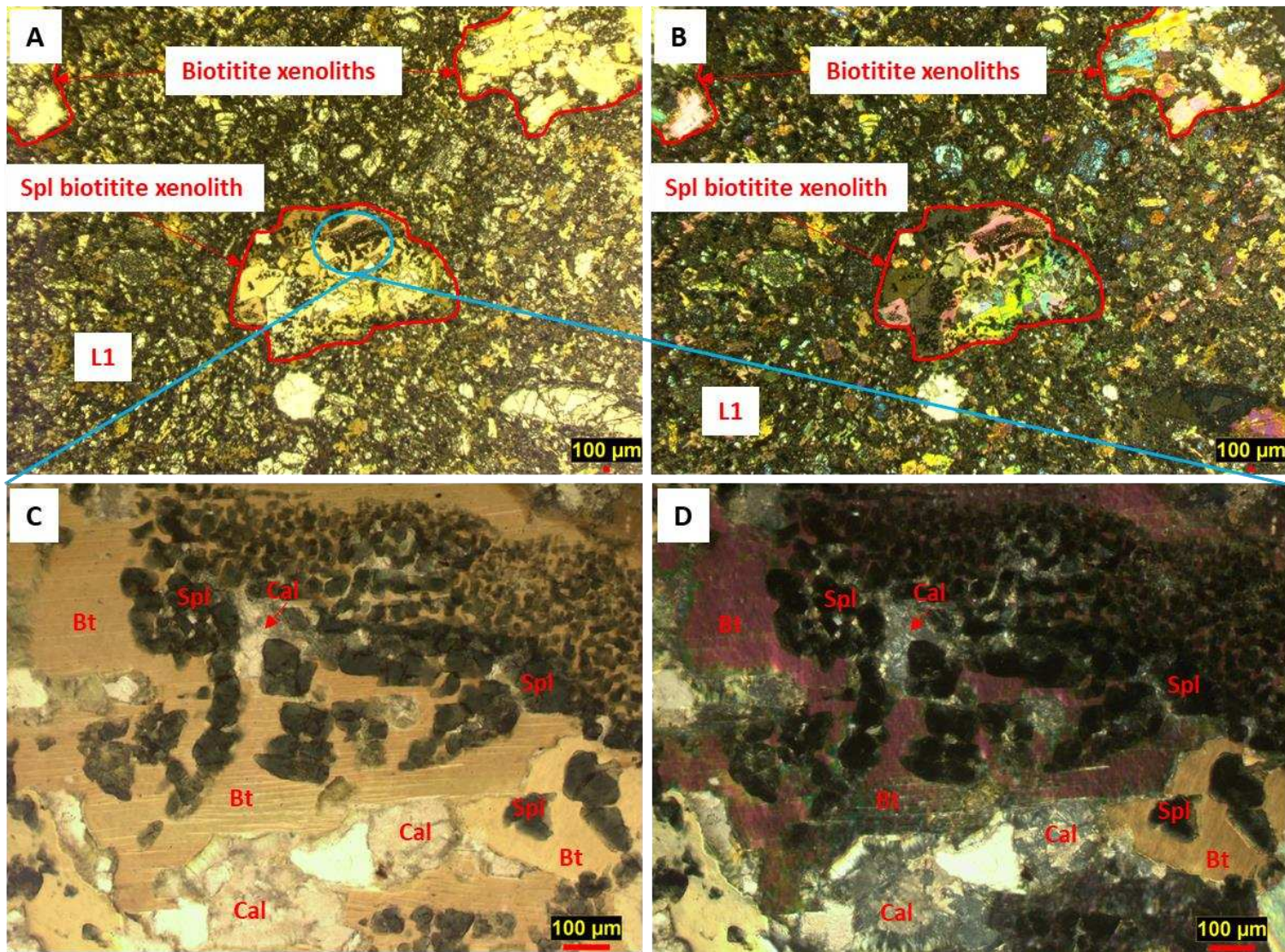


Figure 5.37. Representative biotite xenoliths in lamprophyre 1 (L1) thin section EM7c. In pictures A and B there are three separate xenoliths composed almost entirely of biotite with minor clinopyroxene and calcite alteration. Image C and D are zoomed in photomicrographs of a spinel biotite. Spinel is euhedral and dark blue and concentrated on biotite phenocrysts. There is minor calcite alteration in this xenolith.

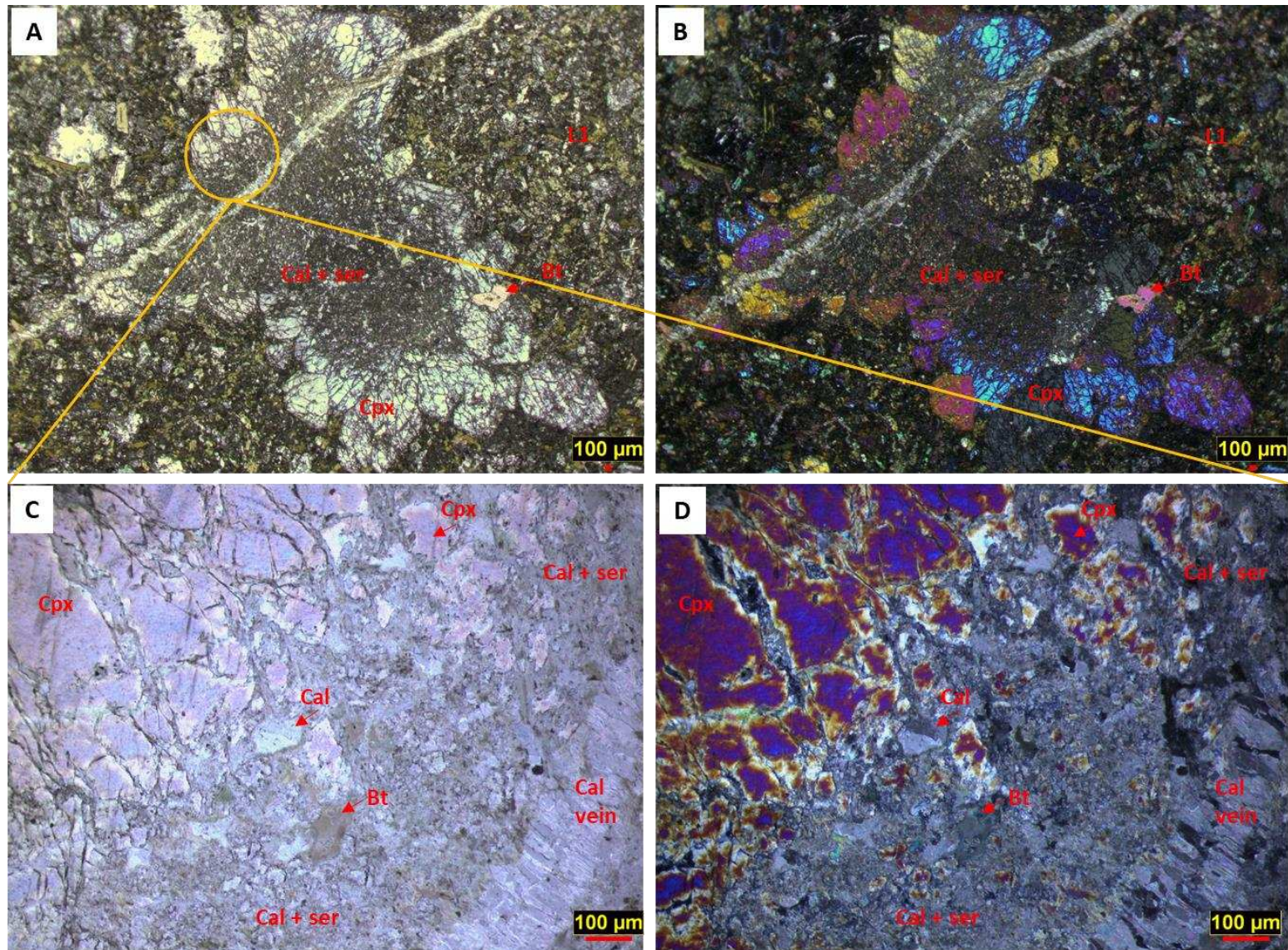


Figure 5.38. Altered ultramafic xenolith with a core that has been nearly completely replaced by calcite and presumably sericite and a margin of clinopyroxene with euhedral terminations into matrix. This photomicrograph was taken from lamprophyre 1 (L1) sample EM10a.

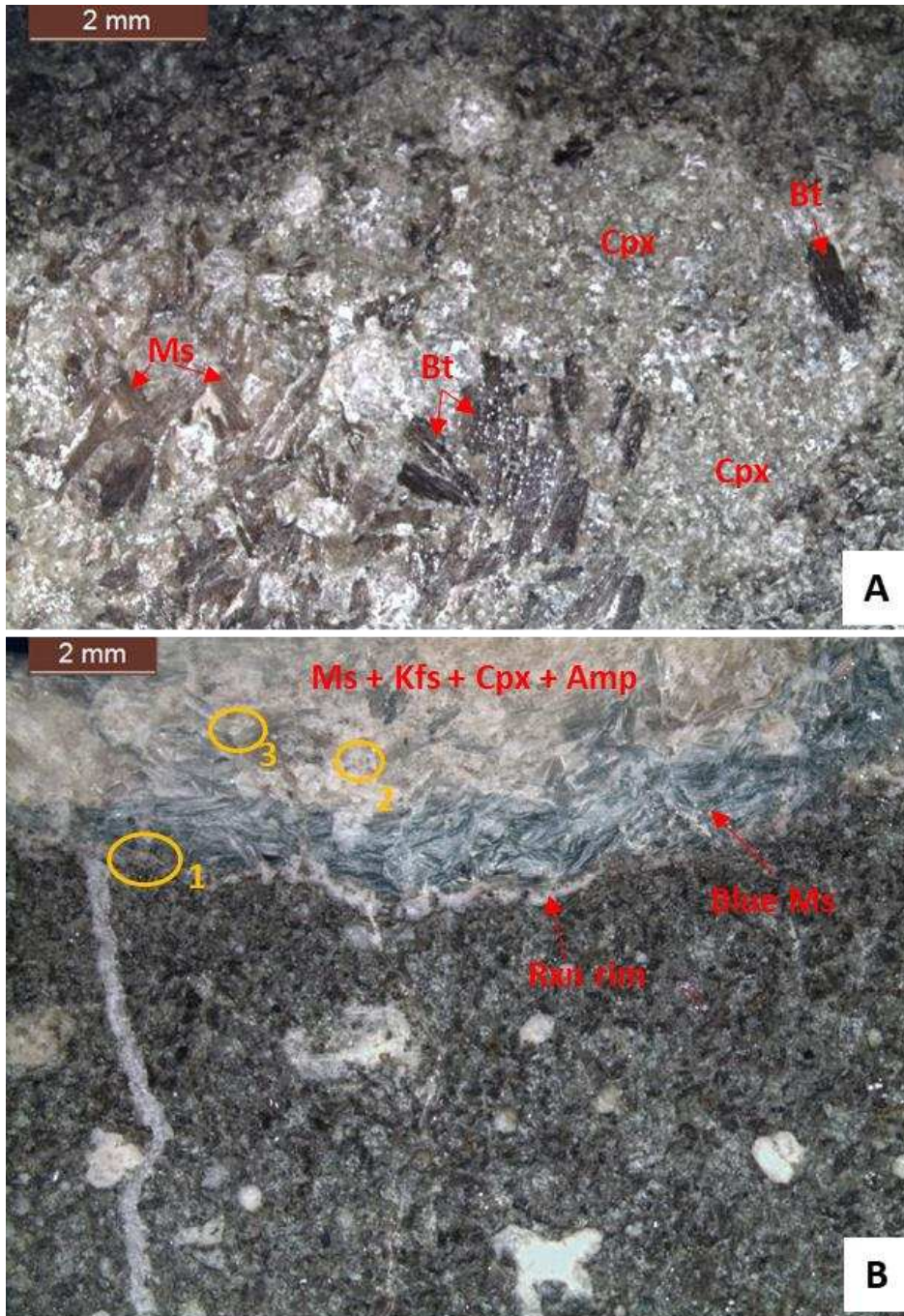


Figure 5.39. Cut slabs of lamprophyre 1 samples EM47b (A) and EM14b (B). A. Mafic xenolith with muscovite (Ms). Biotite (Bt) and clinopyroxene (Cpx) are present though clinopyroxene is altered. B. Zoned mafic xenolith with a core of muscovite, potassium feldspar, clinopyroxene, and amphibole (Amp), followed by a zone of blue muscovite, and finally a reaction rim of a fine intergrowth of calcite and other light-colored minerals. These zones are further explored in figure 5.40.

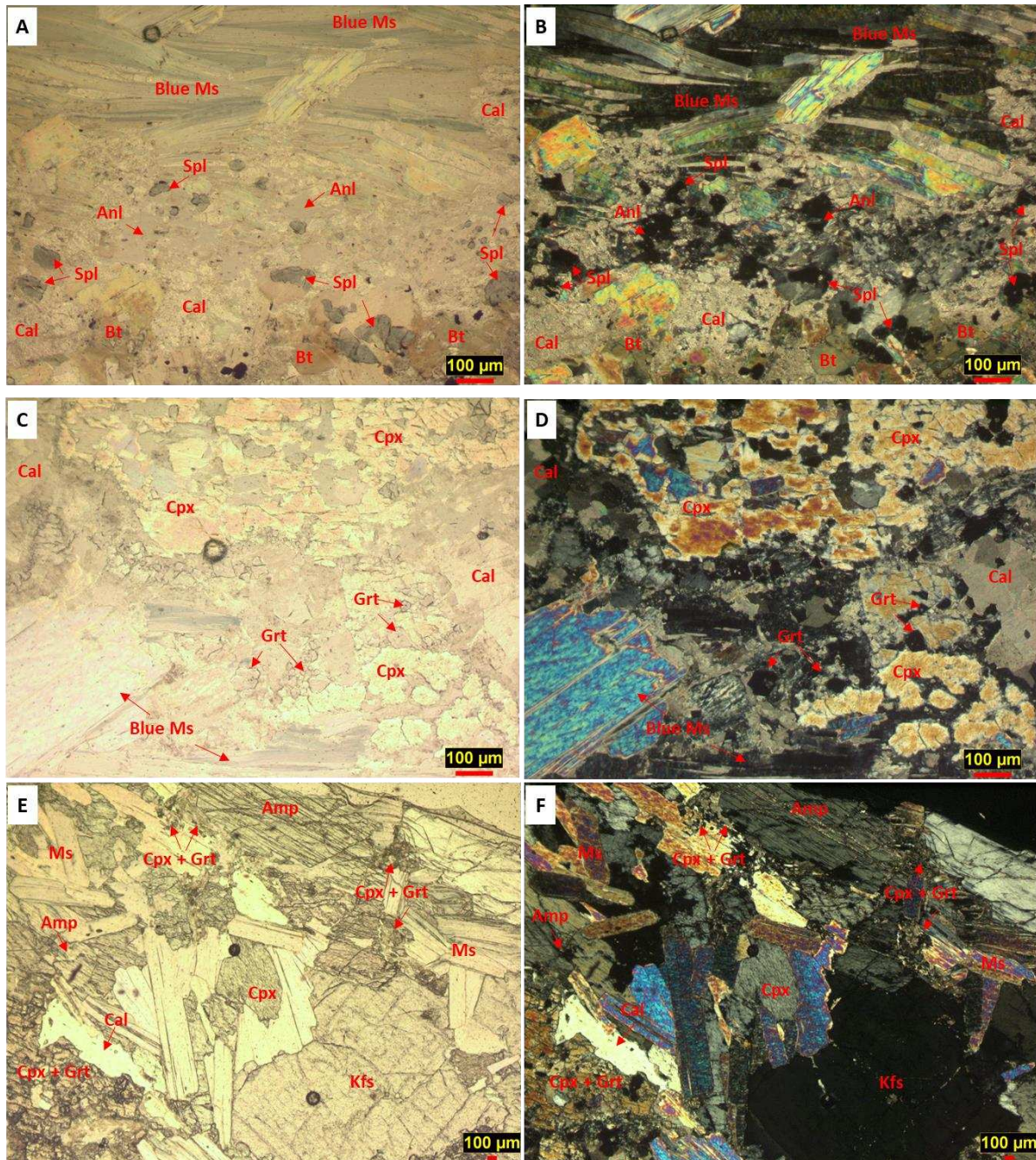


Figure 5.40. Photomicrographs of sample EM14b. Images A/B correspond to circle 1, C/D to circle 2 and E/F to circle 3 of figure 5.39. A/B show fine grained light blue spinel (Spl), calcite (Cal) and analcime (Anl) in the reaction rim of the mafic xenolith, biotite from the host lamprophyre is weakly intergrown with the reaction rim. C/D shows very fine garnet (Grt) intergrown with anhedral clinopyroxene (Cpx), calcite is present as alteration. E/F is of the least altered core of the xenolith showing potassium feldspar (Kfs) with muscovite (Ms) alteration, euhedral clinopyroxene as well as fine aggregates of clinopyroxene + garnet, and tremolitic amphibole (Amp).

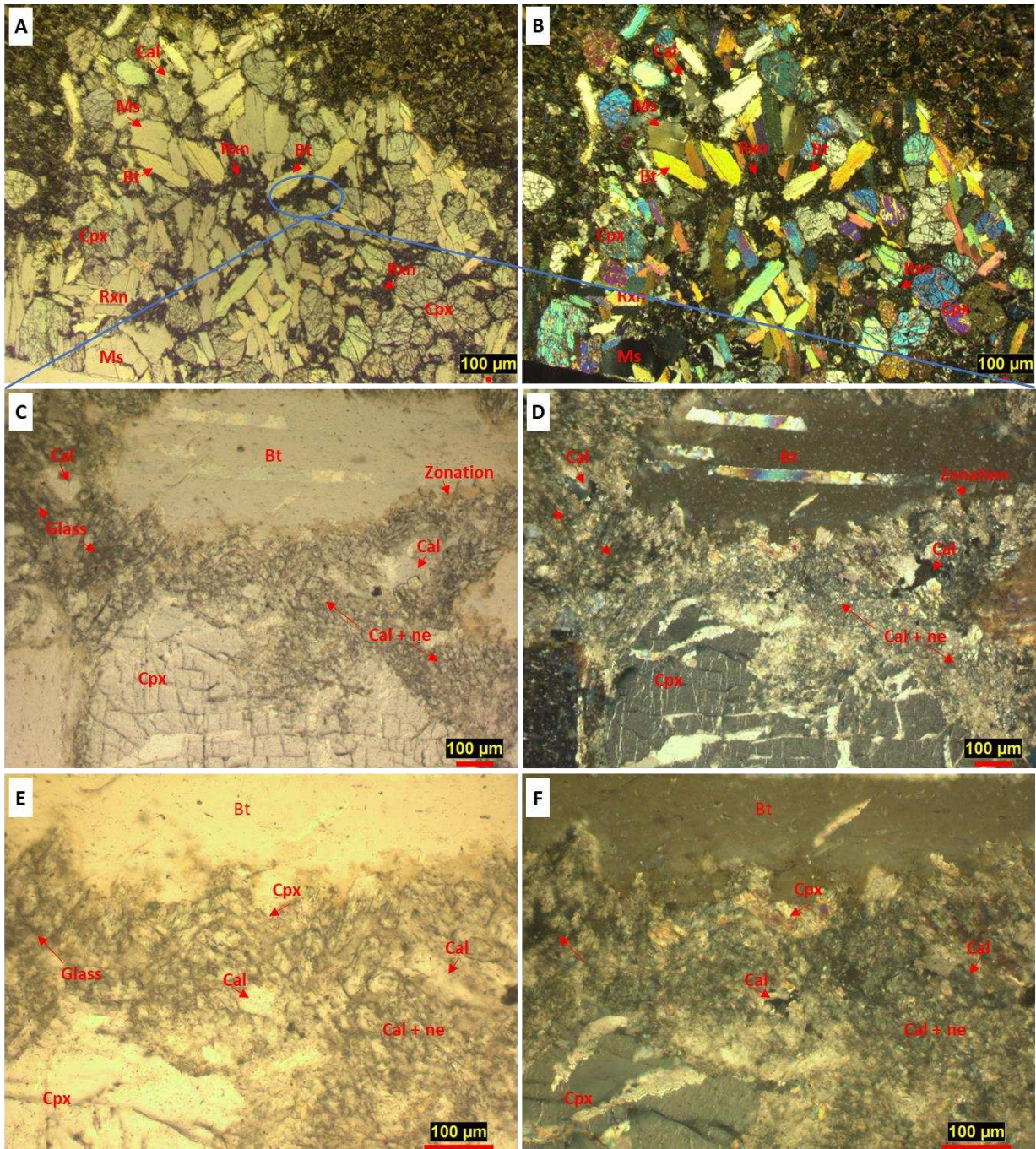


Figure 5.41. Sample EM47b. A and B mafic xenolith with clinopyroxene biotite and muscovite with a reaction rim around grains. C and D close-up of reaction zone, dusty isotropic material is glass. E and F show sparry calcite crystals, with a calcite in a nepheline series feldspathoid matrix with dusty isotropic patches of glass.

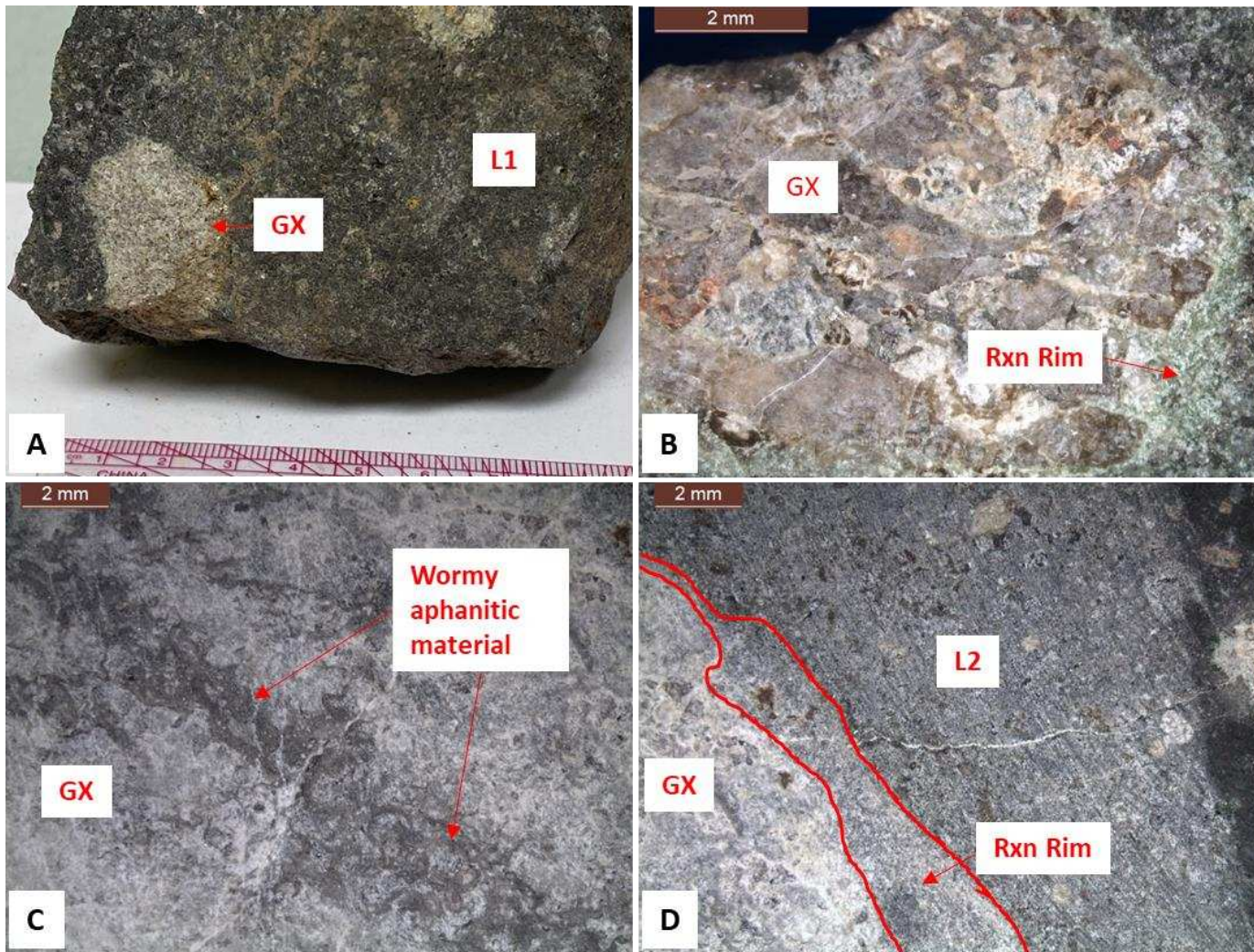


Figure 5.42. A. Lamprophyre 1 (L1) hand sample EM40 showing a granite xenolith (GX) composed of quartz with potassium feldspar and muscovite, B. Cut slab of lamprophyre sample EM12a showing a granite xenolith composed of largely potassium feldspar and quartz with a reaction (Rxn) rim composed of an intergrowth of fine clinopyroxene, calcite and other light-colored minerals. C. cut slab of lamprophyre 2 sample EMOct showing the core of a granitic xenolith with a weak fabric defined by an aphanitic grey, wormy, material. D. Cut slab of EMOct showing the margin of the granite xenolith described in C, with a diffuse reaction rim of fine light-colored minerals.

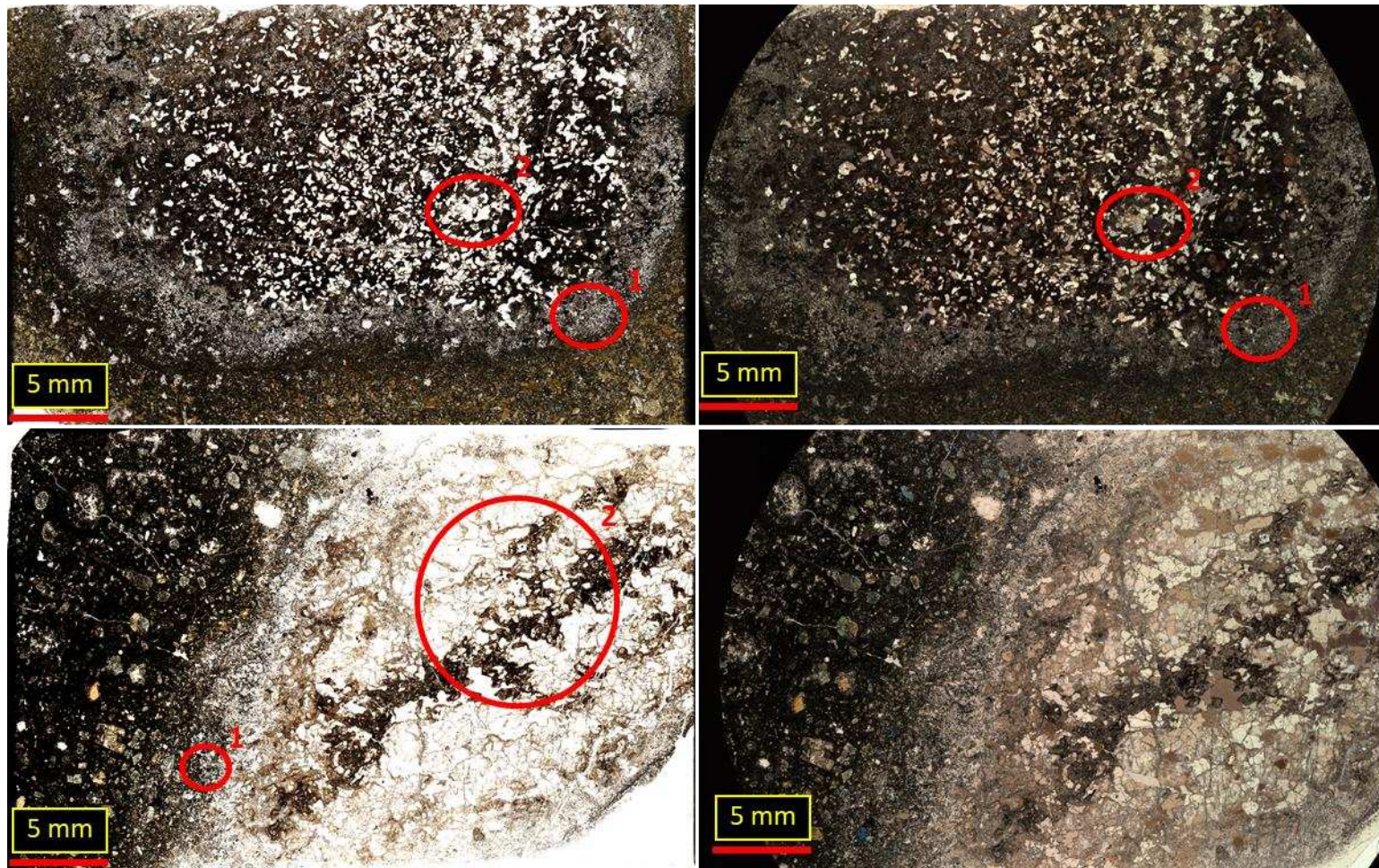


Figure 5.43. A/B. Scans of petrographic thin section EM3b, showing a granite xenolith with a reaction rim of relative constant thickness. The granite xenolith has a spongy texture of dark, aphanitic material that encapsulates the light-colored minerals. C/D. Scans of petrographic thin section EMOctc, showing a granite xenolith with a reaction rim of varying thickness, the top being the thinnest and thickening toward the bottom of the slide. This granite has a zone of spongy texture dark, aphanitic material through its center. Circled areas in these images correspond with the following photomicrographs.

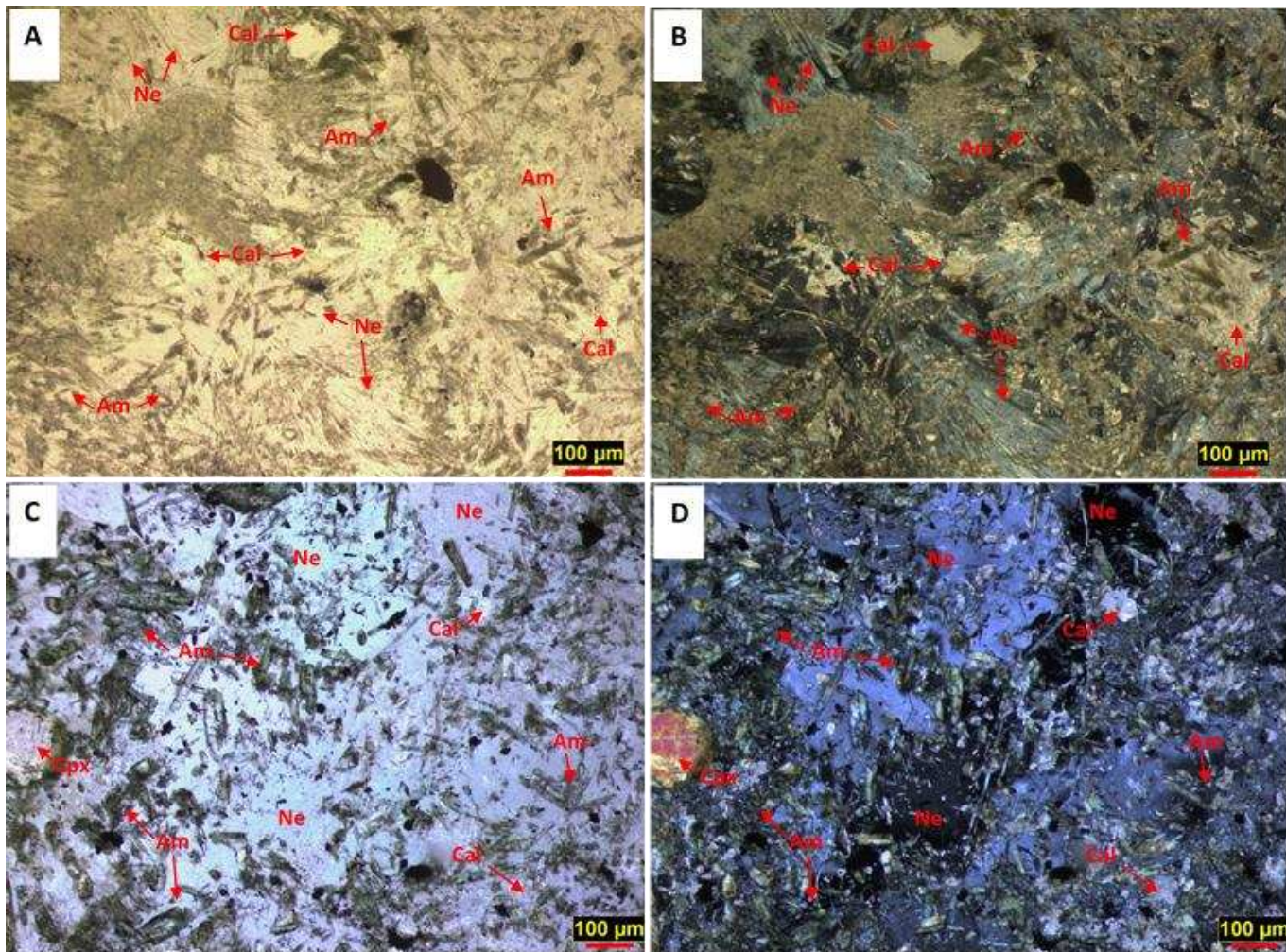


Figure 5.44. A/B. Photomicrographs of the reaction rim (circle 1) of the granitic xenolith in sample EM3b (Fig. 5.43). The amphibole needles in this sample have been largely pseudomorphed by calcite, the remaining mineralogy of reaction rim is dominated by fibrous nepheline series feldspathoids and crystalline calcite. C/D. Photomicrographs of the reaction rim (circle 1) of the granitic xenolith in sample EMOctc. Amphiboles in this sample are as fresh, euhedral needles and rosettes, nepheline series feldspathoids and minor calcite make up the ground mass of the reaction rim. There is one euhedral clinopyroxene which is situated nearest the lamprophyre on the left-hand side of the phenocryst, not included in this image.

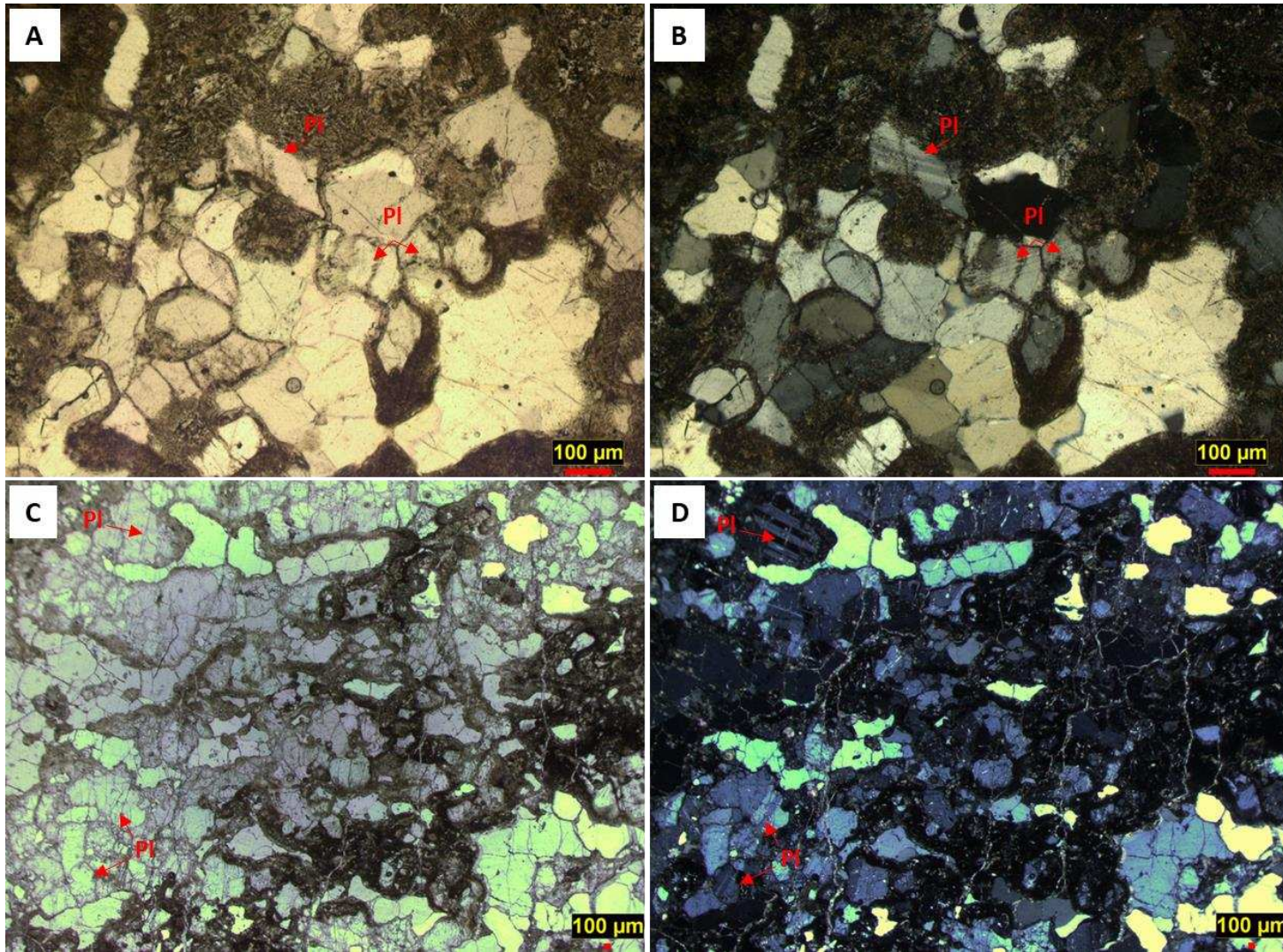


Figure 5.45. A/B. Photomicrographs of the granite xenolith in sample EM3b (Fig. 5.43, circle 2). Irregular shaped quartz and plagioclase are surrounded by spongy isotropic material which is presumably glass after melt. C/D. Photomicrographs of the granite xenolith in sample EMOctc (circle 2). Preferential orientation of glass after melt going from the southwest to the northeast corner of the slide. Quartz has a weak fabric of the same orientation suggesting this may have been a granitic gneiss as opposed to a granite.

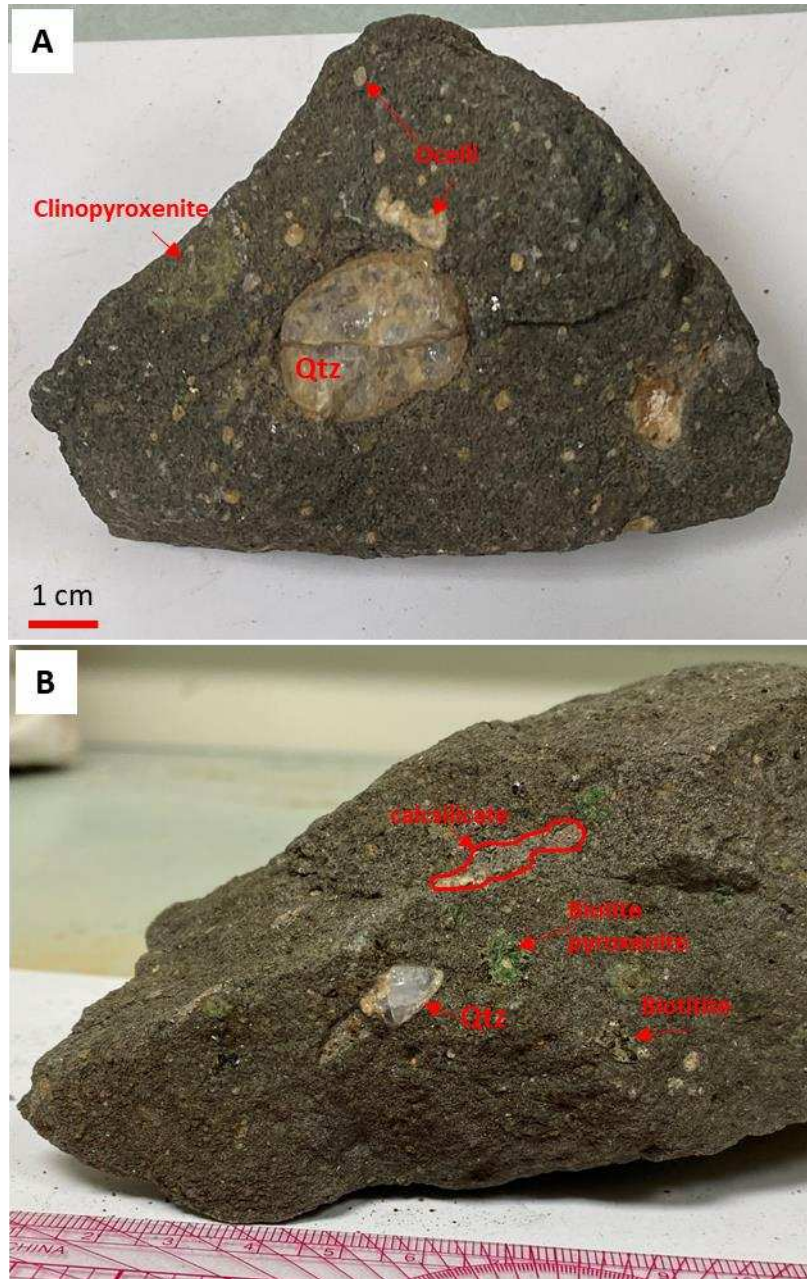


Figure 5.46. A. Rounded quartz xenolith in hand sample EM17 with a reaction rim of a fine intergrowth of light-colored minerals. B. Angular quartz xenolith in hand sample EM47 with a large reaction rim on the southeast end of the xenolith composed of a mixture of fine light-colored minerals. In both images' xenoliths of different types and ocelli are marked.

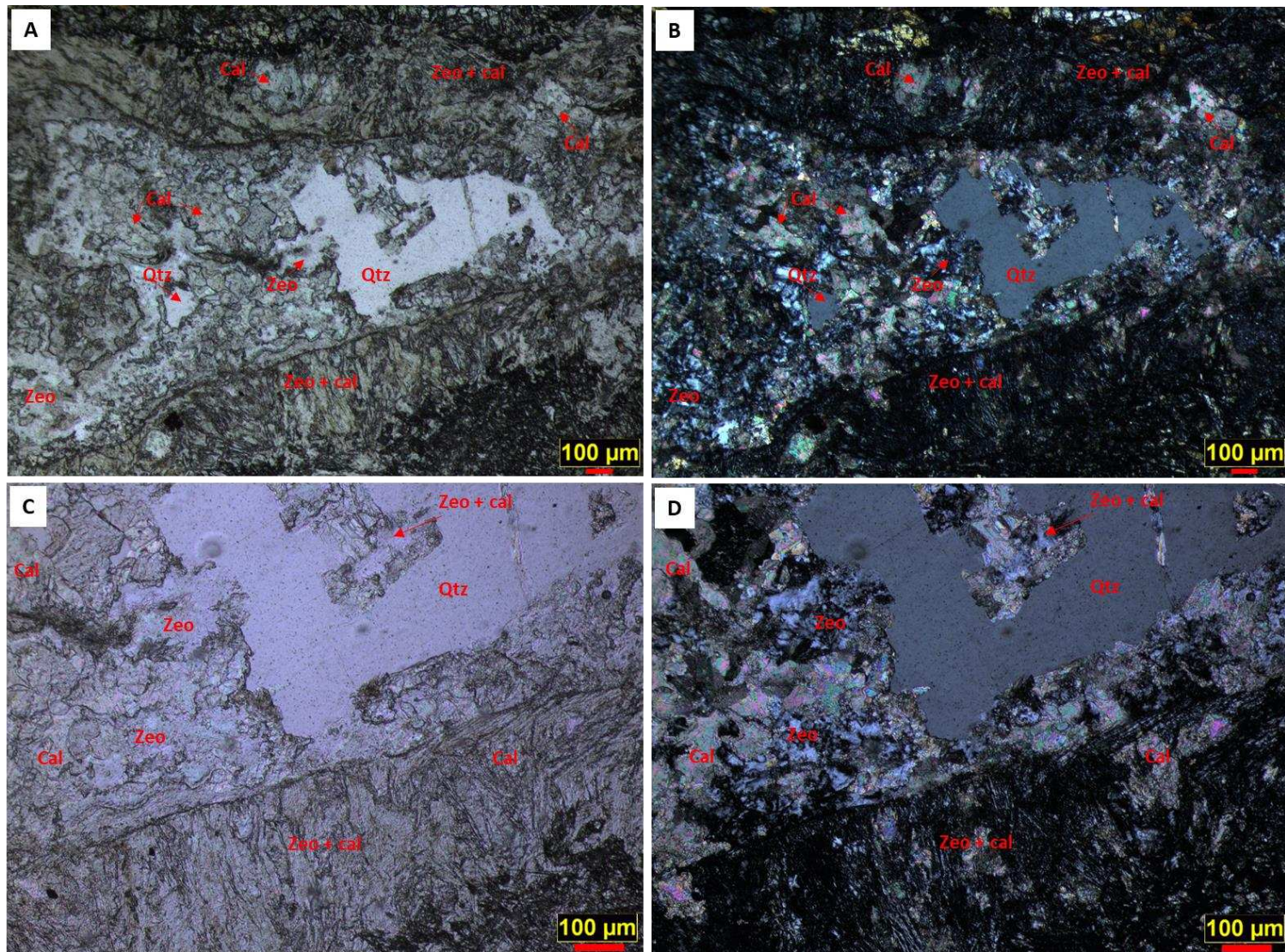


Figure 5.47. Photomicrographs of a zoned quartz xenolith in sample EM10b. Quartz in the inner zone of the xenolith has been largely replaced by zeolites and calcite, leaving behind an ameboid crystal of quartz. The outer zone is composed of mainly of fine zeolites (Zeo) with minor calcite (Cal). Zeolites have a fibrous texture and appear to have grown perpendicular to the margin of the xenolith.

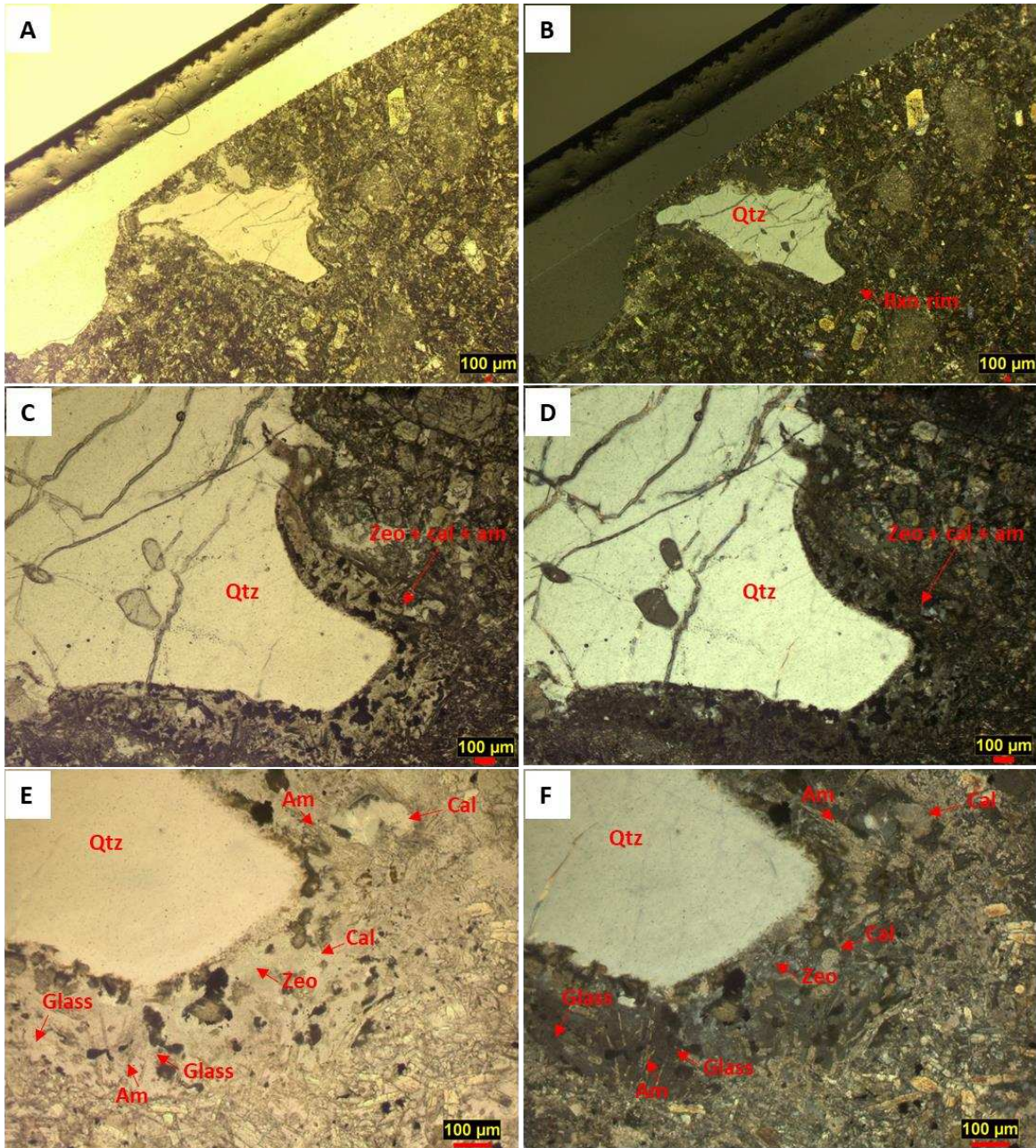


Figure 5.48. Photomicrograph of an irregular shaped quartz xenolith in sample VM6b. The reaction rim of this xenolith has zeolites with fine needles of amphibole that has been replaced by calcite. There are also isotropic areas that may be glass after melt.

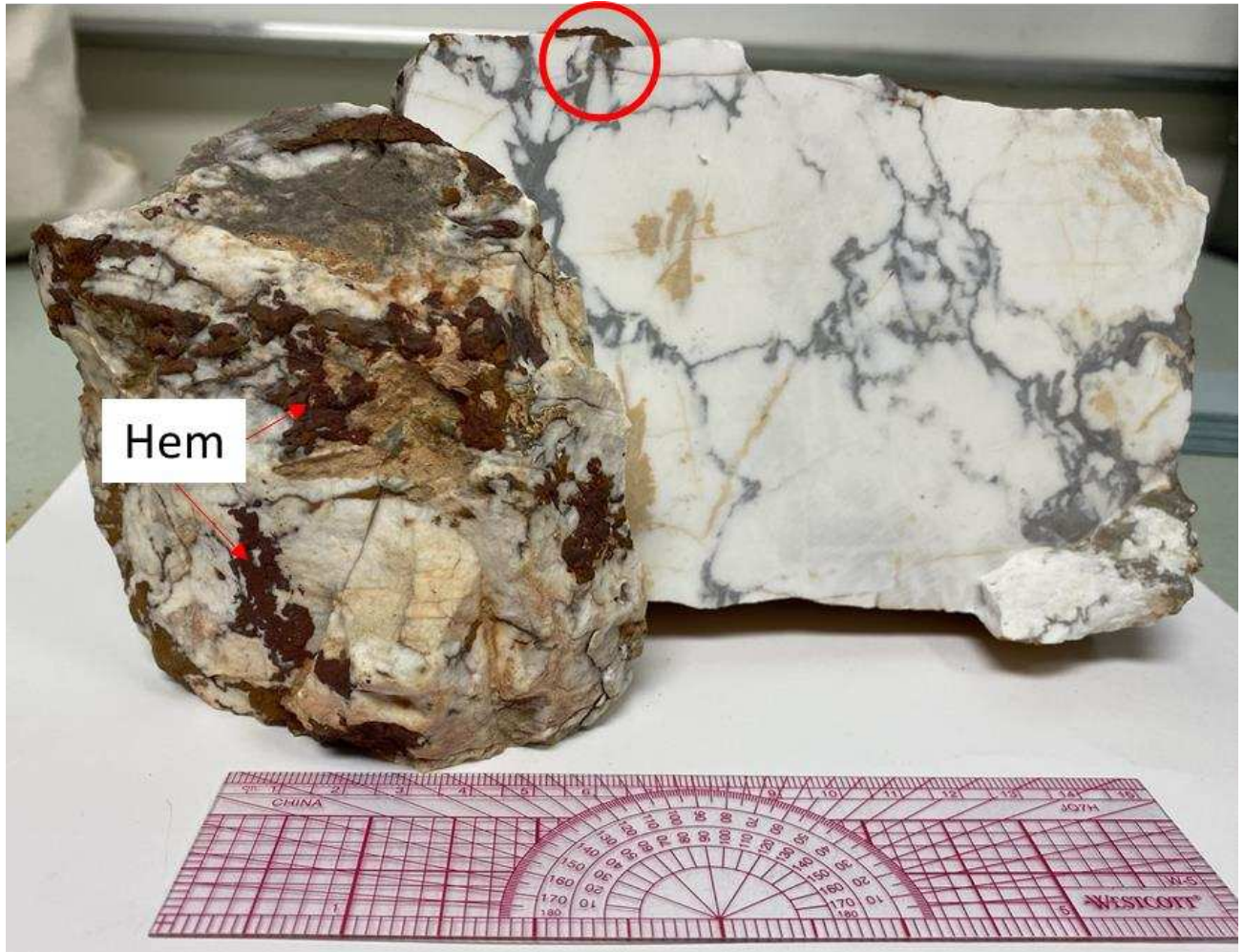


Figure 5.49. Hand sample Q3 from the western end of the Middle Mine cut. The outside of the sample is white to tan to grey with veinlike seams of hematite. The fresh inside of the sample shows a vaguely stylolite like texture of grey carbonate silt that grades into the hematite rich seams viewed on the weathered surface of the rock (circled). Tan patches of calcite tend to be coarser grained and appear to be in center of white carbonate.



Figure 5.50. Top. Polished section of sample Q4 showing the tan coarser calcite with two small vugs. Bottom. Polished section of sample Q4 fine grey carbonate with white granoblastic calcite.



Figure 5.51. Hand sample Q2 showing the overall appearance of the organic rich xenolith. The outside is black with some minor brecciation of red to yellow carbonate rich clasts. Bedding is alternating bands of black and grey, a variation in the amount of organic material in the differing layers. On the lower left-hand side of the xenolith the bedding has been folded but original orientation is unknown.



Figure 5.52. Polished section of sample Q2 showing a close up of the brecciated area in the sample. Tan clasts are silty limestone and the pink to peach clasts are carbonate siltstones with hematite cementing. Calcite dominates as the matrix in the upper section but less so in the bottom organic rich zone.

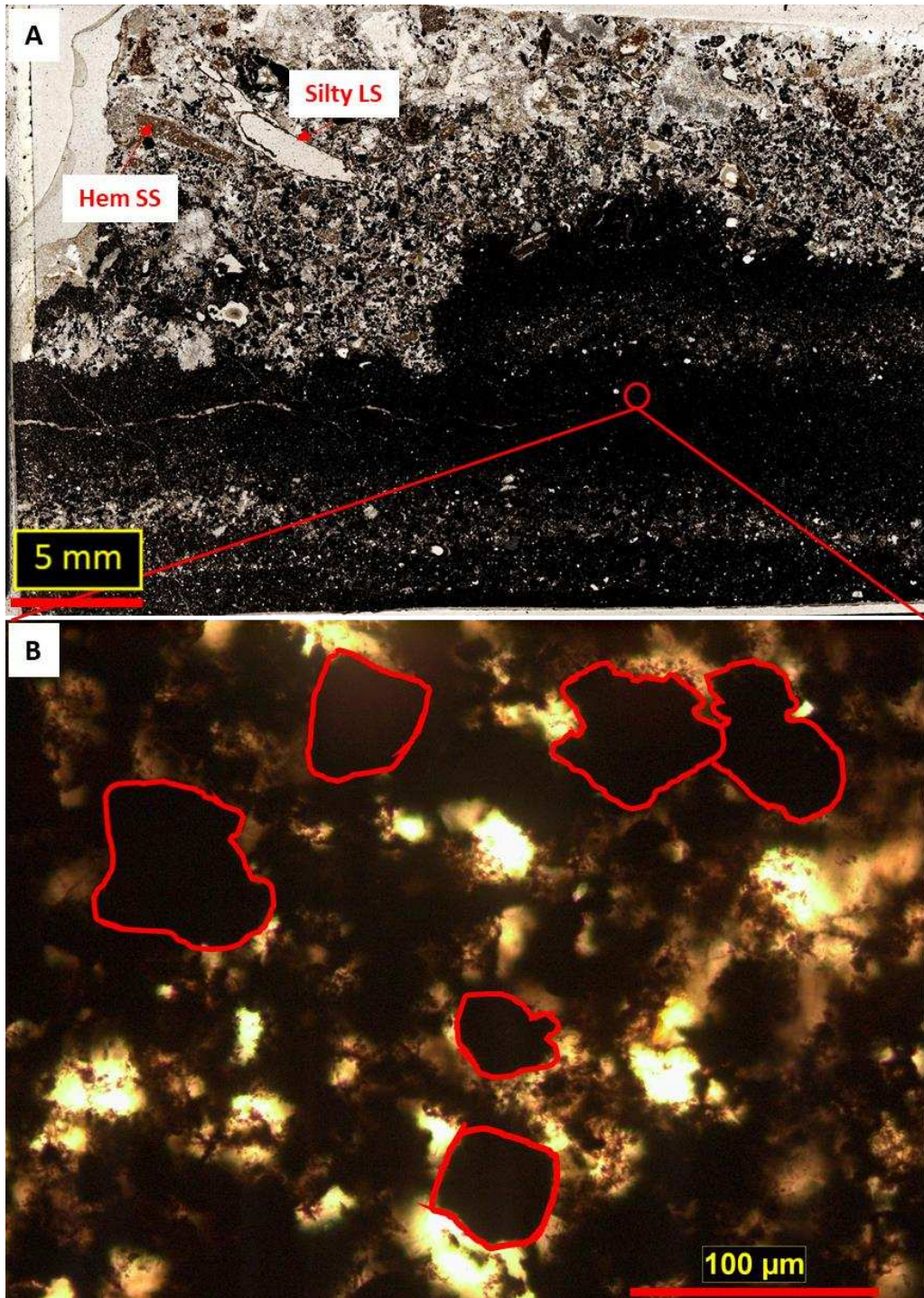


Figure 5.53. A. Scan of petrographic thin section for reference to microphotograph B. B. Shows crystallization of an oxide in the organic rich material.

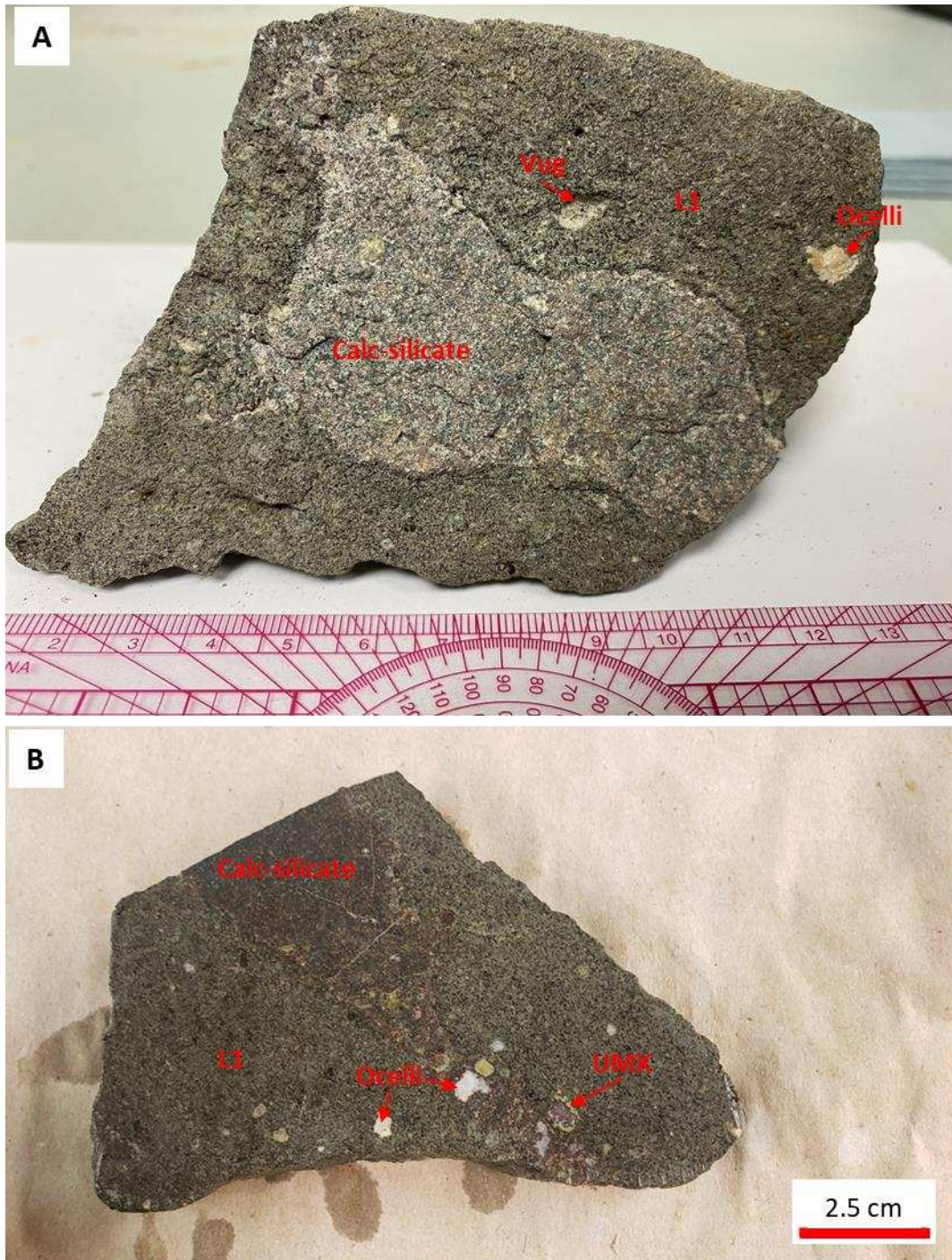


Figure 5.54. Irregular shaped calc-silicate xenolith of unknown origin from lamprophyre 1 (L1) sample EM15. The stretched-out appearance of this xenolith may suggest it was partially molten when it was included into the lamprophyre. There is not an obvious reaction rim around this xenolith. In image B there is an ultramafic xenolith (UMX) comprised mainly of clinopyroxene.

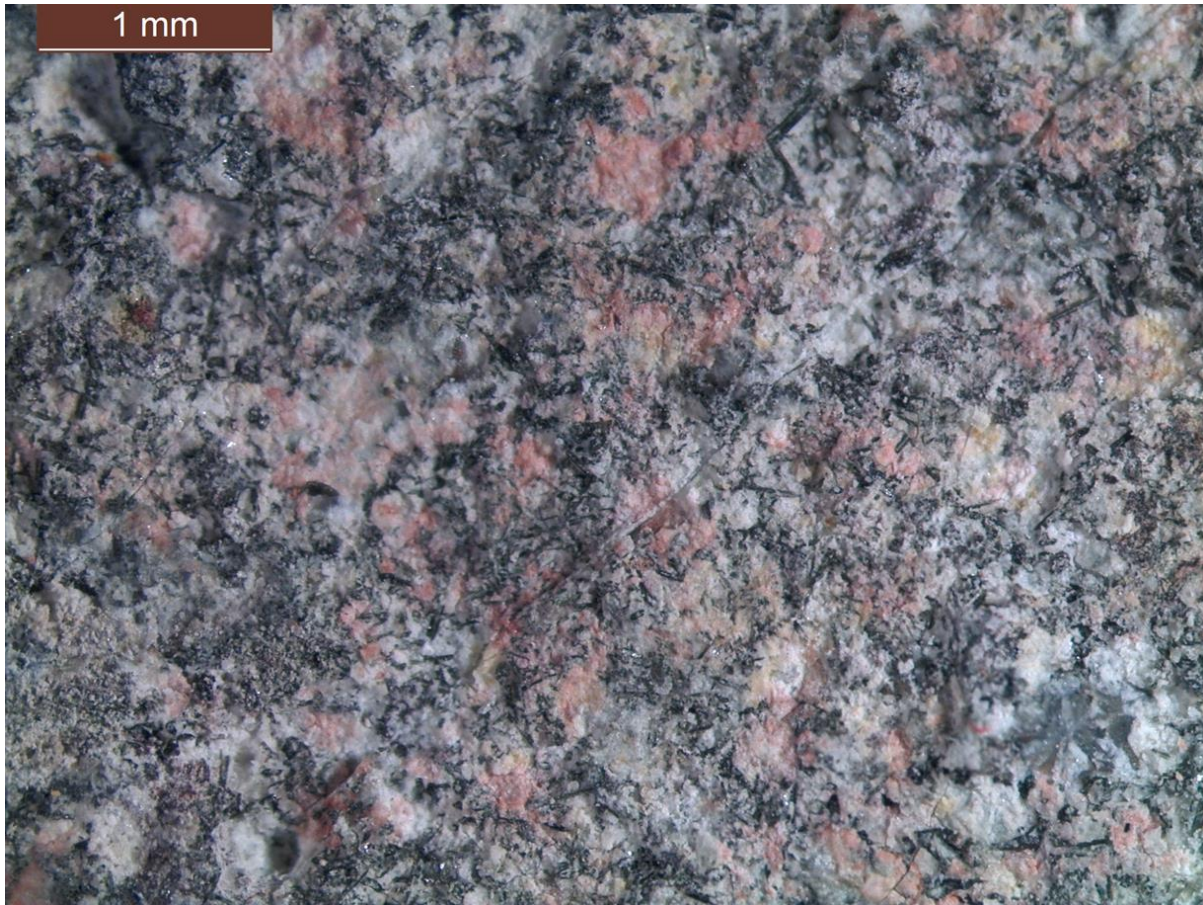


Figure 5.55. Close up photograph of the calc-silicate xenolith from sample EM15. The peach-colored minerals are presumed to be a feldspathoid while the white areas are a mixture of fine calcite and another light-colored mineral, the black needle like crystals are amphibole.

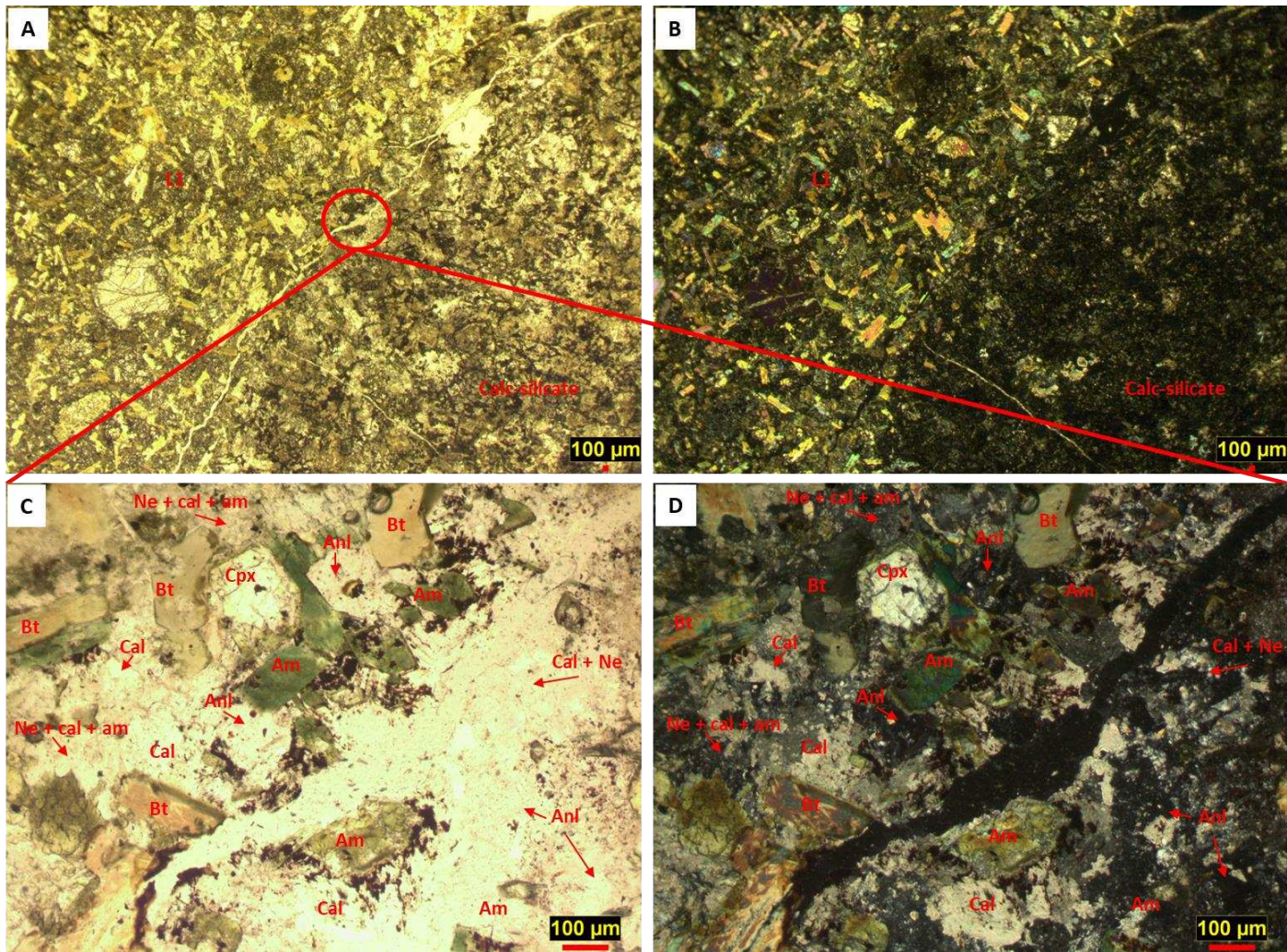


Figure 5.56. Photomicrographs of calc-silicate xenolith in sample EM15. A/B show the lack of interaction between the xenolith with lamprophyre 1 (L1). C/D. Show a close-up of the boundary between the lamprophyre and the xenolith. There is a fracture between the two but no obvious signs of interaction besides some amphibole crystallization on the margin of the lamprophyre.

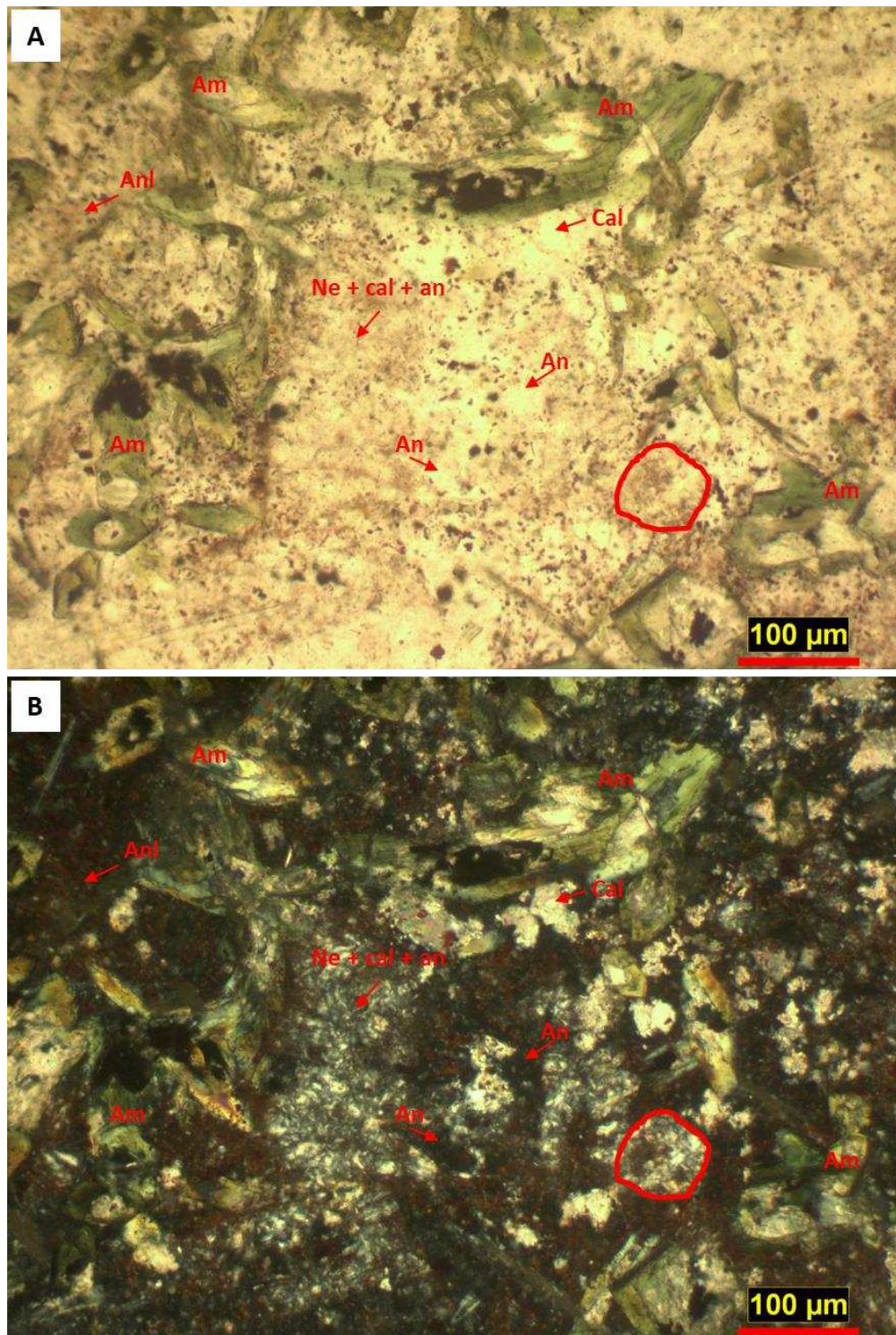


Figure 5.57. Photomicrograph of the interior of the calc-silicate xenolith from sample EM15. The area has a moderate concentration of dusty red opaques, fresh amphiboles, calcite, and patches of nepheline series feldspathoids with calcite and possible analcime. There is a replaced phenocryst (circled) by the same mixture. Analcime makes up isotropic areas within this xenolith. The fine dusting of red opaques may have been the result of iron released during feldspathoid alteration similar to the same reaction seen in potassium feldspar.

Chapter VI. Geochemistry

This section describes the geochemistry of eight fresh lamprophyre samples, eight weathered lamprophyre samples and two minette samples (Tables 6.1a and 6.1b). They have been divided into two sapphire-bearing lamprophyre groups, Lamprophyre 1, and Lamprophyre 2 respectfully, and a separate group for the two minette samples. These groups correspond with Lamprophyres 1 and 2 in chapter V. Classification diagrams are discussed first, followed by lamprophyre discrimination plots from Rock (1991), plots investigating mineralogical controls on composition, and portable X-ray Fluorescence (pXRF) data on xenoliths and ocelli. Geochemistry from previous work at Yogo by Dahy (1988) and Gauthier (1995) as well as on samples from around the Central Montana Alkalic Province are compared to geochemistry from this project in the following section on classification.

Classification diagrams

Total Alkali Silicate (TAS)

Geochemical data of the eight fresh samples of lamprophyre and two minette samples procured during this research as well as one sample from Dahy (1988) and six samples from Gauthier (1995) are compared to other samples from the Central Montana Alkalic Province on a Total Alkali Silicate plot (Fig. 6.1). All lamprophyre from Yogo samples plot in an undefined field and are low in SiO_2 but with moderate $\text{Na}_2\text{O} + \text{K}_2\text{O}$ which supports earlier assumptions that the samples are dominated by feldspathoids in the ground mass.

The minettes plot in the trachyandesite field and upon further comparison can be confirmed as such by subtracting 2.0 from the Na_2O concentration and comparing that to the K_2O concentration. According to the TAS plot there is no relationship between the minettes and

lamprophyres at Yogo, nor is there a similarity between the samples from the Central Montana Alkalic Province and Yogo lamprophyres. One outlier from the Golden Sunlight samples plots within the cluster of samples from Yogo but further discrimination with additional parameters is needed.

Discrimination of lamprophyre types using major and trace element geochemistry plots

Lamprophyres from Yogo are different from other Central Montana Alkalic Province rocks in that they have the lowest silica content and thus need further investigation to examine relationships. Classification of Yogo lamprophyres was determined using diagrams to differentiate alkaline lamprophyres (AL), calc-alkaline lamprophyres (CAL), ultramafic lamprophyres (UML), kimberlites (KIL), and lamproites (LL) from Rock (1991) as a guide. Note that these classifications are based on petrogenetic relationships of lamprophyres and not composition. For instance, while all lamprophyres are alkaline, if they plot in the calc-alkaline field they are associated with calc-alkaline rocks and thus classified as calc-alkaline lamprophyres. There are two plots using major element chemistry and one plot using rare earth elements (REE) to classify samples from Yogo. It is expected that Yogo will plot as alkaline because it is clearly associated with other alkaline igneous rocks. The plots shown here are based on what trace element values were analyzed.

Discrimination plots MgO vs CaO and $\text{Fe}_2\text{O}_3/\text{Al}_2\text{O}_3$ vs $\text{K}_2\text{O}/\text{Al}_2\text{O}_3$ show both Lamprophyre 1 and Lamprophyre 2 samples and samples provided by Clabaugh (1952), Dahy (1988) and Gauthier (1995) plot as broadly alkaline but close to and overlapping the ultramafic field (Figs. 6.2 and 6.3). While plots MgO vs CaO and $\text{Fe}_2\text{O}_3/\text{Al}_2\text{O}_3$ vs $\text{K}_2\text{O}/\text{Al}_2\text{O}_3$ show a broad alkaline to ultramafic composition, Sm vs Ce/Yb does not classify lamprophyres in the same way. Lamprophyre samples from Yogo plot in the unnamed field between calc-alkaline,

kimberlite, and lamproite compositions with no overlap as alkaline or ultramafic lamprophyre (Fig. 6.4).

Rock (1991) showed that most minettes plot as broadly calc-alkaline on various x,y plots and discrimination plots and such is the case in plots MgO vs CaO, and Sm vs Ce/Yb (Figs. 6.2 and 6.4). He also showed that calc-alkaline lamprophyres plot within and around the trachyandesite field, supporting the above chemical classification of the minettes (Fig. 6.1). Surprisingly, the minette samples plot near the alkaline and ultramafic boundary on the $\text{Fe}_2\text{O}_3/\text{Al}_2\text{O}_3$ vs $\text{K}_2\text{O}/\text{Al}_2\text{O}_3$ plot, as opposed to the CAL field in the previous plot (Fig. 6.3).

The spider diagram of incompatible elements in samples collected at Yogo confirm that the minettes in the study area are not petrogenetically related to the lamprophyre dike (Fig. 6.5). While there is some geochemical variability among the lamprophyre samples from Yogo, the spider diagram suggests they are from the same source. A comparative spider diagram of the minimum and maximum values of incompatible elements at Yogo versus samples from around the Central Montana Alkalic Province show similarity with both Crazy Mountains and Highwood and lamprophyres at Yogo (Fig. 6.6). Though there are some similarities, overall, the samples from the rest of the CMAP came from a different mantle source.

Different phases of lamprophyres

Fresh lamprophyres

Major element and trace element geochemistry shows evidence of two separate magmas in the Yogo Dike and possible fractionation and/or mixing between the two. The following section describes the subtle but consistent geochemical differences between Lamprophyres 1 and 2 and distinct geochemical differences in the minettes.

Major element chemistry has shown that Lamprophyre 2 is enriched in FeO and slightly depleted in Al₂O₃ relative to lamprophyre 1 (Fig. 6.7). Silica has a subtle offset in trend between Lamprophyres 1 and 2 that is clearly seen on the SiO₂ vs Al₂O₃ plot, showing that Lamprophyre 1 has a slightly higher SiO₂ content than Lamprophyre 2. The minettes are higher in silica and aluminum, unsurprisingly, as they are rich in aluminum silicates (by definition). Ratios between CaO/Al₂O₃ vs TiO₂/P₂O₅ show a separation between the two lamprophyres as well (Fig. 6.8). The ratio CaO/Al₂O₃ is low in Lamprophyre 1 while TiO₂/P₂O₅ is higher. Discrimination plot Fe₂O₃/Al₂O₃ vs K₂O/Al₂O₃ from Rock (1991) also shows a subtle, but distinct grouping between Lamprophyre 1 and 2 (Fig. 6.4).

Trace element geochemistry has shown that both lamprophyres are enriched in Rare Earth Elements (REE). Although, there are subtle differences between the two. Figures 6.9 and 6.10 show that Lamprophyre 2 is more enriched in light REEs such as cerium and lanthanum but remain semi-constant for medium REEs such as samarium.

Weathered lamprophyre

The weathered parts of the Yogo lamprophyre are what miners are interested in because they have been the easiest to extract intact sapphires from. Field relationships have shown different facies of weathering at various depths and locations along the lamprophyre intrusion. This section describes the leaching and enrichment of major elements and trace elements.

Above strike of the main dike, where it has not been completely excavated, lamprophyre is present in some areas of the polymict rubble breccia. This lamprophyre has been weathered to grey green and retains apple to sea green flecks of altered clinopyroxene and unaltered biotite, refer to the chapter on petrography for a more in-depth description. Importantly, this weathered

facies of the lamprophyre retains much of its original appearance making it easy to identify in the field. Underground, at a depth of 30.5 meters (100 ft) below the surface, in the Vortex Mine weathered lamprophyre of this facies is present in the same breccia. These facies of weathering are plotted on graphs as “Near surface weathered – green” in the following figures.

At depths of 40, 80, and 94.5 meters (130, 260, and 310 ft) in the Vortex mine there are more extreme weathering facies preserved. Along the exposed length of the dike there are areas of fresh Lamprophyre 2 dike that grades into a weathered grey-green rock, to red facies, and to a yellow facies. Samples of the red and yellow facies are clay rich; the only remaining texture of the original rock is apple to sea green flecks of altered clinopyroxene. These samples are plotted as “Underground weathered – red” and “Underground weathered – yellow” in the figures.

Major element geochemistry shows overall reduction of SiO_2 and an enrichment of CaO on weathering (Fig. 6.11). The enrichment of CaO may be due to a residual effect or addition. Plots of the ratios to immobile major elements shows leaching of both SiO_2 and MgO with different degrees of leaching occurring with respect to the different weathering facies (Fig. 6.12). $\text{TiO}_2/\text{Al}_2\text{O}_3$ is constant hence these elements are behaving as immobile as expected. There is a spread in data where the least weathered (Near surface weathered – green) samples are closer in composition to the fresh lamprophyres and the most weathered (Underground weathered – yellow and red) samples have the greatest decrease in SiO_2 and MgO compared to fresh samples.

Trace element geochemistry shows an enrichment of Rare Earth Elements (REE) such as cerium and lanthanum (Fig. 6.13). This is more likely due to a residual effect by the removal of silica and magnesium. Immobile elements and ratios such as La vs Hf/Ce remain constant, but as the concentration of silica and magnesium decreases, it creates a trend of enrichment from the least weathered samples to the most weathered samples (Fig. 6.13). Importantly, these ratios are

remaining constant and can be used to geochemically identify lamprophyres even where weathered. Mobile elements such as thorium and uranium are variably leached but uranium most strongly (Fig. 6.14). Phosphorus is increased by residual enrichment while vanadium is constant with few outliers.

To summarize, the Above ground weathered – green samples are the least affected by weathering and compositionally more similar to Lamprophyre 1 samples and the Underground weathered samples are affected the most by weathering but are still compositionally more similar to Lamprophyre 2. Chemical variability exists between the two facies of underground weathering as well; the red is the least affected and the yellow is the most affected.

Mineralogical controls on geochemical variability

When determining which minerals may play a role in compositional melt variation, major minerals seen in hand sample and thin section and corresponding elements that may have higher than background concentrations were considered. It is suspected that biotite, clinopyroxene, olivine, apatite and zircon may be important and various concentrations and ratios of trace and major elements that may be hosted in these minerals are tested here.

Elevated concentrations of phosphorous as well as REEs such as cerium and lanthanum suggest that apatite plays a role in REE distribution (Fig. 6.15). Although described in earlier studies as being hosted in both the matrix and as inclusions in clinopyroxene and phlogopite, apatite is only seen in thin section within the pleochroic rims of biotite (Dahy, 1988; Gauthier, 1995). These ratios of phosphorous, cerium and lanthanum also show discrimination between Lamprophyres 1 and 2 where Lamprophyre 2 has higher LREEs than Lamprophyre 1.

The presence of phlogopite in hand sample and thin section would suggest that it plays a large role in element distribution especially where K_2O is concerned (6.16). K_2O is variable with respect to the mobile trace element rubidium and the immobile element titanium. The difficulty of interpretation is that these elements may also be being controlled by another potassium rich mineral such as a feldspathoid. Geochemical plots suggest that phlogopite plays a weak role in trace element distribution.

Large amounts of clinopyroxene found in Lamprophyres 1 and 2 would suggest that it plays a role in element distribution. Trace elements chromium and titanium were plotted to determine the relationship (6.17). Surprisingly, there was a point distribution of the samples suggesting clinopyroxene does not play a role in chemical variation. The plot also shows that clinopyroxene in both lamprophyres are chemically similar.

Element distributions of nickel and magnesium were plotted to determine if olivine, though only a minor phase in most samples, displays a relationship in fractionation (Fig. 6.18). There is a weak linear trend between MgO and Ni within the Lamprophyre 1 samples, but there is no strong evidence that olivine plays a role in element distribution. However, although Lamprophyre 2 has more olivine, it does not have the expected higher concentration of Mg and Ni .

The relationship between zirconium and hafnium is puzzling. The main host for both elements is zircon which is primarily formed in igneous rocks with an average ratio of zirconium to hafnium 33:1 but the samples from Yogo show a negative $Zr:Hf$ trend and average ratio of 27:1 (Fig. 6.19). This suggests that an extremely small amount of partial melting has affected the Yogo dike (Jones III et al, 2017). Furthermore, there is -again- differentiation between

Lamprophyre 1 and Lamprophyre 2 samples regarding Zr vs Hf, where Lamprophyre 1 has elevated zirconium and less hafnium than Lamprophyre 2.

Portable X-Ray Fluorescence (pXRF) analysis of dike components

Semi-quantitative geochemical data of ocelli and xenoliths was determined with pXRF. The data is semi-quantitative because there is no normalization standard of ocelli or the various xenolith types found in the lamprophyres at Yogo. The data is used here to show semi-quantitative concentrations of specific elements to confirm xenolith types and chemical variability in ocelli.

Ocelli

Limestone breccia clasts from the monomict rubble breccia in the study area, as well as recrystallized limestone xenoliths were used to compare how pXRF data on nearly pure calcite would plot on diagrams of SiO_2 vs CaO and $\text{Fe}_2\text{O}_3(\text{T})$ vs CaO . The ocelli plot away from the sedimentary and metasedimentary clasts to lower CaO and higher concentrations of $\text{Fe}_2\text{O}_3(\text{T})$ and SiO_2 (Fig. 6.20). This implies that the ocelli are not purely composed of carbonate.

Xenoliths

Xenoliths are suspected to originate potentially from the mantle, lower crust, the Belt Supergroup, and immediately underlying Paleozoic sequence. The geochemical data plotted is to illustrate what the overall geochemical range of the xenoliths is; the lamprophyres are plotted as comparison. To determine overall rock type a combination of xenolith description, which can be found in the petrography chapter, with an immobile element plot (Ti versus Zr) from Hallberg (1976) was used (6.21). Under the assumption that extrusive and intrusive rocks have the same chemical composition, the Ti vs Zr plot is appropriately used. The host lamprophyres were

plotted to show the difference between them and the xenoliths. Confirmed granites and the organic rich metasedimentary xenoliths are highlighted. Samples that have a suspected ultramafic or mafic composition are circled, as well as the calcsilicate samples.

Granitic xenoliths plot as expected in the felsic dacite and rhyolite fields, while the lamprophyres plot in the mafic basalt/andesite boundary. The suspected ultramafic and mafic samples plot on the boundary between andesite and dacite, which suggests they are more felsic than originally interpreted but this could be due to some levels of diffusion of elements between xenoliths and host. The calcsilicate xenoliths plot high in the rhyolite field and are unusually high in zirconium and the organic rich metasedimentary xenolith plots on the basalt/andesite boundary with lesser concentrations of titanium than the lamprophyres. Further geochemical discrimination is needed to determine what the organic metasedimentary xenolith may be. All other samples plot broadly in a the dacite field and hence have an intermediate composition suggesting they could have intermediate igneous origins or clastic sedimentary origins.

A chromium versus zirconium plot was used to further explore the ultramafic and mafic xenoliths (Fig. 6.22). Xenoliths that had chromium values were plotted as well as the lamprophyres and organic rich metasedimentary xenoliths. The confirmed ultramafic and mafic xenoliths plot in the komatiite and komatiite basalt fields supporting ultramafic to mafic mineralogy seen in hand sample and thin section. Lamprophyres plot low in the basalt field this may be due to the anomalous relationship between zirconium and hafnium shown in figure 6.11. Importantly, all xenoliths are significantly enriched in chromium and zirconium, with the ultramafic/mafic xenoliths being anomalously high in zirconium. The organic rich metasedimentary xenoliths plot with the lamprophyres and need further geochemical discrimination.

As the name implies, the organic rich metasedimentary xenoliths are high in carbon. This suggests that it could have they may have originated as a rock enriched in crude oil. The crude oil origin is supported by anomalously high vanadium, chromium, and nickel concentrations (Horr et al, 1961). Enrichment of these metals are found in crude oil and ashed crude oil samples which suggests that this sample includes ashed crude oil (Horr et al, 1961). A more comprehensive geochemical study is needed to confirm this.

Table 6.1a. Whole rock geochemical data from fresh samples.

Key: EM = English Mine, KC = Kelly Coulee, VM = Vortex Mine, Octc = October sample c, B = Breccia, M = Minette

Analyte Symbol	Unit Symbol	Detection Limit	Analysis Method	EM17	EM4	EM26	KC1	EMOctc	VM9	VM7	VM10a	M1+X	M1-X
SiO ₂	%	0.01	FUS-ICP	38.85	39.52	40.39	39.18	38.72	37.13	36.09	37.75	52.32	52.86
Al ₂ O ₃	%	0.01	FUS-ICP	10.82	10.68	11.37	11.21	9.52	8.74	8.63	10.78	12.87	13.65
Fe ₂ O ₃ (T)	%	0.01	FUS-ICP	7.66	7.25	7.66	7.1	7.5	8.14	8.02	7.14	7.57	8.07
MnO	%	0.01	FUS-ICP	0.15	0.13	0.14	0.13	0.14	0.15	0.15	0.14	0.11	0.11
MgO	%	0.01	FUS-ICP	10.33	11.05	11.53	10.98	9.95	12.59	12	8.4	5.71	5.89
CaO	%	0.01	FUS-ICP	16.88	16.7	15.13	15.98	16.05	15.27	14.53	17.76	6.75	7.09
Na ₂ O	%	0.01	FUS-ICP	1.23	1.26	1.02	1.54	1.17	1.52	0.74	2.18	2.91	2.93
K ₂ O	%	0.01	FUS-ICP	2.07	2.26	2.7	2.04	2.54	2.23	3.93	1.5	4.93	4.95
TiO ₂	%	0.005	FUS-ICP	0.999	1.052	1.035	1.009	1.088	1.052	1.052	1.049	0.716	0.753
P ₂ O ₅	%	0.01	FUS-ICP	1.2	1.13	1.19	1.23	1.28	1.35	1.37	1.25	0.5	0.54
LOI	%		GRAV	8.01	6.71	7.59	8.15	10.44	9.76	11.35	10.6	4.15	3.67
Total	%	0.01	FUS-ICP	98.2	97.74	99.75	98.54	98.42	97.94	97.86	98.54	98.53	100.5
Au	ppb	5	INAA	< 5	< 5	< 5	< 5	< 5	< 5	14	< 5	< 5	< 5
Ag	ppm	0.5	MULT INAA / TD-ICP	< 0.5	< 0.5	< 0.5	< 0.5	< 0.5	< 0.5	< 0.5	< 0.5	< 0.5	< 0.5
As	ppm	2	INAA	5	< 2	< 2	< 2	2	4	3	7	< 2	< 2
Ba	ppm	3	MULT INAA/FUSICP	3320	3630	3190	3010	3130	3910	3600	4420	1920	1810
Be	ppm	1	FUS-ICP	2	2	2	2	2	2	2	3	3	2
Bi	ppm	2	TD-ICP	< 2	< 2	< 2	< 2	< 2	< 2	< 2	< 2	< 2	< 2
Br	ppm	1	INAA	< 1	< 1	< 1	< 1	< 1	< 1	< 1	< 1	< 1	< 1

Cd	ppm	0.5	TD-ICP	< 0.5	< 0.5	< 0.5	< 0.5	< 0.5	< 0.5	< 0.5	< 0.5	< 0.5	< 0.5
Co	ppm	1	INAA	32	33	33	33	34	38	35	37	24	22
Cr	ppm	1	INAA	850	1110	897	993	1030	1020	954	871	350	384
Cs	ppm	0.5	INAA	244	155	97.8	309	123	197	36.9	247	1.4	< 0.5
Cu	ppm	1	TD-ICP	68	67	67	64	72	72	71	75	56	58
Hf	ppm	0.5	INAA	5.9	5.3	5.7	6	5.5	6.8	6.2	5.8	4.2	4.3
Hg	ppm	1	INAA	< 1	< 1	< 1	< 1	< 1	< 1	< 1	< 1	< 1	< 1
Ir	ppb	5	INAA	< 5	< 5	< 5	< 5	< 5	< 5	< 5	< 5	< 5	< 5
Mo	ppm	2	TD-ICP	< 2	< 2	< 2	< 2	< 2	< 2	< 2	< 2	< 2	< 2
Ni	ppm	1	TD-ICP	178	206	205	210	170	243	219	162	73	73
Pb	ppm	5	TD-ICP	17	12	8	15	13	15	18	15	6	7
Rb	ppm	20	INAA	60	80	140	100	70	110	90	130	200	210
S	%	0.001	TD-ICP	0.067	0.055	0.064	0.064	0.09	0.071	0.063	0.178	0.007	0.009
Sb	ppm	0.2	INAA	5.6	3.5	2.6	6.9	3.1	4.3	1.1	5.8	< 0.2	< 0.2
Sc	ppm	0.1	INAA	23.3	25.1	23.9	24.8	26.5	26	25.3	23.2	21.9	22.9
Se	ppm	3	INAA	< 3	< 3	< 3	< 3	< 3	< 3	< 3	< 3	< 3	< 3
Sr	ppm	2	FUS-ICP	1934	1501	1433	1855	2411	2971	2604	2488	537	604
Ta	ppm	1	INAA	< 1	< 1	< 1	< 1	< 1	< 1	< 1	< 1	< 1	< 1
Th	ppm	0.5	INAA	19.1	16.1	17.3	16	22.6	22.1	21.4	21.2	9.4	10
U	ppm	0.5	INAA	2.3	1.4	1.7	1.8	2.4	3.5	3	2.3	1	0.9
V	ppm	5	FUS-ICP	156	149	154	144	156	154	153	161	161	171
W	ppm	3	INAA	< 3	< 3	< 3	< 3	< 3	< 3	< 3	< 3	< 3	< 3
Y	ppm	1	FUS-ICP	20	19	21	20	22	21	21	22	16	17

Zn	ppm	1	TD-ICP	70	59	65	83	90	72	70	72	57	56
Zr	ppm	2	FUS-ICP	152	184	163	168	152	96	125	156	142	145
La	ppm	0.2	INAA	175	153	162	157	189	198	193	183	45.5	44.9
Ce	ppm	3	INAA	346	315	316	313	372	388	380	351	90	88
Nd	ppm	5	INAA	177	132	154	158	170	200	202	184	38	44
Sm	ppm	0.1	INAA	18.7	18.1	17.7	18	20	20.9	20.6	19.3	6.2	6.2
Eu	ppm	0.1	INAA	4.3	3.9	4.1	1.8	4.5	4.8	4.6	4.1	1.4	1.3
Tb	ppm	0.5	INAA	< 0.5	< 0.5	1.4	< 0.5	< 0.5	< 0.5	1.1	< 0.5	< 0.5	< 0.5
Yb	ppm	0.1	INAA	1.5	1.4	1.7	1.7	1.5	1.5	1.3	2.2	1.5	1.6
Lu	ppm	0.05	INAA	< 0.05	< 0.05	< 0.05	< 0.05	< 0.05	< 0.05	0.07	< 0.05	0.24	0.18
Mass	g		INAA	1.753	1.729	2.014	1.839	1.868	1.799	1.906	1.833	1.978	2.01

Table 6.1b. Whole rock geochemical data from weathered samples.

Key: EM = English Mine, VMWD = Vortex Mine weathered dike, IGWD = Intergem weathered dike

Analyte Symbol	Unit Symbol	Detection Limit	Analysis Method	EM42	EM44	VMWD1	VMWD2	VMWD4	VMWD5	VMWD6	IGWD1
SiO ₂	%	0.01	FUS-ICP	34.13	34.06	43.17	27.16	27.78	26.6	22.81	28.71
Al ₂ O ₃	%	0.01	FUS-ICP	10.74	11.66	21.89	10.61	13.98	10.65	11.57	10.73
Fe ₂ O ₃ (T)	%	0.01	FUS-ICP	8.62	8.18	4.93	7.87	4.99	6.68	2.22	6.02
MnO	%	0.01	FUS-ICP	0.12	0.11	0.01	0.05	0.03	0.08	< 0.01	0.07
MgO	%	0.01	FUS-ICP	10.91	9.86	1.42	3.45	2.56	3.43	1.06	5.66
CaO	%	0.01	FUS-ICP	14.79	14.18	6.43	19.51	20.95	20.82	29.24	19.74
Na ₂ O	%	0.01	FUS-ICP	0.24	0.19	0.02	0.06	0.04	0.06	0.01	0.07
K ₂ O	%	0.01	FUS-ICP	1.12	1.11	0.25	1.91	0.86	2.03	0.06	1.26
TiO ₂	%	0.005	FUS-ICP	1.166	1.241	2.815	1.296	1.705	1.312	1.424	1.149
P ₂ O ₅	%	0.01	FUS-ICP	1.49	1.6	3.64	1.7	2.28	1.75	1.93	1.44
LOI	%		GRAV	15.19	16.45	14.18	20.29	22.47	20.83	28.33	23.15
Total	%	0.01	FUS-ICP	98.52	98.65	98.76	93.93	97.65	94.25	98.67	98.01
Au	ppb	5	INAA	6	< 5	< 5	< 5	< 5	< 5	< 5	< 5
Ag	ppm	0.5	MULT INAA / TD-ICP	< 0.5	< 0.5	< 0.5	< 0.5	< 0.5	< 0.5	< 0.5	< 0.5
As	ppm	2	INAA	6	10	241	20	29	9	68	3
Ba	ppm	3	MULT INAA/FUSICP	4210	4600	100	28200	2230	27600	61	4840
Be	ppm	1	FUS-ICP	3	3	3	2	2	2	1	2
Bi	ppm	2	TD-ICP	< 2	< 2	< 2	< 2	< 2	< 2	< 2	< 2
Br	ppm	1	INAA	< 1	< 1	< 1	< 1	< 1	< 1	< 1	< 1

Cd	ppm	0.5	TD-ICP	< 0.5	< 0.5	< 0.5	< 0.5	< 0.5	< 0.5	< 0.5	< 0.5
Co	ppm	1	INAA	41	33	10	20	12	31	< 1	34
Cr	ppm	1	INAA	970	1040	2870	1050	1410	1120	1050	965
Cs	ppm	0.5	INAA	< 0.5	< 0.5	< 0.5	30.2	8.1	27	< 0.5	1.8
Cu	ppm	1	TD-ICP	74	74	175	90	71	84	66	77
Hf	ppm	0.5	INAA	5.7	7.2	13.2	9.1	9.2	10	6.4	7.3
Hg	ppm	1	INAA	< 1	< 1	< 1	< 1	< 1	< 1	< 1	< 1
Ir	ppb	5	INAA	< 5	< 5	< 5	< 5	< 5	< 5	< 5	< 5
Mo	ppm	2	TD-ICP	< 2	< 2	< 2	< 2	< 2	< 2	< 2	< 2
Ni	ppm	1	TD-ICP	204	165	174	178	288	209	59	194
Pb	ppm	5	TD-ICP	7	7	17	10	10	18	5	9
Rb	ppm	20	INAA	< 20	< 20	< 20	50	< 20	140	< 20	< 20
S	%	0.001	TD-ICP	0.016	0.011	0.02	0.039	0.019	0.029	0.021	0.023
Sb	ppm	0.2	INAA	< 0.2	< 0.2	3.1	0.7	1.6	0.6	1.1	< 0.2
Sc	ppm	0.1	INAA	27.2	27.4	19.2	30.5	44.5	32.4	13.8	24.4
Se	ppm	3	INAA	< 3	< 3	< 3	< 3	< 3	< 3	< 3	< 3
Sr	ppm	2	FUS-ICP	928	886	933	876	1102	843	502	1051
Ta	ppm	1	INAA	2	7	15	4	8	7	4	7
Th	ppm	0.5	INAA	19.2	20.5	52.7	24.5	31.3	23.9	27.6	21.2
U	ppm	0.5	INAA	2.2	< 0.5	4.3	< 0.5	< 0.5	< 0.5	3.5	1.4
V	ppm	5	FUS-ICP	168	176	357	120	213	129	181	162
W	ppm	3	INAA	< 3	< 3	< 3	< 3	< 3	< 3	< 3	< 3
Y	ppm	1	FUS-ICP	20	20	41	22	29	24	22	18

Zn	ppm	1	TD-ICP	80	71	270	336	294	302	105	119
Zr	ppm	2	FUS-ICP	230	253	427	275	307	276	278	242
La	ppm	0.2	INAA	215	217	455	255	359	263	242	195
Ce	ppm	3	INAA	362	369	848	395	517	426	455	322
Nd	ppm	5	INAA	151	170	398	198	342	180	222	141
Sm	ppm	0.1	INAA	19.8	19.3	44.8	22.9	32.7	23.1	23.9	17.7
Eu	ppm	0.1	INAA	4.1	4	9.6	5.4	6.8	4.6	5.7	3.5
Tb	ppm	0.5	INAA	< 0.5	0.5	< 0.5	< 0.5	< 0.5	0.8	< 0.5	< 0.5
Yb	ppm	0.1	INAA	1.4	1.4	2.2	1.7	2.1	1.5	1.8	1.4
Lu	ppm	0.05	INAA	< 0.05	< 0.05	0.11	0.05	< 0.05	< 0.05	< 0.05	0.05
Mass	g		INAA	1.556	1.342	1.303	1.465	1.297	1.397	1.458	1.39

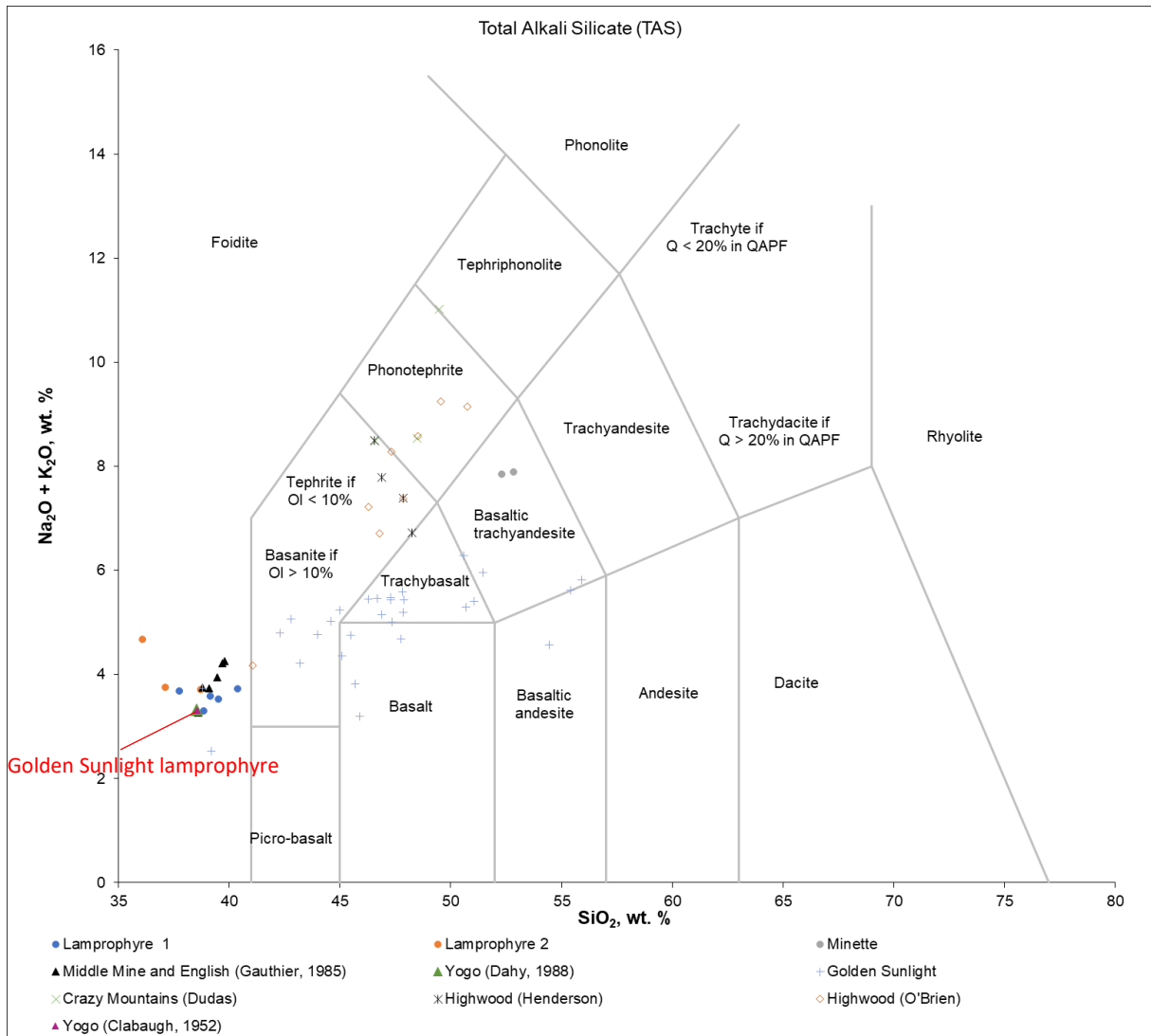


Figure 6.1. Total Alkali Silicate (TAS) plot showing the distribution of samples from Yogo procured during this research as well as samples from Dahy (1988) and Gauthier (1995), compared to other samples from the Central Montana Alkalic Province (Dudas, 1991; O'Brien, 1992; DeWitt et al, 1996).

As expected, lamprophyre samples plot low in SiO₂ and Na₂O + K₂O, lower than basanite. Lamprophyres plot in the unnamed field because of the dilution effects of carbonate on SiO₂. Analyses of have not been recalibrated on an anhydrous basis. According to this diagram there is no relationship between the minette in the study area and the lamprophyres. Nor is there a definitive relationship between the other localities from the Central Montana Alkalic province, although there is one lamprophyre from Golden Sunlight that plots in the cluster of the more mafic lamprophyres from Yogo.

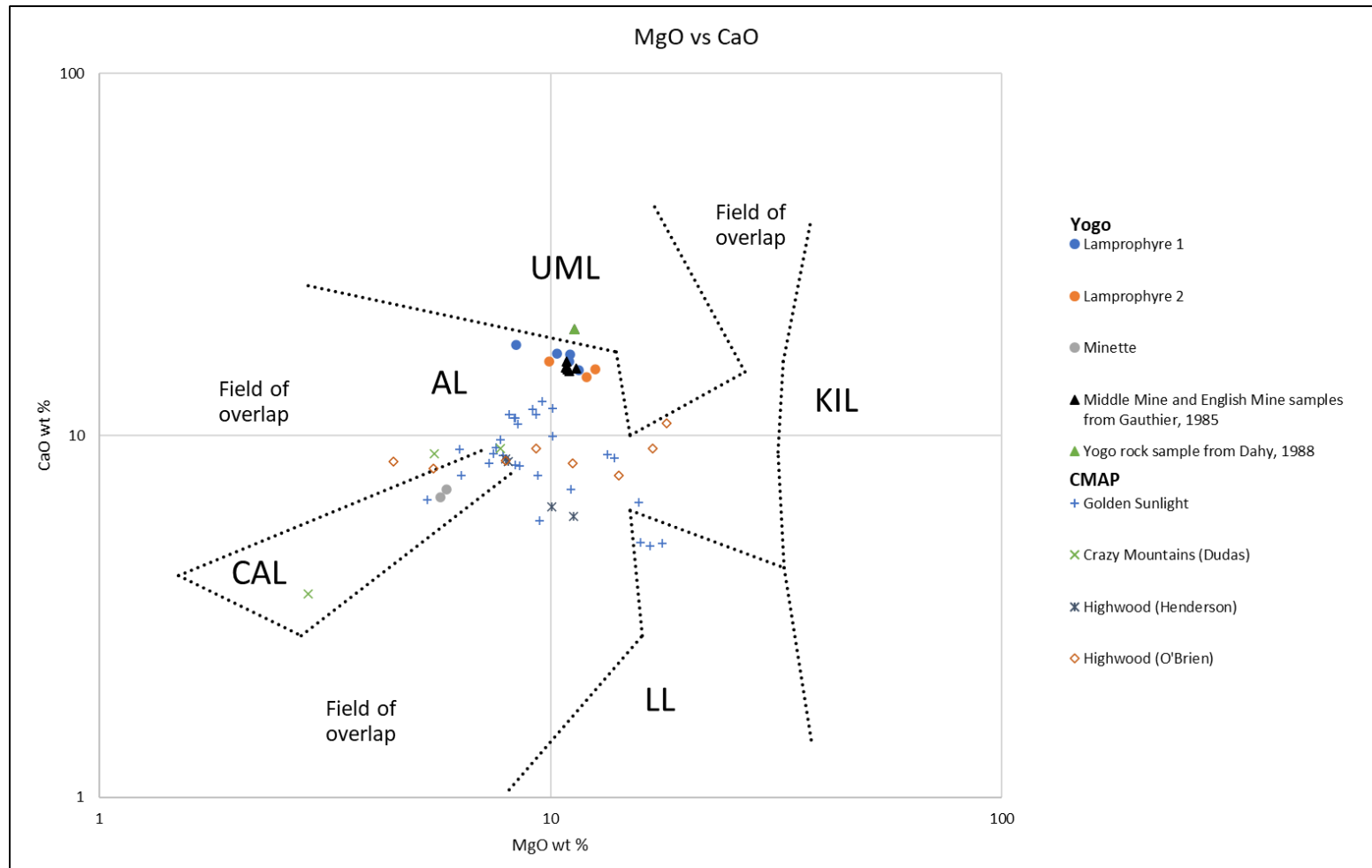


Figure 6.2. This plot shows discrimination between lamprophyres vs minettes at Yogo and lamprophyres at Yogo vs samples from around the Central Montana Alkalic Province (CMAP). Lamprophyres at Yogo plot near boundary between the Alkaline Lamprophyre (AL) and Ultramafic Lamprophyre fields, with the single sample from Dahy (1988) plotting just into the UML field. The minettes plot in the Calc-alkaline (CAL) field. Samples from the Central Montana Alkalic Province plot in the CAL, AL, and lamprophyte (LL) fields, with no samples in the Kimberlite (KIL) field. Classification scheme developed from Rock (1991).

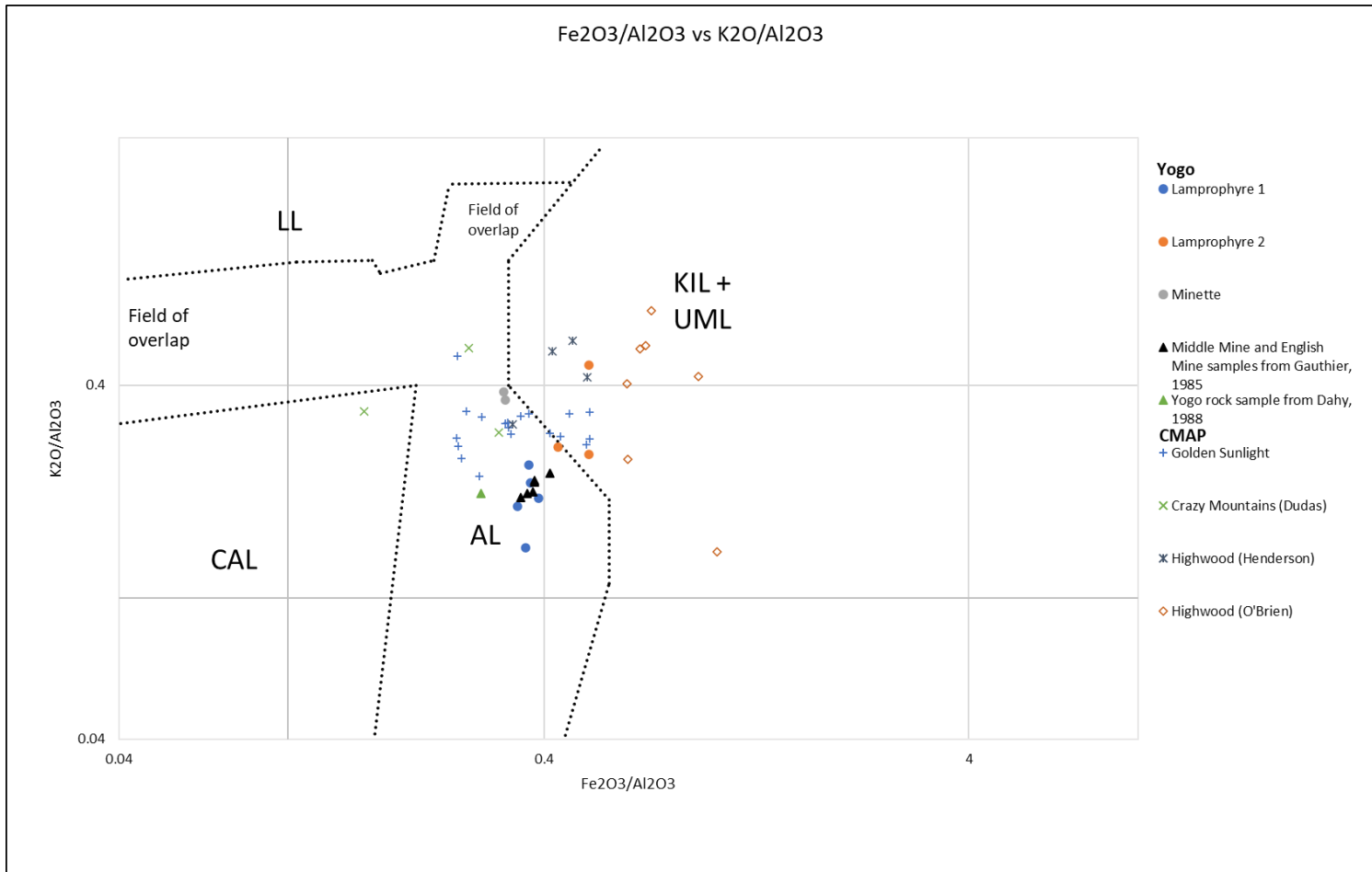


Figure 6.3. Lamprophyres from Yogo, again, plot near and into the boundary between KIL + UML and AL fields. Outliers in both Lamprophyres 1 and 2 exist in the KIL + UML and AL fields. In contrast to the previous plot, minette samples plot within the AL field next to the boundary between Al and KIL + UML fields. Classification scheme developed from Rock (1991).

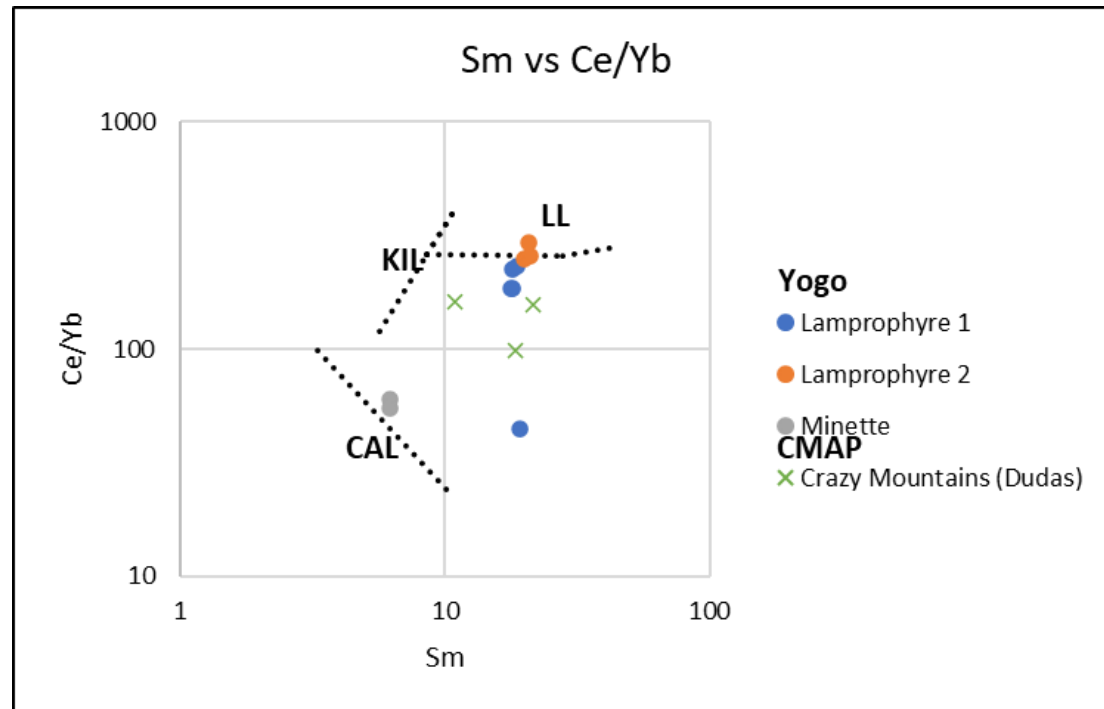


Figure 6.4. This plot supports the CAL signature of minettes but does not give a definitive classification for Lamprophyres 1 and 2 or samples from the Central Montana Alkaline Province (Dudas, 1991). The samples plot in the field of overlap between LL, KIL, and CAL. There are no UML or AL fields represented here and there for may not be and accurate representation of the chemical variability between samples. This graph shows is a greater concentration of REE in Lamprophyre 2 suggesting more fractionation has occurred in this lamprophyre as opposed to Lamprophyre 1. Discrimination diagram developed from Rock (1991).

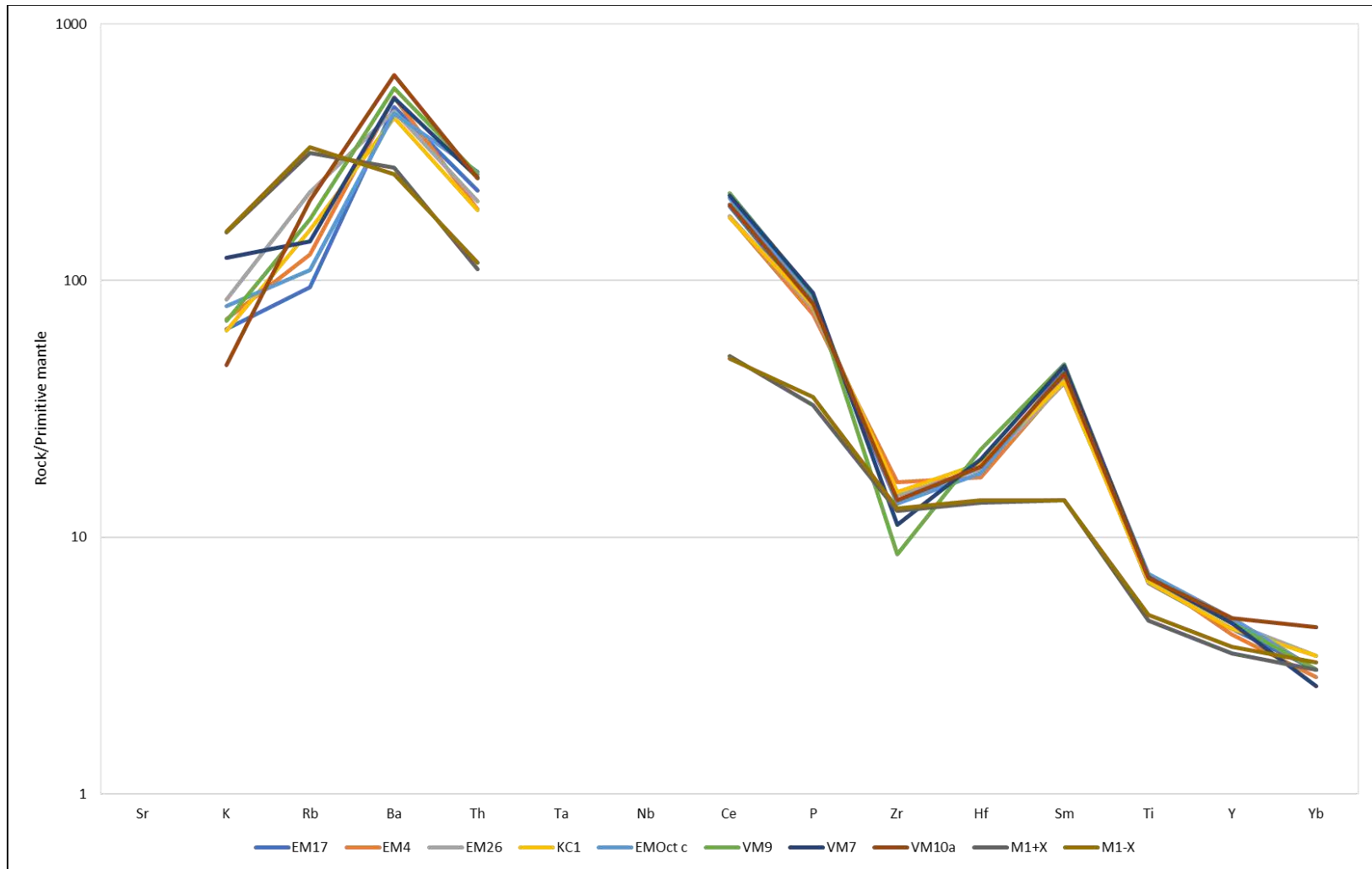


Figure 6.5. Multielement spider diagram plotting concentrations of incompatible elements normalized to primitive mantle values of all samples from Yogo. EM, KC, and VM are lamprophyres, while M1 samples are minettes. M1+X is a sample including xenoliths and M1-X is a sample excluding xenoliths. Regardless of contamination by xenoliths the similar patterns imply they come from the same source. The lamprophyres samples retain their overall line shape comparative to one another suggesting they come from broadly the same source. Lamprophyres and minettes are clearly from different sources, as their line shapes are different from one another.

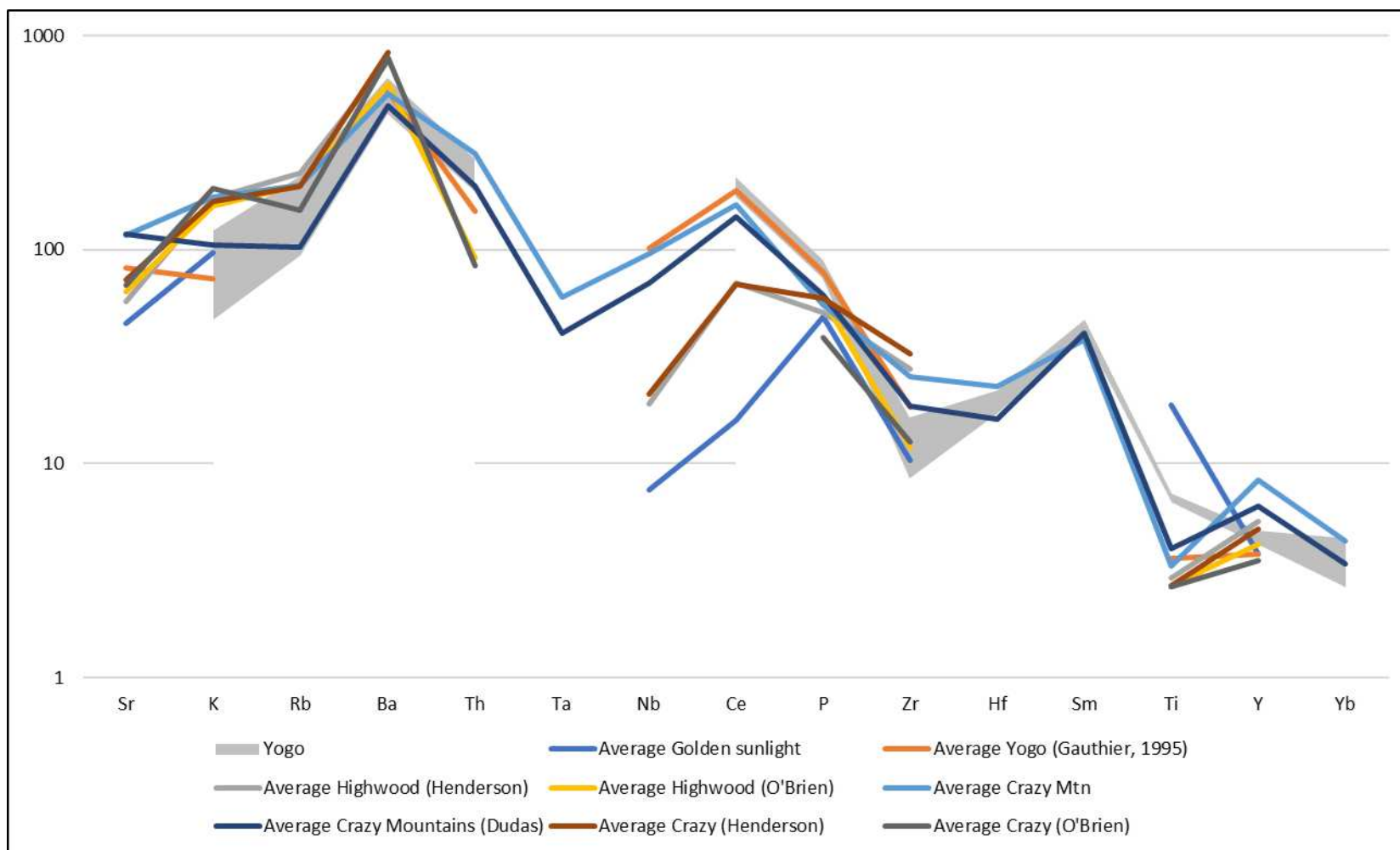


Figure 6.6. The spider diagram compares the minimum and maximum concentrations of elements against the primitive normalized values at Yogo (shaded region) to average samples collected around the Central Montana Alkalic Province (R). According to this diagram samples at Yogo are similar to but not closely petrogenetically related to other rocks in the Central Montana Alkalic Province.

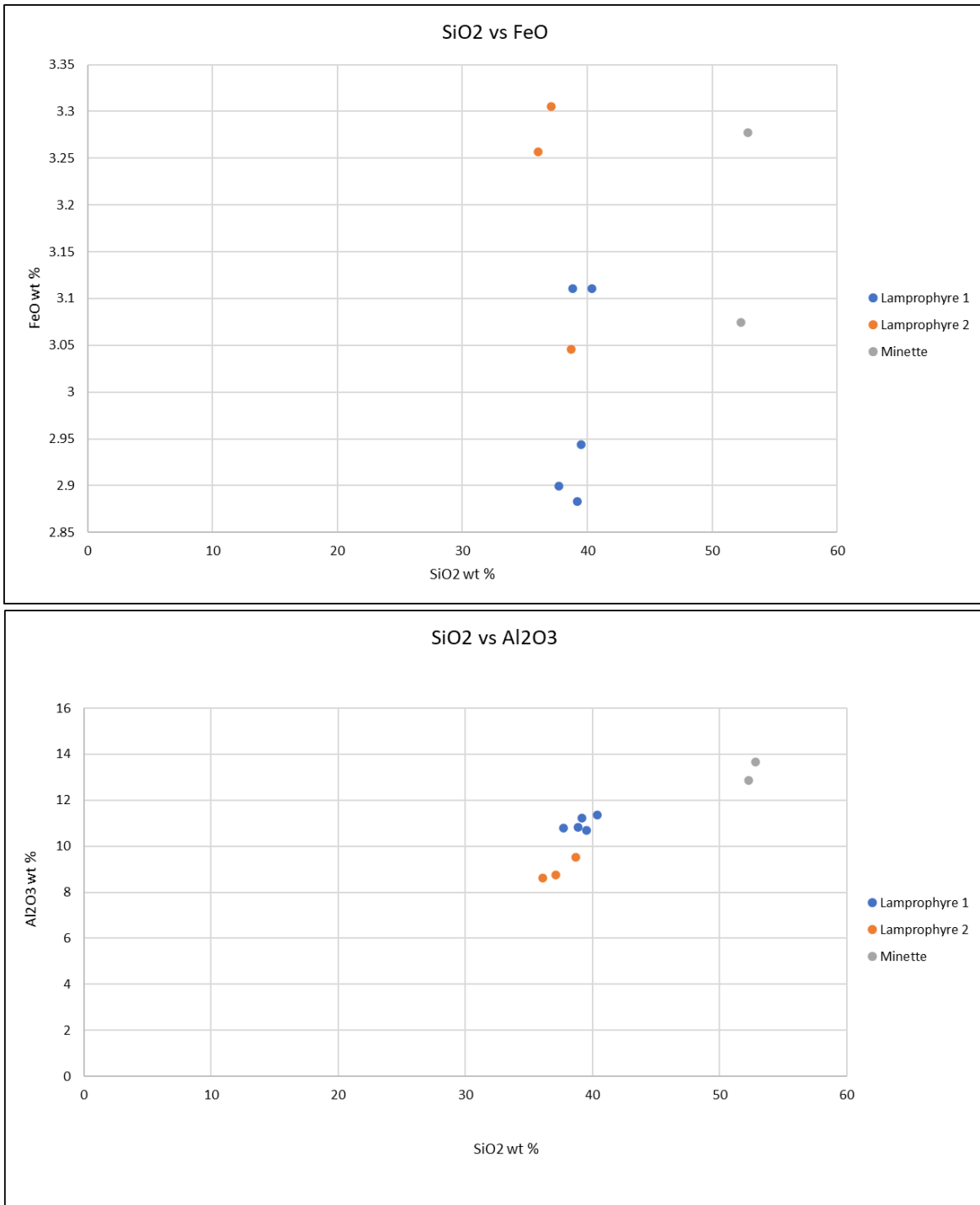


Figure 6.7. Plots to illustrate systematic geochemical differences between Lamprophyres 1 and 2. The top graph shows a spread between the samples with Lamprophyre 2 being generally higher in iron than Lamprophyre 1. There is a zone between two lamprophyres where samples from each overlap. The bottom plot shows similar Silica concentrations between the two but are slightly offset from each other, with Lamprophyre 2 having slightly lower aluminum contents. The minettes plot high in silica and aluminum as expected.

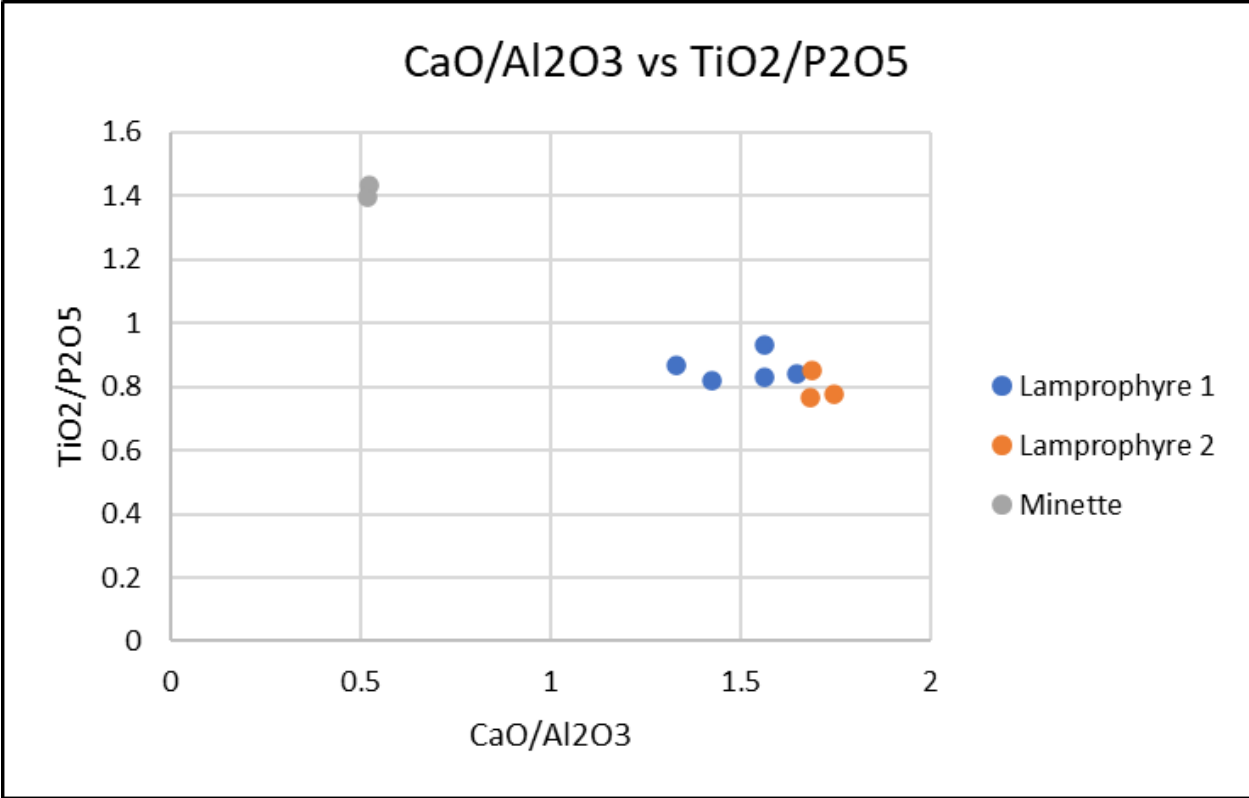


Figure 6.8. This plot shows the variability in CaO/Al₂O₃ vs TiO₂/P₂O₅ between Lamprophyres 1 and 2. Lamprophyre one is more variable and lower in CaO/Al₂O₃ and higher in TiO₂/P₂O₅. The minette plots low in CaO/Al₂O₃ and high in TiO₂/P₂O₅ than the lamprophyres

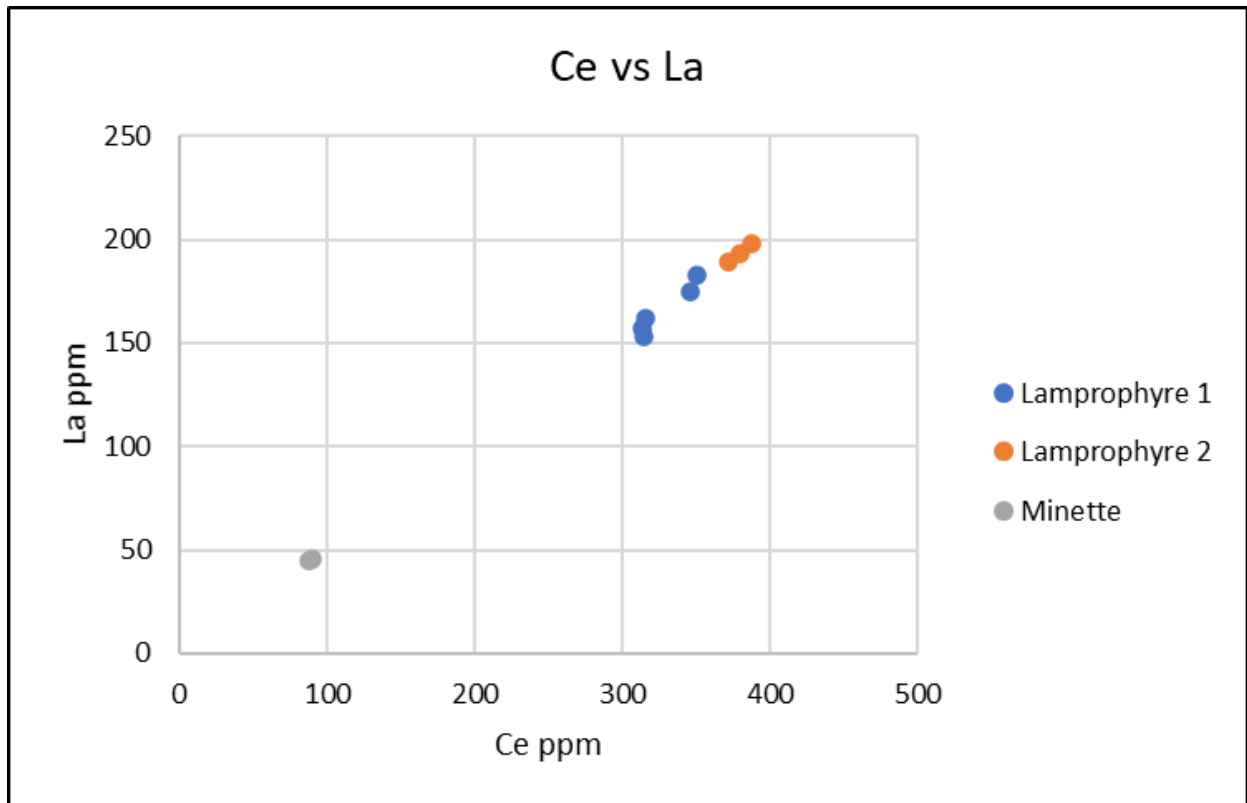


Figure 6.9. This plot shows that Lamprophyre 2 is more enriched in cerium and lanthanum than Lamprophyre 1. There is an apparent linear relationship between the minette and lamprophyre samples, where the minettes are low in the LREEs, Lamprophyre 1 is high in LREEs, and Lamprophyre 2 is even higher.

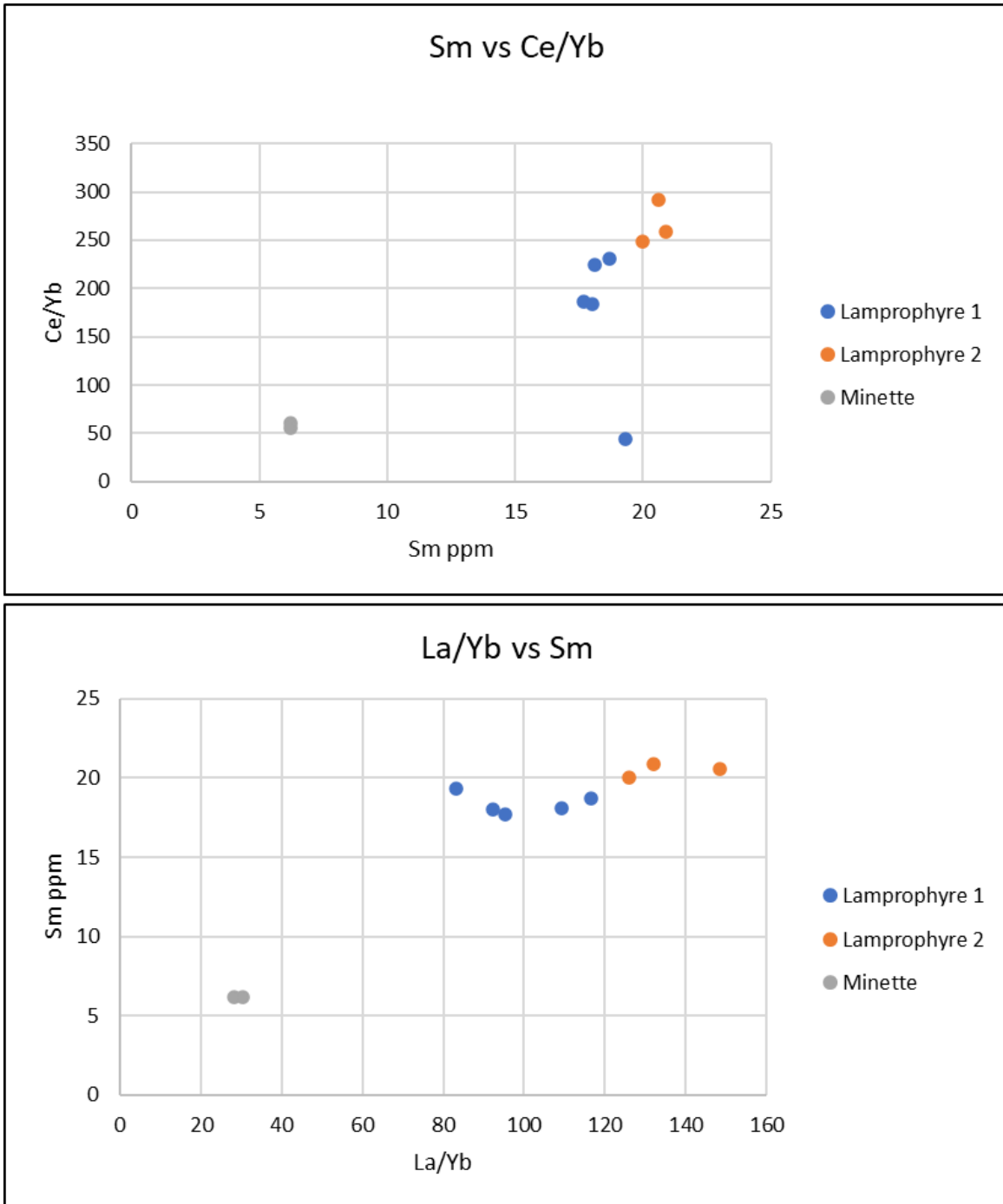


Figure 6.10. Plots of LREE/HREE ratios to Sm, a MREE, that illustrate the subtle difference in rare earth contents found in both lamprophyres. High ratios of Ce/Yb and La/Yb in Lamprophyre 2 may suggest it is slightly more fractionated compositionally than Lamprophyre 1.

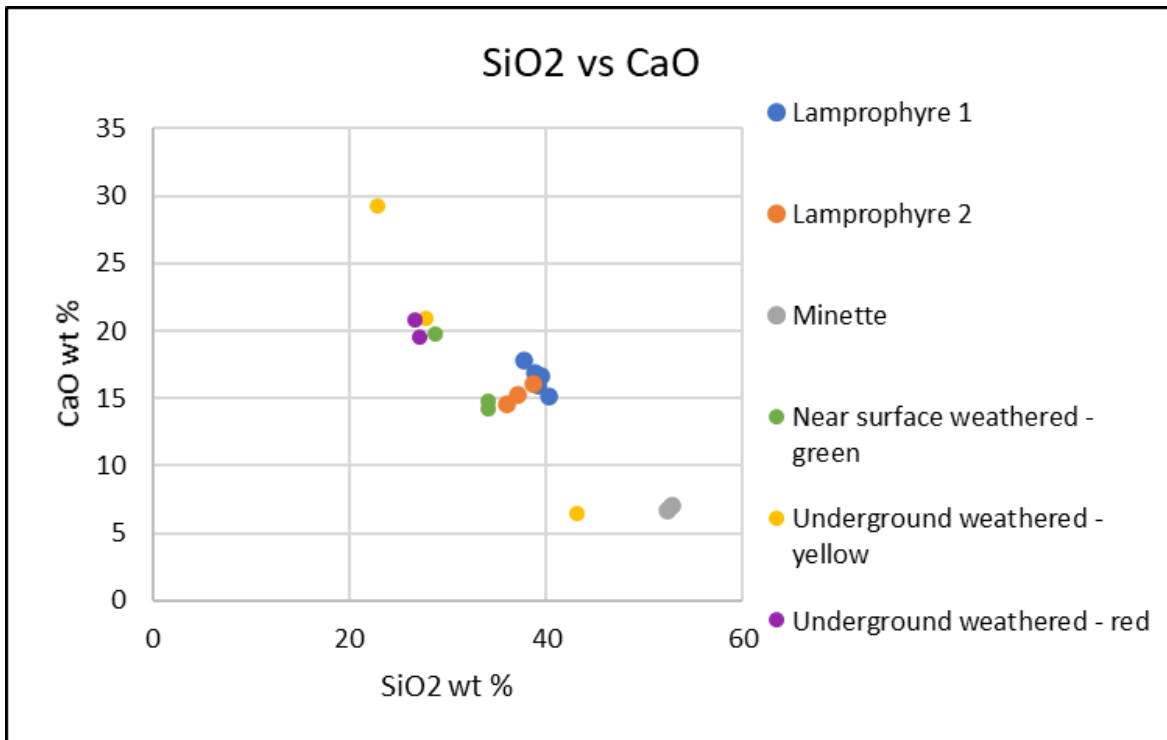


Figure 6.11. This plot shows that, overall, SiO₂ is depleted and CaO is enriched during the weathering of both Lamprophyres 1 and 2. The above ground weathered – green samples show less chemical variability from parent Lamprophyre 1. The underground weathered – red samples are moderately weathered with respect to the less weathered above ground samples and the underground weathered – yellow samples. Samples from the underground weathered – yellow facies have more variability but are found to be the most enriched in CaO and leached in SiO₂. While weathering of lamprophyre generally involves addition of calcite, it may be leached locally as the anomalous “underground – weathered yellow” sample suggests. There is segregation between Lamprophyres 1 and 2 as well as segregation between the above ground samples and underground samples which suggests more intense weathering at depth.

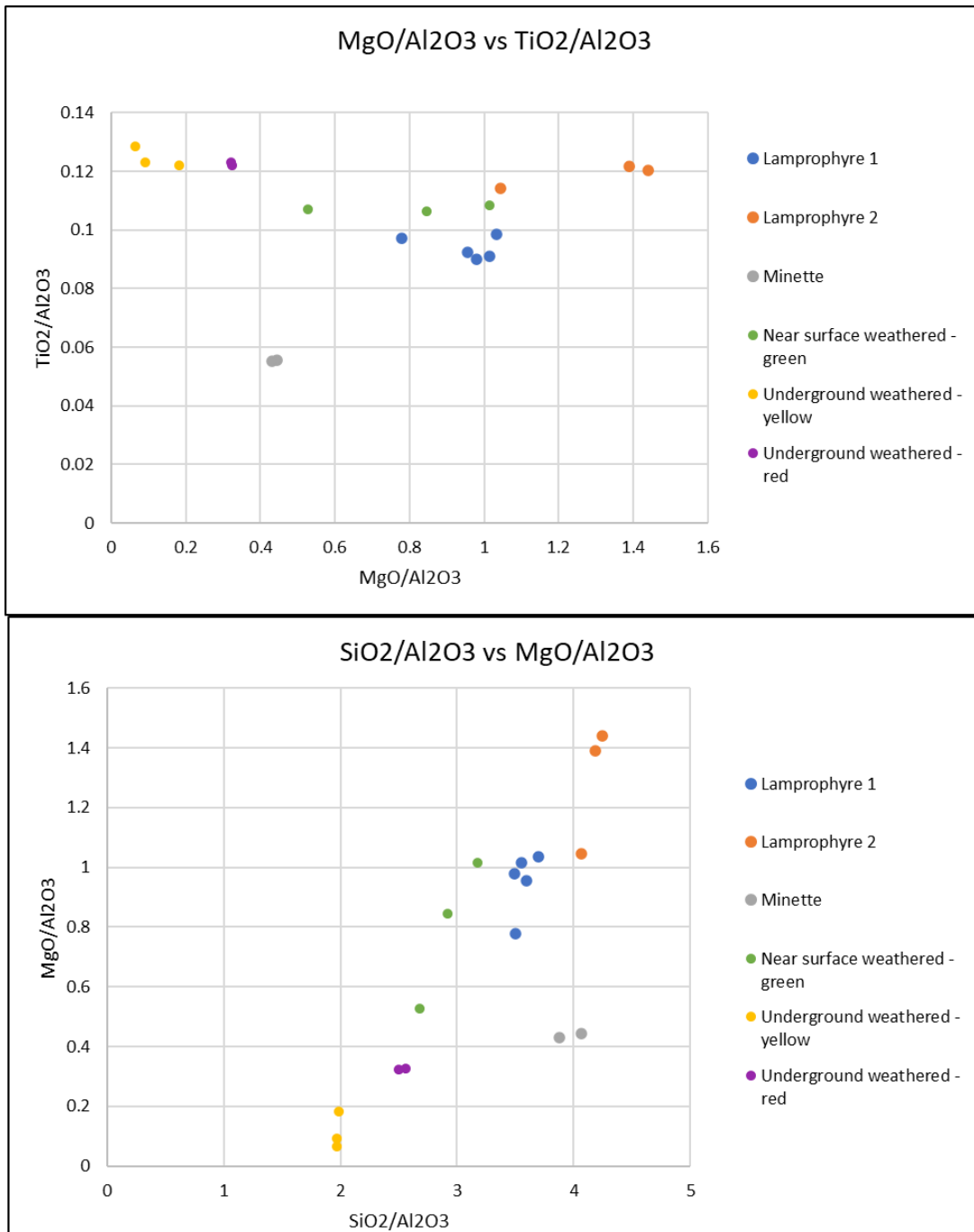


Figure 6.12. These plots show the weathering effects on potentially mobile (Si, Mg) elements ratioed to immobile (Al, Ti) elements. Both plots show near complete leaching of MgO from the most intensely weathered rock, while the bottom also shows leaching of silica. With respect to the fresh lamprophyre samples, there are different degrees of leaching occurring. The above ground samples are the least leached, followed by the Underground weathered – red samples and then the most leached Underground weathered – yellow samples. The top plot shows leaching of MgO with the same division of samples as the bottom plot and TiO2/Al2O3 is behaving as expected and staying constant.

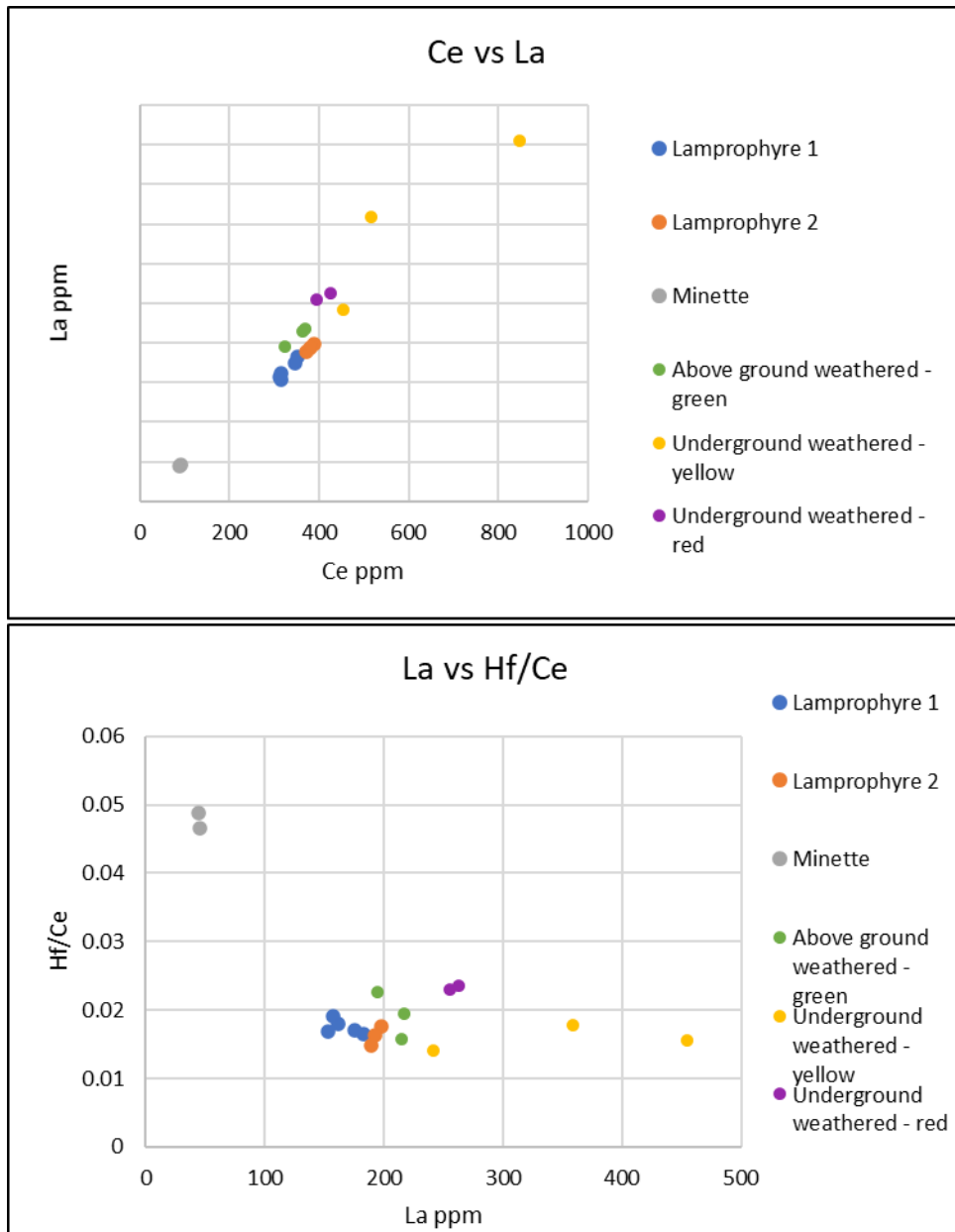


Figure 6.13. The top plot shows that the Rare Earth Elements Ce and La are enriched on weathering, while the bottom shows the ratio of REE immobile elements staying the same, as expected. Both plots show a similar spread in data; the above ground weathered samples are closer to the fresh lamprophyres and the underground samples are further from the fresh lamprophyres showing more enrichment, the Underground weathered – yellow samples being the most extremely weathered. Since the ratio of REEs stays constant they can be used as geochemical diagnostic of weathered lamprophyre.

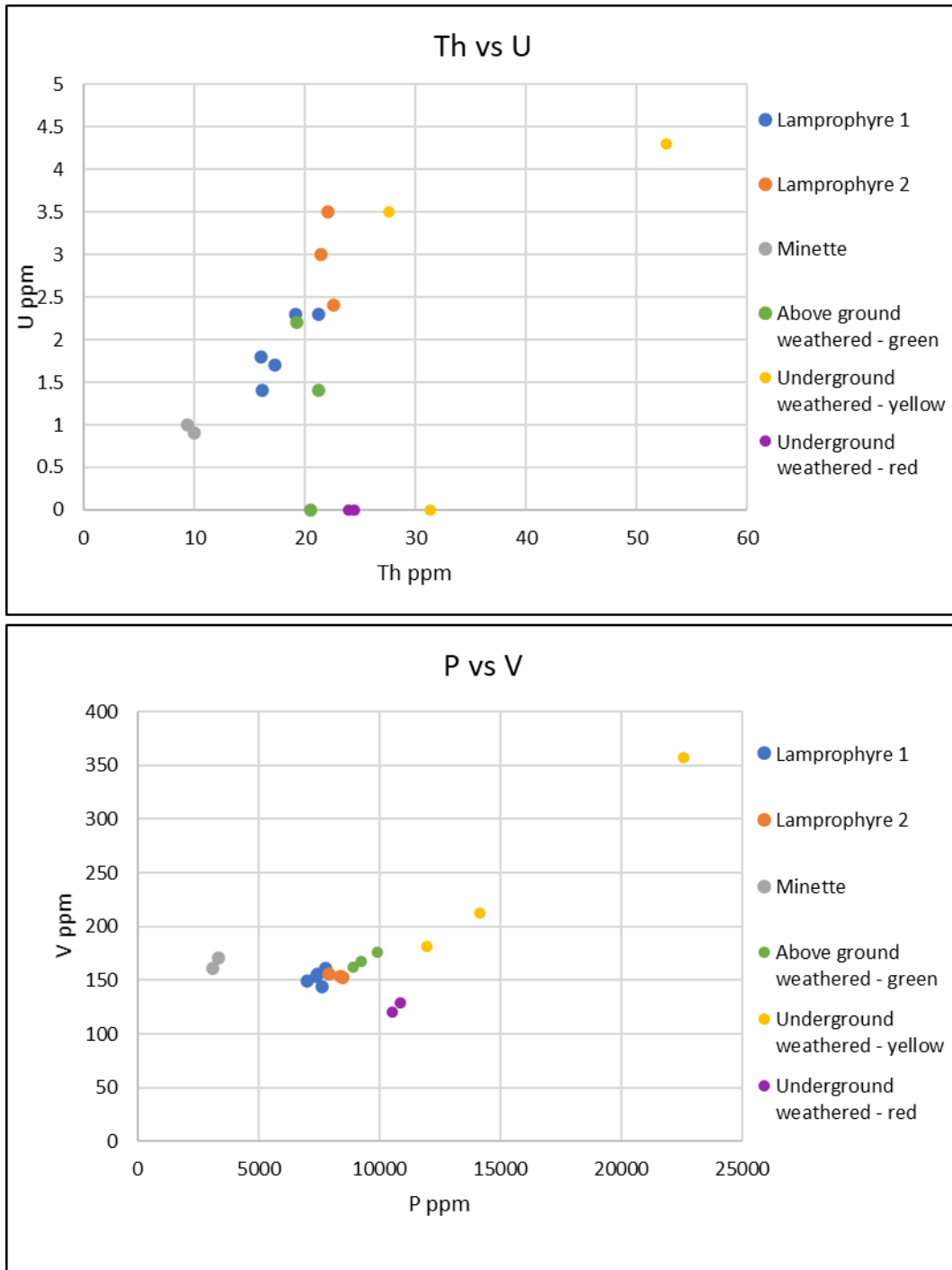


Figure 6.14. The effects of weathering on trace elements. The top plot shows that both U and Th are being leached but leaching of uranium, while variable across the sample suite, is stronger. Thorium is remaining mostly immobile as expected. The bottom plot shows enrichment of phosphorous in weathered samples due to residual enrichment with somewhat variable concentrations of vanadium.

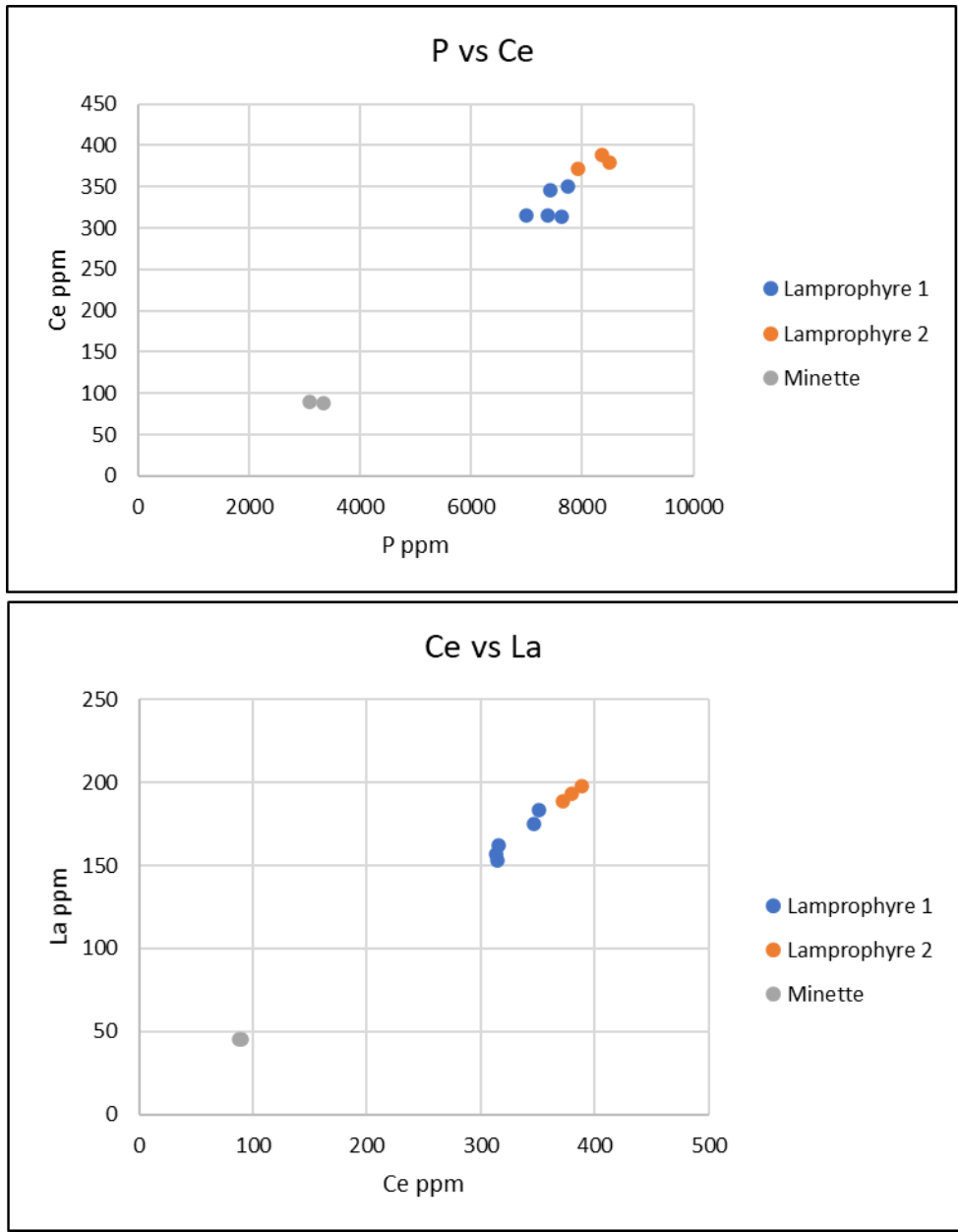


Figure 6.15. The top plot shows a linear relationship between phosphorus and cerium, while the bottom shows a linear relationship between cerium and lanthanum. This tells us that the REEs are dominantly in apatite.

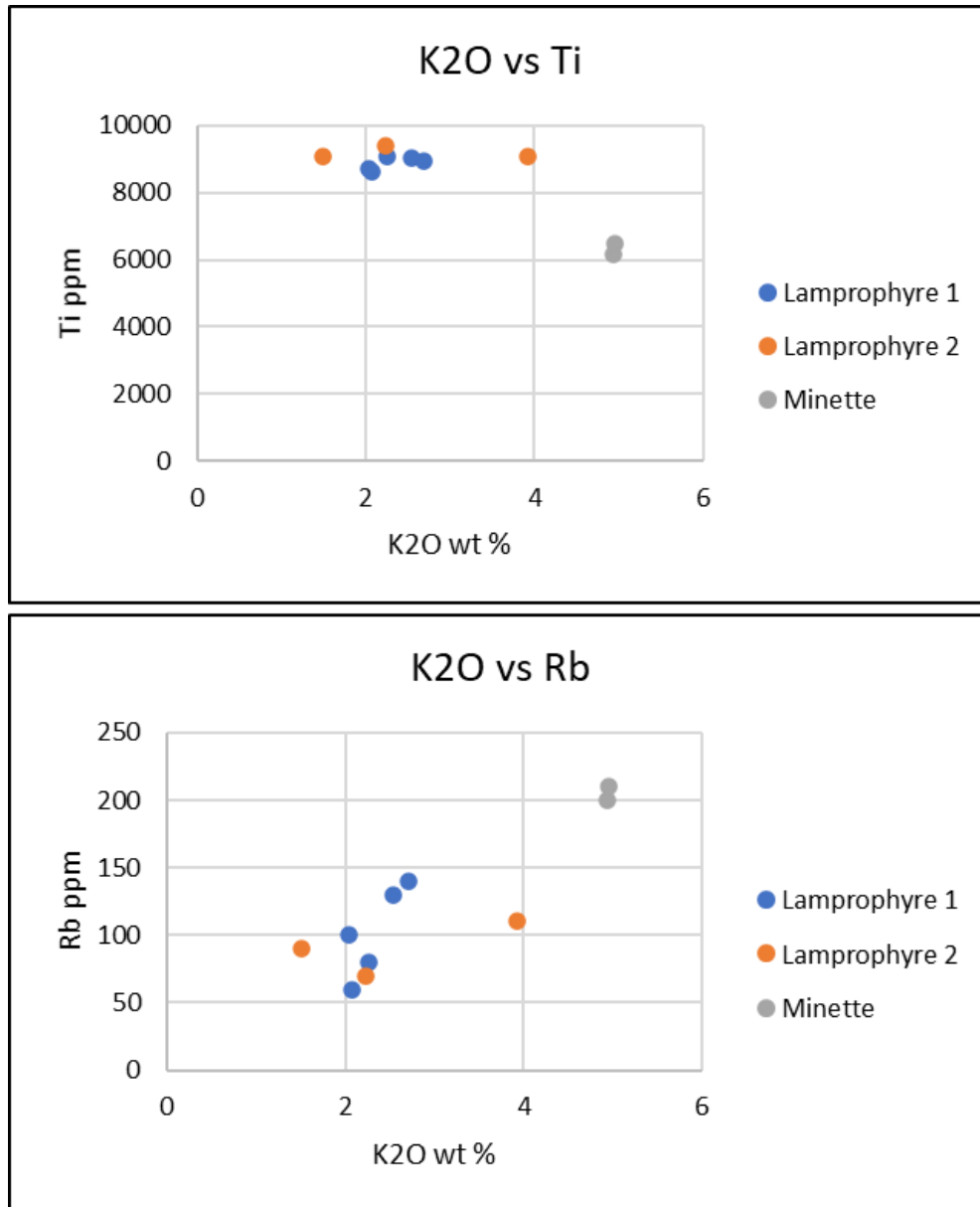


Figure 6.16. These plots show how phlogopite may play a role in element distribution. The first plot shows no defined relationship between potassium and titanium, and hence tells us that minerals in addition to phlogopite are affecting either or both of K₂O and TiO₂. The second plot shows a weak relationship between K₂O and Rb but scatter suggests other potassium rich minerals besides phlogopite may play a role in chemical variation.

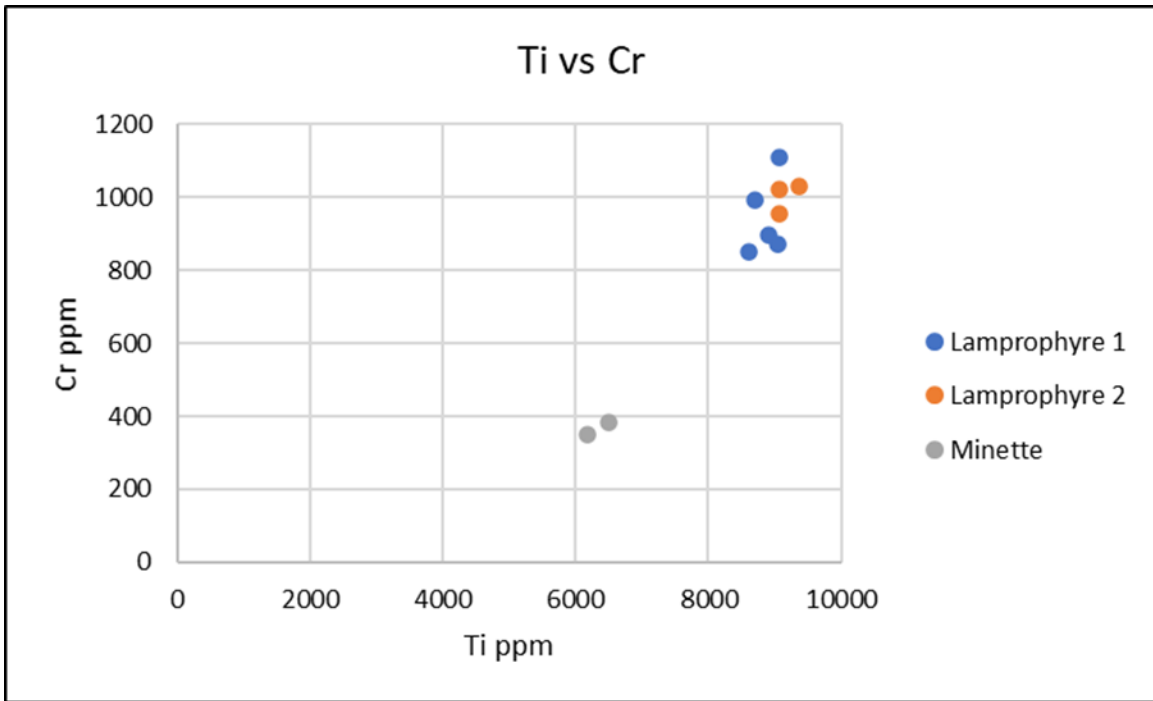


Figure 6.17. Clinopyroxene is likely to host both titanium and chromium. This plot shows there does not appear to be a control on element distribution by clinopyroxene and suggests that the amount and chemistry of clinopyroxene in both lamprophyres are similar.

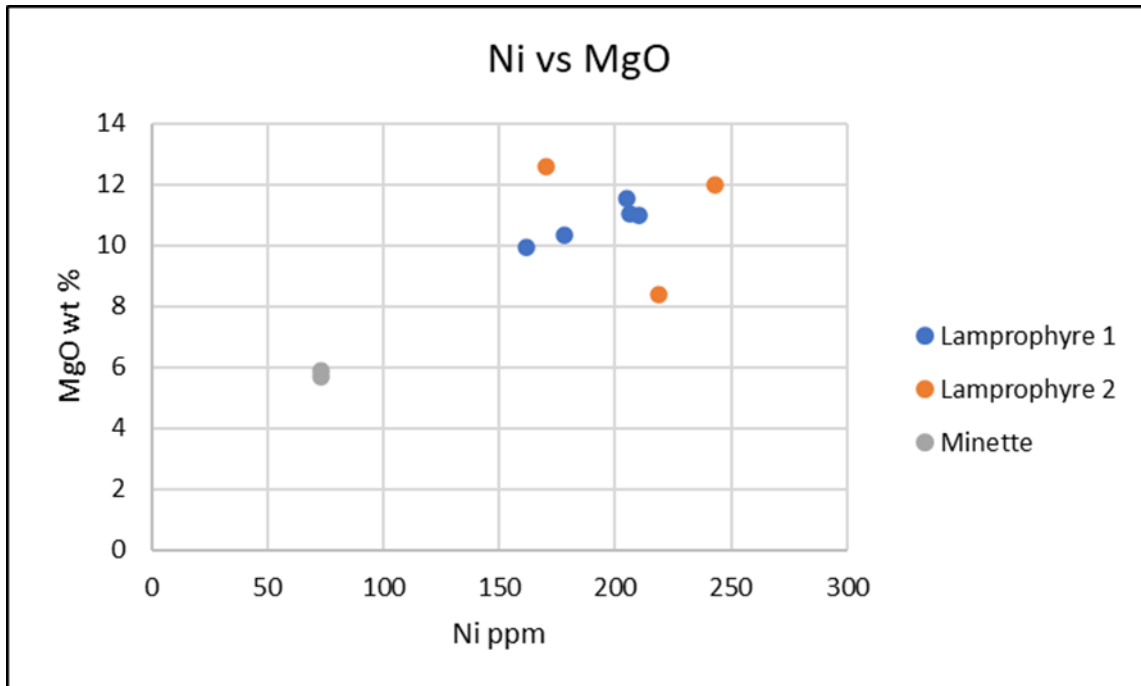


Figure 6.18. Olivine hosts both nickel and magnesium, thus these elements were plotted against each other to show whether olivine may play a role in element distributions. While there appears to be a weak trend within Lamprophyre 1 samples, the plot shows no definitive evidence that olivine plays a role in element distribution.

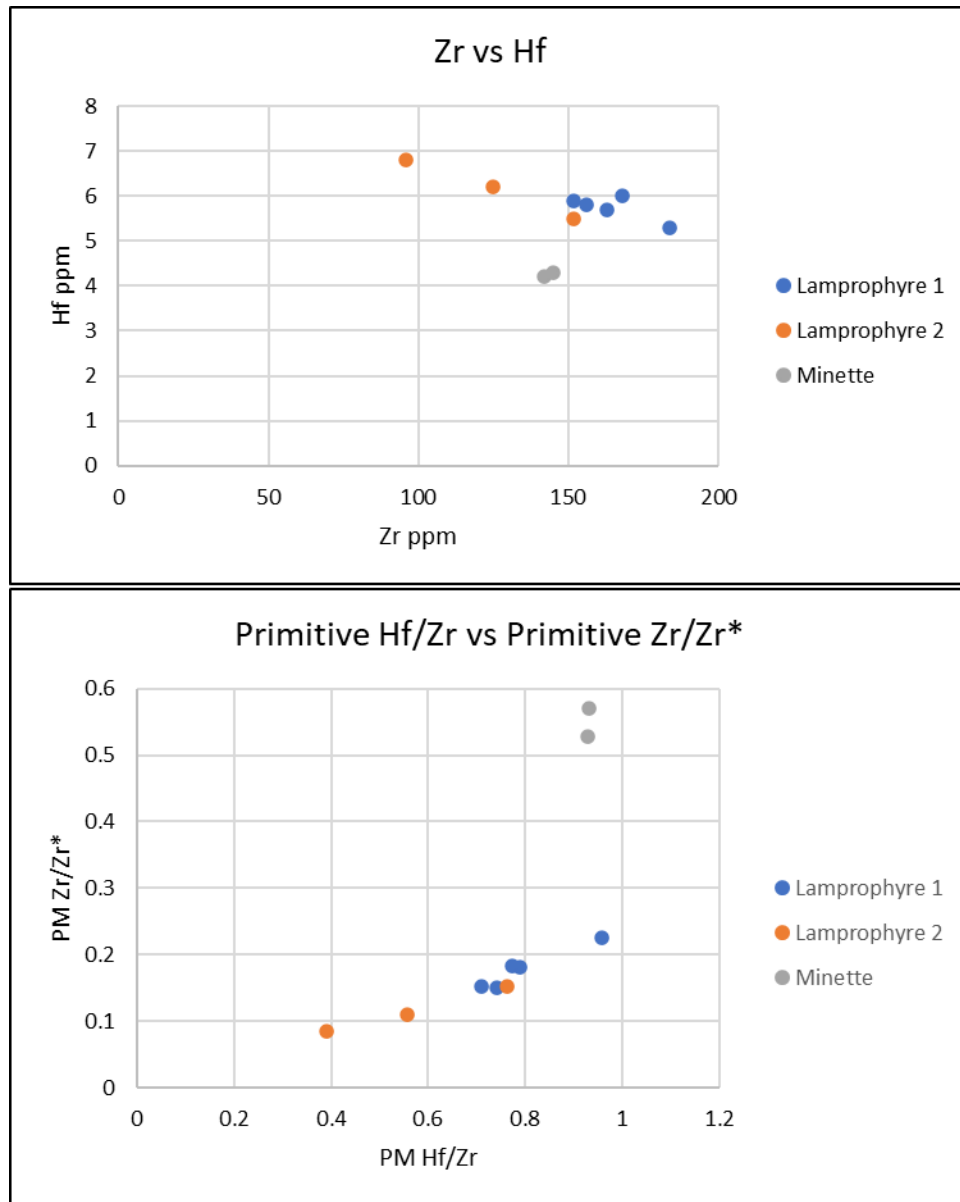


Figure 6.19. This plot shows a variable and average ratio of 27:1 between zirconium and hafnium which is unexpected because in almost all igneous rocks they are known to have constant ratio of 33:1. See text for further description as to why this is happening but there is still differentiation between Lamprophyres 1 and 2. The bottom plot was created from Jorgensen et al (2018). The x-axis value is a ratio of primitive mantle normalized hafnium to zirconium and the y-axis is the ratio primitive mantle (PM) Zr to Zr*.

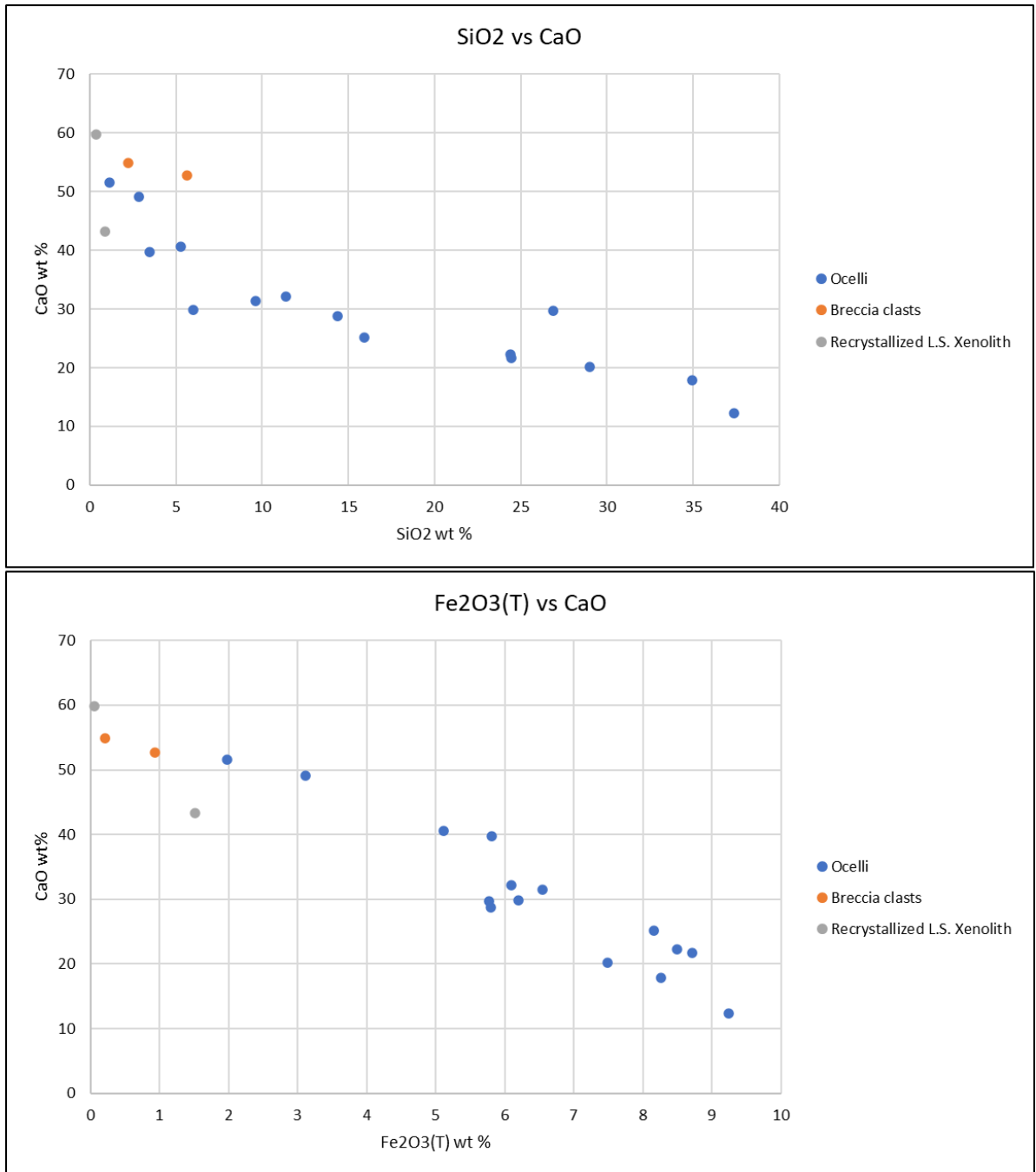


Figure 6.20. These plots show the chemical variability in the lamprophyre-hosted ocelli. The breccia clasts, composed of limestone, and the recrystallized L.S. xenoliths represent pure or almost pure calcite. The ocelli vary from pure calcite to assemblages with higher SiO₂ and Fe₂O₃(T) values.

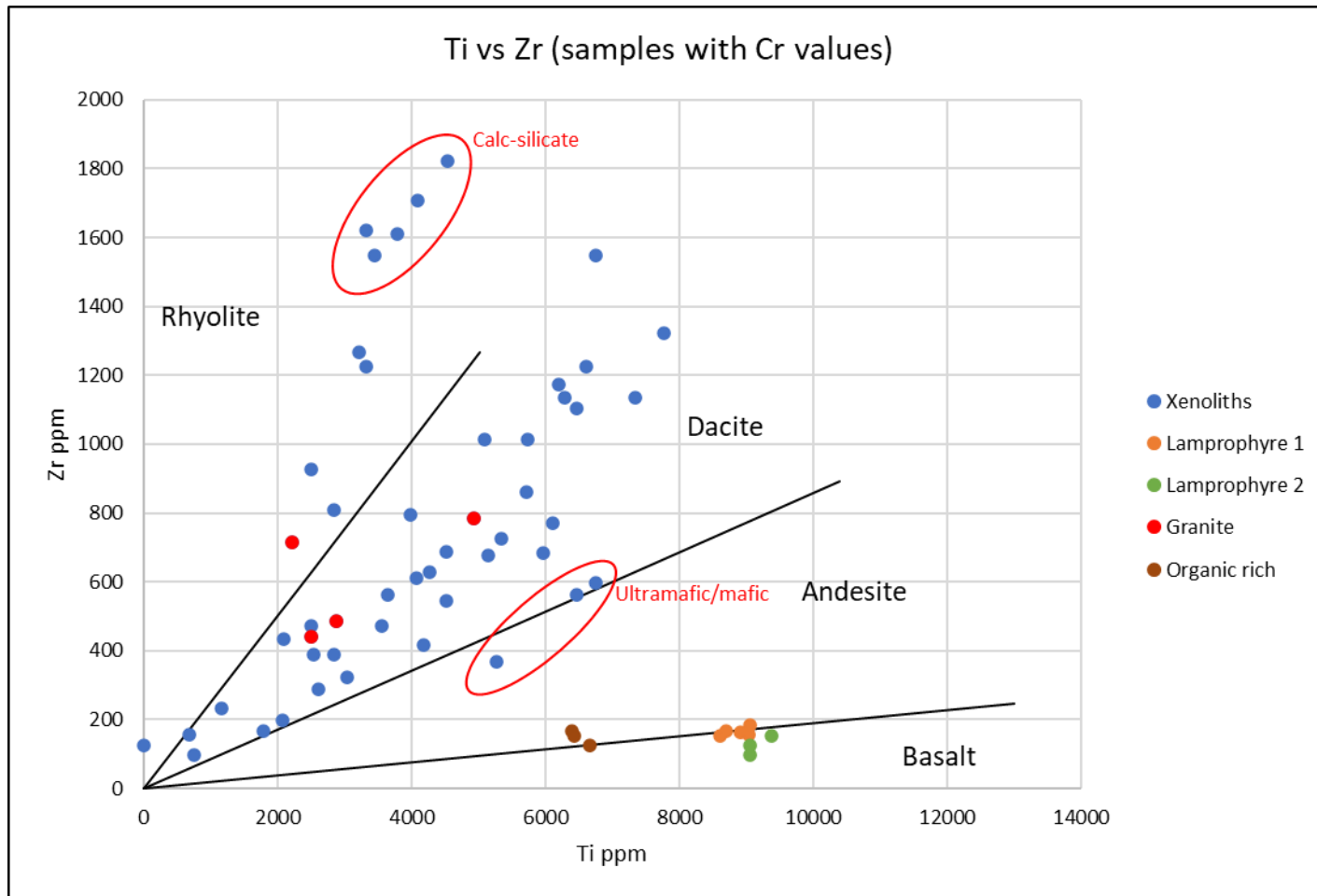


Figure 6.21. This plot represents the overall spread of immobile elements Ti and Zr procured from pXRF on xenoliths within the lamprophyre samples. Only samples with chromium values were used and plotted against Lamprophyres 1 and 2 to show any effects on immobile elements by diffusion between the host rock and xenoliths were minor. Samples that were suspected to be ultramafic or mafic plot low in zirconium, while suspected granites plot as expected within the dacite and rhyolite zones. The calc-silicate xenoliths plot high into the rhyolite zone. The remaining xenoliths plot within the dacite field suggesting an intermediate composition, these could be originated from intermediate igneous rocks or clastic sedimentary rocks. The organic rich metasedimentary xenolith plots on the boundary of the basalt and andesite fields. From Hallberg, 1976.

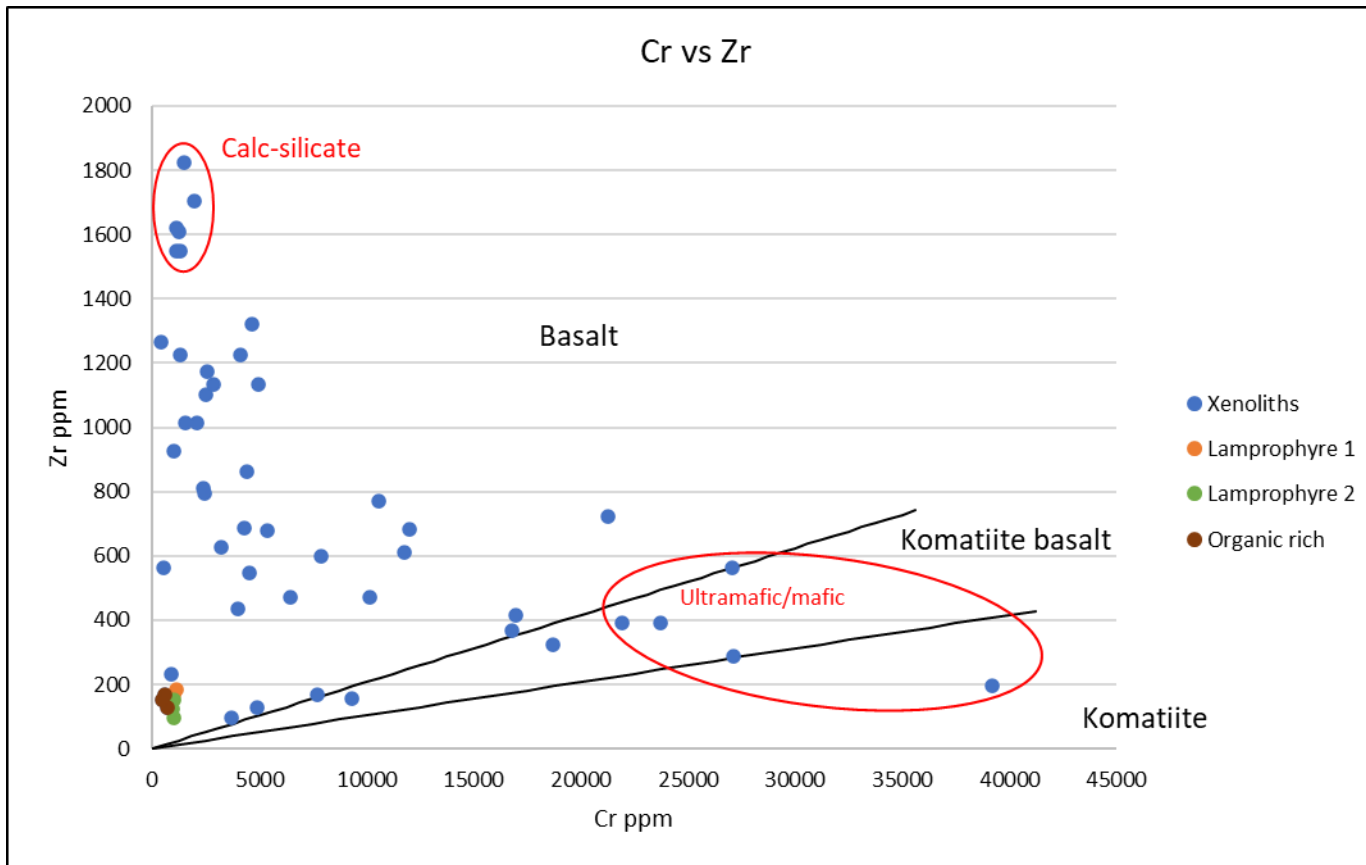


Figure 6.22. Xenoliths with chromium concentrations were plotted against the lamprophyres and show significantly greater and more variable concentrations of chromium and zircon. The ultramafic and mafic xenoliths plot as expected in the komatiite and komatiite basalt fields while the remaining samples plot into the basalt field. Note that ultramafic xenoliths are significantly higher zirconium and that both chromium and zirconium are enriched in all xenoliths. This may be due to diffusion between the lamprophyre and xenoliths. The organic rich metasedimentary xenolith plots with Lamprophyres 1 and 2 and needs further discrimination.

Chapter VII. Discussion

The results of field observations, petrography, and geochemistry are interpreted here. Origin of breccias, relationship between breccias and lamprophyres as well as the role of karst in weathering of the dike rock are discussed. Petrographic and whole rock geochemical data are used to interpret two different lamprophyres and semiquantitative pXRF data with petrography is used to infer the origin of xenoliths. These relationships allow inferences upon sapphire genesis.

Origin of breccias

Paleokarst

The two main types of karst breccia have been described in the Madison Group regionally. These karst types are seen at Yogo.

Descriptions of the monomict breccia in this research fits with the main collapse breccia described as containing mostly clasts of the host Mission Canyon Limestone of the Madison Group in literature (Middleton, 1961; Sando, 1974; Sando, 1988; Demiralin, 1993). Varied clasts to matrix ratio are seen both regionally and at Yogo, some are entirely clast supported and may have minor cement while others are matrix supported with varying degrees of quartz silt and sand within the matrix that is well cemented. Similar clast types and color for collapse breccias described in the Madison Group are seen at Yogo as described regionally. They are described as grey to tan in color and as fossiliferous and oolitic limestones with yellow to ochre colored weathering product. The fresh Madison Limestone fragments vary in color based upon their organic material content, the darker grey, the more organic material while the varied color of the weathering product is believed to be related to the amount of disseminated hematite or iron-hydroxides in the matrix of the breccias. Although not systematically assessed, it is qualitatively

interpreted that the monomict breccia is the most common solution collapse breccia found in the upper Madison Group.

The polymict breccia described in the study area fits the description of the second most dominant collapse breccia of the Madison Group discussed in the literature. These breccias are polymict and are dominated by semi-consolidated to the unconsolidated red siltstones, sandstones, and shales of the overlying Kibbey Formation. Regionally, the Kibbey Formation filled sink holes and enlarged joints in the upper 200 ft of the Mission Canyon Limestone and the overlying weight of the Kibbey caused collapse creating a mixture of monomict and polymict breccias in the top of the Madison Group. Although the Kibbey Formation only outcrops at the eastern section of the dike (Intergem cut), it is interpreted that the red polymict breccias underlying or adjacent to the monomict breccias are collapsed sediment cones and infilled areas composed of the semi-consolidated to unconsolidated red sandstones, siltstones, and shales of the Kibbey Formation.

Further support for interpretation of the breccias as paleokarst breccias is added by the morphology of the breccia bodies themselves. Crackle and rubble breccias are distinguished in karst and are recognized at Yogo. As defined in Chapter IV, crackle breccias are those that have had little clast displacement and retain clast orientation close to that of unbrecciated rock, while rubble breccias have significant clast displacement and represent the most intense zone of collapse. Crackle breccias generally occur at the top and along margins of collapsed caverns while rubble breccias occupy the center of the body.

At Yogo these breccias are exposed in the mined-out sections of the English Mine and Middle Mine cuts, as well as in limestone walls along the Yogo Gulch valley. It is interpreted here that the polymict breccias infilled sinkholes and enlarged joints which later collapsed either

because of the overlying weight of the Big Snowy Group that was then eroded away on the western end of the mine cut, or collapse occurred during Laramide uplift (Sando, 1974; 1988).

The monomict breccia is found in both crackle and rubble fabrics and may or may not overlie or flank the polymict breccia which is always of the rubble variety.

Dike emplacement influenced by paleokarst.

Paleokarst with lamprophyre inclusions

An unusual feature of the lamprophyre is that it is found as clasts and dikelets (only) in the polymict breccias a long and above strike of the dike. Previous work suggested these occurrences are either the result of collapse brecciation after dike intrusion or explosive brecciation at the time of intrusion (Dahy, 1988).

Field observations and petrography show that lamprophyre injected into the soft sediment of the polymict breccia. Aligned phlogopite and flow fabrics preserved in the weathered lamprophyre is seen along breccia clasts. While there is no quenching or evidence of an explosive reaction between the semi-consolidated to unconsolidated sediment, some of the breccia clasts have been fractured and calcite has crystallized along the fractures and around the margin of clasts. It is suggested here that forceful injection of magma during emplacement fractured these clasts and the heat from the dike caused expansion and subsequent shrinkage during cooling. Calcite preferentially crystallized in the voids of fractured clasts and along margins between the lamprophyre and breccia clasts.

Peperite

Peperite is a term applied to a rock that has both igneous and sedimentary components (McPhie et al, 1993; Skilling et al, 2002). It is interpreted to be the result of magma intruding or extruding over unconsolidated to semi-consolidated wet sediments. They commonly occur in denser concentrations of igneous rock near the magma/sediment boundary and can be dispersed up to 100 m from the intrusion. Peperites can be described as fluidal, blocky, or ragged and/or there may be a mixture of all three present (McPhie et al, 1993; Skilling et al, 2002).

Fluidal peperites are found where the sediments are fine and well sorted, this allows for an insulating vapor film to be formed evenly between the sediments and magma. The vapor film insulates the magma from the sediments and deadens the effects of quenching and chance of explosion (McPhie et al, 1993; Skilling et al, 2002). Morphology of the igneous clasts themselves can be lobate, pod-like, amoeboid to globular, and irregular in shape with veinlets and laminae (Fig. 7.1). Larger bodies may be connected by narrow dikes or “dike-lets.” The added pressure of the insulating vapor can fracture sedimentary clasts and aid in magma injection further into the sediments as flow fabrics and veinlets suggest (McPhie et al, 1993; Skilling et al, 2002).

Blocky peperites are usually found where the sediments are poorly sorted. Variable clasts size and sorting makes it difficult for an insulating vapor to be formed and sustained which results in explosive reactions between the water in the wet sediment and the intrusion (McPhie et al, 1993; Skilling et al, 2002). The magma is fragmented and forms angular igneous clasts that tend to have a jig-saw fit texture. There is commonly quenching associated with these peperites (McPhie et al, 1993; Skilling et al, 2002). In situations in which the pressure of overlying

sediments and/or water exceeds the critical pressure of water (~221 bars) an insulating vapor film can form and impede explosions, regardless of clast size and sorting (McPhie et al, 1993).

It is proposed here that the polymict breccia with lamprophyre inclusions is a previously undescribed karst peperite. Igneous inclusions in the polymict breccia at Yogo are a combination of blocky and angular clasts as well as bulbous, lensoidal, and lobate, with irregular blebs and veinlets amidst an array of semi-consolidated to unconsolidated, poorly sorted karst breccia. This combination of igneous clasts suggests that it is possible that there were both explosive and fluidal interactions occurred at Yogo (Figs. 4.9 and 4.13).

Angular blocks and fragments of lamprophyre seen within the poorly sorted polymict breccia at Yogo suggest explosive interactions, but no quenching textures were observed in the field. This may be due to the chemical instability of the glass would have formed if there had been quenching. It is more likely that fluidal processes dominated emplacement of karst peperite in the area as the shape and lack of quenching suggests. Upon closer inspection of karst peperite hand samples and thin sections the sedimentary clasts are commonly fractured with flow fabrics in the lamprophyre around and injected in between clasts sediments. Calcite veins have formed around most of the sedimentary clasts and may be evidence of where the insulating vapor film was, which buffered the effects of the magma interacting with the wet sediment. It is presumed that the eroded sedimentary rocks no longer present above the peperite provided the pressure to suppress explosive reactions at Yogo. An estimated 2640 – 4670 m (8660 – 15325 ft) of late Mississippian to Cretaceous sediments have been removed from the top, which would provide well over the needed pressure to force a fluidal reaction.

Role of karst on weathering

Madison Group karst aquifers have been described across parts of Montana, Wyoming, and South Dakota (Busby, 1983; Plummer et al, 1990). Secondary permeability was developed in the upper unit Mission Canyon Limestone as a result of the dissolution along joints and bedding planes (Plummer et al, 1990). Joints are regionally attributed to Laramide tectonics, and it is assumed to be the same here, a comprehensive study on the structural geology of the Yogo study area was outside the scope of this research. Dahy (1988) described northeast-southwest trending high angle normal and reverse faults that occurred before the Tertiary aged magmatism but gives no suggestion on what tectonic event they are associated with. Field relationships did not find evidence of post dike fault movement.

Early miners realized the importance of water in the role of weathering the lamprophyre and the relationship stands today (Voynick, 1985). The secondary permeability of joints, karst, and karst breccias at Yogo has allowed meteoric water to infiltrate to a depth of at least 310 feet in the Vortex Mine. Polymict breccias are exposed near the surface and to 130 feet below ground inside the Vortex mine. Where karst peperite has formed within the polymict breccias the lamprophyre is always weathered to a friable grey-green mass with flecks of biotite. It is assumed that the secondary porosity of the breccias and karst is what has been allowed to hold enough water to break down the blebs and veinlets of lamprophyre. The ease of which miners extract this material is why the polymict breccias seem to hold the most sapphires.

Inside the Vortex Mine lamprophyre dikes are seen in contact with solid Madison Group limestone, where no obvious contact metamorphism or quenching along dike margins has occurred. Weathering of the in-situ dike is less pervasive and is likely attributed to secondary permeability of joints at these depths. There are three weathering facies observed at depth from

near fresh rock to the most weathered: grey-green, red-maroonish, and yellow in color. A more comprehensive description of the weathering facies is given in the next section.

New information on the genesis of the dike

Petrographic and geochemical evidence suggests that there are two lamprophyre magma types at Yogo and that neither fit the currently prescribed name, ouachitite, as other researchers have suggested (Brownlow and Komorowski, 1988; Gauthier, 1995). Semiquantitative data from Portable X-ray Fluorescence, along with petrographic evidence, provide valuable information about where xenoliths may have come and the composition of ocelli. This new information allows us to speculate further upon sapphire origin.

Lamprophyres 1 vs 2

Petrography

Lamprophyres at Yogo differ in their texture, matrix to phenocryst ratio, mineral size, and abundance, as well as xenolith and ocelli content. Lamprophyre 1 has a microcrystalline matrix (30-48%) composed of carbonate, feldspathoids and analcime + microphenocrysts of subhedral to euhedral phlogopite while Lamprophyre 2 has a cryptocrystalline matrix (30-50%) composed of mostly devitrified glass with microphenocrysts of phlogopite and minor clinopyroxene.

Phenocrysts, ocelli, and xenoliths in Lamprophyre 1 are in concentrations of 15-45% clinopyroxene, 25-50% phlogopite, 1-4% analcime, $\leq 1\%$ altered olivine, ubiquitous apatite hosted in phlogopite as microscopic grains, $< 1-4\%$ ocelli, and 1-10% xenoliths. In Lamprophyre 2 phenocrysts, ocelli, and xenolith range from 20-80% clinopyroxene, 10-19% variably altered

olivine, 1% phlogopite, ubiquitous apatite hosted in microphenocrysts of biotite, with no ocelli, and 1-2% xenoliths.

Importantly Lamprophyre 1 has a microcrystalline matrix has more abundant phlogopite and has ocelli as well as more xenoliths while Lamprophyre 2 has a cryptocrystalline -devitrified glass- matrix, has more abundant clinopyroxene and olivine, lacks ocelli and has fewer xenoliths. The notable differences in mineralogy and texture suggests that they are different from each other. Geochemistry further supports this interpretation.

Geochemistry

There are subtle but consistent differences in major and trace element geochemistry between the lamprophyres at Yogo. While they are different, multielement spider diagrams show they are very similar and from the same source. The minette has been analyzed as representative of the other alkaline rocks of the Little Belt Mountains and behaves according to normal behavior and is not related to Yogo dike.

The two lamprophyres have similar contents of SiO₂, but Lamprophyre 1 has elevated concentrations of Al₂O₃ while Lamprophyre 2 has elevated concentrations of FeO and the ratio CaO/Al₂O₃. Both lamprophyres have similar Sm concentrations, but Lamprophyre 2 has elevated Ce and La (LREEs) as well as Zr and Hf. This suggests that Lamprophyre 2 has undergone greater fractionation than Lamprophyre 1 or is the result of lower percentage partial melt.

Differences both in chemistry and petrography support that there are two lamprophyres in the area. Lamprophyre 1 is higher in Al₂O₃, is coarser grained with a microcrystalline ground mass and has more phlogopite. Lamprophyre 2 is higher in FeO and the ratio Ca/Al₂O₃, has elevated LREEs and has an aphanitic, glassy ground mass and more clinopyroxene phenocrysts.

Mineral controls on geochemistry

Mineral controls on geochemistry help to explain the variation in geochemistry within the lamprophyres, specifically that variation is a result of fractionation of, or the accumulation of these minerals. The minerals concerned here are clinopyroxene, biotite, olivine, apatite, and zircon. Elevated concentrations of both trace and major elements were considered when investigating mineral controls. Chromium vs titanium as a marker for clinopyroxene because both are expected to be in high concentration, the same logic is used for the following elemental pairs potassium vs titanium and potassium vs rubidium for biotite, nickel vs magnesium for olivine, phosphorous vs REEs for apatite, and zirconium vs hafnium for zircon.

The most abundant phenocrysts overall, clinopyroxene and phlogopite, do not play as big of a role in element distribution as suspected. Clinopyroxene plays host to both titanium and chromium, the point distribution of data from Lamprophyres 1 and 2 on figure 6.18 suggests that clinopyroxenes are chemically similar and petrographic thin section supports this. Phlogopite also does not play a strong role in elemental distribution. The lack of strong correlation in potassium vs titanium and potassium vs rubidium suggests another mineral besides phlogopite controls these elements, possibly a feldspathoid. Olivine hosts both nickel and magnesium but since it is largely altered geochemical data on the role it plays is inconclusive. While Lamprophyres 1 and 2 have differing mineralogy (Lamprophyre 1 has more phlogopite and Lamprophyre 2 has more clinopyroxene) these mineralogical differences are not reflected when investigating the mineral controls on geochemistry.

Although apatite is microscopic and only seen in the pleochroic rims of phlogopite it plays a strong role in REE distribution. Elemental substitution between phosphorous and cerium,

as well as other light REEs, shows a constant positive ratio (Fig. 6.16). These plots also show that Lamprophyre 2 is more elevated in LREEs and thus more fractionated than Lamprophyre 1.

The mineral zircon is assumed to play a role in abnormal (background) concentrations of hafnium and zirconium. As previously discussed in Chapter 6, the relationship between the two elements differs from what is normally seen in igneous rocks – hafnium is increasing as zirconium decreases. Most igneous rocks have an average hafnium to zirconium ratio of 33:1, but a negative correlation is found at Yogo with an average ratio of 27:1 (Jones III et al, 2017). The decoupling of Hafnium from Zirconium and the ratios of Zr/Hf and Zr/Zr^* using Jorgensen et al (2018) and comparing the two ratios indicates that an extremely small amount of partial melting may have affected the Yogo dike. Furthermore, there is -again- a segregation between Lamprophyre 1 samples and Lamprophyre 2 samples. Lamprophyre 2 has undergone even lower partial degrees of melting than Lamprophyre 1. It is unclear where and when the partial melting has occurred. There are two possibilities; small amounts of partial melting occurred in the mantle, or it was the result of the magma picking up and partially melting crustal rocks prior to dike emplacement. Further research is needed to explore this phenomenon.

Classifying the Yogo dike

Total Alkali Silicate (TAS) plots show that the Yogo dike is the most silica undersaturated of the samples from the Central Montana Alkaline Province that have been analyzed (Dudas, 1991; O'Brien, 1992; DeWitt et al, 1996). Further discrimination is needed when describing the lamprophyre at Yogo. It is important to note that Rock's (1991) classification scheme is used here, but Streckeisen (1979) also developed a classification scheme.

Using classification plots from Rock (1991) it has been determined that Lamprophyres 1 and 2 of this research, as well as the samples from Clabaugh (1952), Dahy (1988), and Gauthier (1985) plot as broadly alkaline but close to and inside ultramafic lamprophyre fields in plots MgO vs CaO and $\text{Fe}_2\text{O}_3/\text{Al}_2\text{O}_3$ vs $\text{K}_2\text{O}/\text{Al}_2\text{O}_3$. The trace element classification plot Sm vs Ce/Yb does not have representative fields for ultramafic and alkaline lamprophyres and rocks from Yogo plot in an undefined area and across the lamproite boundary. These discrimination plots suggest that lamprophyres at Yogo cannot be described as purely alkaline or ultramafic as Brownlow and Komorowski (1988) and Gauthier (1995) suspected but may be a hybrid of the two.

Hand sample and petrographic evidence supports the idea that the lamprophyres are not simply ouachatites of the ultramafic lamprophyres or monchiquites of the alkaline lamprophyres. Ouachatites are identified as having combinations of olivine, clinopyroxene, phlogopite, amphiboles, and primary carbonate in a matrix of similar composition and monchiquites are described as having phenocrysts of olivine, kaersutite, titanaugite, and titanobiotite with a ground mass of similar composition with feldspathoids, analcime, no olivine and may have glass, as an essential phase (Rock, 1991).

The abundance of glass in the matrix of Lamprophyre 2 samples and the presence of analcime in Lamprophyre 1 samples supports the idea that they have monchiquite characteristics (Rock, 1991). Phlogopite and clinopyroxene suggests ouachitite and olivine phenocrysts, though altered, across the samples could suggest either an ouachitite or monchiquite. This suggests that the Yogo intrusion is a hybrid ouachitite-monchiquite, but electron microprobe would be needed to look at the titanium content in biotite and the mineralogy of the matrix to confirm if this is the case. In view of abundance, alteration, and partial melting of xenoliths, another suggestion as to

why Yogo appears to be a hybrid lamprophyre a could be because of the partial melting and metasomatism of xenoliths.

Weathering

Weathering of the Yogo dike is important because it is the main process needed to extract intact sapphires from the lamprophyre, one control on this process is depth. Lamprophyre 1 was only clearly viewed as irregular inclusions in the polymict breccia in the near surface under monomict breccias while Lamprophyre 2 was only clearly viewed at depths between 30 – 100 meters below ground. Rocks at lower depths are saturated for a greater proportion of the time, hence Lamprophyres 1 and 2 appear to weather in different ways. Lamprophyre 1 is found near the surface as grey-green friable masses with flecks of phlogopite and sea green to apple green flecks of weathered clinopyroxene, it is found as igneous clasts in the karst peperite. Exposed portions of the dike underground show fresh Lamprophyre 2 at depth grading from near black to a grey-green rock and if weathering is pervasive enough it will become a clay rich maroon-red rock and if conditions persist a clay rich yellow rock. The presence of sea green flecks of presumably altered clinopyroxene may be present in all facies. When hefted the yellow rock is the lightest, followed by red, grey-green, and the densest is the fresh dike rock, this suggests significant leaching has occurred during weathering.

Geochemical data supports the weathered grey-green lamprophyre is closely related to Lamprophyre 1 as it plots near unweathered samples on major and trace element plots. It has also undergone the least amount of leaching, while the red and yellow samples associated with Lamprophyre 2 have undergone the most. All weathered lamprophyre samples show reduction of major elements SiO₂ and MgO with enrichment of CaO, which may be residual or addition. TiO₂ is immobile as expected and increases in concentration.

Rare Earth Elements and REE ratios Ce, La, and Hf/Ce are being enriched at constant ratios creating a recognizable trend away from fresh lamprophyre samples which suggests they can be used as a geochemical marker of weathered lamprophyre.

Differences in weathering may have to do with the amount of water and time the different lamprophyres are exposed to said water. Past mining operations have relied on laying the dike rock out over the winter months to expose it to snow and rain, which in turn breaks down the rock and releases sapphires. It is presumed that the longer the lamprophyre rocks soak, the more they break down.

More intense weathering has occurred along underground portions of the Lamprophyre 2 dike, this may be because karst, karst breccias, and joints carry meteoric water down to depths of at least ~94.5 m (310') from the surface. It is assumed here that some parts of the exposed dike underground have water supplied to it along the contact between the host Madison Group and the lamprophyre dike at a relatively constant rate. Under these conditions more intense weathering can occur locally. Devitrification of glass in the matrix of fresh Lamprophyre 2 samples may also play a role in intense weathering. Near surface Lamprophyre 1 is not exposed to as much water because water drains further down, but enough weathering has occurred that it is easily dug into with a rock pick. The lesser degree of weathering may also have to do with abundance of clay in the karst peperite, which may inhibit the flow of water to lamprophyre clasts.

Origin of components of the dike

Portable X-Ray Fluorescence (pXRF) was used to semi quantitatively analyze ocelli and xenoliths found in the lamprophyres. Mineralogy and geochemistry cannot be used to directly identify xenolith types because they have been altered during incorporation into the lamprophyre

and therefore may not be exactly as they were pre-incorporation. For instance, potassium from the lamprophyre melt may alter the plagioclase in a mafic xenolith to potassium feldspar, making identification tricky. Also, felsic xenoliths will melt more than mafic xenoliths which can change the appearance and chemistry of the overall xenolith in varying degrees of intensity. Trace element chemistry and mineralogy can be used to speculate their origins.

Ocelli

Chemical variability suggests that while ocelli do have near a pure carbonate composition in some respects they also demonstrate “fractionation” and vary in concentrations of SiO_2 and $\text{Fe}_2\text{O}_3(\text{T})$. Although in hand sample they look similar, this suggests they are not breccia clasts or recrystallized limestone, further geochemical data is needed to confirm (isotopes). In thin section some ocelli are pure calcite, but others are zoned. The outer margins may be a mixture of feldspathoids and amphiboles that have been largely replaced by calcite, followed by coarse calcite, fine calcite, with a core of zeolites. It is unclear if the ocelli are related to xenoliths.

Xenoliths

Different amounts of alteration may be a marker of how long the xenolith has been in the magma and the chemical interactions between the host lamprophyre and xenolith. The longer a xenolith has been in the magma the thicker the reaction rim will be (and vice versa), a thin reaction rim may equate to a shorter time in the magma. Chemistry is also a factor, if a more felsic xenolith is incorporated into the lamprophyre, it will more than likely have the most alteration, while the mafic/ultramafic xenoliths will have the least. Classification of the xenoliths is based on immobile element ratios and is discussed in the coming paragraphs.

Ultramafic xenolith types are clinopyroxenites, and biotite clinopyroxenites with or without spinel. There is no reaction rim found on these xenoliths. Mafic xenoliths contain a mixture of aluminous and mafic minerals such as muscovite, clinopyroxene, and potassium feldspar with minor spinel and garnet. This mixture is presumed to be the result of alteration after incorporation into the lamprophyre magma. For instance, the addition of potassium alters plagioclase to potassium feldspar and that in turn may alter to muscovite. They are enriched in titanium and chromium which supports a mafic origin. There is evidence of melt in the mafic xenoliths which is expressed by small inclusions of glass in the ground mass of known mafic xenoliths seen in thin section. This also suggests that the lamprophyre magma was high enough in temperature to produce melting in the xenoliths.. Mineralogy and elevated concentrations of chromium in ultramafic xenoliths and titanium in mafic xenoliths suggests that these xenoliths may have originated in the upper mantle.

Felsic xenoliths are found as partially melted granitic clasts with thick irregular shaped reaction rims of a feldspathoids, calcite and amphibole that has been largely altered. Granitic clasts have irregular to amoeboid shaped quartz and plagioclase grains with black to brown devitrified glass found along grain boundaries. Geochemically they have elevated silica and zirconium, which supports a granitic origin. These xenoliths more than likely came from the lower crust.

Individual xenoliths composed of quartz are found to be coarsely crystalline, with some only containing one individual crystal, that have thick reaction rims composed of feldspathoids, and amphibole that has been largely replaced by calcite. Quartz xenoliths are interpreted to have originated from quartz veins from an unknown level.

Calcsilicate xenoliths are rounded to irregular shaped and generally do not have a reaction rim which suggests that it was in equilibrium with the host lamprophyre when it was emplaced. Their mineralogy is unclear as most of the matrix of the xenoliths is isotropic, but it clearly has hornblende, calcite and feldspathoids. Interestingly, its mineralogy in thin section looks similar to the mineralogy of some reaction rims of other xenoliths as well as the outer zones of some ocelli and hence possibly been completely replaced. Further research needs to be done to identify where these xenoliths may have come from. It is important to note that the mineralogy of the calcsilicate xenoliths and the reaction rims of xenoliths and ocelli are similar to metasomatic fenites found around carbonatites of alkaline intrusions at the Rainy Creek Alkaline-Ultramafic Igneous Complex (Boettcher, 1967).

Metasedimentary xenoliths of recrystallized limestone and the bedded ashed crude oil sedimentary rock were found as float and are presumed to have been picked up during the final stages of emplacement and are from the immediately underlying sedimentary units or underlying Belt Supergroup.

Known granites and ultramafic xenoliths plot in their respective fields according to figure 6.21, although they are all elevated in Zr. Most of the xenoliths plot in the dacite field which suggest they have intermediate compositions. All the xenoliths are elevated in chromium and zirconium that could have been introduced by the lamprophyre through diffusion. Stable isotopes are needed to constrain xenolith types and origins. Specifically, oxygen isotopes would be very distinct in mantle, crust, and sedimentary rocks.

Implications for the origin of the sapphires

The origin of the sapphires was not a central concern of this work. However, the results allow certain interpretations to be made. The array of xenoliths outlined above acts as a profile of the upper mantle and lower crust. Sapphires could be xenocrysts or components of xenoliths. No sapphires were seen associated with xenoliths, so it is unclear if they were picked up from another source as Meyer and Mitchell (1988), Dahy (1991), Gauthier (1995), and Mychaluk (1995) have suggested. Some of the granitic xenoliths have been partially melted which supports Palke's (2016) assumption that there was a more felsic and aluminum rich melt incorporated into the lamprophyre melt that could have allowed for the formation of sapphires. An alternative origin of sapphires could be tied to the distinct chemistry of the Yogo Dike compared to other alkaline rocks in the area. Sapphires may be hosted in the Yogo dike because its low silica composition promoted specific reactions within the melt that allowed for sapphire crystallization.

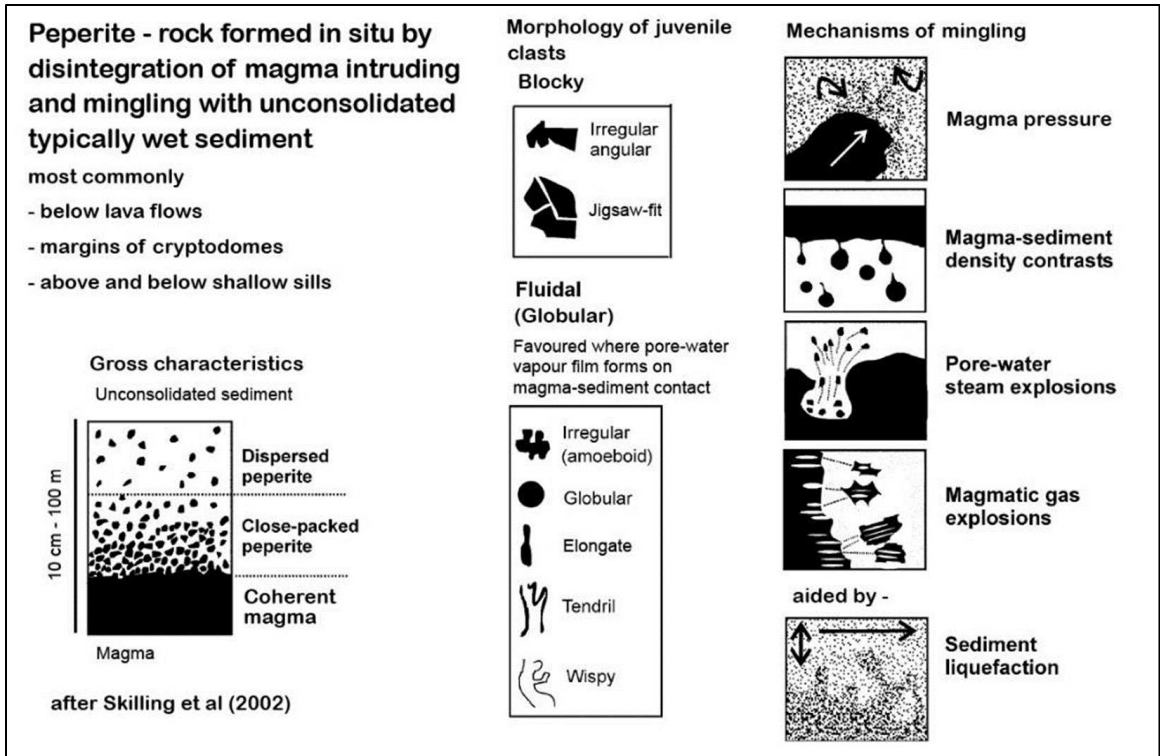


Figure 7.1. Diagram illustrating the various clast textures found in blocky and fluidal peperite formation processes.

Chapter VIII: Conclusions

While the Yogo sapphire deposit remains incompletely understood this research has shed light on the relationship between lamprophyre and breccias and lamprophyre and its components. It has been proven that: (1) Geochemically, texturally, and mineralogically there are two distinct lamprophyres at Yogo and while they appear to be a hybrid between monchiquite and an ouachitite, ouachitite is the most fitting name. (2) The Yogo dike intruded into an area with a variety of karst features which resulted in low-temperature karst peperite formation in polymict rubble breccias. (3) Karst features, such as collapse breccias (both monomict and polymict), joints and natural passageways allowed local weathering at depth. (4) The origin of components seen in the dike have been determined to be an array of xenoliths profiling the upper mantle, lower crust, the Belt Supergroup as well as the immediate sedimentary sequence underlying the deposit and that these xenoliths have been mineralogically and chemically altered as a result of reaction with the dike magma (5) Evidence of melt in felsic xenoliths may support the suggestion of Palke (2016) that sapphires were formed as a result of the peritectic melting between the lamprophyre and aluminum rich xenoliths such as anorthosite or granite. Ocelli are proven both petrographically and geochemically to be unrelated to limestone xenoliths, hence could be immiscible carbonatite melt.

Suggested research

While this research has answered the original questions posed, it has created more questions that need to be assessed. While pXRF has given clues as to the origins of xenoliths, they are incompletely answered. Geothermometry and geobarometry by Electron Microprobe on a variety of xenolith types can give us more information about the depths and origins of the

xenoliths. Stable isotopes of xenoliths can further constrain depths and origins of xenoliths and stable isotopes of ocelli can confirm if they are from carbonatite melts. In view of the karst control on water infiltration a study of structural controls on karst may lead to an exploration tool to determine where weathered lamprophyre from which sapphires may be easily extracted can be found at depth.

References

- Baker, D.W., 1991, Laramide Tectonics and Magmatism in The Central Montana Alkalic Province: Little Belt Mountains, *in* Baker, D.W., and Berg, R.B., eds, Guidebook: Central Montana Alkalic Province: Montana Bureau of Mines and Geology, Special Publication 100, p. 128-130.
- Berger, A.L., and Berg, R.B., 2006, The Silver Bow sapphire occurrence, Montana: Evidence for a volcanic bedrock source for Montana's alluvial sapphire deposits: *Economic Geology*, v. 101, p. 679-684.
- Berg, R.B, and Dahy, J.P, 2002, Montana sapphires and speculation on their origin, *in* Scott, P.W. and Bristow, C.M., eds., *Industrial Minerals and Extractive Industry Geology*: Geological Society, London, p. 199-204.
- Boettcher, A.L., 1967, The Rainy Creek Alkaline-ultramafic Igneous Complex near Libby, Montana I: Ultramafic Rocks and Fenite: *The Journal of Geology*, v. 75, no. 5, p. 524-553.
- Reynolds, M.W., and Brandt, T.R., compilers, 2007, Preliminary geological map of the White Sulphur Springs 30' x 60' Quadrangle, Montana, scale 1:100,000.
- Brownlow, A.H. and Komorowski, J., 1988, Geology and Origin of the Yogo Sapphire deposit, Montana: *Economic Geology*, v. 83, p. 875-880.
- Busby, J.F., Lee, R.W., Hanshaw, B.B., 1983, Major Geochemical Processes Related to the Hydrology of the Madison Aquifer System and Associated Rocks in Parts of Montana, South Dakota, and Wyoming: U.S. Geological Survey, Water-Resources Investigation Report 83-4093.
- Clabaugh, S.E., 1952, Corundum Deposits of Montana: *Geological Survey Bulletin* 983, p. 6-21.
- Dahy, J., 1988, The Geology and Igneous Rocks of the Yogo Sapphire Deposit and the Surrounding Area [Master Thesis]: Montana College of Mineral Science and Technology Butte, Montana, p. 101.
- Dahy, J., 1991, Geology and Igneous Rocks of the Yogo Sapphire Deposit, Little Belt Mountains, Montana, *in*, Baker, D.W., and Berg, R.B., eds, Guidebook: Central Montana Alkalic Province: Montana Bureau of Mines and Geology, Special Publication 100, p. 45-54.
- Demiralin, A.S., Hurley, N., Oesleby, T.W., 1993, Karst Breccias in the Madison Limestone (Mississippian), Garland Field, Wyoming, *in*, Fritz, R.D., Wilson, J.L., and Yurewicz, D.A., eds., *Paleokarst related Hydrocarbon reservoirs*: Society of Economic Paleontologists and Mineralogists, United States, p 101-118.
- DeWitt, E.D., Foord, E.E., Zartman, R.E., Pearson, R.C., and Foster, F., 1996, Chronology of Late Cretaceous Igneous and Hydrothermal Events at the Golden Sunlight Gold-Silver Breccia Pipe, Southwestern Montana: U.S. Geological survey bulletin 2155, 53 p.

- Dudas, F.O., 1991, Geochemistry of Igneous Rocks from the Crazy Mountains, Montana, and Tectonic Models for the Montana Alkalic Province: *Journal of Geophysical Research*, v. 96, p. 13,261-13,277.
- Evans, K.V., 1986, Middle Proterozoic deformation and plutonism in Idaho, Montana, and British Columbia, *in*, Roberts, S.M, ed. Belt Supergroup: A Guide to Proterozoic Rocks of Western Montana and Adjacent Areas. Montana Bureau of Mines and Geology Special Publication 94, p. 237-244.
- Garland, M.I., 2002, The alluvial sapphire deposits of western Montana [Master Thesis]: Department of Geology, University of Toronto, p. 562.
- Gauthier, G., 1995, Mineralogy, geochemistry, and geochronology of the Yogo Dike Sapphire Deposit, Montana [Master Thesis]: Department of Geological Sciences, University of British Columbia.
- Greene, E.A., and Rahn, P.H., 1995, Localized Anisotropic Transmissivity in Karst Aquifer: *Ground Water*, p. 806-816.
- Hallberg, J.A., 1984, A geochemical aid to igneous rock type identification in deeply weathered terrain: *Journal of Geochemical Exploration*, v. 20, p. 1-8.
- Harlan, S.S., 1996, Timing of emplacement of the sapphire-bearing Yogo dike, Little Belt Mountains, Montana: *Economic Geology*, v. 91, p. 1159-1162.
- Horr, C.A., Myers, A.T., Dunton, P.J., and Hyden, H.J., 1961, Uranium and Other Metals in Crude Oils: *Geological Survey Bulletin* 1100, 124 p.
- Jones III, J.V., Piatak, N.M., and Bedinger, G.M., 2017, Zirconium and hafnium, *in* Schulz, K.J., DeYoung, Jr., J.H., Seal, R.R., and Bradley, D.C., eds, Critical mineral resources of the United States-Economic and environmental geology and prospects for future supply: U.S. Geological Survey Professional Paper 1802-V, 38 p.
- Jørgensen, T.R.C., Tinkham, D.K., Leshner, C.M., and Petrus, J.A., 2018, Decoupling of Zr-Hf during contact metamorphic anatexis of metabasalts and timing of zircon growth, Sudbury, Canada: *Geology*, v. 46, p. 159-162.
- Kunz, G.F., 1897, On the Sapphires from Montana with Special Reference to Those from Yogo Gulch in Fergus County: *American Journal of Science*, Fourth Series, v. III, p. 417-419.
- Luebking, G.A., Longman, M.W., and Carlisle, W.J., 2001, Unconformity-related chert/dolomite production in the Pennsylvanian Amsden Formation, Wolf Springs fields, Bull Mountains basin of central Montana: *American Association of Petroleum Geologists*, v. 85, p. 131-148.
- Ma, G.S.-K., Wang, K., Malpas, J., Iizuka, Y., Xenophontos, C., Turkmani, A.A., Chan, G., H.-N., Usuki, T., Chan, Q.H.-S., 2015, Melt Pockets and Spongy Clinopyroxenes in Mantle Xenoliths from the Plio-Quaternary Al Ghab Volcanic Field, NW Syria: Implications for

- the Metasomatic Evolution of the Lithosphere, *in*, Khan, A., Deschamps, F. ed. The Earth's Heterogeneous Mantle. Springer Geophysics, p. 205-257.
- Marvin, R.F., Witkind, I.J., Keefer, W.R., Mehnert, H.H., 1973, Radiometric Ages of Intrusive Rocks in the Little Belt Mountains, Montana: Geological Society of American Bulletin, v. 84, p. 1977-1986.
- McPhie, J., Doyle, M., and Allen, R., 1993, Volcanic textures: a guide to the interpretation of textures in volcanic rocks: CODES Key Centre, Hobart, Australia, 196 p.
- Meyer, H.O.A., and Mitchell, R.H., 1988, Sapphire-bearing ultramafic lamprophyre from Yogo, Montana: A ouachitite: Canadian Mineralogist, v. 26, p. 81-88.
- Middleton, G.V., 1961, Evaporite breccias from the Mississippian of southwest Montana: Journal of Sedimentary Petrology, v. 31, p. 189-195.
- Morrow, D.W., 1982, Descriptive field classification of sedimentary and diagenetic breccia fabrics in carbonate rocks: Bulletin of Canadian Petroleum Geology, v. 30, p. 227-229.
- Mychaluk, K.A., 1995, The Yogo Sapphire Deposit: Gems and Gemology, v. 31, p. 28-41.
- Obermajer, M., Osadetz, K.G., Fowler, M.G., Silliman, J., Hansen, W.B., and Clark, M., 2002, Delineating compositional variabilities among crude oils from Central Montana, USA, using light hydrocarbon and biomarker characteristics: Organic Geochemistry 33, p. 1343-1359.
- O'Brien, H.E., Irving, A.J., and McCallum, I.S., 1991, Eocene potassic magmatism in the Highwood Mountains, Montana: Petrology, geochemistry, and tectonic implications: Journal of geophysical research, v. 96, p. 13237-13260.
- Paces, J.B., Palmer, M.V., Palmer, A.N., Long, A.J., and Emmons, M.P., 2020, 300,000 yr history of water-table fluctuations at Wind Cave, South Dakota, USA—Scale, timing, and groundwater mixing in the Madison Aquifer: GSA Bulletin, v. 132, p. 1447-1468.
- Palke, A.C., Renfro, N.D., and Berge, R.B., 2016, Origin of sapphires from a lamprophyre dike at Yogo Gulch, Montana, USA: Clues from their melt inclusions: Lithos 260, p. 339-344.
- Palke, A.C., Renfro, N.D., and Berge, R.B., 2017, Melt inclusions in alluvial sapphires from Montana, USA: Formation of sapphires as restitic component of lower crustal melting?: Lithos, p.43-53.
- Palke, A.C., Wong, J., Verdel, C., Avila, J.N., 2018, A common origin for Thai/Cambodian rubies and blue and violet sapphires from Yogo Gulch, Montana, U.S.A.: American Mineralogist, v. 103, p. 469-479.
- Parker, S.D., and Pearson, D.M., 2021, Pre-Thrusting Stratigraphic Control on the Transition From a Thin-Skinned to Thick-skinned Structural Style: An Example From the Double-Decker Idaho-Montana Fold-Thrust Belt: Tectonics 40.

- Plummer, N.L., Busby, J.F., Lee, R.W., 1990, Geochemical Modeling of the Madison Aquifer in Parts of Montana, Wyoming, and South Dakota: *Water Resources Research*, v. 26, p. 1981-2014.
- Pratt, J.H., 1897, On the Crystallography of the Montana Sapphires: *American Journal of Science*, Fourth series, v. III, p. 424-425.
- Prisson, J.H., 1897, On the Corundum-bearing Rock from Yogo Gulch, Montana: *American Journal of Science*, Fourth series, v. III, p. 421-423.
- Renfro, N.D., Palke, A.C., and Berg, R.B., 2018, Gemological Characterization of Sapphires from Yogo Gulch, Montana: *Gems and Gemology*, v. 54, p. 184-201.
- Rock, N.M.S., 1991, *Lamprophyres*: Springer Science+Business Media New York, originally published by Blackie and Son Ltd, 285 p.
- Sandberg, C.A., 1965, Nomenclature and correlation of lithologic subdivisions of the Jefferson and Three Forks Formations of Southern Montana and Northern Wyoming: *Geological Survey Bulletin* 1194-N, 18 p.
- Sando, W.J., 1974, Ancient solution phenomena in the Madison Limestone (Mississippian) of north-central Wyoming: *Journal of Research of the U.S. Geological Survey*, v. 2, p. 133-141.
- Sando, W.J., 1988, Madison Limestone (Mississippian), in, James, N.P., and Choquette, P.W., eds, *Paleokarst: A Geologic Synthesis*, p. 256-277.
- Sando, W.J., and Dutro, JR. J.T., 1974, Type sections of the Madison Group (Mississippian) and its Subdivisions in Montana: *Geological Survey Professional paper* 842.
- Sangster, D.F., 1988, Breccia-Hosted Lead-Zinc Deposits in Carbonate Rocks, James, N.P., and Choquette, P.W., eds, *Paleokarst: A Geologic Synthesis*, p. 102-116.
- Sarkar, A., Brophy, J.G., Ripley, E.M., Li, C., and Kamo, S.L., 2009, Geochemical and isotopic studies of the Lady of the Lake Intrusion and associated tobacco root Batholith: Constraints on the genetic relation between Cretaceous mafic and silicic magmatism in Southwestern Montana, *Lithos* 113, p. 555-569.
- Skilling, I.P., White, J.D.L., McPhie, J., 2002, Peperite: a review of magma-sediment mingling: *Journal of Volcanology and Geothermal Research* 114, p. 1-17.
- Streckeisen, A.B., and Le Maitre, R.W., 1979, A Chemical Approximation of the Modal QAPF Classification of the Igneous Rocks: *Neues Jahrbuch Für Mineralogie*, v. 136, 169 p.
- Voynick, S.M., 1985, *Yogo the Great American Sapphire*: Mountain Press Publishing Company, Missoula Montana, 215 p.
- Vuke, S.M. (compiler), 2015, *Geologic Road Map of Montana*, Montana Bureau of Mines and Geology GM 65, scale 1:1,000,000

- Vuke, M.S., Porter, K.W., Lonn, J.D., and Lopez, D.A., 2007, Geologic map of Montana; Montana Bureau of Mines and Geology, Geologic Map 62.
- Weed, W.H., 1899, Geology of the Little Belt Mountains, Montana: United States Geological Survey 20th Annual Report, p. 257-581.
- Winston, D., 1986, Stratigraphic correlation and nomenclature of the Middle Proterozoic Belt Supergroup, Montana, Idaho, and Washinton, *in*, Roberts, S.M, ed. Belt Supergroup: A Guide to Proterozoic Rocks of Western Montana an Adjacent Areas. Montana Bureau of Mines and Geology Special Publication 94, p. 69-84.
- Woodward, L.A, 1991, Metallic Mineralization in the Yogo and Running Wolf Mining Districts, Little Belt Mountains, Montana, *in*, Baker, D.W., and Berg, R.B., Guidebook: Central Montana Alkalic Province: Montana Bureau of Mines and Geology, Special Publication 100, p. 19-27.

APPENDICES

APPENDICES: TABLE OF CONTENTS

Appendix 1.1: Sample locations: Northeast of study area185
Appendix 1.2: Sample locations southwest of study area.....186
Appendix 1.3: Sample location of minettes187
Appendix 2.1: Analytical results for unweathered lamprophyres188
Appendix 2.2: Analytical results for weathered lamprophyres190
Appendix 2.3: Analytical results from pXRF on xenoliths, ocelli, clasts, and/or matrix192
 Appendix 2.3a: Elements Mg-Si.....192
 Appendix 2.3b: Elements Ca-v196
 Appendix 2.3c: Elements Cr-Fe.....200
 Appendix 2.3d: Elements Co-Cu204
 Appendix 2.3e: Elements Zn-Rb.....208
 Appendix 2.3f: Elements Sr-Zr.....212
 Appendix 2.3g: Elements Nb-Rh.....216
 Appendix 2.3h: Elements Pb-Cd.....220
 Appendix 2.3i: Elements Sn-W224



Appendix 1.1 Sample locations on the northeast side of the study area. Purple: Peperite, blue: lamprophyre, yellow: metasedimentary xenoliths. All lamprophyre samples are associated with the main dike and have the initials EM in the sample number.



Appendix 1.2. Sample locations on the southwest side of the study area. Purple: Peperite, blue: lamprophyre, red: karst breccias. Lamprophyre samples were taken from both the Vortex Mine (VM) dump and from the interior of the mine (southernmost yellow “x”). Kelly Coulee (KC) samples were from a small dump inside the coulee. English Mine (EM) samples were taken in front of the portal into the American/Kunisaki tunnel (northernmost yellow “x”) and peperites associated with the main dike were taken along strike of the lamprophyre intrusion.



Appendix 1.3. Sample location of minettes relative to Sapphire Village to the immediate northeast and the Yogo dike to the southwest.

Appendix 2.1. Analytical results for unweathered lamprophyre samples.

Sample: EM = English Mine, KC = Kelly Coulee, VM = Vortex, M = minette

FUS-ICP – Fusion Inductively Coupled Plasma Mass Spectrometry, INAA - Instrumental Neutron Activation Analysis, TD-ICP - Near-Total Digestion

Inductively Couple Mass Spectrometry

Analyte Symbol	Unit	Detection Limit	Analysis Method	EM17	EM4	EM26	KC1	EMOct c	VM9	VM7	VM10a	M1+X	M1-X
SiO2	%	0.01	FUS-ICP	38.85	39.52	40.39	39.18	38.72	37.13	36.09	37.75	52.32	52.86
Al2O3	%	0.01	FUS-ICP	10.82	10.68	11.37	11.21	9.52	8.74	8.63	10.78	12.87	13.65
Fe2O3(T)	%	0.01	FUS-ICP	7.66	7.25	7.66	7.1	7.5	8.14	8.02	7.14	7.57	8.07
MnO	%	0.01	FUS-ICP	0.15	0.13	0.14	0.13	0.14	0.15	0.15	0.14	0.11	0.11
MgO	%	0.01	FUS-ICP	10.33	11.05	11.53	10.98	9.95	12.59	12	8.4	5.71	5.89
CaO	%	0.01	FUS-ICP	16.88	16.7	15.13	15.98	16.05	15.27	14.53	17.76	6.75	7.09
Na2O	%	0.01	FUS-ICP	1.23	1.26	1.02	1.54	1.17	1.52	0.74	2.18	2.91	2.93
K2O	%	0.01	FUS-ICP	2.07	2.26	2.7	2.04	2.54	2.23	3.93	1.5	4.93	4.95
TiO2	%	0.005	FUS-ICP	0.999	1.052	1.035	1.009	1.088	1.052	1.052	1.049	0.716	0.753
P2O5	%	0.01	FUS-ICP	1.2	1.13	1.19	1.23	1.28	1.35	1.37	1.25	0.5	0.54
LOI	%		GRAV	8.01	6.71	7.59	8.15	10.44	9.76	11.35	10.6	4.15	3.67
Total	%	0.01	FUS-ICP	98.2	97.74	99.75	98.54	98.42	97.94	97.86	98.54	98.53	100.5
Au	ppb	5	INAA	< 5	< 5	< 5	< 5	< 5	< 5	14	< 5	< 5	< 5
Ag	ppm	0.5	MULT INAA / TD-ICP	< 0.5	< 0.5	< 0.5	< 0.5	< 0.5	< 0.5	< 0.5	< 0.5	< 0.5	< 0.5
As	ppm	2	INAA	5	< 2	< 2	< 2	2	4	3	7	< 2	< 2
Ba	ppm	3	MULT INAA/FUSICP	3320	3630	3190	3010	3130	3910	3600	4420	1920	1810
Be	ppm	1	FUS-ICP	2	2	2	2	2	2	2	3	3	2
Bi	ppm	2	TD-ICP	< 2	< 2	< 2	< 2	< 2	< 2	< 2	< 2	< 2	< 2
Br	ppm	1	INAA	< 1	< 1	< 1	< 1	< 1	< 1	< 1	< 1	< 1	< 1
Cd	ppm	0.5	TD-ICP	< 0.5	< 0.5	< 0.5	< 0.5	< 0.5	< 0.5	< 0.5	< 0.5	< 0.5	< 0.5
Co	ppm	1	INAA	32	33	33	33	34	38	35	37	24	22
Cr	ppm	1	INAA	850	1110	897	993	1030	1020	954	871	350	384
Cs	ppm	0.5	INAA	244	155	97.8	309	123	197	36.9	247	1.4	< 0.5

Cu	ppm	1	TD-ICP	68	67	67	64	72	72	71	75	56	58
Hf	ppm	0.5	INAA	5.9	5.3	5.7	6	5.5	6.8	6.2	5.8	4.2	4.3
Hg	ppm	1	INAA	< 1	< 1	< 1	< 1	< 1	< 1	< 1	< 1	< 1	< 1
Ir	ppb	5	INAA	< 5	< 5	< 5	< 5	< 5	< 5	< 5	< 5	< 5	< 5
Mo	ppm	2	TD-ICP	< 2	< 2	< 2	< 2	< 2	< 2	< 2	< 2	< 2	< 2
Ni	ppm	1	TD-ICP	178	206	205	210	170	243	219	162	73	73
Pb	ppm	5	TD-ICP	17	12	8	15	13	15	18	15	6	7
Rb	ppm	20	INAA	60	80	140	100	70	110	90	130	200	210
S	%	0.001	TD-ICP	0.067	0.055	0.064	0.064	0.09	0.071	0.063	0.178	0.007	0.009
Sb	ppm	0.2	INAA	5.6	3.5	2.6	6.9	3.1	4.3	1.1	5.8	< 0.2	< 0.2
Sc	ppm	0.1	INAA	23.3	25.1	23.9	24.8	26.5	26	25.3	23.2	21.9	22.9
Se	ppm	3	INAA	< 3	< 3	< 3	< 3	< 3	< 3	< 3	< 3	< 3	< 3
Sr	ppm	2	FUS-ICP	1934	1501	1433	1855	2411	2971	2604	2488	537	604
Ta	ppm	1	INAA	< 1	< 1	< 1	< 1	< 1	< 1	< 1	< 1	< 1	< 1
Th	ppm	0.5	INAA	19.1	16.1	17.3	16	22.6	22.1	21.4	21.2	9.4	10
U	ppm	0.5	INAA	2.3	1.4	1.7	1.8	2.4	3.5	3	2.3	1	0.9
V	ppm	5	FUS-ICP	156	149	154	144	156	154	153	161	161	171
W	ppm	3	INAA	< 3	< 3	< 3	< 3	< 3	< 3	< 3	< 3	< 3	< 3
Y	ppm	1	FUS-ICP	20	19	21	20	22	21	21	22	16	17
Zn	ppm	1	TD-ICP	70	59	65	83	90	72	70	72	57	56
Zr	ppm	2	FUS-ICP	152	184	163	168	152	96	125	156	142	145
La	ppm	0.2	INAA	175	153	162	157	189	198	193	183	45.5	44.9
Ce	ppm	3	INAA	346	315	316	313	372	388	380	351	90	88
Nd	ppm	5	INAA	177	132	154	158	170	200	202	184	38	44
Sm	ppm	0.1	INAA	18.7	18.1	17.7	18	20	20.9	20.6	19.3	6.2	6.2
Eu	ppm	0.1	INAA	4.3	3.9	4.1	1.8	4.5	4.8	4.6	4.1	1.4	1.3
Tb	ppm	0.5	INAA	< 0.5	< 0.5	1.4	< 0.5	< 0.5	< 0.5	1.1	< 0.5	< 0.5	< 0.5
Yb	ppm	0.1	INAA	1.5	1.4	1.7	1.7	1.5	1.5	1.3	2.2	1.5	1.6
Lu	ppm	0.05	INAA	< 0.05	< 0.05	< 0.05	< 0.05	< 0.05	< 0.05	0.07	< 0.05	0.24	0.18
Mass	g		INAA	1.753	1.729	2.014	1.839	1.868	1.799	1.906	1.833	1.978	2.01

Appendix 2-2. Analytical results for weathered lamprophyre samples.

EM = English Mine, VMWD = Vortex Mine weathered dike, IGWD = Intergem weathered dike

FUS-ICP – Fusion Inductively Coupled Plasma Mass Spectrometry, INAA - Instrumental Neutron Activation Analysis, TD-ICP - Near-Total Digestion Inductively Couple Mass Spectrometry

Analyte Symbol	Unit	Detection Limit	Analysis Method	EM42	EM44	VMWD1	VMWD2	VMWD4	VMWD5	VMWD6	IGWD1
SiO2	%	0.01	FUS-ICP	34.13	34.06	43.17	27.16	27.78	26.6	22.81	28.71
Al2O3	%	0.01	FUS-ICP	10.74	11.66	21.89	10.61	13.98	10.65	11.57	10.73
Fe2O3(T)	%	0.01	FUS-ICP	8.62	8.18	4.93	7.87	4.99	6.68	2.22	6.02
MnO	%	0.01	FUS-ICP	0.12	0.11	0.01	0.05	0.03	0.08	< 0.01	0.07
MgO	%	0.01	FUS-ICP	10.91	9.86	1.42	3.45	2.56	3.43	1.06	5.66
CaO	%	0.01	FUS-ICP	14.79	14.18	6.43	19.51	20.95	20.82	29.24	19.74
Na2O	%	0.01	FUS-ICP	0.24	0.19	0.02	0.06	0.04	0.06	0.01	0.07
K2O	%	0.01	FUS-ICP	1.12	1.11	0.25	1.91	0.86	2.03	0.06	1.26
TiO2	%	0.005	FUS-ICP	1.166	1.241	2.815	1.296	1.705	1.312	1.424	1.149
P2O5	%	0.01	FUS-ICP	1.49	1.6	3.64	1.7	2.28	1.75	1.93	1.44
LOI	%		GRAV	15.19	16.45	14.18	20.29	22.47	20.83	28.33	23.15
Total	%	0.01	FUS-ICP	98.52	98.65	98.76	93.93	97.65	94.25	98.67	98.01
Au	ppb	5	INAA	6	< 5	< 5	< 5	< 5	< 5	< 5	< 5
Ag	ppm	0.5	MULT INAA / TD-ICP	< 0.5	< 0.5	< 0.5	< 0.5	< 0.5	< 0.5	< 0.5	< 0.5
As	ppm	2	INAA	6	10	241	20	29	9	68	3
Ba	ppm	3	MULT INAA/FUSICP	4210	4600	100	28200	2230	27600	61	4840
Be	ppm	1	FUS-ICP	3	3	3	2	2	2	1	2
Bi	ppm	2	TD-ICP	< 2	< 2	< 2	< 2	< 2	< 2	< 2	< 2
Br	ppm	1	INAA	< 1	< 1	< 1	< 1	< 1	< 1	< 1	< 1
Cd	ppm	0.5	TD-ICP	< 0.5	< 0.5	< 0.5	< 0.5	< 0.5	< 0.5	< 0.5	< 0.5
Co	ppm	1	INAA	41	33	10	20	12	31	< 1	34
Cr	ppm	1	INAA	970	1040	2870	1050	1410	1120	1050	965
Cs	ppm	0.5	INAA	< 0.5	< 0.5	< 0.5	30.2	8.1	27	< 0.5	1.8
Cu	ppm	1	TD-ICP	74	74	175	90	71	84	66	77
Hf	ppm	0.5	INAA	5.7	7.2	13.2	9.1	9.2	10	6.4	7.3

Hg	ppm	1	INAA	< 1	< 1	< 1	< 1	< 1	< 1	< 1	< 1
Ir	ppb	5	INAA	< 5	< 5	< 5	< 5	< 5	< 5	< 5	< 5
Mo	ppm	2	TD-ICP	< 2	< 2	< 2	< 2	< 2	< 2	< 2	< 2
Ni	ppm	1	TD-ICP	204	165	174	178	288	209	59	194
Pb	ppm	5	TD-ICP	7	7	17	10	10	18	5	9
Rb	ppm	20	INAA	< 20	< 20	< 20	50	< 20	140	< 20	< 20
S	%	0.001	TD-ICP	0.016	0.011	0.02	0.039	0.019	0.029	0.021	0.023
Sb	ppm	0.2	INAA	< 0.2	< 0.2	3.1	0.7	1.6	0.6	1.1	< 0.2
Sc	ppm	0.1	INAA	27.2	27.4	19.2	30.5	44.5	32.4	13.8	24.4
Se	ppm	3	INAA	< 3	< 3	< 3	< 3	< 3	< 3	< 3	< 3
Sr	ppm	2	FUS-ICP	928	886	933	876	1102	843	502	1051
Ta	ppm	1	INAA	2	7	15	4	8	7	4	7
Th	ppm	0.5	INAA	19.2	20.5	52.7	24.5	31.3	23.9	27.6	21.2
U	ppm	0.5	INAA	2.2	< 0.5	4.3	< 0.5	< 0.5	< 0.5	3.5	1.4
V	ppm	5	FUS-ICP	168	176	357	120	213	129	181	162
W	ppm	3	INAA	< 3	< 3	< 3	< 3	< 3	< 3	< 3	< 3
Y	ppm	1	FUS-ICP	20	20	41	22	29	24	22	18
Zn	ppm	1	TD-ICP	80	71	270	336	294	302	105	119
Zr	ppm	2	FUS-ICP	230	253	427	275	307	276	278	242
La	ppm	0.2	INAA	215	217	455	255	359	263	242	195
Ce	ppm	3	INAA	362	369	848	395	517	426	455	322
Nd	ppm	5	INAA	151	170	398	198	342	180	222	141
Sm	ppm	0.1	INAA	19.8	19.3	44.8	22.9	32.7	23.1	23.9	17.7
Eu	ppm	0.1	INAA	4.1	4	9.6	5.4	6.8	4.6	5.7	3.5
Tb	ppm	0.5	INAA	< 0.5	0.5	< 0.5	< 0.5	< 0.5	0.8	< 0.5	< 0.5
Yb	ppm	0.1	INAA	1.4	1.4	2.2	1.7	2.1	1.5	1.8	1.4
Lu	ppm	0.05	INAA	< 0.05	< 0.05	0.11	0.05	< 0.05	< 0.05	< 0.05	0.05
Mass	g		INAA	1.556	1.342	1.303	1.465	1.297	1.397	1.458	1.39

Appendix 2-3a. Analytical data from pXRF on xenoliths, ocelli, clasts, and/or matrix. Elements Mg-Ca.**Date:** 12/2/202. Elapsed total time – total time in seconds used to evaluated area of interest. All elements measured in weight %.

Time	Reading	Mode	Elapsed Time Total	Mg	Mg +/-	Al	Al +/-	Si	Si +/-	Ca	Ca +/-
11:19:11	#1	Cal Check	15.07								
11:21:21	#2	Geochem	87.29	4.29	0.35	1.3083	0.0458	0.5258	0.0125	0.261	0.0036
11:54:55	#3	Geochem	58.88	6.05	0.23	3.2	0.05	15.73	0.08	17.84	0.07
12:02:44	#4C	Geochem	61.24	5.65	0.54	3.97	0.15	16.1	0.22	12.68	0.16
12:10:00	#5C	Geochem	60.05	2.09	0.52	1.93	0.12	7.43	0.13	22.65	0.32
12:18:48	#6	Geochem	59.58	6.68	0.22	2.3253	0.0481	18.29	0.08	18.06	0.07
12:22:40	#7C	Geochem	60.6	7.13	0.56	3.56	0.15	16.93	0.23	11.96	0.15
12:25:52	#8C	Geochem	60.01	6.06	0.57	4.29	0.16	18.08	0.25	11.45	0.15
12:28:42	#9C	Geochem	60	7.51	0.55	4.11	0.15	18.66	0.24	12.57	0.15
12:32:21	#10C	Geochem	60.19	6.06	0.52	4.76	0.16	16.92	0.23	11.41	0.14
12:34:36	#11C	Geochem	60.12	4.47	0.5	6.42	0.18	16.34	0.23	12.80	0.16
12:39:25	#12C	Geochem	60.58	1.41	0.35	5.2	0.16	26.55	0.3	7.70	0.09
12:41:22	#13C	Geochem	60.06	1.38	0.35	5.68	0.17	26.83	0.3	4.90	0.06
12:43:19	#14C	Geochem	60.29	1.35	0.32	7.13	0.18	27.61	0.29	3.70	0.04
12:45:02	#15C	Geochem	60.57	1.63	0.34	7.33	0.18	25.38	0.28	7.54	0.08
12:46:55	#16C	Geochem	60	4.74	0.47	5.97	0.17	18.5	0.24	10.99	0.13
12:48:48	#17C	Geochem	60.64	6.91	0.52	3	0.13	18.51	0.24	13.00	0.15
12:51:36	#18	Geochem	58.85	5.55	0.21	5.42	0.07	17.99	0.08	11.64	0.05
12:54:10	#19	Geochem	60.09	5.52	0.2	6.24	0.07	17.14	0.08	12.14	0.05
12:56:29	#20	Geochem	59.22	<LOD	0.35	<LOD	0.0998	0.1712	0.0126	42.73	0.16
12:58:18	#21	Geochem	60.24	8.16	0.29	<LOD	0.071	0.4181	0.0135	30.93	0.15
13:01:07	#22	Geochem	58.9	1.62	0.25	<LOD	0.0677	1.0425	0.0175	39.23	0.18
13:03:14	#23	Geochem	58.96	1.2	0.23	0.8719	0.0422	2.6395	0.026	37.67	0.17
13:05:12	#24	Geochem	59.2	2.13	0.13	8.31	0.07	28.97	0.1	2.22	0.01
13:07:21	#25C	Geochem	61.1	3.6	0.44	5.39	0.16	15.46	0.21	9.29	0.11

13:09:03	#26C	Geochem	60.55	2.94	0.38	8.29	0.2	22.69	0.27	1.62	0.03
13:10:29	#27C	Geochem	60.22	2.77	0.38	8.99	0.2	24.58	0.29	2.06	0.03
13:12:08	#28C	Geochem	60.58	2.79	0.38	8.94	0.2	23.74	0.28	5.29	0.06
13:14:34	#29C	Geochem	61.94	2.1	0.49	0.52	0.08	2.02	0.05	35.59	0.46
13:16:30	#30	Geochem	59.23	5.61	0.2	4.87	0.06	16.29	0.08	10.43	0.04
13:19:36	#31C	Geochem	59.97	2.79	0.46	3.34	0.14	10.09	0.15	20.71	0.27
13:22:30	#32C	Geochem	61.5	2.08	0.47	0.87	0.09	2.79	0.06	34.76	0.45
13:25:13	#33C	Geochem	59.99	6.1	0.53	3.01	0.13	10.89	0.16	15.69	0.20
13:27:29	#34	Geochem	59.9	5.34	0.19	5.84	0.06	19.62	0.08	8.86	0.03
13:30:33	#35	Geochem	59.21	1.86	0.23	1.0128	0.0443	4.0181	0.0318	37.02	0.16
13:32:01	#36	Geochem	59.27	1.04	0.22	0.9918	0.0438	3.6113	0.0301	35.67	0.15
13:33:49	#37	Geochem	58.8	2.23	0.21	2.26	0.05	4.3822	0.0354	35.79	0.15
13:35:40	#38	Geochem	58.98	0.92	0.23	<LOD	0.0689	0.3823	0.0189	40.30	0.19
13:37:16	#39	Geochem	58.87	0.86	0.23	0.2598	0.0372	1.5408	0.0206	40.01	0.18
13:42:35	#40	Geochem	58.96	7.83	0.21	5.64	0.07	18.49	0.08	10.81	0.04
13:57:19	#41C	Geochem	60	5.11	0.5	5.68	0.17	12.02	0.17	12.43	0.16
13:59:36	#42C	Geochem	60.86	4.32	0.49	3.29	0.13	11.53	0.17	20.22	0.25
14:01:51	#43C	Geochem	60.79	4.37	0.46	5.18	0.16	17.22	0.23	10.00	0.12
14:03:36	#44C	Geochem	60.77	5.33	0.51	3.3	0.14	15.02	0.21	15.83	0.20
14:05:17	#45C	Geochem	60.87	6.37	0.53	3.31	0.14	18.87	0.25	12.87	0.16
14:07:43	#46C	Geochem	60.04	1.32	0.33	4.44	0.15	34.65	0.36	7.60	0.08
14:09:15	#47C	Geochem	60.02	1.8	0.34	7.32	0.18	29	0.31	8.21	0.09
14:12:08	#48	Geochem	58.78	2.98	0.16	8.32	0.07	18.62	0.08	7.80	0.03
14:14:29	#49	Geochem	60.02	2.79	0.16	8.49	0.07	18.77	0.08	7.04	0.03
14:16:24	#50	Geochem	59.82	2.32	0.16	7.93	0.07	17.56	0.08	6.99	0.03
14:18:17	#51C	Geochem	61.77	1.95	0.41	6.93	0.19	15.75	0.24	6.39	0.09
14:20:25	#52C	Geochem	60.05	2.51	0.44	7.01	0.19	15.88	0.24	6.63	0.09
14:22:25	#54C	Geochem	60.01	6.15	0.57	3.7	0.16	12.84	0.2	12.74	0.17
14:24:04	#55C	Geochem	60.04	<LOD	1.21	1.97	0.11	4.34	0.09	27.85	0.38
14:25:56	#56C	Geochem	60.06	4.05	0.51	4.22	0.15	8.96	0.15	16.82	0.23

14:28:27	#57C	Geochem	61.32	5.5	0.55	4.09	0.16	16.63	0.24	11.55	0.15
14:31:05	#58	Geochem	59.77	7.85	0.25	5.59	0.07	16.32	0.09	15.64	0.07
14:33:30	#59C	Geochem	60.92	7.93	0.58	2.38	0.13	12.75	0.19	16.57	0.21
14:35:04	#60C	Geochem	60.81	7.25	0.56	2.12	0.12	15.61	0.22	14.96	0.19
14:36:35	#61C	Geochem	60.18	8.29	0.57	2.07	0.12	13.77	0.2	15.28	0.19
14:38:41	#62C	Geochem	60.02	5.77	0.52	5.22	0.17	11.7	0.18	15.01	0.19
14:41:07	#63C	Geochem	59.98	8.48	0.62	1.38	0.1	6.72	0.12	20.54	0.28
14:43:00	#64C	Geochem	60.02	2.14	0.52	0.84	0.09	2.47	0.06	29.04	0.39
14:44:39	#65C	Geochem	68.46	4.24	0.49	1.07	0.08	2.82	0.06	21.29	0.30
14:46:45	#66C	Geochem	60.87	<LOD	0.91	0.28	0.07	1.331	0.041	35.09	0.45
14:49:05	#67C	Geochem	60.01	4.85	0.54	2.45	0.12	5.31	0.1	23.01	0.30
14:50:37	#68C	Geochem	59.95	1.77	0.47	<LOD	0.1388	0.5292	0.0303	36.82	0.49
14:52:09	#69C	Geochem	60.38	2.82	0.5	0.59	0.08	1.6332	0.0461	28.41	0.39
14:54:13	#70C	Geochem	60.06	4.96	0.47	7.57	0.19	14.79	0.2	10.03	0.12
14:55:45	#71C	Geochem	61.14	7.1	0.58	1.75	0.11	4.5	0.09	22.46	0.31
14:57:34	#72C	Geochem	60.02	7.08	0.56	4.01	0.15	11.41	0.17	15.95	0.20
14:59:31	#73C	Geochem	61.97	7.69	0.53	4.22	0.15	11.44	0.17	15.49	0.19
15:01:19	#74C	Geochem	60.11	6.36	0.51	5.94	0.17	13.56	0.19	14.42	0.17
15:03:16	#75C	Geochem	59.99	3.78	0.46	3.55	0.13	12.56	0.18	21.25	0.26
15:05:52	#76C	Geochem	60.01	<LOD	1.25	7.48	0.18	32.76	0.33	3.65	0.04
15:08:03	#77C	Geochem	60.02	1.56	0.34	8.16	0.19	26.15	0.3	3.34	0.04
15:09:31	#78C	Geochem	61.91	1.32	0.34	5.92	0.17	24.35	0.28	6.90	0.08
15:11:33	#79C	Geochem	60.75	4.72	0.5	2.29	0.12	7.86	0.13	19.99	0.26
15:13:30	#80C	Geochem	61.02	5.26	0.54	0.74	0.09	6.28	0.11	24.34	0.33
15:15:41	#81C	Geochem	61.21	7.38	0.51	5.53	0.16	16.19	0.21	9.35	0.11
15:17:46	#82C	Geochem	61.51	8.04	0.56	2.05	0.11	5.43	0.1	21.24	0.28
15:19:15	#83C	Geochem	60.66	8.01	0.6	0.92	0.09	3	0.07	25.82	0.35
15:21:48	#84	Geochem	59.35	5.83	0.2	5.15	0.06	17.57	0.08	13.04	0.05
15:24:25	#85C	Geochem	60.18	4.83	0.47	6.26	0.17	13.81	0.19	12.38	0.15
15:25:54	#86C	Geochem	61.24	4.47	0.52	1.02	0.09	3.66	0.07	25.98	0.35

15:27:58	#87	Geochem	58.93	7.93	0.22	4.09	0.06	15.91	0.08	13.9	0.06
15:29:44	#88C	Geochem	60.06	1.46	0.36	0.74	0.09	32.18	0.35	12.04	0.13
15:31:15	#89C	Geochem	60.03	<LOD	1.1	0.75	0.09	31.15	0.33	10.41	0.11
15:33:01	#90C	Geochem	60.92	4.63	0.48	3.87	0.14	14.95	0.2	14.99	0.18
15:34:49	#91C	Geochem	60.08	8.32	0.56	3.44	0.14	7.44	0.12	17.98	0.23
15:36:20	#92C	Geochem	61.14	5.44	0.48	4.96	0.16	17.46	0.23	8.79	0.11
15:38:08	#93	Geochem	59.5	5.09	0.18	7.42	0.07	16.99	0.07	10.8851	0.0422
15:40:00	#94	Geochem	59.11	8.5	0.22	2.7056	0.0499	19.97	0.09	14.6	0.06
15:41:55	#95C	Geochem	60.02	8.71	0.56	1.33	0.11	20.42	0.26	13.78	0.17
15:43:38	#96C	Geochem	60.29	7.14	0.54	3.78	0.15	17.81	0.24	12.82	0.16
15:45:23	#97C	Geochem	59.98	8.5	0.54	3.32	0.14	19.12	0.24	13.37	0.16

Appendix 2-3b. Analytical data from pXRF on xenoliths, ocelli, clasts, and/or matrix. Elements Ti-Mn.**Date:** 12/2/202. Elapsed total time – total time in seconds used to evaluated area of interest. All elements measured in weight %.

Time	Reading	Mode	Elapsed Time Total	Ti	Ti +/-	V	V +/-	Cr	Cr +/-	Mn	Mn +/-
11:19:11	#1	Cal Check	1:40:48								
11:21:21	#2	Geochem	87.29	0.4044	0.0089	<LOD	0.014	<LOD	0.008	<LOD	0.58
11:54:55	#3	Geochem	58.88	0.3562	0.0099	0.08	0.005	0.1273	0.0033	0.0968	0.0028
12:02:44	#4C	Geochem	61.24	0.6111	0.037	0.1214	0.0174	0.2094	0.0126	0.1255	0.0098
12:10:00	#5C	Geochem	60.05	0.2511	0.0305	0.0569	0.0156	0.2008	0.0138	0.1213	0.0107
12:18:48	#6	Geochem	59.58	0.1158	0.0074	0.0289	0.0039	0.0177	0.0019	0.315	0.0044
12:22:40	#7C	Geochem	60.60	0.53	0.04	0.11	0.0169	0.33	0.02	0.09	0.01
12:25:52	#8C	Geochem	60.01	0.57	0.04	0.14	0.0179	0.04	0.01	0.08	0.01
12:28:42	#9C	Geochem	60.00	0.41	0.03	0.10	0.016	0.23	0.01	0.09	0.01
12:32:21	#10C	Geochem	60.19	0.73	0.04	0.19	0.0197	0.10	0.01	0.11	0.01
12:34:36	#11C	Geochem	60.12	0.56	0.04	0.14	0.0188	0.03	0.01	0.13	0.01
12:39:25	#12C	Geochem	60.58	0.22	0.03	0.05	0.0143	<LOD	0.05	0.06	0.01
12:41:22	#13C	Geochem	60.06	0.49	0.04	0.05	0.0151	<LOD	0.05	0.03	0.01
12:43:19	#14C	Geochem	60.29	0.25	0.03	0.08	0.0145	<LOD	0.05	0.03	0.00
12:45:02	#15C	Geochem	60.57	0.29	0.03	0.06	0.0147	<LOD	0.04	0.02	0.00
12:46:55	#16C	Geochem	60.00	0.68	0.04	0.18	0.0193	0.03	0.01	0.14	0.01
12:48:48	#17C	Geochem	60.64	0.45	0.03	0.12	0.0168	0.09	0.01	0.15	0.01
12:51:36	#18	Geochem	58.85	0.78	0.01	0.17	0.0061	0.09	0.00	0.13	0.00
12:54:10	#19	Geochem	60.09	0.63	0.01	0.13	0.0057	0.06	0.00	0.12	0.00
12:56:29	#20	Geochem	59.22	0.04	0.01	<LOD	0.0317	<LOD	0.02	0.01	0.00
12:58:18	#21	Geochem	60.24	<LOD	0.02	<LOD	0.0293	<LOD	0.02	0.02	0.00
13:01:07	#22	Geochem	58.90	0.04	0.01	<LOD	0.0308	<LOD	0.02	0.01	0.00
13:03:14	#23	Geochem	58.96	0.07	0.01	<LOD	0.0325	0.01	0.00	0.01	0.00
13:05:12	#24	Geochem	59.20	0.32	0.01	0.08	0.0046	0.01	0.00	0.06	0.00

13:07:21	#25C	Geochem	61.10	0.32	0.03	0.06	0.0126	<LOD	0.05	0.10	0.01
13:09:03	#26C	Geochem	60.55	0.58	0.03	0.08	0.0142	<LOD	0.05	0.07	0.01
13:10:29	#27C	Geochem	60.22	0.68	0.04	0.07	0.015	<LOD	0.05	0.08	0.01
13:12:08	#28C	Geochem	60.58	0.47	0.03	0.08	0.0155	<LOD	0.05	0.06	0.01
13:14:34	#29C	Geochem	61.94	0.08	0.02	<LOD	0.1088	<LOD	0.05	0.75	0.02
13:16:30	#30	Geochem	59.23	0.37	0.01	0.06	0.0042	0.01	0.00	0.18	0.00
13:19:36	#31C	Geochem	59.97	0.18	0.03	0.04	0.0136	<LOD	0.06	0.41	0.02
13:22:30	#32C	Geochem	61.50	0.09	0.02	<LOD	0.1112	<LOD	0.06	0.62	0.02
13:25:13	#33C	Geochem	59.99	0.33	0.03	<LOD	0.1054	<LOD	0.05	0.13	0.01
13:27:29	#34	Geochem	59.90	0.40	0.01	0.04	0.0041	0.05	0.00	0.09	0.00
13:30:33	#35	Geochem	59.21	0.64	0.01	0.45	0.0098	0.01	0.00	5.19	0.03
13:32:01	#36	Geochem	59.27	0.67	0.01	0.49	0.0101	0.01	0.00	5.59	0.03
13:33:49	#37	Geochem	58.80	0.64	0.01	0.45	0.0098	0.01	0.00	5.17	0.03
13:35:40	#38	Geochem	58.98	0.03	0.01	0.02	0.0044	<LOD	0.02	0.02	0.00
13:37:16	#39	Geochem	58.87	0.04	0.01	<LOD	0.0322	<LOD	0.02	0.02	0.00
13:42:35	#40	Geochem	58.96	0.68	0.01	0.14	0.0058	0.16	0.00	0.09	0.00
13:57:19	#41C	Geochem	60.00	0.50	0.03	0.29	0.0215	<LOD	0.07	0.27	0.01
13:59:36	#42C	Geochem	60.86	0.18	0.03	0.05	0.0139	0.15	0.01	0.12	0.01
14:01:51	#43C	Geochem	60.79	0.66	0.04	0.16	0.0185	0.08	0.01	0.13	0.01
14:03:36	#44C	Geochem	60.77	0.45	0.04	0.08	0.0168	0.09	0.01	0.13	0.01
14:05:17	#45C	Geochem	60.87	0.43	0.03	0.07	0.0158	0.06	0.01	0.14	0.01
14:07:43	#46C	Geochem	60.04	0.29	0.03	0.06	0.0164	<LOD	0.05	0.06	0.01
14:09:15	#47C	Geochem	60.02	0.24	0.03	0.05	0.0154	<LOD	0.05	0.08	0.01
14:12:08	#48	Geochem	58.78	0.34	0.01	0.09	0.0047	0.02	0.00	0.25	0.00
14:14:29	#49	Geochem	60.02	0.33	0.01	0.10	0.0047	0.02	0.00	0.25	0.00
14:16:24	#50	Geochem	59.82	0.38	0.01	0.12	0.0051	0.02	0.00	0.24	0.00
14:18:17	#51C	Geochem	61.77	0.45	0.03	0.11	0.0159	0.03	0.01	0.26	0.01
14:20:25	#52C	Geochem	60.05	0.41	0.03	0.10	0.0157	0.04	0.01	0.24	0.01
14:22:25	#54C	Geochem	60.01	0.65	0.04	0.12	0.0184	0.53	0.02	0.12	0.01
14:24:04	#55C	Geochem	60.04	0.17	0.03	0.05	0.0156	<LOD	0.06	0.29	0.01

14:25:56	#56C	Geochem	60.06	0.28	0.03	0.11	0.0168	0.05	0.01	0.22	0.01
14:28:27	#57C	Geochem	61.32	0.54	0.04	0.10	0.0174	0.42	0.02	0.12	0.01
14:31:05	#58	Geochem	59.77	0.62	0.01	0.13	0.007	0.05	0.00	0.16	0.00
14:33:30	#59C	Geochem	60.92	0.30	0.03	0.06	0.0147	0.37	0.02	0.14	0.01
14:35:04	#60C	Geochem	60.81	0.26	0.03	<LOD	0.1111	0.54	0.02	0.13	0.01
14:36:35	#61C	Geochem	60.18	0.28	0.03	0.05	0.0142	0.47	0.02	0.13	0.01
14:38:41	#62C	Geochem	60.02	0.27	0.03	<LOD	0.1165	<LOD	0.06	0.18	0.01
14:41:07	#63C	Geochem	59.98	0.14	0.02	<LOD	0.1074	<LOD	0.06	0.12	0.01
14:43:00	#64C	Geochem	60.02	0.07	0.02	<LOD	0.0967	<LOD	0.05	0.12	0.01
14:44:39	#65C	Geochem	68.46	0.14	0.02	<LOD	0.1015	<LOD	0.05	0.11	0.01
14:46:45	#66C	Geochem	60.87	0.44	0.04	0.28	0.0255	<LOD	0.07	0.21	0.01
14:49:05	#67C	Geochem	60.01	0.74	0.04	0.50	0.0292	<LOD	0.08	0.14	0.01
14:50:37	#68C	Geochem	59.95	<LOD	0.04	0.04	0.014	<LOD	0.05	0.17	0.01
14:52:09	#69C	Geochem	60.38	0.07	0.02	<LOD	0.0963	<LOD	0.05	0.12	0.01
14:54:13	#70C	Geochem	60.06	0.25	0.03	0.10	0.0152	0.02	0.01	0.18	0.01
14:55:45	#71C	Geochem	61.14	0.14	0.02	<LOD	0.1046	<LOD	0.06	0.09	0.01
14:57:34	#72C	Geochem	60.02	0.47	0.03	0.08	0.016	0.04	0.01	0.17	0.01
14:59:31	#73C	Geochem	61.97	0.43	0.03	0.09	0.0159	0.04	0.01	0.14	0.01
15:01:19	#74C	Geochem	60.11	0.32	0.03	0.12	0.0169	0.03	0.01	0.15	0.01
15:03:16	#75C	Geochem	59.99	0.48	0.04	0.17	0.0198	0.06	0.01	0.06	0.01
15:05:52	#76C	Geochem	60.01	0.11	0.02	<LOD	0.0924	<LOD	0.05	0.03	0.01
15:08:03	#77C	Geochem	60.02	0.51	0.03	0.07	0.0155	0.03	0.01	0.09	0.01
15:09:31	#78C	Geochem	61.91	0.34	0.03	0.13	0.0177	<LOD	0.06	0.11	0.01
15:11:33	#79C	Geochem	60.75	0.21	0.03	0.04	0.0137	0.08	0.01	0.15	0.01
15:13:30	#80C	Geochem	61.02	0.07	0.02	<LOD	0.0994	0.18	0.01	0.16	0.01
15:15:41	#81C	Geochem	61.21	0.57	0.03	0.13	0.0166	0.09	0.01	0.13	0.01
15:17:46	#82C	Geochem	61.51	0.14	0.02	<LOD	0.0979	<LOD	0.05	0.16	0.01
15:19:15	#83C	Geochem	60.66	0.19	0.03	<LOD	0.0965	<LOD	0.06	0.15	0.01
0.640139	#84	Geochem	59.35	0.6475	0.0118	0.1155	0.0055	0.0492	0.0024	0.1445	0.003
0.641956	#85C	Geochem	60.18	0.1722	0.0245	0.0693	0.0144	<LOD	0.0602	0.1765	0.0103

0.642986	#86C	Geochem	61.24	<LOD	0.0553	<LOD	0.0915	<LOD	0.0505	0.0842	0.008
0.644421	#87	Geochem	58.93	0.515	0.011	0.1059	0.0053	0.1063	0.0031	0.1406	0.0031
0.645648	#88C	Geochem	60.06	<LOD	0.0902	<LOD	0.0983	0.0964	0.0099	0.0785	0.0082
0.646701	#89C	Geochem	60.03	0.0759	0.0213	<LOD	0.088	0.0735	0.0086	0.0524	0.0068
0.647928	#90C	Geochem	60.92	0.6133	0.0368	0.0875	0.0163	0.1075	0.0096	0.104	0.0087
0.649178	#91C	Geochem	60.08	0.2942	0.0284	0.0682	0.0149	<LOD	0.061	0.2229	0.0117
0.650231	#92C	Geochem	61.14	0.4531	0.0312	0.0712	0.0141	0.0877	0.0083	0.052	0.0066
0.651481	#93	Geochem	59.5	0.3333	0.0092	0.0804	0.0048	0.0254	0.0021	0.2135	0.0035
0.652778	#94	Geochem	59.11	0.2545	0.0086	0.0448	0.0043	0.4337	0.0056	0.107	0.0032
0.654109	#95C	Geochem	60.02	0.2084	0.0265	<LOD	0.0987	0.7745	0.0245	0.0902	0.0112
0.655301	#96C	Geochem	60.29	0.5962	0.0373	0.1097	0.0174	0.2378	0.0136	0.1048	0.0094
0.656516	#97C	Geochem	59.98	0.4182	0.0328	0.0881	0.016	0.3349	0.0158	0.1126	0.0101

Appendix 2-3c. Analytical data from pXRF on xenoliths, ocelli, clasts, and/or matrix. Elements Fe-Cu.**Date:** 12/2/202. Elapsed total time – total time in seconds used to evaluated area of interest. All elements measured in weight %.

Time	Reading	Mode	Elapsed Time Total	Fe	Fe +/-	Co	Co +/-	Ni	Ni +/-	Cu	Cu +/-
11:19:11	#1	Cal Check	1:40:48								
11:21:21	#2	Geochem	87.29	<LOD	0.0149	<LOD	0.0051	10.07	0.07	34.55	0.24
11:54:55	#3	Geochem	58.88	4.5196	0.0229	<LOD	0.0321	0.0256	0.0008	0.0026	0.0004
12:02:44	#4C	Geochem	61.24	6.06	0.09	<LOD	0.1148	0.0166	0.0024	0.0071	0.0015
12:10:00	#5C	Geochem	60.05	5.63	0.1	<LOD	0.1247	0.0426	0.0036	0.0052	0.0017
12:18:48	#6	Geochem	59.58	4.1232	0.0209	<LOD	0.0312	0.0066	0.0006	<LOD	0.0056
12:22:40	#7C	Geochem	60.60	4.76	0.07	<LOD	0.11	0.05	0.00	<LOD	0.02
12:25:52	#8C	Geochem	60.01	7.95	0.11	<LOD	0.13	0.01	0.00	0.01	0.00
12:28:42	#9C	Geochem	60.00	5.09	0.07	<LOD	0.11	0.02	0.00	0.01	0.00
12:32:21	#10C	Geochem	60.19	6.74	0.09	<LOD	0.12	0.03	0.00	0.01	0.00
12:34:36	#11C	Geochem	60.12	5.78	0.09	<LOD	0.12	0.01	0.00	0.01	0.00
12:39:25	#12C	Geochem	60.58	1.65	0.03	<LOD	0.06	<LOD	0.02	<LOD	0.02
12:41:22	#13C	Geochem	60.06	2.10	0.04	<LOD	0.07	<LOD	0.02	<LOD	0.02
12:43:19	#14C	Geochem	60.29	1.45	0.03	<LOD	0.06	<LOD	0.02	<LOD	0.01
12:45:02	#15C	Geochem	60.57	1.21	0.03	<LOD	0.05	<LOD	0.02	<LOD	0.02
12:46:55	#16C	Geochem	60.00	5.89	0.08	<LOD	0.11	<LOD	0.02	<LOD	0.02
12:48:48	#17C	Geochem	60.64	5.63	0.08	<LOD	0.11	<LOD	0.02	<LOD	0.02
12:51:36	#18	Geochem	58.85	7.26	0.03	<LOD	0.04	0.02	0.00	0.01	0.00
12:54:10	#19	Geochem	60.09	6.44	0.03	<LOD	0.04	0.01	0.00	0.01	0.00
12:56:29	#20	Geochem	59.22	0.04	0.00	<LOD	0.01	<LOD	0.01	0.00	0.00
12:58:18	#21	Geochem	60.24	1.06	0.01	<LOD	0.02	<LOD	0.01	<LOD	0.01
13:01:07	#22	Geochem	58.90	0.14	0.00	<LOD	0.01	<LOD	0.01	<LOD	0.01
13:03:14	#23	Geochem	58.96	0.66	0.01	<LOD	0.02	0.00	0.00	0.00	0.00
13:05:12	#24	Geochem	59.20	3.16	0.01	<LOD	0.03	0.00	0.00	0.00	0.00

13:07:21	#25C	Geochem	61.10	10.28	0.13	<LOD	0.13	<LOD	0.02	0.01	0.00
13:09:03	#26C	Geochem	60.55	6.39	0.08	<LOD	0.11	<LOD	0.02	0.00	0.00
13:10:29	#27C	Geochem	60.22	6.50	0.08	<LOD	0.11	<LOD	0.02	0.01	0.00
13:12:08	#28C	Geochem	60.58	4.60	0.06	<LOD	0.10	<LOD	0.02	<LOD	0.02
13:14:34	#29C	Geochem	61.94	1.48	0.04	<LOD	0.07	<LOD	0.02	<LOD	0.02
13:16:30	#30	Geochem	59.23	7.02	0.03	<LOD	0.04	0.01	0.00	0.01	0.00
13:19:36	#31C	Geochem	59.97	4.52	0.07	<LOD	0.11	<LOD	0.02	0.01	0.00
13:22:30	#32C	Geochem	61.50	2.22	0.05	<LOD	0.09	<LOD	0.02	0.01	0.00
13:25:13	#33C	Geochem	59.99	7.69	0.11	<LOD	0.13	<LOD	0.02	0.02	0.00
13:27:29	#34	Geochem	59.90	6.74	0.03	<LOD	0.04	0.01	0.00	0.02	0.00
13:30:33	#35	Geochem	59.21	0.60	0.01	<LOD	0.01	0.01	0.00	0.01	0.00
13:32:01	#36	Geochem	59.27	0.62	0.01	<LOD	0.02	0.01	0.00	0.01	0.00
13:33:49	#37	Geochem	58.80	0.85	0.01	<LOD	0.02	0.01	0.00	0.01	0.00
13:35:40	#38	Geochem	58.98	0.10	0.00	<LOD	0.01	<LOD	0.01	0.00	0.00
13:37:16	#39	Geochem	58.87	0.31	0.00	<LOD	0.01	<LOD	0.01	0.00	0.00
13:42:35	#40	Geochem	58.96	5.62	0.03	<LOD	0.03	0.05	0.00	0.01	0.00
13:57:19	#41C	Geochem	60.00	5.46	0.08	<LOD	0.10	<LOD	0.02	<LOD	0.02
13:59:36	#42C	Geochem	60.86	4.67	0.07	<LOD	0.11	0.05	0.00	0.01	0.00
14:01:51	#43C	Geochem	60.79	7.37	0.10	<LOD	0.12	0.02	0.00	0.01	0.00
14:03:36	#44C	Geochem	60.77	4.48	0.07	<LOD	0.10	<LOD	0.03	<LOD	0.02
14:05:17	#45C	Geochem	60.87	5.19	0.08	<LOD	0.11	<LOD	0.02	0.01	0.00
14:07:43	#46C	Geochem	60.04	1.61	0.03	<LOD	0.06	<LOD	0.02	<LOD	0.02
14:09:15	#47C	Geochem	60.02	1.59	0.03	<LOD	0.06	<LOD	0.02	<LOD	0.02
14:12:08	#48	Geochem	58.78	8.01	0.03	<LOD	0.04	0.00	0.00	0.00	0.00
14:14:29	#49	Geochem	60.02	7.82	0.03	<LOD	0.04	0.00	0.00	0.00	0.00
14:16:24	#50	Geochem	59.82	7.57	0.03	<LOD	0.04	0.00	0.00	0.00	0.00
14:18:17	#51C	Geochem	61.77	7.64	0.12	<LOD	0.13	<LOD	0.02	0.00	0.00
14:20:25	#52C	Geochem	60.05	7.42	0.11	<LOD	0.13	<LOD	0.02	<LOD	0.02
14:22:25	#54C	Geochem	60.01	5.39	0.09	<LOD	0.12	0.04	0.00	0.01	0.00
14:24:04	#55C	Geochem	60.04	4.17	0.07	<LOD	0.11	<LOD	0.02	<LOD	0.02

14:25:56	#56C	Geochem	60.06	6.18	0.10	<LOD	0.12	<LOD	0.02	<LOD	0.02
14:28:27	#57C	Geochem	61.32	6.03	0.09	<LOD	0.12	0.02	0.00	0.01	0.00
14:31:05	#58	Geochem	59.77	6.77	0.04	<LOD	0.04	0.01	0.00	0.01	0.00
14:33:30	#59C	Geochem	60.92	4.23	0.07	<LOD	0.10	0.02	0.00	0.01	0.00
14:35:04	#60C	Geochem	60.81	4.41	0.07	<LOD	0.10	0.03	0.00	<LOD	0.02
14:36:35	#61C	Geochem	60.18	4.76	0.07	<LOD	0.10	0.03	0.00	<LOD	0.02
14:38:41	#62C	Geochem	60.02	5.27	0.08	<LOD	0.11	<LOD	0.02	<LOD	0.02
14:41:07	#63C	Geochem	59.98	4.06	0.07	<LOD	0.09	<LOD	0.02	0.02	0.00
14:43:00	#64C	Geochem	60.02	3.58	0.06	<LOD	0.10	<LOD	0.02	<LOD	0.02
14:44:39	#65C	Geochem	68.46	4.34	0.07	<LOD	0.10	<LOD	0.02	<LOD	0.02
14:46:45	#66C	Geochem	60.87	2.18	0.05	<LOD	0.08	<LOD	0.02	<LOD	0.02
14:49:05	#67C	Geochem	60.01	4.26	0.07	<LOD	0.10	<LOD	0.02	<LOD	0.02
14:50:37	#68C	Geochem	59.95	1.39	0.03	<LOD	0.07	<LOD	0.02	<LOD	0.02
14:52:09	#69C	Geochem	60.38	4.07	0.07	<LOD	0.10	<LOD	0.02	<LOD	0.02
14:54:13	#70C	Geochem	60.06	5.43	0.08	<LOD	0.10	<LOD	0.02	<LOD	0.02
14:55:45	#71C	Geochem	61.14	4.58	0.08	<LOD	0.11	<LOD	0.02	<LOD	0.02
14:57:34	#72C	Geochem	60.02	5.94	0.09	<LOD	0.12	<LOD	0.02	0.00	0.00
14:59:31	#73C	Geochem	61.97	6.10	0.09	<LOD	0.11	<LOD	0.02	0.01	0.00
15:01:19	#74C	Geochem	60.11	5.24	0.08	<LOD	0.11	<LOD	0.02	0.01	0.00
15:03:16	#75C	Geochem	59.99	4.04	0.06	<LOD	0.10	0.01	0.00	0.01	0.00
15:05:52	#76C	Geochem	60.01	0.75	0.02	<LOD	0.04	<LOD	0.02	0.00	0.00
15:08:03	#77C	Geochem	60.02	2.35	0.04	<LOD	0.07	<LOD	0.02	<LOD	0.02
15:09:31	#78C	Geochem	61.91	2.71	0.04	<LOD	0.08	<LOD	0.02	0.01	0.00
15:11:33	#79C	Geochem	60.75	7.20	0.11	<LOD	0.13	0.02	0.00	0.01	0.00
15:13:30	#80C	Geochem	61.02	4.97	0.08	<LOD	0.11	0.02	0.00	<LOD	0.02
15:15:41	#81C	Geochem	61.21	7.74	0.10	<LOD	0.12	0.06	0.00	0.01	0.00
15:17:46	#82C	Geochem	61.51	4.29	0.07	<LOD	0.10	<LOD	0.02	<LOD	0.02
15:19:15	#83C	Geochem	60.66	4.47	0.07	<LOD	0.11	<LOD	0.02	<LOD	0.02
15:21:48	#84	Geochem	59.35	6.5712	0.0292	<LOD	0.0363	0.0191	0.0008	0.0234	0.0007
15:24:25	#85C	Geochem	60.18	5.48	0.08	<LOD	0.1069	<LOD	0.02	0.0061	0.0013

15:25:54	#86C	Geochem	61.24	4.78	0.08	<LOD	0.112	<LOD	0.022	<LOD	0.0164
15:27:58	#87	Geochem	58.93	6.1367	0.0289	<LOD	0.0358	0.0237	0.0008	0.0338	0.0008
15:29:44	#88C	Geochem	60.06	1.8139	0.0352	<LOD	0.0671	0.0371	0.003	<LOD	0.0242
15:31:15	#89C	Geochem	60.03	1.6584	0.0318	<LOD	0.0609	0.0224	0.0024	<LOD	0.0193
15:33:01	#90C	Geochem	60.92	6.04	0.09	<LOD	0.1142	0.0176	0.0024	0.0063	0.0015
15:34:49	#91C	Geochem	60.08	5.71	0.09	<LOD	0.1129	<LOD	0.022	<LOD	0.0153
15:36:20	#92C	Geochem	61.14	6.47	0.09	<LOD	0.1149	0.0555	0.0035	0.0248	0.0023
15:38:08	#93	Geochem	59.5	6.9907	0.0304	<LOD	0.0371	0.0111	0.0007	0.0049	0.0004
15:40:00	#94	Geochem	59.11	4.382	0.0214	<LOD	0.0312	0.0257	0.0008	0.0018	0.0004
15:41:55	#95C	Geochem	60.02	4.06	0.06	<LOD	0.0988	0.0236	0.0026	<LOD	0.0196
15:43:38	#96C	Geochem	60.29	5.28	0.08	<LOD	0.1091	0.0155	0.0024	0.0061	0.0015
15:45:23	#97C	Geochem	59.98	5.24	0.08	<LOD	0.108	0.028	0.0028	0.0056	0.0015

Appendix 2-3d. Analytical data from pXRF on xenoliths, ocelli, clasts, and/or matrix. Elements Zn-Sr.**Date:** 12/2/202. Elapsed total time – total time in seconds used to evaluated area of interest. All elements measured in weight %.

Time	Reading	Mode	Elapsed Time Total	Zn	Zn +/-	As	As +/-	Rb	Rb +/-	Sr	Sr +/-
11:19:11	#1	Cal Check	1:40:48								
11:21:21	#2	Geochem	87.29	<LOD	0.0139	<LOD	0.0231	<LOD	0.0016	<LOD	0.0012
11:54:55	#3	Geochem	58.88	0.0048	0.0003	<LOD	0.0034	0.0017	0.0001	0.0753	0.0004
12:02:44	#4C	Geochem	61.24	0.0058	0.0009	<LOD	0.0103	0.0044	0.0004	0.1116	0.0019
12:10:00	#5C	Geochem	60.05	0.0044	0.0009	<LOD	0.0113	0.0014	0.0003	0.043	0.0011
12:18:48	#6	Geochem	59.58	0.0032	0.0002	<LOD	0.0031	0.0003	0.0001	0.0216	0.0002
12:22:40	#7C	Geochem	60.60	0.01	0.00	<LOD	0.01	0.00	0.00	0.07	0.00
12:25:52	#8C	Geochem	60.01	0.01	0.00	<LOD	0.01	0.01	0.00	0.09	0.00
12:28:42	#9C	Geochem	60.00	0.00	0.00	<LOD	0.01	0.01	0.00	0.12	0.00
12:32:21	#10C	Geochem	60.19	0.01	0.00	<LOD	0.01	0.01	0.00	0.16	0.00
12:34:36	#11C	Geochem	60.12	0.01	0.00	<LOD	0.01	0.01	0.00	0.24	0.00
12:39:25	#12C	Geochem	60.58	0.00	0.00	<LOD	0.01	0.01	0.00	0.05	0.00
12:41:22	#13C	Geochem	60.06	<LOD	0.01	<LOD	0.01	0.01	0.00	0.03	0.00
12:43:19	#14C	Geochem	60.29	<LOD	0.01	<LOD	0.01	0.01	0.00	0.06	0.00
12:45:02	#15C	Geochem	60.57	<LOD	0.01	<LOD	0.01	0.01	0.00	0.08	0.00
12:46:55	#16C	Geochem	60.00	0.01	0.00	<LOD	0.01	0.01	0.00	0.17	0.00
12:48:48	#17C	Geochem	60.64	0.01	0.00	<LOD	0.01	0.00	0.00	0.17	0.00
12:51:36	#18	Geochem	58.85	0.01	0.00	<LOD	0.00	0.01	0.00	0.18	0.00
12:54:10	#19	Geochem	60.09	0.01	0.00	<LOD	0.00	0.01	0.00	0.20	0.00
12:56:29	#20	Geochem	59.22	0.00	0.00	<LOD	0.00	<LOD	0.00	0.07	0.00
12:58:18	#21	Geochem	60.24	0.00	0.00	0.00	0.00	<LOD	0.00	0.06	0.00
13:01:07	#22	Geochem	58.90	0.01	0.00	0.00	0.00	<LOD	0.00	0.01	0.00
13:03:14	#23	Geochem	58.96	0.01	0.00	0.00	0.00	0.00	0.00	0.01	0.00
13:05:12	#24	Geochem	59.20	0.00	0.00	<LOD	0.00	0.02	0.00	0.05	0.00

13:07:21	#25C	Geochem	61.10	0.01	0.00	<LOD	0.01	0.01	0.00	0.04	0.00
13:09:03	#26C	Geochem	60.55	0.00	0.00	<LOD	0.01	0.02	0.00	0.12	0.00
13:10:29	#27C	Geochem	60.22	0.00	0.00	<LOD	0.01	0.02	0.00	0.13	0.00
13:12:08	#28C	Geochem	60.58	0.00	0.00	<LOD	0.01	0.02	0.00	0.12	0.00
13:14:34	#29C	Geochem	61.94	<LOD	0.01	<LOD	0.01	0.00	0.00	0.03	0.00
13:16:30	#30	Geochem	59.23	0.01	0.00	0.00	0.00	0.01	0.00	0.04	0.00
13:19:36	#31C	Geochem	59.97	0.00	0.00	<LOD	0.01	0.00	0.00	0.04	0.00
13:22:30	#32C	Geochem	61.50	<LOD	0.01	<LOD	0.01	<LOD	0.01	0.04	0.00
13:25:13	#33C	Geochem	59.99	0.01	0.00	<LOD	0.01	0.01	0.00	0.02	0.00
13:27:29	#34	Geochem	59.90	0.01	0.00	<LOD	0.00	0.01	0.00	0.05	0.00
13:30:33	#35	Geochem	59.21	0.02	0.00	<LOD	0.01	0.00	0.00	0.07	0.00
13:32:01	#36	Geochem	59.27	0.02	0.00	0.00	0.00	0.00	0.00	0.08	0.00
13:33:49	#37	Geochem	58.80	0.03	0.00	<LOD	0.01	0.00	0.00	0.08	0.00
13:35:40	#38	Geochem	58.98	0.00	0.00	0.00	0.00	<LOD	0.00	0.01	0.00
13:37:16	#39	Geochem	58.87	0.01	0.00	0.00	0.00	0.00	0.00	0.01	0.00
13:42:35	#40	Geochem	58.96	0.01	0.00	<LOD	0.00	0.01	0.00	0.10	0.00
13:57:19	#41C	Geochem	60.00	0.01	0.00	<LOD	0.01	0.01	0.00	0.12	0.00
13:59:36	#42C	Geochem	60.86	0.01	0.00	<LOD	0.01	<LOD	0.01	0.04	0.00
14:01:51	#43C	Geochem	60.79	0.01	0.00	<LOD	0.01	0.01	0.00	0.22	0.00
14:03:36	#44C	Geochem	60.77	0.00	0.00	<LOD	0.01	0.00	0.00	0.11	0.00
14:05:17	#45C	Geochem	60.87	0.01	0.00	<LOD	0.01	0.00	0.00	0.12	0.00
14:07:43	#46C	Geochem	60.04	<LOD	0.01	<LOD	0.02	0.01	0.00	0.21	0.00
14:09:15	#47C	Geochem	60.02	<LOD	0.01	<LOD	0.01	0.01	0.00	0.10	0.00
14:12:08	#48	Geochem	58.78	0.01	0.00	0.00	0.00	0.01	0.00	0.20	0.00
14:14:29	#49	Geochem	60.02	0.01	0.00	<LOD	0.00	0.01	0.00	0.19	0.00
14:16:24	#50	Geochem	59.82	0.01	0.00	0.00	0.00	0.01	0.00	0.20	0.00
14:18:17	#51C	Geochem	61.77	0.01	0.00	<LOD	0.01	0.01	0.00	0.23	0.00
14:20:25	#52C	Geochem	60.05	0.01	0.00	<LOD	0.01	0.01	0.00	0.19	0.00
14:22:25	#54C	Geochem	60.01	0.01	0.00	<LOD	0.01	0.01	0.00	0.11	0.00
14:24:04	#55C	Geochem	60.04	0.00	0.00	<LOD	0.01	<LOD	0.02	0.46	0.01

14:25:56	#56C	Geochem	60.06	0.01	0.00	<LOD	0.01	0.00	0.00	0.28	0.00
14:28:27	#57C	Geochem	61.32	0.01	0.00	<LOD	0.01	0.00	0.00	0.12	0.00
14:31:05	#58	Geochem	59.77	0.01	0.00	<LOD	0.00	0.01	0.00	0.30	0.00
14:33:30	#59C	Geochem	60.92	0.00	0.00	<LOD	0.01	0.00	0.00	0.13	0.00
14:35:04	#60C	Geochem	60.81	0.00	0.00	<LOD	0.01	0.00	0.00	0.11	0.00
14:36:35	#61C	Geochem	60.18	0.00	0.00	<LOD	0.01	0.00	0.00	0.16	0.00
14:38:41	#62C	Geochem	60.02	0.00	0.00	<LOD	0.02	0.01	0.00	0.63	0.01
14:41:07	#63C	Geochem	59.98	<LOD	0.01	0.00	0.00	<LOD	0.02	0.74	0.01
14:43:00	#64C	Geochem	60.02	<LOD	0.01	<LOD	0.01	<LOD	0.01	0.05	0.00
14:44:39	#65C	Geochem	68.46	0.00	0.00	<LOD	0.01	0.00	0.00	0.08	0.00
14:46:45	#66C	Geochem	60.87	<LOD	0.01	<LOD	0.01	<LOD	0.01	0.03	0.00
14:49:05	#67C	Geochem	60.01	0.00	0.00	<LOD	0.01	0.00	0.00	0.11	0.00
14:50:37	#68C	Geochem	59.95	<LOD	0.01	<LOD	0.01	<LOD	0.01	0.01	0.00
14:52:09	#69C	Geochem	60.38	0.00	0.00	<LOD	0.01	<LOD	0.01	0.07	0.00
14:54:13	#70C	Geochem	60.06	0.01	0.00	<LOD	0.01	0.01	0.00	0.20	0.00
14:55:45	#71C	Geochem	61.14	0.00	0.00	<LOD	0.01	0.00	0.00	0.08	0.00
14:57:34	#72C	Geochem	60.02	0.00	0.00	<LOD	0.01	0.00	0.00	0.17	0.00
14:59:31	#73C	Geochem	61.97	0.01	0.00	<LOD	0.01	0.00	0.00	0.16	0.00
15:01:19	#74C	Geochem	60.11	0.00	0.00	<LOD	0.01	0.01	0.00	0.15	0.00
15:03:16	#75C	Geochem	59.99	0.01	0.00	<LOD	0.01	0.00	0.00	0.06	0.00
15:05:52	#76C	Geochem	60.01	0.00	0.00	<LOD	0.01	0.01	0.00	0.04	0.00
15:08:03	#77C	Geochem	60.02	0.02	0.00	<LOD	0.01	0.01	0.00	0.04	0.00
15:09:31	#78C	Geochem	61.91	0.00	0.00	<LOD	0.01	0.01	0.00	0.11	0.00
15:11:33	#79C	Geochem	60.75	0.01	0.00	0.00	0.00	0.00	0.00	0.10	0.00
15:13:30	#80C	Geochem	61.02	0.00	0.00	<LOD	0.01	<LOD	0.01	0.08	0.00
15:15:41	#81C	Geochem	61.21	0.01	0.00	<LOD	0.01	0.01	0.00	0.13	0.00
15:17:46	#82C	Geochem	61.51	0.00	0.00	<LOD	0.01	0.00	0.00	0.17	0.00
15:19:15	#83C	Geochem	60.66	0.00	0.00	<LOD	0.01	<LOD	0.01	0.16	0.00
15:21:48	#84	Geochem	59.35	0.006	0.0003	<LOD	0.0035	0.0046	0.0001	0.1164	0.0006
15:24:25	#85C	Geochem	60.18	0.0063	0.0009	<LOD	0.0136	0.0083	0.0005	0.1778	0.0026

15:25:54	#86C	Geochem	61.24	0.002	0.0006	<LOD	0.0093	<LOD	0.011	0.0489	0.0011
15:27:58	#87	Geochem	58.93	0.0057	0.0003	<LOD	0.0034	0.0049	0.0001	0.1203	0.0006
15:29:44	#88C	Geochem	60.06	<LOD	0.0133	0.0029	0.0005	<LOD	0.0108	0.0268	0.0007
15:31:15	#89C	Geochem	60.03	<LOD	0.0104	0.0021	0.0004	<LOD	0.0108	0.0217	0.0006
15:33:01	#90C	Geochem	60.92	0.0061	0.0009	<LOD	0.0094	0.0013	0.0002	0.0481	0.001
15:34:49	#91C	Geochem	60.08	0.0056	0.0009	<LOD	0.0117	0.0048	0.0004	0.1726	0.0027
15:36:20	#92C	Geochem	61.14	0.0091	0.0011	<LOD	0.009	0.0017	0.0002	0.022	0.0006
15:38:08	#93	Geochem	59.5	0.0108	0.0004	0.0053	0.0003	0.0089	0.0002	0.1627	0.0008
15:40:00	#94	Geochem	59.11	0.004	0.0002	<LOD	0.0032	0.0017	0.0001	0.0991	0.0005
15:41:55	#95C	Geochem	60.02	0.0034	0.0007	<LOD	0.0085	0.0007	0.0002	0.0477	0.001
15:43:38	#96C	Geochem	60.29	0.0032	0.0008	<LOD	0.0102	0.0045	0.0004	0.1248	0.002
15:45:23	#97C	Geochem	59.98	0.0023	0.0007	<LOD	0.0102	0.0025	0.0003	0.084	0.0015

Appendix 2-3e. Analytical data from pXRF on xenoliths, ocelli, clasts, and/or matrix. Elements Y-Mo.**Date:** 12/2/202. Elapsed total time – total time in seconds used to evaluated area of interest. All elements measured in weight %.

Time	Reading	Mode	Elapsed Time Total	Y	Y +/-	Zr	Zr +/-	Nb	Nb +/-	Mo	Mo +/-
11:19:11	#1	Cal Check	1:40:48								
11:21:21	#2	Geochem	87.29	<LOD	0.0059	0.0218	0.0008	0.0207	0.0006	0.0187	0.0004
11:54:55	#3	Geochem	58.88	0.0012	0.0001	0.0093	0.0002	0.0024	0.0002	<LOD	0.0129
12:02:44	#4C	Geochem	61.24	0.0011	0.0003	0.0152	0.0007	0.0068	0.0006	<LOD	0.0376
12:10:00	#5C	Geochem	60.05	0.0009	0.0003	0.0093	0.0006	0.0036	0.0006	<LOD	0.043
12:18:48	#6	Geochem	59.58	0.0013	0.0001	0.0046	0.0001	<LOD	0.0129	<LOD	0.0128
12:22:40	#7C	Geochem	60.60	0.00	0.00	0.01	0.00	0.00	0.00	<LOD	0.04
12:25:52	#8C	Geochem	60.01	<LOD	0.02	0.02	0.00	0.01	0.00	<LOD	0.04
12:28:42	#9C	Geochem	60.00	<LOD	0.02	0.01	0.00	0.00	0.00	<LOD	0.04
12:32:21	#10C	Geochem	60.19	0.00	0.00	0.02	0.00	0.01	0.00	<LOD	0.04
12:34:36	#11C	Geochem	60.12	0.00	0.00	0.02	0.00	0.02	0.00	<LOD	0.04
12:39:25	#12C	Geochem	60.58	<LOD	0.02	0.01	0.00	0.00	0.00	<LOD	0.04
12:41:22	#13C	Geochem	60.06	<LOD	0.02	0.02	0.00	0.00	0.00	<LOD	0.04
12:43:19	#14C	Geochem	60.29	<LOD	0.02	0.01	0.00	<LOD	0.04	<LOD	0.04
12:45:02	#15C	Geochem	60.57	<LOD	0.02	0.01	0.00	0.00	0.00	<LOD	0.04
12:46:55	#16C	Geochem	60.00	0.00	0.00	0.03	0.00	0.03	0.00	<LOD	0.04
12:48:48	#17C	Geochem	60.64	0.00	0.00	0.01	0.00	0.01	0.00	<LOD	0.04
12:51:36	#18	Geochem	58.85	0.00	0.00	0.03	0.00	0.01	0.00	<LOD	0.01
12:54:10	#19	Geochem	60.09	0.00	0.00	0.02	0.00	0.01	0.00	<LOD	0.01
12:56:29	#20	Geochem	59.22	<LOD	0.01	0.00	0.00	<LOD	0.02	<LOD	0.02
12:58:18	#21	Geochem	60.24	<LOD	0.01	0.00	0.00	<LOD	0.02	<LOD	0.02
13:01:07	#22	Geochem	58.90	0.00	0.00	0.00	0.00	<LOD	0.02	<LOD	0.02
13:03:14	#23	Geochem	58.96	0.00	0.00	0.00	0.00	<LOD	0.02	<LOD	0.02

13:05:12	#24	Geochem	59.20	0.00	0.00	0.03	0.00	0.00	0.00	<LOD	0.01
13:07:21	#25C	Geochem	61.10	0.00	0.00	0.01	0.00	<LOD	0.03	<LOD	0.03
13:09:03	#26C	Geochem	60.55	<LOD	0.02	0.10	0.00	<LOD	0.04	<LOD	0.04
13:10:29	#27C	Geochem	60.22	0.00	0.00	0.07	0.00	<LOD	0.04	<LOD	0.04
13:12:08	#28C	Geochem	60.58	0.00	0.00	0.04	0.00	<LOD	0.04	<LOD	0.04
13:14:34	#29C	Geochem	61.94	0.00	0.00	<LOD	0.03	<LOD	0.05	<LOD	0.05
13:16:30	#30	Geochem	59.23	0.00	0.00	0.01	0.00	0.00	0.00	<LOD	0.01
13:19:36	#31C	Geochem	59.97	0.00	0.00	0.01	0.00	<LOD	0.04	<LOD	0.04
13:22:30	#32C	Geochem	61.50	0.00	0.00	<LOD	0.04	<LOD	0.05	<LOD	0.05
13:25:13	#33C	Geochem	59.99	0.00	0.00	0.01	0.00	0.00	0.00	<LOD	0.04
13:27:29	#34	Geochem	59.90	0.00	0.00	0.02	0.00	0.00	0.00	<LOD	0.01
13:30:33	#35	Geochem	59.21	0.00	0.00	0.00	0.00	<LOD	0.01	0.00	0.00
13:32:01	#36	Geochem	59.27	0.00	0.00	0.00	0.00	<LOD	0.01	0.00	0.00
13:33:49	#37	Geochem	58.80	<LOD	0.01	0.00	0.00	<LOD	0.01	0.00	0.00
13:35:40	#38	Geochem	58.98	0.00	0.00	<LOD	0.01	<LOD	0.02	<LOD	0.02
13:37:16	#39	Geochem	58.87	0.00	0.00	0.00	0.00	<LOD	0.02	<LOD	0.02
13:42:35	#40	Geochem	58.96	0.00	0.00	0.01	0.00	0.01	0.00	<LOD	0.01
13:57:19	#41C	Geochem	60.00	0.00	0.00	0.01	0.00	0.02	0.00	<LOD	0.04
13:59:36	#42C	Geochem	60.86	0.00	0.00	0.00	0.00	<LOD	0.04	<LOD	0.04
14:01:51	#43C	Geochem	60.79	0.00	0.00	0.02	0.00	0.01	0.00	<LOD	0.04
14:03:36	#44C	Geochem	60.77	0.00	0.00	0.01	0.00	0.01	0.00	<LOD	0.04
14:05:17	#45C	Geochem	60.87	0.00	0.00	0.01	0.00	0.01	0.00	<LOD	0.04
14:07:43	#46C	Geochem	60.04	<LOD	0.02	0.03	0.00	0.02	0.00	<LOD	0.05
14:09:15	#47C	Geochem	60.02	<LOD	0.02	0.02	0.00	0.00	0.00	<LOD	0.05
14:12:08	#48	Geochem	58.78	0.00	0.00	0.03	0.00	0.07	0.00	<LOD	0.01
14:14:29	#49	Geochem	60.02	0.00	0.00	0.03	0.00	0.06	0.00	<LOD	0.01
14:16:24	#50	Geochem	59.82	0.00	0.00	0.03	0.00	0.07	0.00	<LOD	0.01
14:18:17	#51C	Geochem	61.77	0.00	0.00	0.04	0.00	0.08	0.00	<LOD	0.04
14:20:25	#52C	Geochem	60.05	0.00	0.00	0.03	0.00	0.07	0.00	<LOD	0.04
14:22:25	#54C	Geochem	60.01	0.00	0.00	0.01	0.00	0.01	0.00	<LOD	0.04

14:24:04	#55C	Geochem	60.04	0.00	0.00	0.01	0.00	0.02	0.00	<LOD	0.05
14:25:56	#56C	Geochem	60.06	0.00	0.00	0.02	0.00	0.02	0.00	<LOD	0.04
14:28:27	#57C	Geochem	61.32	0.00	0.00	0.01	0.00	0.01	0.00	<LOD	0.04
14:31:05	#58	Geochem	59.77	0.00	0.00	0.02	0.00	0.02	0.00	<LOD	0.01
14:33:30	#59C	Geochem	60.92	<LOD	0.02	0.01	0.00	0.00	0.00	<LOD	0.04
14:35:04	#60C	Geochem	60.81	0.00	0.00	0.01	0.00	<LOD	0.04	<LOD	0.04
14:36:35	#61C	Geochem	60.18	<LOD	0.02	0.01	0.00	<LOD	0.04	<LOD	0.04
14:38:41	#62C	Geochem	60.02	0.00	0.00	0.02	0.00	0.04	0.00	<LOD	0.04
14:41:07	#63C	Geochem	59.98	<LOD	0.02	0.01	0.00	0.00	0.00	<LOD	0.04
14:43:00	#64C	Geochem	60.02	<LOD	0.02	0.00	0.00	<LOD	0.04	<LOD	0.04
14:44:39	#65C	Geochem	68.46	<LOD	0.02	0.01	0.00	0.00	0.00	<LOD	0.04
14:46:45	#66C	Geochem	60.87	<LOD	0.02	<LOD	0.03	<LOD	0.05	<LOD	0.05
14:49:05	#67C	Geochem	60.01	<LOD	0.02	0.01	0.00	0.01	0.00	<LOD	0.04
14:50:37	#68C	Geochem	59.95	<LOD	0.02	<LOD	0.03	<LOD	0.05	<LOD	0.05
14:52:09	#69C	Geochem	60.38	0.00	0.00	<LOD	0.04	<LOD	0.05	<LOD	0.04
14:54:13	#70C	Geochem	60.06	0.00	0.00	0.02	0.00	0.03	0.00	<LOD	0.04
14:55:45	#71C	Geochem	61.14	<LOD	0.02	0.00	0.00	0.00	0.00	<LOD	0.04
14:57:34	#72C	Geochem	60.02	0.00	0.00	0.02	0.00	0.01	0.00	<LOD	0.04
14:59:31	#73C	Geochem	61.97	0.00	0.00	0.02	0.00	0.01	0.00	<LOD	0.04
15:01:19	#74C	Geochem	60.11	0.00	0.00	0.01	0.00	0.01	0.00	<LOD	0.04
15:03:16	#75C	Geochem	59.99	0.00	0.00	0.01	0.00	0.00	0.00	<LOD	0.04
15:05:52	#76C	Geochem	60.01	<LOD	0.02	0.01	0.00	<LOD	0.04	<LOD	0.04
15:08:03	#77C	Geochem	60.02	0.00	0.00	0.02	0.00	<LOD	0.04	<LOD	0.04
15:09:31	#78C	Geochem	61.91	<LOD	0.02	0.01	0.00	0.01	0.00	<LOD	0.04
15:11:33	#79C	Geochem	60.75	0.00	0.00	0.01	0.00	0.00	0.00	<LOD	0.04
15:13:30	#80C	Geochem	61.02	<LOD	0.02	0.00	0.00	<LOD	0.04	<LOD	0.04
15:15:41	#81C	Geochem	61.21	0.00	0.00	0.02	0.00	0.01	0.00	<LOD	0.03
15:17:46	#82C	Geochem	61.51	<LOD	0.02	0.01	0.00	0.00	0.00	<LOD	0.04
15:19:15	#83C	Geochem	60.66	<LOD	0.02	0.00	0.00	0.00	0.00	<LOD	0.04
15:21:48	#84	Geochem	59.35	0.0017	0.0001	0.0218	0.0002	0.0108	0.0002	<LOD	0.0121

15:24:25	#85C	Geochem	60.18	0.0023	0.0003	0.0178	0.0008	0.0327	0.001	<LOD	0.0388
15:25:54	#86C	Geochem	61.24	<LOD	0.0164	0.0019	0.0005	<LOD	0.0413	<LOD	0.0403
15:27:58	#87	Geochem	58.93	0.0011	0.0001	0.0134	0.0002	0.0079	0.0002	<LOD	0.0122
15:29:44	#88C	Geochem	60.06	0.0011	0.0002	0.0025	0.0004	<LOD	0.045	<LOD	0.0451
15:31:15	#89C	Geochem	60.03	<LOD	0.0168	0.0019	0.0004	<LOD	0.0431	<LOD	0.0427
15:33:01	#90C	Geochem	60.92	0.0013	0.0003	0.017	0.0006	0.0046	0.0006	<LOD	0.0378
15:34:49	#91C	Geochem	60.08	0.0022	0.0003	0.0182	0.0008	0.0237	0.0009	<LOD	0.0388
15:36:20	#92C	Geochem	61.14	<LOD	0.0137	0.006	0.0004	<LOD	0.0353	<LOD	0.0355
15:38:08	#93	Geochem	59.5	0.0025	0.0001	0.0242	0.0003	0.0405	0.0003	<LOD	0.012
15:40:00	#94	Geochem	59.11	0.0008	0.0001	0.0077	0.0002	0.0041	0.0002	<LOD	0.0126
15:41:55	#95C	Geochem	60.02	<LOD	0.0156	0.0039	0.0005	<LOD	0.0412	<LOD	0.0403
15:43:38	#96C	Geochem	60.29	0.0009	0.0003	0.0135	0.0007	0.0048	0.0006	<LOD	0.0393
15:45:23	#97C	Geochem	59.98	0.0009	0.0003	0.0082	0.0006	0.0033	0.0006	<LOD	0.0398

Appendix 2-3f. Analytical data from pXRF on xenoliths, ocelli, clasts, and/or matrix. Elements Rh-Cd.**Date:** 12/2/202. Elapsed total time – total time in seconds used to evaluated area of interest. All elements measured in weight %.

Time	Reading	Mode	Elapsed Time Total	Rh	Rh +/-	Pd	Pd +/-	Ag	Ag +/-	Cd	Cd +/-
11:19:11	#1	Cal Check	1:40:48								
11:21:21	#2	Geochem	87.29	<LOD	0	0.3612	0.006	0.0754	0.0018	<LOD	0.015
11:54:55	#3	Geochem	58.88	<LOD	0	<LOD	0.3	<LOD	0.0676	<LOD	0.0848
12:02:44	#4C	Geochem	61.24	<LOD	0	<LOD	0.86	<LOD	0.2	<LOD	0.24
12:10:00	#5C	Geochem	60.05	<LOD	0	<LOD	1	<LOD	0.23	<LOD	0.28
12:18:48	#6	Geochem	59.58	<LOD	0	<LOD	0.3	<LOD	0.0691	<LOD	0.0865
12:22:40	#7C	Geochem	60.60	<LOD	0.00	<LOD	0.93	<LOD	0.21	<LOD	0.26
12:25:52	#8C	Geochem	60.01	<LOD	0.00	<LOD	0.82	<LOD	0.18	<LOD	0.23
12:28:42	#9C	Geochem	60.00	<LOD	0.00	<LOD	0.9	<LOD	0.2	<LOD	0.25
12:32:21	#10C	Geochem	60.19	<LOD	0.00	<LOD	0.83	<LOD	0.19	<LOD	0.23
12:34:36	#11C	Geochem	60.12	<LOD	0.00	<LOD	0.91	<LOD	0.21	<LOD	0.26
12:39:25	#12C	Geochem	60.58	<LOD	0.00	<LOD	1.02	<LOD	0.23	<LOD	0.29
12:41:22	#13C	Geochem	60.06	<LOD	0.00	<LOD	1	<LOD	0.23	<LOD	0.29
12:43:19	#14C	Geochem	60.29	<LOD	0.00	<LOD	0.96	<LOD	0.22	<LOD	0.27
12:45:02	#15C	Geochem	60.57	<LOD	0.00	<LOD	1.01	<LOD	0.23	<LOD	0.29
12:46:55	#16C	Geochem	60.00	<LOD	0.00	<LOD	0.84	<LOD	0.19	<LOD	0.24
12:48:48	#17C	Geochem	60.64	<LOD	0.00	<LOD	0.88	<LOD	0.19	<LOD	0.25
12:51:36	#18	Geochem	58.85	<LOD	0.00	<LOD	0.26	<LOD	0.0589	<LOD	0.0738
12:54:10	#19	Geochem	60.09	<LOD	0.00	<LOD	0.27	<LOD	0.0608	<LOD	0.0762
12:56:29	#20	Geochem	59.22	<LOD	0.00	<LOD	0.41	<LOD	0.0928	<LOD	0.1167
12:58:18	#21	Geochem	60.24	<LOD	0.00	<LOD	0.37	<LOD	0.0839	<LOD	0.1048
13:01:07	#22	Geochem	58.90	<LOD	0.00	<LOD	0.4	<LOD	0.0913	<LOD	0.1143

13:03:14	#23	Geochem	58.96	<LOD	0.00	<LOD	0.4	<LOD	0.0919	<LOD	0.1152
13:05:12	#24	Geochem	59.20	<LOD	0.00	<LOD	0.29	<LOD	0.0662	<LOD	0.0827
13:07:21	#25C	Geochem	61.10	<LOD	0.00	<LOD	0.71	<LOD	0.16	<LOD	0.2
13:09:03	#26C	Geochem	60.55	<LOD	0.00	<LOD	0.78	<LOD	0.17	<LOD	0.22
13:10:29	#27C	Geochem	60.22	<LOD	0.00	<LOD	0.81	<LOD	0.19	<LOD	0.23
13:12:08	#28C	Geochem	60.58	<LOD	0.00	<LOD	0.89	<LOD	0.2	<LOD	0.26
13:14:34	#29C	Geochem	61.94	<LOD	0.00	<LOD	1.14	<LOD	0.26	<LOD	0.32
13:16:30	#30	Geochem	59.23	<LOD	0.00	<LOD	0.26	<LOD	0.0589	<LOD	0.0737
13:19:36	#31C	Geochem	59.97	<LOD	0.00	<LOD	0.98	<LOD	0.22	<LOD	0.28
13:22:30	#32C	Geochem	61.50	<LOD	0.00	<LOD	1.15	<LOD	0.26	<LOD	0.33
13:25:13	#33C	Geochem	59.99	<LOD	0.00	<LOD	0.84	<LOD	0.19	<LOD	0.24
13:27:29	#34	Geochem	59.90	<LOD	0.00	<LOD	0.25	<LOD	0.0582	<LOD	0.0727
13:30:33	#35	Geochem	59.21	<LOD	0.00	<LOD	0.32	<LOD	0.0748	<LOD	0.0936
13:32:01	#36	Geochem	59.27	<LOD	0.00	<LOD	0.32	<LOD	0.0736	<LOD	0.0923
13:33:49	#37	Geochem	58.80	<LOD	0.00	<LOD	0.32	<LOD	0.0738	<LOD	0.0924
13:35:40	#38	Geochem	58.98	<LOD	0.00	<LOD	0.43	<LOD	0.097	<LOD	0.1221
13:37:16	#39	Geochem	58.87	<LOD	0.00	<LOD	0.4	<LOD	0.0923	<LOD	0.116
13:42:35	#40	Geochem	58.96	<LOD	0.00	<LOD	0.28	<LOD	0.063	<LOD	0.0789
13:57:19	#41C	Geochem	60.00	<LOD	0.00	<LOD	0.86	<LOD	0.2	<LOD	0.24
13:59:36	#42C	Geochem	60.86	<LOD	0.00	<LOD	0.97	0.0054	0.0017	<LOD	0.27
14:01:51	#43C	Geochem	60.79	<LOD	0.00	<LOD	0.8	<LOD	0.18	<LOD	0.23
14:03:36	#44C	Geochem	60.77	<LOD	0.00	<LOD	0.97	<LOD	0.22	<LOD	0.28
14:05:17	#45C	Geochem	60.87	<LOD	0.00	<LOD	0.92	<LOD	0.21	<LOD	0.26
14:07:43	#46C	Geochem	60.04	<LOD	0.00	<LOD	1.04	<LOD	0.24	<LOD	0.3
14:09:15	#47C	Geochem	60.02	<LOD	0.00	<LOD	1.04	<LOD	0.24	<LOD	0.3
14:12:08	#48	Geochem	58.78	<LOD	0.00	<LOD	0.24	<LOD	0.0539	<LOD	0.0672
14:14:29	#49	Geochem	60.02	<LOD	0.00	<LOD	0.24	<LOD	0.0539	<LOD	0.0674
14:16:24	#50	Geochem	59.82	<LOD	0.00	<LOD	0.24	<LOD	0.055	<LOD	0.0691
14:18:17	#51C	Geochem	61.77	<LOD	0.00	<LOD	0.78	<LOD	0.18	<LOD	0.22
14:20:25	#52C	Geochem	60.05	<LOD	0.00	<LOD	0.79	<LOD	0.18	<LOD	0.22

14:22:25	#54C	Geochem	60.01	<LOD	0.00	<LOD	0.93	<LOD	0.21	<LOD	0.27
14:24:04	#55C	Geochem	60.04	<LOD	0.00	<LOD	0.99	<LOD	0.22	<LOD	0.28
14:25:56	#56C	Geochem	60.06	<LOD	0.00	<LOD	0.87	<LOD	0.19	<LOD	0.24
14:28:27	#57C	Geochem	61.32	<LOD	0.00	<LOD	0.9	<LOD	0.21	<LOD	0.26
14:31:05	#58	Geochem	59.77	<LOD	0.00	<LOD	0.28	<LOD	0.0719	<LOD	0.0897
14:33:30	#59C	Geochem	60.92	<LOD	0.00	<LOD	0.96	<LOD	0.22	<LOD	0.27
14:35:04	#60C	Geochem	60.81	<LOD	0.00	<LOD	0.94	<LOD	0.21	<LOD	0.27
14:36:35	#61C	Geochem	60.18	<LOD	0.00	<LOD	0.9	<LOD	0.21	<LOD	0.26
14:38:41	#62C	Geochem	60.02	<LOD	0.00	<LOD	0.86	<LOD	0.2	<LOD	0.25
14:41:07	#63C	Geochem	59.98	<LOD	0.00	<LOD	0.87	<LOD	0.2	<LOD	0.25
14:43:00	#64C	Geochem	60.02	<LOD	0.00	<LOD	1.02	<LOD	0.23	<LOD	0.29
14:44:39	#65C	Geochem	68.46	<LOD	0.00	<LOD	0.96	<LOD	0.22	<LOD	0.27
14:46:45	#66C	Geochem	60.87	<LOD	0.00	<LOD	1.14	<LOD	0.26	<LOD	0.33
14:49:05	#67C	Geochem	60.01	<LOD	0.00	<LOD	0.96	<LOD	0.22	<LOD	0.27
14:50:37	#68C	Geochem	59.95	<LOD	0.00	<LOD	1.18	<LOD	0.27	<LOD	0.34
14:52:09	#69C	Geochem	60.38	<LOD	0.00	<LOD	1.01	<LOD	0.23	<LOD	0.29
14:54:13	#70C	Geochem	60.06	<LOD	0.00	<LOD	0.85	<LOD	0.19	<LOD	0.24
14:55:45	#71C	Geochem	61.14	<LOD	0.00	<LOD	0.98	<LOD	0.22	<LOD	0.28
14:57:34	#72C	Geochem	60.02	<LOD	0.00	<LOD	0.88	<LOD	0.2	<LOD	0.25
14:59:31	#73C	Geochem	61.97	<LOD	0.00	<LOD	0.86	<LOD	0.2	<LOD	0.24
15:01:19	#74C	Geochem	60.11	<LOD	0.00	<LOD	0.9	<LOD	0.21	<LOD	0.26
15:03:16	#75C	Geochem	59.99	<LOD	0.00	<LOD	1	<LOD	0.23	<LOD	0.29
15:05:52	#76C	Geochem	60.01	<LOD	0.00	<LOD	1.04	<LOD	0.24	<LOD	0.3
15:08:03	#77C	Geochem	60.02	<LOD	0.00	<LOD	0.98	<LOD	0.22	<LOD	0.27
15:09:31	#78C	Geochem	61.91	<LOD	0.00	<LOD	0.97	<LOD	0.22	<LOD	0.27
15:11:33	#79C	Geochem	60.75	<LOD	0.00	<LOD	0.86	<LOD	0.2	<LOD	0.24
15:13:30	#80C	Geochem	61.02	<LOD	0.00	<LOD	0.98	<LOD	0.22	<LOD	0.28
15:15:41	#81C	Geochem	61.21	<LOD	0.00	<LOD	0.78	<LOD	0.18	<LOD	0.22
15:17:46	#82C	Geochem	61.51	<LOD	0.00	<LOD	0.95	<LOD	0.22	<LOD	0.27
15:19:15	#83C	Geochem	60.66	<LOD	0.00	<LOD	0.98	<LOD	0.22	<LOD	0.28

15:21:48	#84	Geochem	59.35	<LOD	0	<LOD	0.26	<LOD	0.0604	<LOD	0.0756
15:24:25	#85C	Geochem	60.18	<LOD	0	<LOD	0.86	<LOD	0.19	<LOD	0.24
15:25:54	#86C	Geochem	61.24	<LOD	0	<LOD	0.98	<LOD	0.22	<LOD	0.28
15:27:58	#87	Geochem	58.93	<LOD	0	<LOD	0.27	<LOD	0.0619	<LOD	0.0775
15:29:44	#88C	Geochem	60.06	<LOD	0	<LOD	1.07	<LOD	0.24	<LOD	0.3
15:31:15	#89C	Geochem	60.03	<LOD	0	<LOD	1.03	<LOD	0.24	<LOD	0.3
15:33:01	#90C	Geochem	60.92	<LOD	0	<LOD	0.87	<LOD	0.2	<LOD	0.25
15:34:49	#91C	Geochem	60.08	<LOD	0	<LOD	0.87	<LOD	0.2	<LOD	0.25
15:36:20	#92C	Geochem	61.14	<LOD	0	<LOD	0.84	<LOD	0.19	<LOD	0.24
15:38:08	#93	Geochem	59.5	<LOD	0	<LOD	0.26	<LOD	0.0586	<LOD	0.0731
15:40:00	#94	Geochem	59.11	<LOD	0	<LOD	0.29	<LOD	0.0655	<LOD	0.0824
15:41:55	#95C	Geochem	60.02	<LOD	0	<LOD	0.96	<LOD	0.22	<LOD	0.27
15:43:38	#96C	Geochem	60.29	<LOD	0	<LOD	0.9	<LOD	0.2	<LOD	0.26
15:45:23	#97C	Geochem	59.98	<LOD	0	<LOD	0.92	<LOD	0.21	<LOD	0.26

Appendix 2-3g. Analytical data from pXRF on xenoliths, ocelli, clasts, and/or matrix. Elements Sn-Pt.											
Date: 12/2/202. Elapsed total time – total time in seconds used to evaluated area of interest. All elements measured in weight %.											
Time	Reading	Mode	Elapsed Time Total	Sn	Sn +/-	Sb	Sb +/-	W	W +/-	Pt	Pt +/-
11:19:11	#1	Cal Check	1:40:48								
11:21:21	#2	Geochem	87.29	0.7462	0.007	0.8117	0.008	<LOD	0.0298	<LOD	0.0666
11:54:55	#3	Geochem	58.88	<LOD	0.15	<LOD	0.2	<LOD	0.0335	<LOD	0.0623
12:02:44	#4C	Geochem	61.24	<LOD	0.45	<LOD	0.59	<LOD	0.1109	<LOD	0.22
12:10:00	#5C	Geochem	60.05	<LOD	0.52	<LOD	0.67	<LOD	0.1041	<LOD	0.22
12:18:48	#6	Geochem	59.58	<LOD	0.16	<LOD	0.2	<LOD	0.0335	<LOD	0.0619
12:22:40	#7C	Geochem	60.60	<LOD	0.48	<LOD	0.63	<LOD	0.1174	<LOD	0.19
12:25:52	#8C	Geochem	60.01	<LOD	0.41	<LOD	0.54	<LOD	0.1016	<LOD	0.19
12:28:42	#9C	Geochem	60.00	<LOD	0.46	<LOD	0.61	<LOD	0.0975	<LOD	0.18
12:32:21	#10C	Geochem	60.19	<LOD	0.42	<LOD	0.56	<LOD	0.0996	<LOD	0.16
12:34:36	#11C	Geochem	60.12	<LOD	0.46	<LOD	0.62	<LOD	0.1166	<LOD	0.22
12:39:25	#12C	Geochem	60.58	<LOD	0.53	<LOD	0.68	<LOD	0.1151	<LOD	0.21
12:41:22	#13C	Geochem	60.06	<LOD	0.51	<LOD	0.68	<LOD	0.1136	<LOD	0.19
12:43:19	#14C	Geochem	60.29	<LOD	0.49	<LOD	0.64	<LOD	0.117	<LOD	0.18
12:45:02	#15C	Geochem	60.57	<LOD	0.52	<LOD	0.68	<LOD	0.1067	<LOD	0.21
12:46:55	#16C	Geochem	60.00	<LOD	0.43	<LOD	0.57	<LOD	0.1077	<LOD	0.2
12:48:48	#17C	Geochem	60.64	<LOD	0.45	<LOD	0.59	<LOD	0.111	<LOD	0.19
12:51:36	#18	Geochem	58.85	<LOD	0.1318	<LOD	0.17	<LOD	0.0324	<LOD	0.0609
12:54:10	#19	Geochem	60.09	<LOD	0.1357	<LOD	0.18	<LOD	0.0334	<LOD	0.063
12:56:29	#20	Geochem	59.22	<LOD	0.21	<LOD	0.27	<LOD	0.0466	<LOD	0.0881
12:58:18	#21	Geochem	60.24	<LOD	0.19	<LOD	0.24	<LOD	0.0395	<LOD	0.076
13:01:07	#22	Geochem	58.90	<LOD	0.2	<LOD	0.27	<LOD	0.0456	<LOD	0.0852
13:03:14	#23	Geochem	58.96	<LOD	0.2	<LOD	0.27	<LOD	0.0477	<LOD	0.0777
13:05:12	#24	Geochem	59.20	<LOD	0.148	<LOD	0.2	<LOD	0.0326	<LOD	0.0606

13:07:21	#25C	Geochem	61.10	<LOD	0.37	<LOD	0.49	<LOD	0.0856	<LOD	0.17
13:09:03	#26C	Geochem	60.55	<LOD	0.39	<LOD	0.51	<LOD	0.0877	<LOD	0.16
13:10:29	#27C	Geochem	60.22	<LOD	0.42	<LOD	0.55	<LOD	0.0957	<LOD	0.2
13:12:08	#28C	Geochem	60.58	<LOD	0.46	<LOD	0.6	<LOD	0.0994	<LOD	0.2
13:14:34	#29C	Geochem	61.94	<LOD	0.58	<LOD	0.77	<LOD	0.1189	<LOD	0.2
13:16:30	#30	Geochem	59.23	<LOD	0.1319	<LOD	0.17	<LOD	0.0298	<LOD	0.0546
13:19:36	#31C	Geochem	59.97	<LOD	0.5	<LOD	0.65	<LOD	0.1136	<LOD	0.2
13:22:30	#32C	Geochem	61.50	<LOD	0.59	<LOD	0.78	<LOD	0.1304	<LOD	0.23
13:25:13	#33C	Geochem	59.99	<LOD	0.44	<LOD	0.57	<LOD	0.0999	<LOD	0.2
13:27:29	#34	Geochem	59.90	<LOD	0.1304	<LOD	0.17	<LOD	0.0301	<LOD	0.0546
13:30:33	#35	Geochem	59.21	<LOD	0.17	<LOD	0.22	0.0051	0.001	<LOD	0.0818
13:32:01	#36	Geochem	59.27	<LOD	0.16	<LOD	0.21	0.0049	0.001	<LOD	0.0833
13:33:49	#37	Geochem	58.80	<LOD	0.16	<LOD	0.21	0.0046	0.0011	<LOD	0.0871
13:35:40	#38	Geochem	58.98	<LOD	0.22	<LOD	0.29	<LOD	0.046	<LOD	0.0903
13:37:16	#39	Geochem	58.87	<LOD	0.21	<LOD	0.27	<LOD	0.0437	0.0035	0.0011
13:42:35	#40	Geochem	58.96	<LOD	0.1414	<LOD	0.19	<LOD	0.032	<LOD	0.0574
13:57:19	#41C	Geochem	60.00	<LOD	0.43	<LOD	0.57	<LOD	0.1055	<LOD	0.2
13:59:36	#42C	Geochem	60.86	<LOD	0.49	<LOD	0.65	<LOD	0.1186	<LOD	0.18
14:01:51	#43C	Geochem	60.79	<LOD	0.41	<LOD	0.54	<LOD	0.0987	<LOD	0.22
14:03:36	#44C	Geochem	60.77	<LOD	0.49	<LOD	0.65	<LOD	0.1149	<LOD	0.26
14:05:17	#45C	Geochem	60.87	<LOD	0.47	<LOD	0.63	<LOD	0.1126	<LOD	0.19
14:07:43	#46C	Geochem	60.04	<LOD	0.53	<LOD	0.7	<LOD	0.1191	<LOD	0.22
14:09:15	#47C	Geochem	60.02	<LOD	0.52	<LOD	0.69	<LOD	0.112	<LOD	0.21
14:12:08	#48	Geochem	58.78	<LOD	0.1204	<LOD	0.16	<LOD	0.0306	<LOD	0.0667
14:14:29	#49	Geochem	60.02	<LOD	0.1199	<LOD	0.16	<LOD	0.03	<LOD	0.0657
14:16:24	#50	Geochem	59.82	<LOD	0.1234	<LOD	0.16	<LOD	0.0322	<LOD	0.0685
14:18:17	#51C	Geochem	61.77	<LOD	0.41	<LOD	0.53	<LOD	0.094	<LOD	0.23
14:20:25	#52C	Geochem	60.05	<LOD	0.4	<LOD	0.53	<LOD	0.1073	<LOD	0.24
14:22:25	#54C	Geochem	60.01	<LOD	0.47	<LOD	0.62	<LOD	0.107	<LOD	0.2
14:24:04	#55C	Geochem	60.04	<LOD	0.51	<LOD	0.67	<LOD	0.1419	<LOD	0.27

14:25:56	#56C	Geochem	60.06	<LOD	0.44	<LOD	0.58	<LOD	0.1068	<LOD	0.21
14:28:27	#57C	Geochem	61.32	<LOD	0.47	<LOD	0.62	<LOD	0.1138	<LOD	0.22
14:31:05	#58	Geochem	59.77	<LOD	0.16	<LOD	0.21	<LOD	0.0395	<LOD	0.0752
14:33:30	#59C	Geochem	60.92	<LOD	0.49	<LOD	0.65	<LOD	0.1044	<LOD	0.21
14:35:04	#60C	Geochem	60.81	<LOD	0.49	<LOD	0.63	<LOD	0.1178	<LOD	0.22
14:36:35	#61C	Geochem	60.18	<LOD	0.47	<LOD	0.61	<LOD	0.1175	<LOD	0.23
14:38:41	#62C	Geochem	60.02	<LOD	0.44	<LOD	0.59	<LOD	0.1185	<LOD	0.25
14:41:07	#63C	Geochem	59.98	<LOD	0.44	<LOD	0.58	<LOD	0.1239	<LOD	0.22
14:43:00	#64C	Geochem	60.02	<LOD	0.53	<LOD	0.69	<LOD	0.1173	<LOD	0.23
14:44:39	#65C	Geochem	68.46	<LOD	0.49	<LOD	0.65	<LOD	0.1055	<LOD	0.21
14:46:45	#66C	Geochem	60.87	<LOD	0.59	<LOD	0.78	<LOD	0.141	<LOD	0.21
14:49:05	#67C	Geochem	60.01	<LOD	0.49	<LOD	0.65	<LOD	0.1094	<LOD	0.21
14:50:37	#68C	Geochem	59.95	<LOD	0.61	<LOD	0.81	<LOD	0.1258	<LOD	0.27
14:52:09	#69C	Geochem	60.38	<LOD	0.52	<LOD	0.68	<LOD	0.1074	<LOD	0.26
14:54:13	#70C	Geochem	60.06	<LOD	0.42	<LOD	0.56	<LOD	0.1059	<LOD	0.21
14:55:45	#71C	Geochem	61.14	<LOD	0.5	<LOD	0.65	<LOD	0.1194	<LOD	0.21
14:57:34	#72C	Geochem	60.02	<LOD	0.45	<LOD	0.59	<LOD	0.11	<LOD	0.19
14:59:31	#73C	Geochem	61.97	<LOD	0.44	<LOD	0.57	<LOD	0.114	<LOD	0.22
15:01:19	#74C	Geochem	60.11	<LOD	0.46	<LOD	0.61	<LOD	0.1232	<LOD	0.21
15:03:16	#75C	Geochem	59.99	<LOD	0.51	<LOD	0.67	<LOD	0.1228	<LOD	0.22
15:05:52	#76C	Geochem	60.01	<LOD	0.53	<LOD	0.69	<LOD	0.105	<LOD	0.21
15:08:03	#77C	Geochem	60.02	<LOD	0.49	<LOD	0.64	<LOD	0.1236	<LOD	0.21
15:09:31	#78C	Geochem	61.91	<LOD	0.5	<LOD	0.65	<LOD	0.1184	<LOD	0.19
15:11:33	#79C	Geochem	60.75	<LOD	0.43	<LOD	0.57	<LOD	0.0969	<LOD	0.2
15:13:30	#80C	Geochem	61.02	<LOD	0.5	<LOD	0.66	<LOD	0.1052	<LOD	0.2
15:15:41	#81C	Geochem	61.21	<LOD	0.4	<LOD	0.52	<LOD	0.102	<LOD	0.23
15:17:46	#82C	Geochem	61.51	<LOD	0.49	<LOD	0.65	<LOD	0.1149	<LOD	0.18
15:19:15	#83C	Geochem	60.66	<LOD	0.5	<LOD	0.67	<LOD	0.1179	<LOD	0.2
15:21:48	#84	Geochem	59.35	<LOD	0.1349	<LOD	0.18	<LOD	0.032	<LOD	0.0589
15:24:25	#85C	Geochem	60.18	<LOD	0.44	<LOD	0.58	<LOD	0.1066	<LOD	0.21

15:25:54	#86C	Geochem	61.24	<LOD	0.5	<LOD	0.66	<LOD	0.1077	<LOD	0.16
15:27:58	#87	Geochem	58.93	<LOD	0.1394	<LOD	0.18	<LOD	0.0323	<LOD	0.0583
15:29:44	#88C	Geochem	60.06	<LOD	0.54	<LOD	0.71	<LOD	0.114	<LOD	0.22
15:31:15	#89C	Geochem	60.03	<LOD	0.53	<LOD	0.7	<LOD	0.1084	<LOD	0.19
15:33:01	#90C	Geochem	60.92	<LOD	0.45	<LOD	0.58	<LOD	0.1022	<LOD	0.22
15:34:49	#91C	Geochem	60.08	<LOD	0.45	<LOD	0.59	<LOD	0.1121	<LOD	0.21
15:36:20	#92C	Geochem	61.14	<LOD	0.44	<LOD	0.56	0.008	0.0024	<LOD	0.17
15:38:08	#93	Geochem	59.5	<LOD	0.1306	<LOD	0.17	<LOD	0.0351	<LOD	0.066
15:40:00	#94	Geochem	59.11	<LOD	0.1474	<LOD	0.19	<LOD	0.0331	<LOD	0.062
15:41:55	#95C	Geochem	60.02	<LOD	0.48	<LOD	0.65	<LOD	0.1129	<LOD	0.22
15:43:38	#96C	Geochem	60.29	<LOD	0.46	<LOD	0.61	<LOD	0.1085	<LOD	0.18
15:45:23	#97C	Geochem	59.98	<LOD	0.48	<LOD	0.63	<LOD	0.107	<LOD	0.16

Appendix 2-3h. Analytical data from pXRF on xenoliths, ocelli, clasts, and/or matrix. Elements Au-Bi.											
Date: 12/2/202. Elapsed total time – total time in seconds used to evaluated area of interest. All elements measured in weight %.											
Time	Reading	Mode	Elapsed Time Total	Au	Au +/-	Hg	Hg +/-	Pb	Pb +/-	Bi	Bi +/-
11:19:11	#1	Cal Check	1:40:48								
11:21:21	#2	Geochem	87.29	<LOD	0.0163	<LOD	0.0102	8.33	0.06	<LOD	0.0422
11:54:55	#3	Geochem	58.88	<LOD	0.0138	<LOD	0.0156	0.0009	0.0002	<LOD	0.0592
12:02:44	#4C	Geochem	61.24	<LOD	0.0458	<LOD	0.0462	<LOD	0.044	<LOD	0.18
12:10:00	#5C	Geochem	60.05	<LOD	0.0469	<LOD	0.0519	<LOD	0.0488	<LOD	0.19
12:18:48	#6	Geochem	59.58	<LOD	0.0136	<LOD	0.0158	<LOD	0.0123	0.0034	0.0006
12:22:40	#7C	Geochem	60.60	<LOD	0.0423	<LOD	0.0521	<LOD	0.0356	<LOD	0.18
12:25:52	#8C	Geochem	60.01	<LOD	0.0402	<LOD	0.0485	<LOD	0.0405	<LOD	0.17
12:28:42	#9C	Geochem	60.00	<LOD	0.0402	<LOD	0.047	<LOD	0.0449	<LOD	0.19
12:32:21	#10C	Geochem	60.19	<LOD	0.0407	<LOD	0.0461	<LOD	0.0462	<LOD	0.19
12:34:36	#11C	Geochem	60.12	<LOD	0.0491	<LOD	0.0541	<LOD	0.0501	<LOD	0.23
12:39:25	#12C	Geochem	60.58	<LOD	0.0491	<LOD	0.0552	0.0021	0.0005	<LOD	0.2
12:41:22	#13C	Geochem	60.06	<LOD	0.0462	<LOD	0.048	0.0016	0.0005	<LOD	0.19
12:43:19	#14C	Geochem	60.29	<LOD	0.0463	<LOD	0.0517	0.0025	0.0005	<LOD	0.18
12:45:02	#15C	Geochem	60.57	<LOD	0.0479	<LOD	0.048	0.0021	0.0005	<LOD	0.2
12:46:55	#16C	Geochem	60.00	<LOD	0.0379	<LOD	0.0485	0.0033	0.0007	<LOD	0.22
12:48:48	#17C	Geochem	60.64	<LOD	0.0443	<LOD	0.0504	<LOD	0.0407	<LOD	0.2
12:51:36	#18	Geochem	58.85	<LOD	0.0135	<LOD	0.0147	0.001	0.0002	<LOD	0.0626
12:54:10	#19	Geochem	60.09	<LOD	0.0141	<LOD	0.0153	0.0019	0.0002	<LOD	0.0663
12:56:29	#20	Geochem	59.22	0.0009	0.0002	<LOD	0.0206	<LOD	0.0163	<LOD	0.0795
12:58:18	#21	Geochem	60.24	<LOD	0.017	<LOD	0.0172	<LOD	0.0142	<LOD	0.0713
13:01:07	#22	Geochem	58.90	<LOD	0.0185	<LOD	0.0195	<LOD	0.0155	<LOD	0.0719
13:03:14	#23	Geochem	58.96	<LOD	0.0189	<LOD	0.0206	0.0008	0.0002	<LOD	0.0723
13:05:12	#24	Geochem	59.20	<LOD	0.0136	<LOD	0.0152	0.0014	0.0002	<LOD	0.0596

13:07:21	#25C	Geochem	61.10	<LOD	0.0361	<LOD	0.037	<LOD	0.0326	<LOD	0.135
13:09:03	#26C	Geochem	60.55	<LOD	0.0368	<LOD	0.0388	<LOD	0.0377	<LOD	0.17
13:10:29	#27C	Geochem	60.22	<LOD	0.0402	<LOD	0.0482	<LOD	0.0393	<LOD	0.19
13:12:08	#28C	Geochem	60.58	<LOD	0.0422	<LOD	0.0432	<LOD	0.0479	<LOD	0.2
13:14:34	#29C	Geochem	61.94	<LOD	0.0512	<LOD	0.0535	<LOD	0.0464	<LOD	0.21
13:16:30	#30	Geochem	59.23	<LOD	0.0123	<LOD	0.0142	0.0011	0.0002	<LOD	0.0506
13:19:36	#31C	Geochem	59.97	<LOD	0.0536	<LOD	0.047	<LOD	0.0436	<LOD	0.18
13:22:30	#32C	Geochem	61.50	<LOD	0.0557	<LOD	0.0493	<LOD	0.0524	<LOD	0.22
13:25:13	#33C	Geochem	59.99	<LOD	0.0395	<LOD	0.05	<LOD	0.0421	<LOD	0.16
13:27:29	#34	Geochem	59.90	0.0006	0.0002	<LOD	0.0136	0.005	0.0002	<LOD	0.0516
13:30:33	#35	Geochem	59.21	0.0009	0.0003	0.0013	0.0003	0.0325	0.0006	<LOD	0.0649
13:32:01	#36	Geochem	59.27	<LOD	0.0189	0.0019	0.0003	0.0339	0.0006	<LOD	0.0663
13:33:49	#37	Geochem	58.80	0.0012	0.0003	0.0015	0.0003	0.0346	0.0006	<LOD	0.0659
13:35:40	#38	Geochem	58.98	<LOD	0.0199	<LOD	0.0202	<LOD	0.0172	0.0021	0.0007
13:37:16	#39	Geochem	58.87	<LOD	0.019	<LOD	0.0201	0.001	0.0002	<LOD	0.0732
13:42:35	#40	Geochem	58.96	<LOD	0.0135	<LOD	0.014	0.0009	0.0002	<LOD	0.0597
13:57:19	#41C	Geochem	60.00	<LOD	0.0436	<LOD	0.0435	0.0026	0.0007	<LOD	0.21
13:59:36	#42C	Geochem	60.86	<LOD	0.0418	<LOD	0.0526	<LOD	0.0405	<LOD	0.18
14:01:51	#43C	Geochem	60.79	<LOD	0.0378	<LOD	0.0447	<LOD	0.0458	<LOD	0.21
14:03:36	#44C	Geochem	60.77	<LOD	0.0513	<LOD	0.0508	<LOD	0.0477	<LOD	0.21
14:05:17	#45C	Geochem	60.87	<LOD	0.0494	<LOD	0.0449	<LOD	0.0428	<LOD	0.21
14:07:43	#46C	Geochem	60.04	<LOD	0.0541	<LOD	0.0505	0.0035	0.0007	<LOD	0.25
14:09:15	#47C	Geochem	60.02	<LOD	0.046	<LOD	0.0549	0.0025	0.0006	<LOD	0.22
14:12:08	#48	Geochem	58.78	<LOD	0.0129	<LOD	0.0137	0.0012	0.0002	<LOD	0.0731
14:14:29	#49	Geochem	60.02	<LOD	0.0125	<LOD	0.0138	0.0018	0.0002	<LOD	0.0724
14:16:24	#50	Geochem	59.82	<LOD	0.0133	<LOD	0.0149	0.0017	0.0002	<LOD	0.0747
14:18:17	#51C	Geochem	61.77	<LOD	0.0398	<LOD	0.0464	<LOD	0.0521	<LOD	0.25
14:20:25	#52C	Geochem	60.05	<LOD	0.0453	<LOD	0.0453	<LOD	0.0548	<LOD	0.24
14:22:25	#54C	Geochem	60.01	<LOD	0.0463	<LOD	0.0463	<LOD	0.0428	<LOD	0.2
14:24:04	#55C	Geochem	60.04	<LOD	0.0596	<LOD	0.0635	<LOD	0.0542	<LOD	0.28

14:25:56	#56C	Geochem	60.06	<LOD	0.0495	<LOD	0.0509	<LOD	0.0477	<LOD	0.24
14:28:27	#57C	Geochem	61.32	<LOD	0.0462	<LOD	0.0505	<LOD	0.047	<LOD	0.2
14:31:05	#58	Geochem	59.77	<LOD	0.0162	<LOD	0.0182	0.0026	0.0003	<LOD	0.0862
14:33:30	#59C	Geochem	60.92	<LOD	0.0406	<LOD	0.0426	<LOD	0.041	<LOD	0.19
14:35:04	#60C	Geochem	60.81	<LOD	0.0496	<LOD	0.0471	<LOD	0.0406	<LOD	0.2
14:36:35	#61C	Geochem	60.18	<LOD	0.0476	<LOD	0.0455	<LOD	0.0405	<LOD	0.2
14:38:41	#62C	Geochem	60.02	<LOD	0.0521	<LOD	0.0506	0.0034	0.0008	<LOD	0.3
14:41:07	#63C	Geochem	59.98	<LOD	0.0556	<LOD	0.0511	<LOD	0.0613	<LOD	0.29
14:43:00	#64C	Geochem	60.02	<LOD	0.0519	<LOD	0.0532	<LOD	0.0405	<LOD	0.19
14:44:39	#65C	Geochem	68.46	<LOD	0.0471	<LOD	0.0521	<LOD	0.0406	<LOD	0.19
14:46:45	#66C	Geochem	60.87	<LOD	0.0598	<LOD	0.0555	<LOD	0.043	<LOD	0.2
14:49:05	#67C	Geochem	60.01	<LOD	0.0504	<LOD	0.0494	<LOD	0.044	<LOD	0.21
14:50:37	#68C	Geochem	59.95	<LOD	0.0509	<LOD	0.051	<LOD	0.0403	<LOD	0.21
14:52:09	#69C	Geochem	60.38	<LOD	0.0497	<LOD	0.0432	<LOD	0.0363	<LOD	0.2
14:54:13	#70C	Geochem	60.06	<LOD	0.0429	<LOD	0.0444	0.0022	0.0007	<LOD	0.22
14:55:45	#71C	Geochem	61.14	<LOD	0.0512	<LOD	0.0508	<LOD	0.0503	<LOD	0.2
14:57:34	#72C	Geochem	60.02	<LOD	0.0457	<LOD	0.0477	0.0021	0.0007	<LOD	0.21
14:59:31	#73C	Geochem	61.97	<LOD	0.0453	<LOD	0.0506	<LOD	0.045	<LOD	0.21
15:01:19	#74C	Geochem	60.11	<LOD	0.0491	<LOD	0.0513	<LOD	0.052	<LOD	0.22
15:03:16	#75C	Geochem	59.99	<LOD	0.0521	<LOD	0.0524	<LOD	0.0422	<LOD	0.19
15:05:52	#76C	Geochem	60.01	<LOD	0.0428	<LOD	0.0524	<LOD	0.0474	<LOD	0.2
15:08:03	#77C	Geochem	60.02	<LOD	0.0466	<LOD	0.0526	<LOD	0.0473	<LOD	0.19
15:09:31	#78C	Geochem	61.91	<LOD	0.0502	<LOD	0.0539	0.0019	0.0006	<LOD	0.21
15:11:33	#79C	Geochem	60.75	<LOD	0.041	<LOD	0.0432	<LOD	0.037	<LOD	0.18
15:13:30	#80C	Geochem	61.02	<LOD	0.0448	<LOD	0.0502	<LOD	0.0442	<LOD	0.19
15:15:41	#81C	Geochem	61.21	<LOD	0.0397	<LOD	0.0443	<LOD	0.0384	<LOD	0.18
15:17:46	#82C	Geochem	61.51	<LOD	0.0418	<LOD	0.0554	<LOD	0.0435	<LOD	0.21
15:19:15	#83C	Geochem	60.66	<LOD	0.0562	<LOD	0.0518	<LOD	0.0517	<LOD	0.22
15:21:48	#84	Geochem	59.35	<LOD	0.013	<LOD	0.0146	0.0012	0.0002	<LOD	0.0601
15:24:25	#85C	Geochem	60.18	<LOD	0.0461	<LOD	0.0513	0.0022	0.0007	<LOD	0.23

15:25:54	#86C	Geochem	61.24	<LOD	0.0491	<LOD	0.0501	<LOD	0.036	<LOD	0.19
15:27:58	#87	Geochem	58.93	<LOD	0.0137	<LOD	0.0145	0.001	0.0002	<LOD	0.0599
15:29:44	#88C	Geochem	60.06	<LOD	0.0474	<LOD	0.0502	<LOD	0.0425	<LOD	0.2
15:31:15	#89C	Geochem	60.03	<LOD	0.0481	<LOD	0.0468	<LOD	0.0417	<LOD	0.19
15:33:01	#90C	Geochem	60.92	<LOD	0.0441	<LOD	0.0474	<LOD	0.039	<LOD	0.17
15:34:49	#91C	Geochem	60.08	<LOD	0.0489	<LOD	0.0481	<LOD	0.0484	<LOD	0.22
15:36:20	#92C	Geochem	61.14	<LOD	0.0354	<LOD	0.0502	<LOD	0.0364	<LOD	0.1479
15:38:08	#93	Geochem	59.5	<LOD	0.0149	<LOD	0.0155	0.0082	0.0003	<LOD	0.0707
15:40:00	#94	Geochem	59.11	<LOD	0.0139	<LOD	0.0154	<LOD	0.013	<LOD	0.06
15:41:55	#95C	Geochem	60.02	<LOD	0.0481	<LOD	0.0496	<LOD	0.0351	<LOD	0.18
15:43:38	#96C	Geochem	60.29	<LOD	0.0438	<LOD	0.051	<LOD	0.041	<LOD	0.19
15:45:23	#97C	Geochem	59.98	<LOD	0.0392	<LOD	0.0481	<LOD	0.0426	<LOD	0.18

Appendix 2-3i. Analytical data from pXRF on xenoliths, ocelli, clasts, and/or matrix. Elements Rh-Cd.

Date: 12/2/202. Elapsed total time – total time in seconds used to evaluated area of interest. All elements measured in weight %.

Time	Reading	Mode	Elapsed Time Total	Th	Th +/-	U	U +/-
11:19:11	#1	Cal Check	1:40:48				
11:21:21	#2	Geochem	87.29	0.2	0.0028	<LOD	0.0066
11:54:55	#3	Geochem	58.88	<LOD	0.0414	<LOD	0.0266
12:02:44	#4C	Geochem	61.24	<LOD	0.1279	<LOD	0.0857
12:10:00	#5C	Geochem	60.05	<LOD	0.1368	<LOD	0.0785
12:18:48	#6	Geochem	59.58	<LOD	0.0381	<LOD	0.0215
12:22:40	#7C	Geochem	60.60	<LOD	0.1242	<LOD	0.0778
12:25:52	#8C	Geochem	60.01	<LOD	0.1194	<LOD	0.0733
12:28:42	#9C	Geochem	60.00	<LOD	0.1302	<LOD	0.0944
12:32:21	#10C	Geochem	60.19	<LOD	0.1351	<LOD	0.098
12:34:36	#11C	Geochem	60.12	<LOD	0.16	<LOD	0.1202
12:39:25	#12C	Geochem	60.58	<LOD	0.1412	<LOD	0.0906
12:41:22	#13C	Geochem	60.06	<LOD	0.1297	<LOD	0.0813
12:43:19	#14C	Geochem	60.29	<LOD	0.1284	<LOD	0.0862
12:45:02	#15C	Geochem	60.57	<LOD	0.1401	<LOD	0.0939
12:46:55	#16C	Geochem	60.00	<LOD	0.1494	<LOD	0.0987
12:48:48	#17C	Geochem	60.64	<LOD	0.1383	<LOD	0.0978
12:51:36	#18	Geochem	58.85	0.0015	0.0004	<LOD	0.0309
12:54:10	#19	Geochem	60.09	0.0023	0.0004	<LOD	0.0333
12:56:29	#20	Geochem	59.22	<LOD	0.0559	<LOD	0.0336
12:58:18	#21	Geochem	60.24	<LOD	0.0502	<LOD	0.0307
13:01:07	#22	Geochem	58.90	<LOD	0.0505	<LOD	0.0256

13:03:14	#23	Geochem	58.96	<LOD	0.0507	<LOD	0.0262
13:05:12	#24	Geochem	59.20	0.001	0.0003	<LOD	0.0267
13:07:21	#25C	Geochem	61.10	<LOD	0.0929	<LOD	0.0574
13:09:03	#26C	Geochem	60.55	<LOD	0.1184	<LOD	0.0878
13:10:29	#27C	Geochem	60.22	<LOD	0.1305	<LOD	0.0916
13:12:08	#28C	Geochem	60.58	<LOD	0.1346	<LOD	0.1011
13:14:34	#29C	Geochem	61.94	<LOD	0.1462	<LOD	0.0861
13:16:30	#30	Geochem	59.23	<LOD	0.0349	<LOD	0.0211
13:19:36	#31C	Geochem	59.97	<LOD	0.1246	<LOD	0.0733
13:22:30	#32C	Geochem	61.50	<LOD	0.15	<LOD	0.0853
13:25:13	#33C	Geochem	59.99	<LOD	0.1082	<LOD	0.0577
13:27:29	#34	Geochem	59.90	0.0011	0.0003	<LOD	0.0218
13:30:33	#35	Geochem	59.21	<LOD	0.0446	<LOD	0.0285
13:32:01	#36	Geochem	59.27	<LOD	0.0456	<LOD	0.0289
13:33:49	#37	Geochem	58.80	<LOD	0.0454	<LOD	0.0291
13:35:40	#38	Geochem	58.98	<LOD	0.0534	0.001	0.0002
13:37:16	#39	Geochem	58.87	<LOD	0.0513	0.0007	0.0002
13:42:35	#40	Geochem	58.96	0.001	0.0003	<LOD	0.027
13:57:19	#41C	Geochem	60.00	0.0047	0.0012	<LOD	0.0982
13:59:36	#42C	Geochem	60.86	<LOD	0.1244	<LOD	0.0734
14:01:51	#43C	Geochem	60.79	<LOD	0.1424	<LOD	0.1051
14:03:36	#44C	Geochem	60.77	<LOD	0.1486	<LOD	0.1005
14:05:17	#45C	Geochem	60.87	<LOD	0.143	<LOD	0.0956
14:07:43	#46C	Geochem	60.04	<LOD	0.18	<LOD	0.1304
14:09:15	#47C	Geochem	60.02	<LOD	0.16	<LOD	0.0982
14:12:08	#48	Geochem	58.78	0.0091	0.0005	<LOD	0.0311
14:14:29	#49	Geochem	60.02	0.0087	0.0005	0.0012	0.0003
14:16:24	#50	Geochem	59.82	0.0086	0.0005	0.0014	0.0003
14:18:17	#51C	Geochem	61.77	0.0063	0.0016	<LOD	0.1096
14:20:25	#52C	Geochem	60.05	0.0079	0.0016	<LOD	0.1032

14:22:25	#54C	Geochem	60.01	<LOD	0.1382	<LOD	0.0975
14:24:04	#55C	Geochem	60.04	<LOD	0.2	<LOD	0.17
14:25:56	#56C	Geochem	60.06	<LOD	0.16	<LOD	0.1249
14:28:27	#57C	Geochem	61.32	<LOD	0.1382	<LOD	0.0916
14:31:05	#58	Geochem	59.77	0.0063	0.0005	<LOD	0.0446
14:33:30	#59C	Geochem	60.92	<LOD	0.1353	<LOD	0.0934
14:35:04	#60C	Geochem	60.81	<LOD	0.1388	<LOD	0.0883
14:36:35	#61C	Geochem	60.18	<LOD	0.1408	<LOD	0.0958
14:38:41	#62C	Geochem	60.02	0.0075	0.0018	<LOD	0.17
14:41:07	#63C	Geochem	59.98	<LOD	0.21	<LOD	0.19
14:43:00	#64C	Geochem	60.02	<LOD	0.134	<LOD	0.0811
14:44:39	#65C	Geochem	68.46	<LOD	0.1337	<LOD	0.0809
14:46:45	#66C	Geochem	60.87	<LOD	0.1439	<LOD	0.0817
14:49:05	#67C	Geochem	60.01	<LOD	0.1431	<LOD	0.0928
14:50:37	#68C	Geochem	59.95	<LOD	0.1447	<LOD	0.0774
14:52:09	#69C	Geochem	60.38	<LOD	0.1371	<LOD	0.0856
14:54:13	#70C	Geochem	60.06	<LOD	0.1497	<LOD	0.1082
14:55:45	#71C	Geochem	61.14	<LOD	0.1398	<LOD	0.0953
14:57:34	#72C	Geochem	60.02	<LOD	0.1439	<LOD	0.1058
14:59:31	#73C	Geochem	61.97	<LOD	0.141	<LOD	0.0973
15:01:19	#74C	Geochem	60.11	<LOD	0.1497	<LOD	0.1033
15:03:16	#75C	Geochem	59.99	<LOD	0.1347	<LOD	0.0791
15:05:52	#76C	Geochem	60.01	<LOD	0.1404	<LOD	0.0789
15:08:03	#77C	Geochem	60.02	<LOD	0.1291	<LOD	0.0813
15:09:31	#78C	Geochem	61.91	<LOD	0.1449	<LOD	0.1014
15:11:33	#79C	Geochem	60.75	<LOD	0.1286	<LOD	0.0789
15:13:30	#80C	Geochem	61.02	<LOD	0.1385	<LOD	0.0923
15:15:41	#81C	Geochem	61.21	<LOD	0.1254	<LOD	0.0835
15:17:46	#82C	Geochem	61.51	<LOD	0.1486	<LOD	0.1051
15:19:15	#83C	Geochem	60.66	<LOD	0.15	<LOD	0.1091

15:21:48	#84	Geochem	59.35	0.0018	0.0004	<LOD	0.0274
15:24:25	#85C	Geochem	60.18	0.0048	0.0013	<LOD	0.1027
15:25:54	#86C	Geochem	61.24	<LOD	0.1312	<LOD	0.0812
15:27:58	#87	Geochem	58.93	<LOD	0.0415	<LOD	0.0283
15:29:44	#88C	Geochem	60.06	<LOD	0.1372	<LOD	0.0714
15:31:15	#89C	Geochem	60.03	<LOD	0.1334	<LOD	0.0703
15:33:01	#90C	Geochem	60.92	<LOD	0.1186	<LOD	0.067
15:34:49	#91C	Geochem	60.08	<LOD	0.15	<LOD	0.0984
15:36:20	#92C	Geochem	61.14	<LOD	0.104	<LOD	0.0577
15:38:08	#93	Geochem	59.5	0.006	0.0004	<LOD	0.0307
15:40:00	#94	Geochem	59.11	<LOD	0.0419	<LOD	0.0278
15:41:55	#95C	Geochem	60.02	<LOD	0.1286	<LOD	0.0695
15:43:38	#96C	Geochem	60.29	<LOD	0.1313	<LOD	0.087
15:45:23	#97C	Geochem	59.98	<LOD	0.1267	<LOD	0.0857